CHARACTERIZATION OF CENTRIFUGALLY-LOADED FLAME MIGRATION FOR ULTRA-COMPACT COMBUSTORS

DISSERTATION

Kenneth D. LeBay, Captain, USAF

AFIT/DS/ENY/11-22

DEPARTMENT OF THE AIR FORCE
AIR UNIVERSITY

AIR FORCE INSTITUTE OF TECHNOLOGY

Wright-Patterson Air Force Base, Ohio

AFIT/DS/ENY/11-22

CHARACTERIZATION OF CENTRIFUGALLY-LOADED FLAME MIGRATION FOR ULTRA-COMPACT COMBUSTORS

DISSERTATION

Presented to the Faculty

Graduate School of Engineering and Management

Air Force Institute of Technology

Air University

Air Education and Training Command

in Partial Fulfillment of the Requirements for the

Degree of Doctor of Philosophy

Kenneth D. LeBay, B.S., M.S.

Captain, USAF

October 2011

AFIT/DS/ENY/11-22

CHARACTERIZATION OF CENTRIFUGALLY-LOADED FLAME MIGRATION FOR ULTRA-COMPACT COMBUSTORS

Kenneth D. LeBay, B.S., M.S.
Captain, USAF

Approved:

Marc D. Polanka	3 JAN 2012
Marc D. Polanka, Ph.D. (Chairman)	Date
Paul King	21 Oct 11
Paul I. King, Ph.D. (Member)	Date
Mark F. Reeder	3 Jan 2012
Mark F. Reeder, Ph.D. (Member)	Date
	26 Oct 2011
Kevin C. Gross, Ph.D. (Member)	Date
Joseph Zelina	4 JAN 2012
Joseph Zelina, Ph.D. (Member)	Date

Accepted:

M U Thomas	10 Jan 2012
M. U. Thomas, Ph.D. Dean, Graduate School of Engineering and Management	Date

Abstract

The Air Force Research Laboratory (AFRL) has designed a centrifugally-loaded Ultra-Compact Combustor (UCC) showing viable merit for reducing gas turbine combustor length by as much as 66%. The overarching goal of this research was to characterize the migration of centrifugally-loaded flames in a sectional model of the UCC to enable scaling of the design from 15 cm to the 50-75 cm diameter of most engines. Two-line Planar Laser-Induced Fluorescence thermometry (PLIF) of OH, time-resolved Particle Image Velocimetry (PIV), and high-speed video data were collected. Using a sectional UCC model, the flame migration angle was determined to be a function of the UCC/core velocity ratio (VR) while both the VR and the centrifugal or "g-load" affected the migration quantity. Higher g-loads and lower VRs yielding higher migration but lower VRs had lower core flow temperatures due to higher core air mass flow. A comparison of the straight and curved UCC sections showed the centrifugal load increased the flame migration but increased unsteadiness. The flame migration into the core was estimated using pressure and temperature measurements upstream, and PIV measurements downstream of the core flow interface with constant density and velocity profile assumptions. The flame migration quantity was used to estimate the core flow temperature which was in relatively good agreement with the measured PLIF values. The migration quantity scaled relatively linearly with the UCC tangential velocity, which corresponds to the g-load value, with the slope determined by the VR. A simple analytical model resulted for the dependence of the migration quantity on the tangential velocity and VR. The quantitative relationships determined in this research provided a detailed description of the migration of centrifugally-loaded flames in a sectional UCC.

Acknowledgements

First, I must thank my advisor, Dr. Marc Polanka for all his mentoring, guidance, and countless hours revising this document. I must also like to thank my research committee, Dr. Paul King, Dr. Mark Reeder, Dr. Kevin Gross, and Dr. Joe Zelina, for their invaluable help. A special thanks to Lt. Col. Rich Branam for bringing me onto the UCC project. Also, thank you to the Air Force Office of Scientific Research and the Air Force Research Laboratory, Propulsion Directorate, Combustion Branch for funding this research.

I must also thank the ENY lab technicians under Mr. Jay Anderson, specifically Mr. John Hixenbaugh and Mr. Chris Zickefoose. I would also like to thank the many colleagues, master's students, summer interns, and co-ops who have assisted me. From Jake, Amy, and Stan to Aaron, Levi, Andy, Brian, Firas, Josh, Adam, and JW to the Mike's, Tess, Sam, and Eric, you have all played a significant role in some aspect of my research.

Throughout my life I have had many great mentors who have added fuel to my fire for scientific discovery starting with my parents and family, and my elementary, junior high, and high school teachers. Also, I must specifically thank the professors at the Illinois Institute of Technology and the University of Southern California who taught me fluid mechanics, propulsion, and ultimately combustion that ultimately led me to my own research path. Finally, a special thanks to the AFIT faculty and my fellow Ph.D. classmates who have made this an enjoyable, albeit intense, experience.

Most importantly, I must thank my wife. Without your never-ending love and support, I'm not sure I would have finished this scholastic marathon. Like our love, words simply cannot do justice.

Finally, I must give thanks to God, for I know that I am truly blessed.

Kenneth D. LeBay

Table of Contents

Page

List of Figures

Figure Page

Figure Page

Figure Page

Figure Page

Figure Page

Figure Page

Figure Page

List of Tables

List of Abbreviations

Abbreviation Page

Abbreviation		Page
FFT	Fast Fourier Transform	134
FRS	Filtered Rayleigh Scattering	244

List of Symbols

Symbol		Page
cm	centimeter	4
S	entropy	10
T	temperature	10
T_{03}	combustor inlet temperature	11
T_{04}	combustor exit temperature	11
Q_b	combustor heat addition	11
T_{05}	turbine exit temperature	11
Q_{ab}	afterburner heat addition	11
T_{06}	afterburner exit temperature	11
T_{07}	nozzle exit temperature	11
ϕ	equivalence ratio	23
mm	millimeter	26
$\dot{m}_{UCC}$	UCC mass flow rate	26
$\dot{m}_{core}$	core mass flow rate	26
m	number of vane passages in the sectional model	26
n	total number of vane passages	26
ρ	density	27
V	velocity	27
A	area	27
G	g-load	28
V_{tan}	tangential velocity	28
r	radius of curvature	28

Symbol Page

CHARACTERIZATION OF CENTRIFUGALLY-LOADED FLAME MIGRATION FOR ULTRA-COMPACT COMBUSTORS

I. Introduction

1.1 Research and Design Perspective

Despite the necessity of research in developing alternative energy sources, the realism is that the combustion of hydrocarbon fuels will likely continue to be the prevalent energy source for the foreseeable future. However, this vital process that is the life-blood of society still largely remains a mystery. Paraphrased from a combustion lecture by Dr. Fokion Egolfopoulos [24], "combustion combines turbulent fluid flow, which is not well-understood, with atomic and molecular chemistry, which is also not well-understood, and adds in strange transport phenomena, but we know it works because we all got in our cars and drove here today. This is a major issue from an engineering perspective."

From a military standpoint, the largest percentage of hydrocarbon fuel is used for aviation according to Karbuz [25]. Military design trends typically call for next-generation aircraft to fly faster, farther, and higher than previous aircraft generations, while range and fuel economy are the drivers for commercial aviation. Combining these trends with decreasing gas turbine engine research funding led to the creation of the Versatile Affordable Advanced Turbine Engines (VAATE) initiative [26]. The VAATE initiative calls for aggressive improvement in gas turbine technology such as a 200% increase in engine thrust-to-weight ratio, a 25% reduction in fuel consumption, and a 60% reduction in engine lifecycle costs (development, procurement,

maintenance, disposal) [26]. In order to meet VAATE's aggressive goals every engine component must be examined for improvement. Inline with VAATE, combustors currently under development by the Air Force Research Laboratory (AFRL) have been specifically designed to reduce the size, and subsequently weight, of the combustor by using alternative flow paths from the traditional linear propagation, specifically the high-g Ultra-Compact Combustor (UCC) investigated by Zelina et al. [7].

1.2 Ultra Compact Combustor Concept

Figure 1 shows images of a conventional combustor (top) and the UCC (bottom). The high g-load UCC concept was based on data collected from the Trapped Vortex Combustor (TVC) by Roquemore et al. [6], research on a jet swirled combustor developed by Yonezawa et. al. [27], and the research conducted by Lewis [13] on high-g flame speed. As shown in Figure 1, conventional combustors use a linear flowpath, whereas the UCC uses an off-axis combustor cavity that creates high angular acceleration levels, on the order of 500-4,000 g's, resulting in strong centrifugal and buoyant forces. According to Lewis, the centrifugal forces alone work to significantly increase the flame speed while the combination of the centrifugal and buoyant forces creates strong density gradients [13]. According to Zelina, et al., the UCC air inlets were angled 45 degrees inward from the circumferential direction to promote recirculation within the cavity such that combustion can efficiently occur even in a fuel rich regime, around 97% at $\phi = 2.3$ [7]. As the combustion process nears completion, buoyancy keeps the heavier reacting species in the circumferential cavity while allowing the lighter products to travel out of the cavity and into the main flow. This unique combination works to significantly reduce the required combustor length, with the UCC design projecting approximately 66% length reduction according to Zelina et. al [7]. While existing computational and experimental UCC research has shown the viability

of the design, the research efforts have not focused on gaining an understanding of the physical mechanisms responsible for the performance increase. This is a pivotal problem to be solved before the UCC concept can be scaled to a larger size engine while maintaining the performance increase.

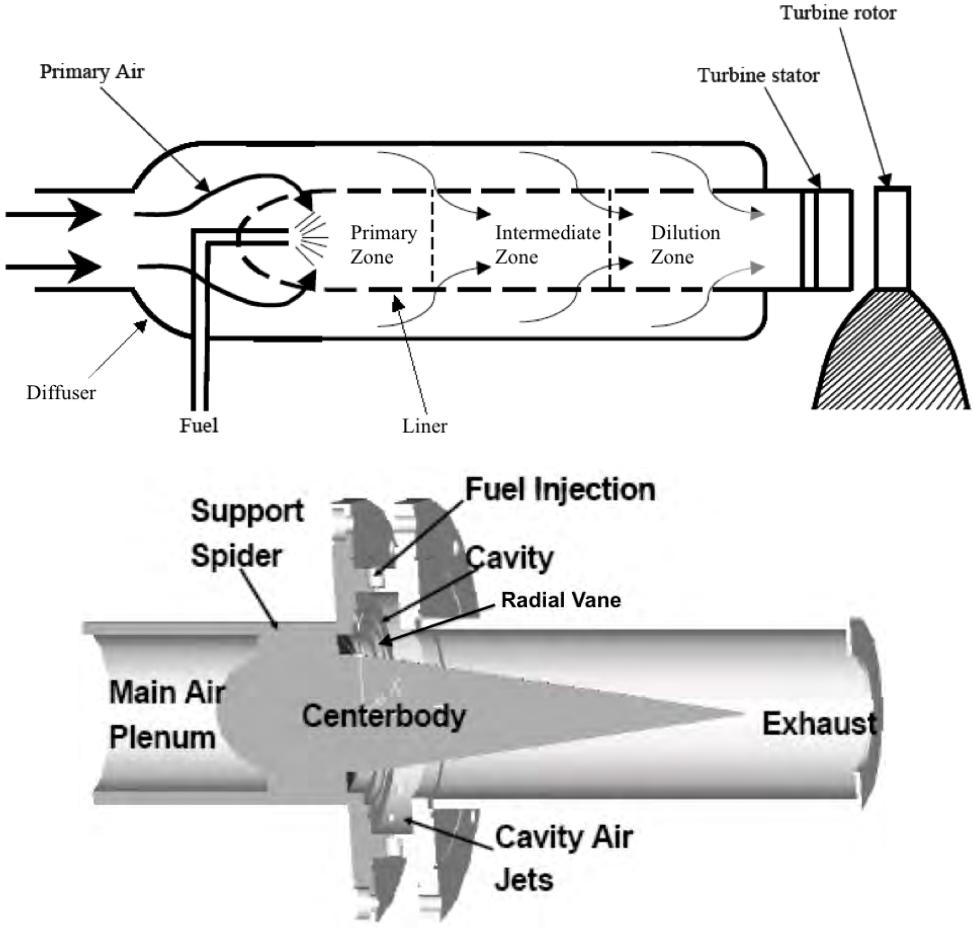

Figure 1. Conventional axial combustor (top) from Mattingly [1] and Ultra Compact Combustor (UCC) (bottom) from Zelina et al. [2]

AFRL's current UCC rig, shown in Figure 1, is approximately 15 cm in diameter and provides g-loading up to 4,000 g's for hydrocarbon fuel depending on mass flow rate as measured by Quaale et al. [28]. However, to fully realize the projected thermodynamic cycle benefits, such as increased Thrust-to-Weight ratio (T/W) and decreased Thrust Specific Fuel Consumption (TSFC), it is desired to scale up the

UCC to a larger class of engines requiring a diameter in the 50-75 cm range. As the centrifugal-load, or g-load is inversely proportional to the radius of curvature, the scaling of a UCC to a larger diameter could reduce the g-load down to the lower limits of the buoyant bubble flame regime, as defined by Lewis [13], or significantly higher tangential velocities would be required to maintain the same g-load. Further, a real engine operation regime would experience large variations in combustor mass flow rates, due to inlet mass flow and/or throttling, and subsequent operation over a large range of g-loads. Thus, it is of vital importance to accurately characterize the effect of the g-load on the UCC design both from a characterization over multiple g-loads side and from a practical side of how the mass flow rates, with heat addition, lead to reaching a specific g-load.

In addition to varying g-load, a larger scale UCC will require a significantly taller radial vane, depicted in Figure 1. This requires the understanding of scaling the radial vane from the previously used 14 mm height, from Drenth and Thomas [9; 29], to the order of 50-60 mm height. The feasibility of hot gas migration across a vane of that height must be demonstrated in addition to characterization of UCC/core Mass Flow Ratio (MFR) and UCC/core Velocity Ratio (VR) scaling as a function of vane height to enhance the span-wise distribution of the migrating mass from the UCC into the core flow across the full radial vane span.

At Air Force Institute of Technology (AFIT) the Combustion Optimization and Analysis Laser laboratory (COAL lab), as designed by Anderson [8], was specifically created to investigate the fundamental UCC dynamics and to determine the UCC's feasibility on larger scale engines. Working in conjunction with AFRL, AFIT researchers focused specifically on using sectional models to characterize the physical phenomena of the UCC design and on demonstrating the feasibility of the UCC on the larger scale. AFIT researchers currently use straight and curved UCC sections as

shown in Figure 2, and by varying the cavity mass flow, the g-loading can be varied from 0 g's (for the straight section) and from 50-2,000 g's (for the curved section) depending on mass flow and fuel used. The straight section removes the g-load contribution in order to isolated variations of the g-load using both the straight and curved UCC sections at identical conditions. Figure 3 shows the location of the radial vane airfoil on both AFRL's full annular rig and in AFIT's sectional rig. This figure illustrates the hardware configurability advantage of using a sectional UCC model instead of an annular model to address the issues of the g-load contribution and scaling of the radial vane height.

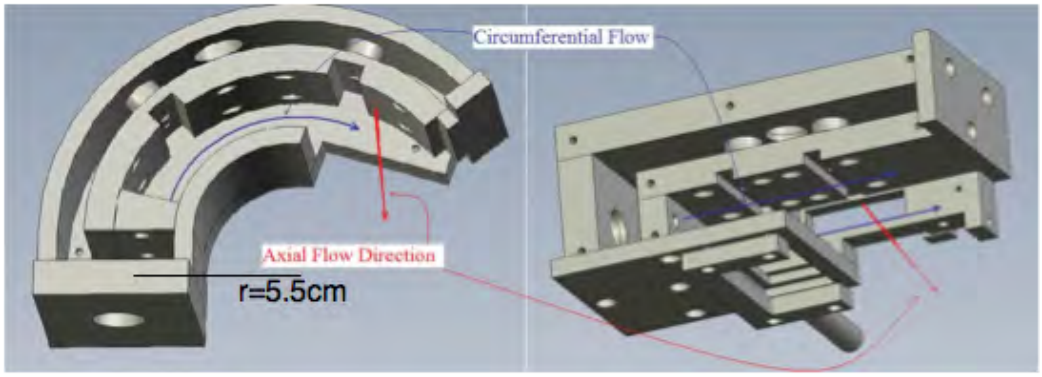

Figure 2. AFIT UCC sections: curved (left) and straight (right) from Hankins [3]

Previous AFIT research by Drenth [9] compared the flame shape at the ambient UCC exit with the straight and curved UCC sections. The straight section ambient exit flame exhibited a distinct v-shape whereas the curved section flame had more of a parabolic shape. This discrepancy must be understood as it may indicate of a change in the flowfield within the UCC due of curvature.

1.3 Inter-Turbine Burning

Jet engine design trend pushes for maximizing thrust-to-weight ratio and efficiency while reducing size and weight according to Vogeler [30]. Engine designers can benefit from the use of a highly compact combustor operating near or above stoichiometric

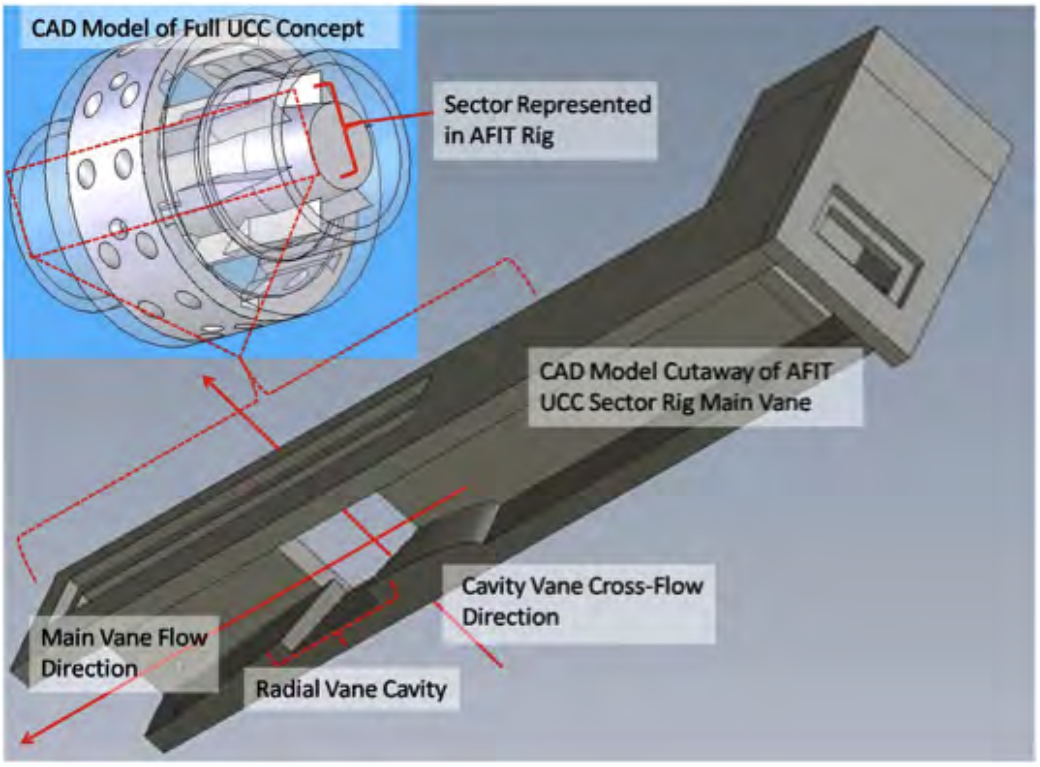

Figure 3. Annular UCC radial vane location from Greenwood [4] (inset) and sectional UCC model radial vane from Hankins [3]

conditions ($\phi = 1.0$), with either inter or intra-turbine burning as illustrated by Vogeler and Sirignano and Liu [30; 5]. The benefit of inter or intra-turbine burning is due to the addition of a reheat segment to the engine's thermodynamic cycle which aligns the heat addition with the expansion through the turbine. The main limitation to using inter or intra-turbine burning is the turbine inlet flow conditions, specifically the need for a uniform temperature profile and complete combustion to avoid adverse effects on the turbine blades as demonstrated by Lukachko, et al. and Kirk et al. [31; 32]. While intra-turbine burning, or the intentional creation of a reacting regime through the turbine flow path, would yield a nearly ideal constant temperature turbine expansion, the high-pressure turbine, which is already material temperature limited, would be a limiting component. Alternatively, inter-turbine burning (ITB), or burning between turbine stages following the main combustor, is still a discrete approximation to a constant temperature cycle, but according to Sirignano and Liu would require a significantly smaller combustor to avoid a weight detriment relative to the added energy [5]. The UCC is an ideal candidate realization of the ITB concept where two UCCs would be contained in the same engine, one as a main combustor reducing the size and weight, and a second between the high pressure turbine and low pressure turbine functioning as an ITB. With the UCC poised as a replacement for a conventional combustor and operating as an ITB, gaining a fundamental understanding of the UCC dynamics is key to the future of the design.

1.4 Research Objectives

The overarching goal of this research was to quantitatively characterize the migration of centrifugally-loaded flames within a sectional UCC model. Underneath that goal are three main objectives. First, further investigation is needed to understand the v-shaped flame at the ambient UCC exit in the absence of a g-load. The

goal of this objective was to understand why there is a fundamental change in the flame shape with the addition of the g-load. Second, a UCC designed for a larger engine would require a significantly taller radial vane which required first demonstration of the feasibility to migrate hot gases across that distance and an understanding of the impact on the mass flow and velocity ratios which directly impact the flame migration resultant from changes in the vane height dimension. The objective was to understand the extent to which the vane height reduced the flame migration into the core flow. Third, due to potentially large changes in g-load over the engine operating regime, the effect of centrifugal-load variation must be understood. The objective was to understand the extent to which the flame migration was lower at reduced g-loads. While these objectives were distinct efforts on their own, the overall result was a more global understanding of the migration of centrifugally-loaded flames.

II. Background

2.1 Conventional Combustors

The purpose of a gas turbine engine is to convert energy stored in the chemical bonds of the fuel into mechanical energy to be used as work in moving an aircraft from one place to another or to generate power. All gas turbine engines have a common gas generator or "core" consisting of a low-pressure compressor, high-pressure compressor, combustor, high pressure turbine (HPT), and low pressure turbine (LPT) as shown in Figure 4 from Mattingly [1]. As stated by Mattingly, this gas generator core is common to all turbojet, turboprop, turbofan, and turboshaft engines. A conventional combustor, such as follows the compressor and preludes the turbine, is shown in Figure 4, from Mattingly [1]. According to Mattingly, an optimal combustor would have the following properties: total combustion, minimum pressure loss, stability, uniform temperature distribution, short length, small cross section, reduced blowout limits, relight capability, and wide operation over varying mass flow rates, pressures, and temperatures [1].

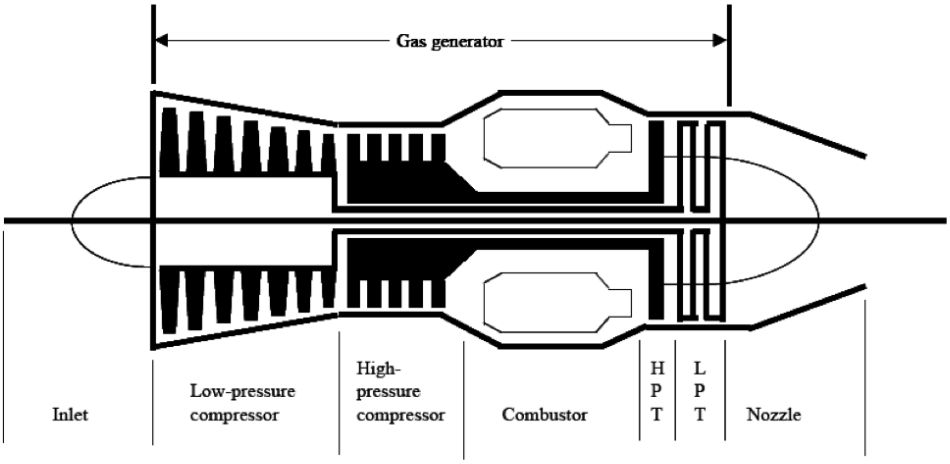

Figure 4. Illustration of a conventional gas turbine engine from Mattingly [1]

A conventional combustor was detailed in Figure 5. This figure illustrates two distinct zones, the primary and secondary zones. As defined by Mattingly, in the primary zone, high-temperature air enters from the compressor and flows around the fuel injectors which spray atomized liquid-droplet fuel and begin the combustion process [1]. Similarly, Mattingly stated that the primary zone establishes flame stability and the fuel air mixture is slightly fuel-rich. In the intermediate and dilution zones, additional air is added to create a fuel-lean mixture, lower than the flame stability limit, where temperatures are cooled below the turbine limits [1]. Since this process occurs in the axial direction, sufficient length is required to reach complete combustion prior to entering the turbine section. Because short length is a design requirement, complete combustion is not always reached and inefficiency results.

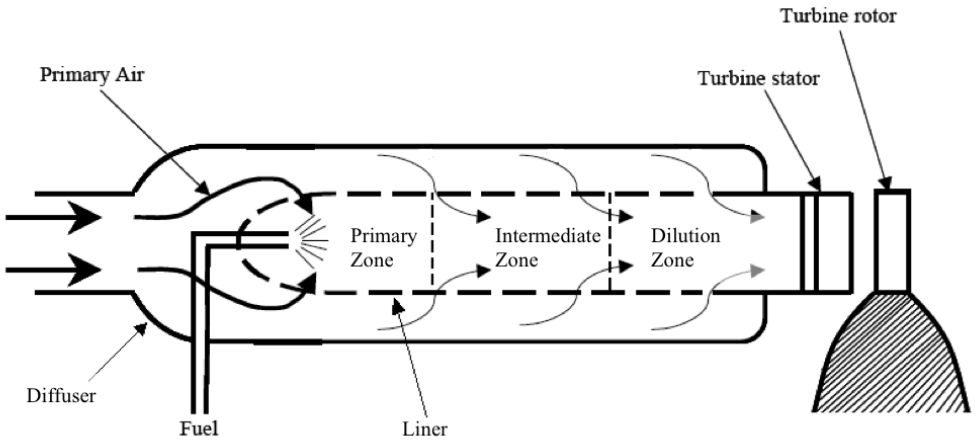

Figure 5. Illustration of a conventional gas turbine engine combustor from Mattingly [1]

Even if complete combustion is reached, the heat addition process, which is necessary for power and thrust generation, produces inefficiencies via entropy generation, according to Mattingly [1]. The relation of the heat addition to entropy, S, generation is represented according to the temperature, T, rise in a T-S diagram. The T-S diagram of a typical turbojet engine with afterburner is shown in Figure 6 and represents

the thermodynamic cycle of the engine. From the inlet to T_{03} is the temperature rise that occurs over the inlet and the compressor where the air is compressed and subsequently the temperature rises, this portion of the process is assumed to be isentropic (constant entropy). From T_{03} to T_{04} is the combustor where Q_b is the heat added due to burning and the resultant temperature and entropy increases. Following the combustor, the gas is ideally expanded isentropically through the turbine and the temperature decreases from T_{04} to T_{05}. Following the turbine, additional heat, Q_{ab}, is added in the afterburner with the temperature and entropy rise from T_{05} to T_{06}. Finally, through the nozzle the gas is again isentropically expanded to T_{07}. Sirignano and Liu stated that significant cycle issues arise in real-world afterburners due to poor combustion efficiency as a result of the process occurring at lower pressures and temperatures. [5].

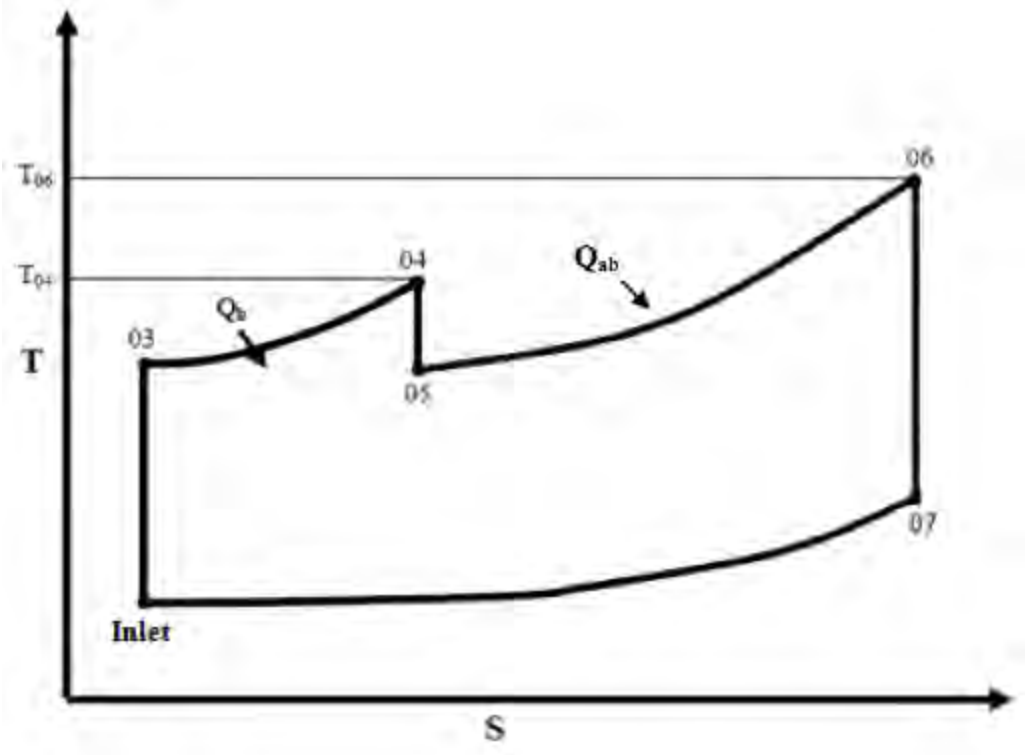

Figure 6. Standard ideal Brayton cycle with afterburner [5]

2.2 Trapped Vortex Combustor

The TVC resulted from an attempt at improving current combustor design trends. The TVC design tested by Roquemore et al. traps the flame in a vortex away from the main axial flow through the combustor as shown in Figure 7 [6]. By vortex trapping, the same flame residence length of a conventional combustor is wrapped into a smaller physical space. This translates into decreased weight, yielding a higher thrust-to-weight ratio and consequently improved performance.

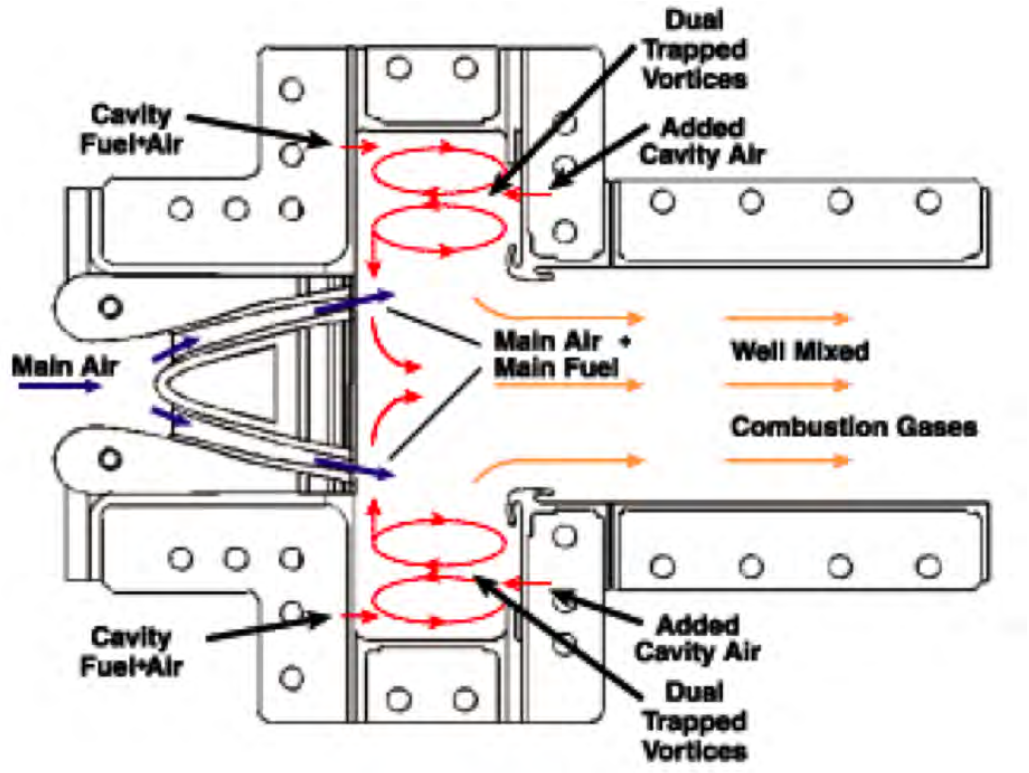

Figure 7. Illustration of the Trapped Vortex Combustor (TVC) concept [6]

2.3 Ultra Compact Combustor

The UCC concept is based on data collected from Roquemore et. al on the TVC [6], research on a jet swirled combustor developed by Yonezawa et. al. [27], and the

research conducted by Lewis [13] on high-g flame speed. Figure 1 contains images of a conventional annular combustor (top) and the UCC (bottom). As shown in this figure, the UCC flow is directed into a 15 cm diameter circumferential cavity. A UCC of this size can create high g-loads, up to 4,000 g's depending on fuel and mass flow, according to Zelina et al. [7]. The flame is allowed to recirculate within the circumferential cavity such that combustion can efficiently occur even in a fuel rich regime, $\phi > 1.0$, according to Zelina et al. [7]. As the combustion process nears completion, the centrifugal force keeps the heavy incompletely burned hydrocarbons in the circumferential cavity while buoyancy allows the lighter, hot gas products to travel out of the cavity and into the main flow. Previous UCC research has included numerical investigations by Sekar et al. and Biones et al. on the radial vane cavity geometry [33; 34] showing increased flame migration with the presence of the radial vane cavity. Also, experimental investigations on the UCC conducted by Quaale et al. using Laser Doppler Velocimetry [28] which measured g-loads in the 1,000-4,000g range, showed high turbulence intensities, and increased combustion efficiency with increased g-load. These results show promise from the combustion standpoint for the UCC design, but future implementation is also dependent on the turbine interface. Zelina et al. also determined stability limits on the g-load and cavity equivalence ratio, ϕ, which are illustrated in Figure 8 [7]. The global equivalence ratio is related to the cavity equivalence ratio by Equation 1.

$$\phi_{global} = \phi_{cav} \frac{\dot{m}_{core}}{\dot{m}_{cav}} \tag{1}$$

It is critically important to ensure thermal and chemical uniformity at the turbine inlet as combustors move towards operating near stoichiometric operating conditions. This is due to increased average temperatures and to avoid creating hot spots on the turbine potentially exceeding the material temperature limits as defined by Lukachko

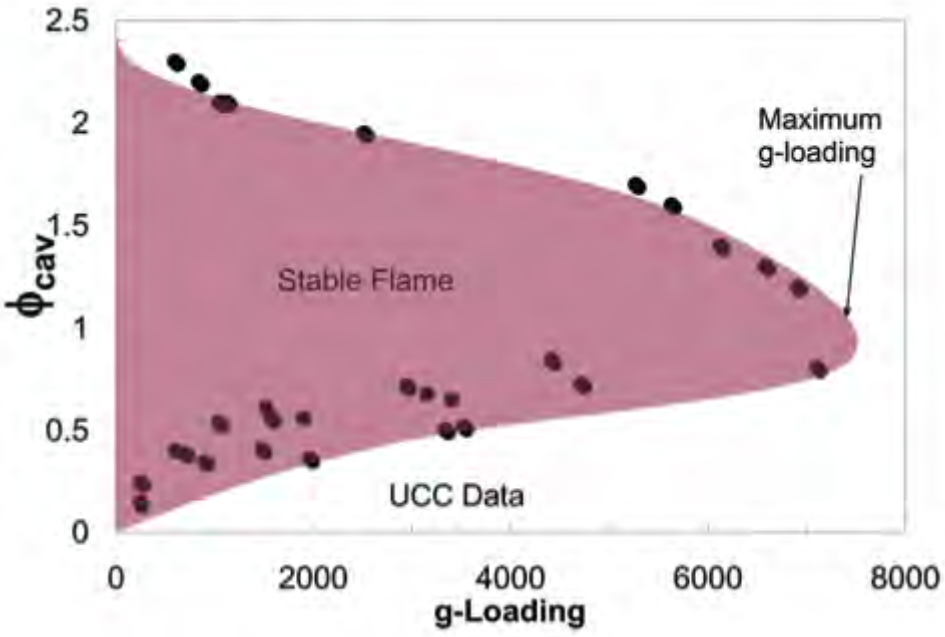

Figure 8. Illustration of the g-loaded flame blowout limit as a function of g-load and ϕ from Zelina [7]

et al. [31]. Thermal non-uniformity weighted to the outer diameter could cause turbine tip durability problems. Also, operation near stoichiometric conditions could lead to chemical non-uniformity, or incomplete reactions, causing excess heat transfer to the turbine blade due to localized heat release. These issues will be even more important for compact combustors, such as the UCC, where the combustor is closely integrated with the turbine and the likelihood of downstream reactions in the turbine is increased. These downstream reactions could have drastic impacts on the turbine durability and overall engine lifetime.

2.3.1 Inter-Turbine Burning.

A constant-temperature (CT) cycle for an ideal engine is illustrated in Figure 9. According to Sirignano and Liu, this cycle is advantageous thermodynamically [5] over a traditional afterburning engine because combustion in an afterburner is inefficient due to the lower temperatures and pressures. The benefit of a CT cycle is illustrated

by the decrease in overall entropy generation over the entire engine cycle as shown in Figure 9. Ideally, a constant temperature cycle engine would require burning within the turbine, but currently turbine blades are already limited in operating temperature by their materials, according to Lukachko et al. [31]. However, burning between turbine stages or inter-turbine burning can approximate a CT cycle, particularly with more than one ITB, without significantly increasing turbine operating temperatures as stated by Vogeler [30]. This concept adds a second combustor between the HPT and LPT. While initial ITB cycle analysis dates back to the late 1990's by Vogeler and Sirignano and Liu [30; 5], implementation of an ITB in an aircraft engine requires significantly reduced combustor length over current conventional sizes. The UCC is a prime candidate for realization of the ITB cycle benefits in an aircraft engine due to its compact size and weight savings, in addition to replacing the main combustor.

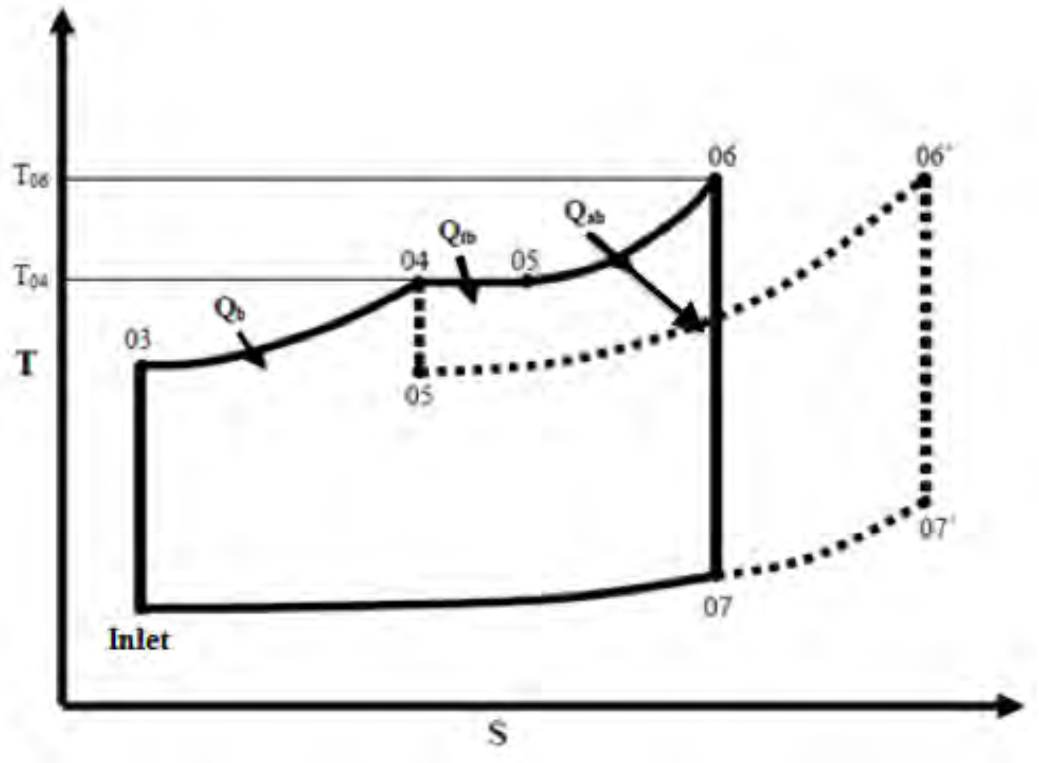

Figure 9. Thermodynamic cycles for a conventional (dashed line) and constant temperature (solid line) gas turbine engine from Sirignano & Liu [5]

Currently, an ITB has not been implemented in an aircraft engine, but according to Hiddeman and Marx, gas turbines for electrical power generation saw realization of the ITB concept in the mid 1990's with the Alstom GT24 and GT26 commercial engines [35]. Hiddeman used the term "sequential combustion" rather than ITB and demonstrated that the benefit of the new Alstom engines was increased power generation for similar turbine temperatures via distribution of the combustion process between the main combustor and second combustor, located in between the HPT and LPT [35]. While the Alstom engines demonstrate the ITB cycle benefits, realization of an ITB for an aircraft engine is subjected to stringent size and weight requirements that are not levied upon power generation engines, according to Zelina et al. [36]. Zelina et al. [36] investigated the UCC as an ITB and showed similar combustion efficiency and lean blowout characteristics for operation as an ITB compared to operation as a main combustor. The work of Zelina et al. [36] demonstrated the UCC's potential in ITB operation for future use in aircraft engines.

ITBs are not without limitations though. Typically in an engine, only the HPT is cooled and not the LPT due to the high temperatures of the combustor. However, using an ITB places another combustor immediately upstream of the LPT which increases the freestream temperatures entering the LPT. The presence of these thermal loads on the LPT would likely require adoption of new material and/or film cooling strategies similar to the HPT. These strategies will likely cause additional cost and weight to the total engine and will necessarily consume some portion of the benefit of an ITB cycle over a traditional cycle.

2.3.2 Radial Vane.

The radial vane is a key component to the UCC design, which seeks to remove the compressor exit guide vane and the turbine inlet guide vane with a single radial vane.

The radial vane has been investigated both experimentally and numerically. Zelina et al. [37] noted decreased combustion efficiency, but improved core flow temperature distribution when the an angled cavity was added to the original flat radial vane having no curvature. Additionally, Zelina et al. [36] compared the angled radial vane cavity (RVC) with a contoured RVC but showed that the contoured design degraded performance (core flow temperature distribution and combustion efficiency) over the angled RVC configuration on the flat vane. However, Radtke [38] investigated a curved radial vane geometry and demonstrated increased combustion efficiency with the curved radial vane over the flat vane used by Zelina et al. [36].

A numerical analysis by Anisko [39] matched the UCC/core velocity ratio (VR) as the radial vane height was increased. Anisko [39] reported decreased combustion efficiency and pressure drop across the vane as the vane height was increased. Bohan [11] showed, in a numerical study, that reducing the pressure across the radial vane led to decreased flow migration from the UCC into the core flow. Bohan [11] accomplished the pressure reduction via increasing the total vane count for an annular UCC numerical model noting that the flow migration regime changed from being dominated by the cross-sectional area blockage of the radial vanes for configurations with less than 20 vanes, whereas for configurations with more than 20 vanes the flow migration was dominated by the pressure drop over the vane.

2.3.3 AFIT Research.

Numerous AFIT master's students played pivotal roles in the construction of the COAL lab, design and build of the sectional UCC model, and laser diagnostic development. A brief summary of some of the AFIT research on the UCC is now presented. Moenter [40] conducted initial computational analysis and design of a sectional UCC model. Anderson's [8] work on the setup of the lab capability laid the groundwork for

the COAL Lab's existence, which was validated by Koether [41], and the final design and build of the sectional UCC model as shown in Figure 10. Hankins [3] and Lakusta [42] made significant progress towards the development of the 2-line PLIF system that was fully implement by Drenth [9]. With regards to investigation within the UCC, Hankins and Lakusta [3; 42] conducted initial investigations using the straight section only, whereas Drenth [9] and Thomas [29] conducted initial investigations with both straight and curved UCC sections.

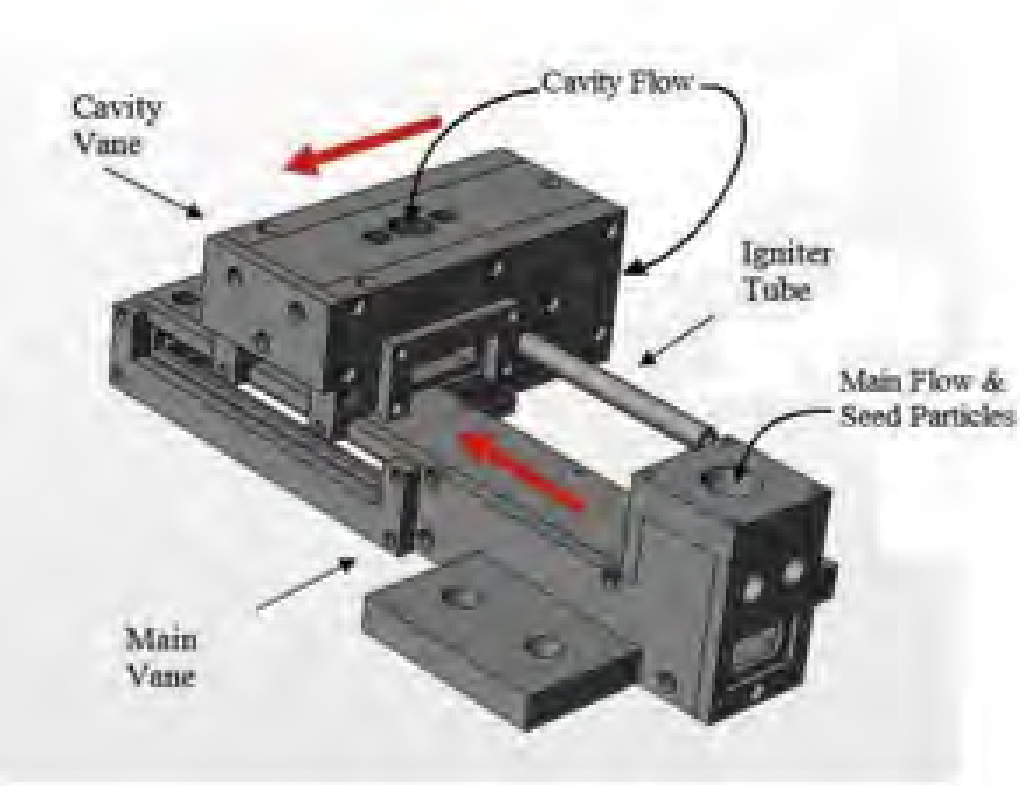

Figure 10. UCC sectional model with straight UCC section mounted to the core flow section with main flow radial vane from Anderson [8]

Drenth collected PLIF data on the hydroxyl (OH) radical at the exit of the straight and curved UCC sections, shown previously in Figure 2, using the 2-line thermometry technique [9]. Figure 11 shows the UCC ambient exit temperature over a range of equivalence ratios. The curved section had a relatively constant 300 K temperature

decrease over the straight section. Drenth postulated the temperature decrease was caused by the increased flame speed resulting from the g-load [9], in accordance with Lewis's research [13].

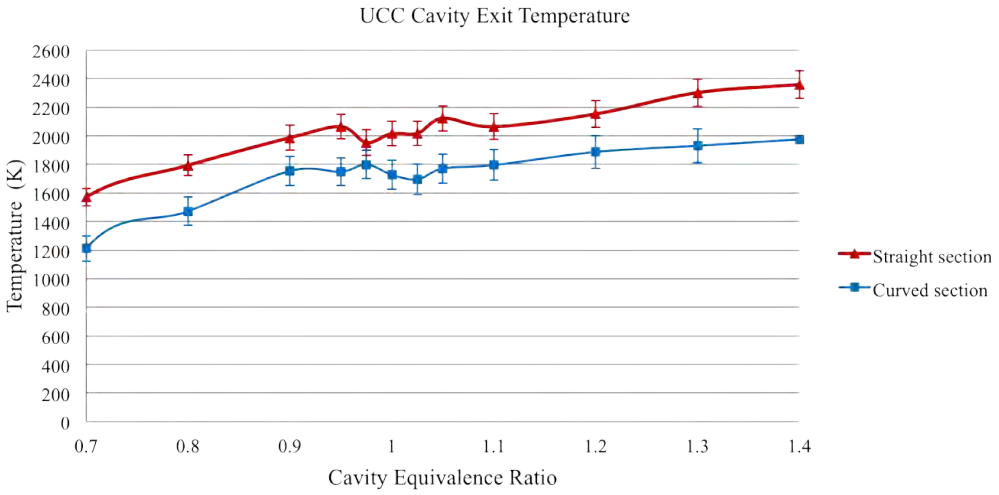

Figure 11. Comparison of ambient UCC exit temperature vs. equivalence ratio illustrating nearly constant 300K decrease with the curved UCC section over the straight from Drenth [9]

One issue with the existing AFIT UCC research was an incongruence between the exit areas of the straight and curved sections. The change in area from 2.33 cm^2 in the curved section to the straight section area of 5.44 cm^2 for the research by Drenth and Thomas [9; 29], as shown in Figure 12, would have caused more of the combustion products to migrate into the core flow instead of out the cavity ambient exit for the straight section. This change in the mass flow split could potentially have a significant effect on the results of the existing AFIT UCC data, particularly for the changes in ambient UCC exit flame structure and temperature with the curved section. This may also change the UCC tangential velocity due to the mass flow split changes. Thus, correction of the curved UCC section's exit area to match the straight section and reevaluation of the existing results is pivotal to continued development of the sectional UCC model.

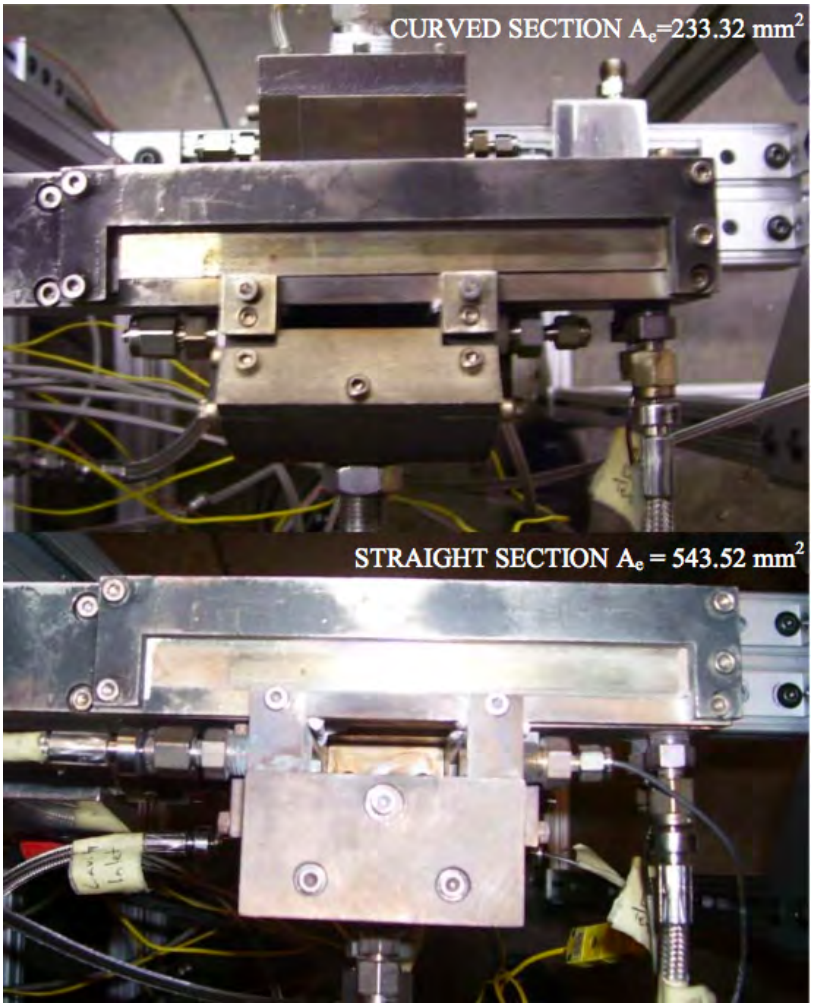

Figure 12. Comparison of the ambient UCC exit area for the curved (top) and straight (bottom) UCC sections from Drenth [9]

2.3.4 V-Shaped Flame.

The v-shaped flame was a bimodal distribution of the flame shape at the ambient exit of the straight UCC section on the AFIT model, first noted by Drenth [9]. The bimodal flame distribution within the UCC expands at the sectional UCC model's ambient exit forming a shape characteristic of the letter V. Drenth observed the straight section produced a v-shape flame at the ambient UCC exit while the curved section did not, as shown in Figure 13 using single-line PLIF for 2D flame location [9]. Drenth postulated that the addition of the g-load caused the elimination of the v-shape [9]. However, this postulate was contrary to the computational results published by Zelina et al. [10]. Zelina et al. [10] reported a bimodal temperature distribution within the small-scale annular UCC, as shown in Figure 14. Bohan [11] also showed a bimodal distribution in the OH concentration within a large-scale UCC, as shown in Figure 15.

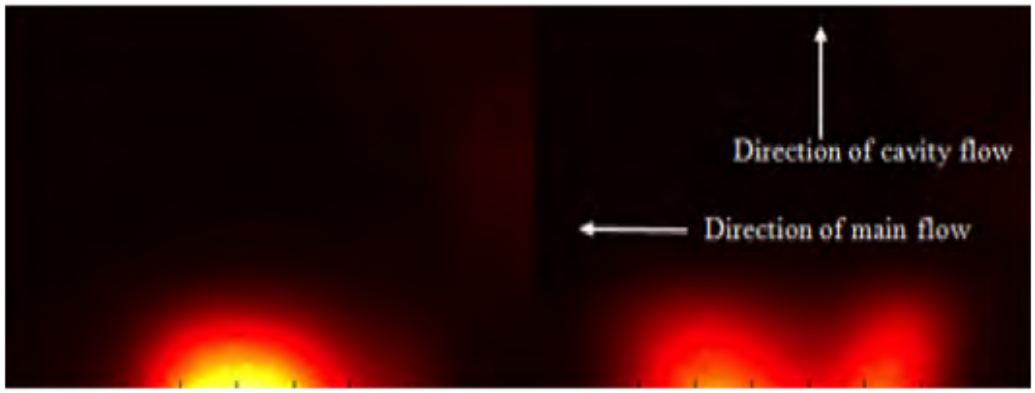

Figure 13. Ambient UCC exit flame location, AFIT sectional model, for curved (left) and straight (right) UCC sections at $MFR = 0.1$ and $\phi = 1.0$ from Drenth [9]

2.4 Combustion Physics

As a starting point to the analysis of a combustor, a basis for combustion physics must be established. This basis is the cornerstone of the combustor design space,

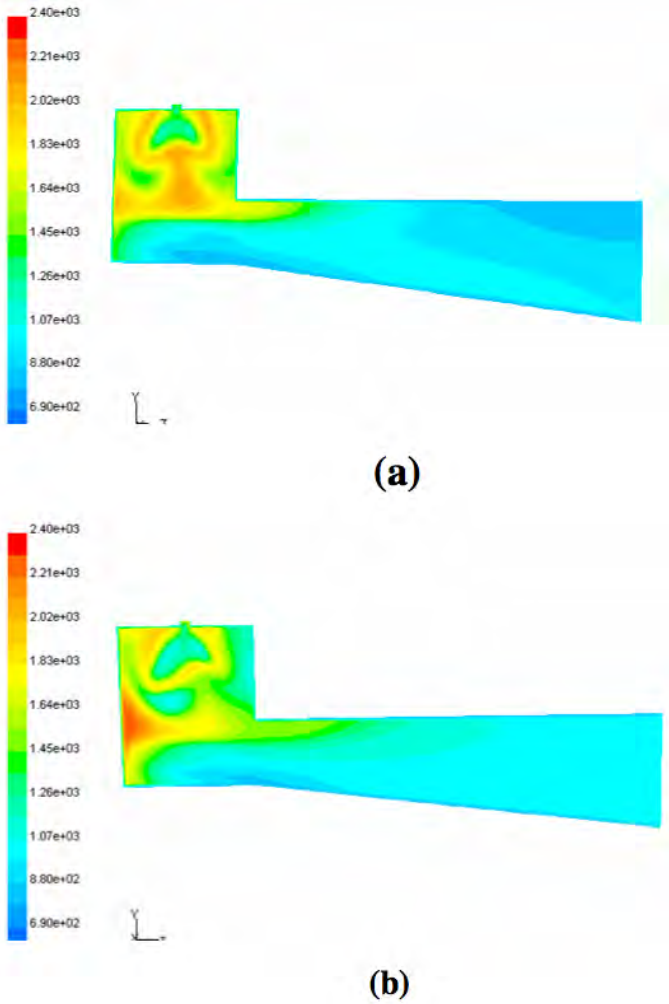

Figure 14. Numerical temperature distributions (K) along the small-scale UCC cross-section for a low g-load (a) and high g-load (b) from Zelina et al. [10]

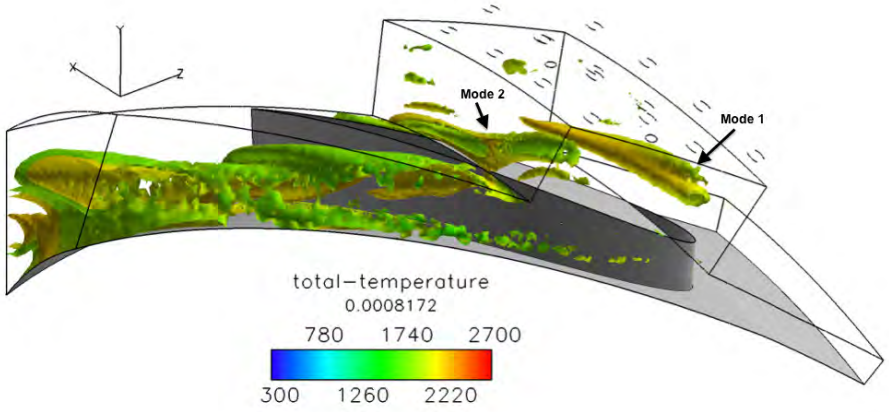

Figure 15. 3D representation of OH concentration colored by total temperature (K) in a large-scale UCC computational model showing 2 modes in the UCC channel, from Bohan [11]

dictating important parameters of interest to every combustor design. First, Law defines the equivalence ratio as a way to relate the ideal, or stoichiometric, chemistry fuel-to-air mixture with that of a given experiment [12]. The equivalence ratio, ϕ, is a parameter that influences the flame dynamics and it is related to the flame temperature. Specifically for the UCC, due to its off-axis design, the UCC/core air mass flow ratio (MFR) has been shown to significantly impact the flame migration from the UCC into the core flow and represents the strength of the shear layer at that interface, according to Thomas [29]. The UCC subjects flames in the circumferential cavity to high angular acceleration, or high g-load. The changes in the g-load produced measurable impacts on the UCC operation, based on the data from Zelina et al. [7]. As determined by Lewis [13], g-loaded combustion is strongly influenced by buoyancy. As such, the fundamental coupling of buoyancy with g-load and combustion must be addressed. These topics cover an introduction to the theory and experimentation for the flame dynamics of the UCC.

2.4.1 Equivalence Ratio.

One important parameter influencing the macroscopic characteristics of the flame is the equivalence ratio, ϕ, which relates the amount of fuel to oxidizer (typically air) for the current conditions relative to stoichiometric conditions. According to Turns, at stoichiometric conditions, the fuel to oxidizer ratio is such that the combustion reaction is exactly completed with neither fuel, intermediary species, nor oxidizer left in the final products [43]. Assuming a generic hydrocarbon fuel with standard sea-level air as the oxidizer, the stoichiometric combustion reaction is shown in Equation 2, using $air = 0.21O_2 + 0.79N_2$ or $4.76\ air = O_2 + 3.76N_2$ from Turns [43].

$$C_xH_y + a(O_2 + 3.76N_2) \rightarrow xCO_2 + \frac{y}{2}H_2O + a(3.76N_2) \tag{2}$$

A simple algebraic balance yields $a = x + \frac{y}{4}$ and leads to the mass fuel/air ratio (F/A) shown in Equation 3 from Turns [43]. For hydrogen fuel the equation simplifies with x = 0. The F/A ratio is approximately 15.57 for propane (C_3H_8) and 34.06 for hydrogen (H_2) using this equation where MW_{fuel} and MW_{air} are the respective molecular weight (MW)s of the fuel and air in $\frac{kg}{kg-mole}$ from Turns[43].

$$\left(\frac{F}{A}\right)_{st} = \frac{MW_{fuel}}{4.76a \times MW_{air}} \tag{3}$$

However, according to Turns, premixed flame combustion rarely occurs at stoichiometric conditions but rather happens in the presence of excess oxidizer, and this is called fuel-lean [43]. Further, the chemical kinetics in the flame change when in the presence of excess fuel and is called fuel-rich according to Law [12]. Thus, from a flame dynamics perspective, there is a need to relate both fuel-lean and fuel-rich conditions to the stoichiometric condition, yielding the equivalence ratio shown in Equation 4.

$$\phi = \frac{(F/A)_{actual}}{(F/A)_{st}} \tag{4}$$

Therefore, according to Law, $\phi < 1$ implies the mixture is fuel-lean, $\phi = 1$ implies stoichiometric, and $\phi > 1$ implies fuel-rich [12]. The equivalence ratio is also related to the ideal or adiabatic flame temperature as shown in Figure 16 from Law [12]. While real situations are not ideal, the adiabatic flame temperature provides a relative estimate on the flame temperature, particularly for the use of nearly-adiabatic burners for diagnostic calibration, such as the Hencken burner. However, a combustor operating with nominal $\phi = 1$ in the primary reaction zone will still have operating conditions spanning fuel-lean and fuel-rich regimes. Thus, it is important to study the performance of a given combustor design at all potential operating regimes. According to Zelina, the UCC operates as a Rich-burn, Quick-quench, Lean-burn (RQL) combustor where the rich-burn occurs in the circumferential cavity with the migrating flame being quick-quenched at the core flow interface to a lean-burn condition in the core flow. This means that the UCC has ϕ locally > 1, in the circumferential cavity, but globally < 1, in the core flow. However, due to ϕ's representation of the global heat addition, understanding variations in ϕ and its implications to the flame migration are required.

2.4.2 UCC-to-Core Air Mass Flow Ratio.

Previous research by Thomas showed the effect of the UCC/core air mass flow ratio (MFR), defined in Equation 5, on the flame migration into the core flow. Increasing the MFR showed increased turbulence in the core flow resultant from increased migration from the UCC, according to Thomas [29]. Results from Quaale et. al. on the AFRL annular UCC indicated a desired MFR in the 0.2-0.3 range [28]. However, application of the MFR to the sectional UCC model should be done with care. The

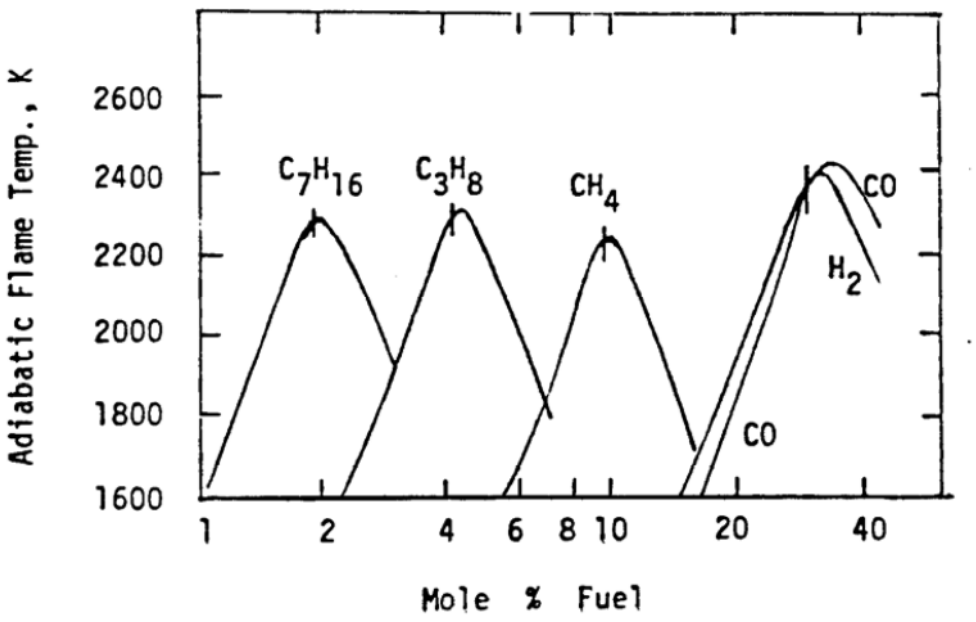

Figure 16. Adiabatic flame temperature as a function of fuel mole % (essentially the equivalence ratio). The vertical bars indicate stoichiometric conditions from Law [12]

AFRL UCC had a slightly larger radius (59 mm vs. 55 mm) and a slightly larger depth (21 mm vs. 14 mm), as defined by Quaale et al. and Drenth, which precludes matching the exact mass flow rates to achieve similarity [28; 9]. Instead, the UCC mass flow rate should be set to produce the necessary tangential velocity for the desired g-load (500 - 2,000g range). The core flow section models one vane passage out of the total six passages which dictates a sixth of the mass flow required to produce the same core flow velocity due to the section containing a sixth of the area. Equation 5 was used to compute the MFR where $\dot{m}_{UCC}$ is the total mass flow rate of air for the UCC or pictorially the sum of all UCC air injectors in Figure 21, $\dot{m}_{core}$ is the mass flow rate of air for the total core flow or for the AFIT sectional model this is six times the mass flow rate of air in the core flow section (since the section is one of six vane passages) as demonstrated in Equation 6 m is the number of vane passages of the sectional model, and n is the total number of vane passages for the full model. While matching the MFR for similar geometry is important, considering the desired

investigation of the radial vane scaling this parameter may not be ideal. Another parameter, the velocity ratio, may also dictate the physics of the interaction between the two flows requiring both parameters to be investigated.

$$MFR = \frac{\dot{m}_{UCC}}{\dot{m}_{core}} \tag{5}$$

$$\dot{m}_{core,sectional} = \frac{m}{n}\dot{m}_{core,annular} \tag{6}$$

Instead of considering the MFR, the UCC/core velocity ratio (VR) may be considered alternatively. If the radial vane height is increased while holding the MFR constant, the core flow velocity will necessarily decrease according to the mass flow rate relation, shown in Equation 7 where ρ is the density, V is the velocity, and A is the area. However, if holding a constant VR, as computed in Equation 8, the MFR will decrease because the core air mass flow will be increased, but the shear layer strength at the UCC/core flow interface will remain the same. Also, slight changes in geometries may produce significant changes in the VR for the same MFR. Further, the sectional model will not have the same steady-state build-up that occurs in the annular model which may produce significant changes in the VR for the same MFR when comparing the two models. Another expression relating the UCC to core flow is with a momentum ratio, as shown in Figure 9. The MR is simply the VR multiplied by the ratio of the UCC to core flow densities, and as such it was not considered a new parameter of interest. Since Quaale et al. and Thomas showed the UCC dynamics to be largely dependent of the flowfield dynamics [28; 29], both the MFR and VR must be examined.

$$\dot{m} = \rho V A \tag{7}$$

$$VR = \frac{V_{UCC}}{V_{core}} \tag{8}$$

$$MR = \frac{\rho_{UCC} V_{UCC}}{\rho_{core} V_{core}} = \frac{\rho_{UCC}}{\rho_{core}} VR \tag{9}$$

2.4.3 Centrifugal Effects.

In addition to the traditional laminar and turbulent flame regimes, Lewis demonstrated the existence of a third regime named the buoyant bubble flame regime [13]. By subjecting a flame to high angular accelerations above 500 g's, the flame speed increased proportional to the square-root of the radial acceleration in g's (see Equation 10) which is typically 3-4 times that of the standard turbulent flame speed as measured by Lewis [13]. Lewis presumed that the cause of the increased flame speed is attributed to the turbulent eddies or bubbles that were forced ahead of the flame front due to the angular acceleration which propagating the flame in tandem [13]. The relationship used by Lewis for determining the g-load value (G) is shown in Equation 11 based on the tangential flow velocity (V_{tan}), the radius of curvature (r), and Earth's gravitational constant (g=9.81 m/s^2 or 32.2 ft/s^2).

$$S_B = 1.25\sqrt{G}\ \ s(ft/s) \tag{10}$$

$$G = \frac{V_{tan}^2}{rg} \tag{11}$$

For this scenario, the radius of the UCC section and Earth's gravitational constant are fixed leaving only the tangential velocity, V_{tan}, variable. Figure 17 compares the tangential velocity (m/s) to the corresponding g-load value for the 55 mm radius UCC section. Figure 18, from Lewis [13], illustrates the relationship of the bubble

velocity and the centrifugal force resultant from the radial acceleration. Lewis [13] showed that under centrifugal forces higher than 500 g's the flame speed increased beyond the turbulent flame speed regime, S_T, into the buoyant bubble flame speed regime, S_B, where the flame speed was proportional to the square root of the g-load value, see Equations 10 and 11. Lewis [13] also showed that for g-loads above 3,500 g's the flame speed began to decrease. This established the buoyant bubble flame regime between g-load values of 500 and 3,500 g's. Zelina et al. [37] verified Lewis's work computationally and also demonstrated experimentally that a centrifugally-loaded combustor operated at high efficiency, 95 to 99%, with significantly reduced flame lengths, upwards of 50% shorter, that could be beneficial to future gas turbine combustor designs.

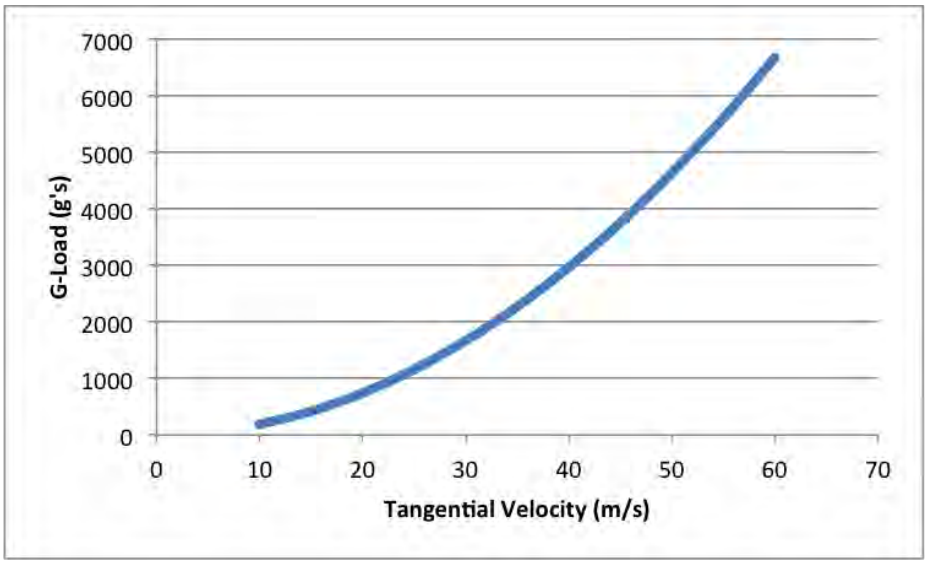

Figure 17. Plot of the tangential velocity (m/s) and the corresponding g-load value (g's) for r=55 mm

Lapsa and Dahm [14] further validated Lewis's research by studying high values of both positive and negative g-load on a step-stabilized flame. Lapsa and Dahm [14] demonstrated that positive g-loads produced large density gradients and buoyant forces that yielded improved combustion in the curved channel, as shown in Figure

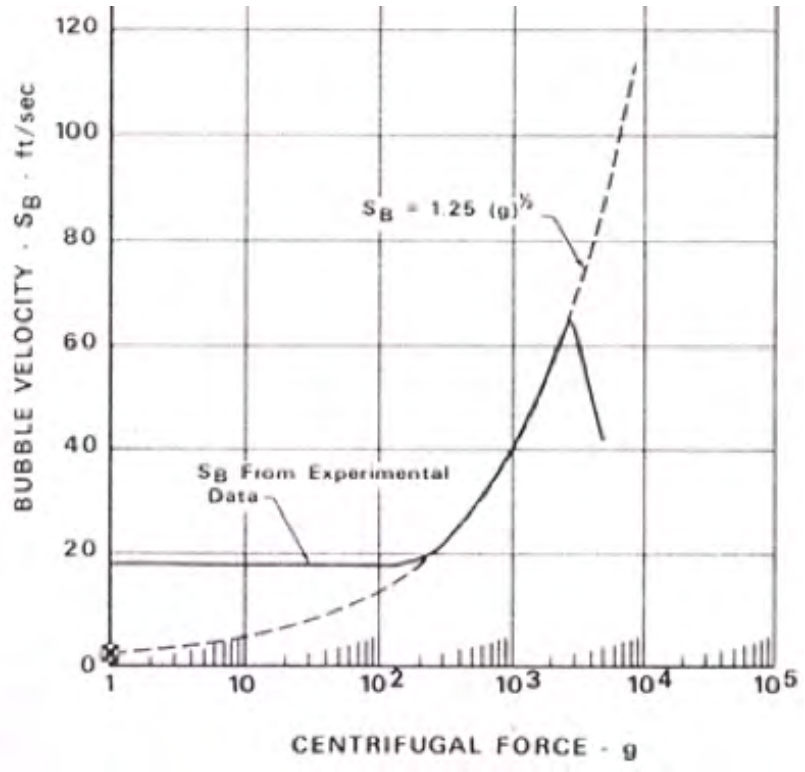

Figure 18. Buoyant bubble flame speed vs. centrifugal force (500 - 3,500 g's) from Lewis [13]

19, while negative g-loads followed the opposite trend of detrimentally impacting combustion, as shown in Figure 20. Thus, the relationship of the g-load to the migration is of pivotal importance to the UCC design space requiring variations in g-load to be investigated.

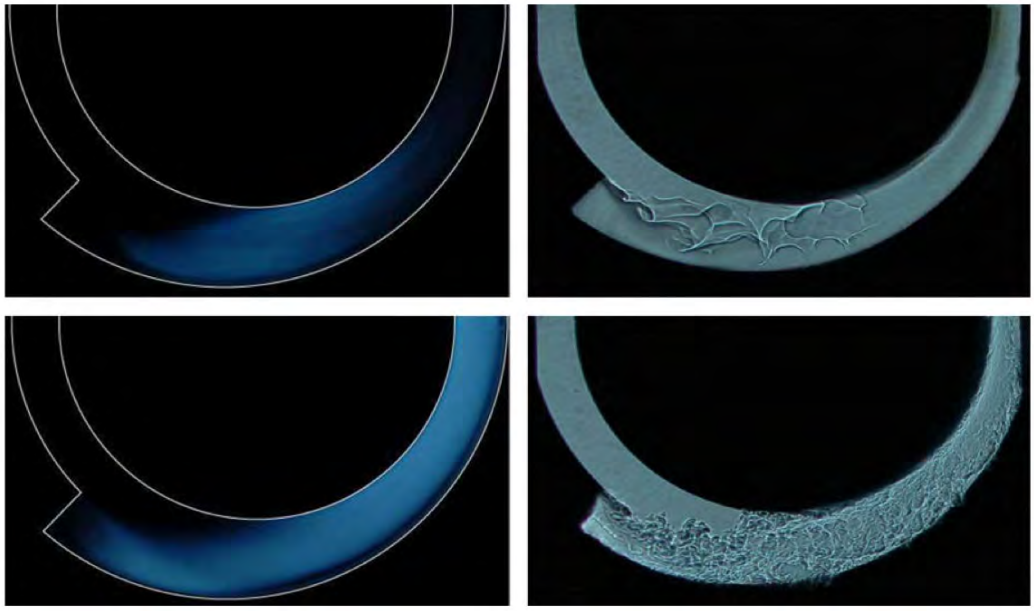

Figure 19. Typical chemiluminescence (left) and shadowgraph (right) images for positive g-load values of +28.5 g's (top) and +2850 g's (bottom) from Lapsa and Dahm [14]

Moenter also investigated the centrifugal force effects numerically using sectional UCC models [40]. Moenter showed that adding the centrifugal force resulted in a decreased pressure drop and increased combustion efficiency [40]. Moenter also showed higher radial velocities in the UCC that led to increased flame migration resulting in increased average heat release into the core flow and also noted that the temperature distribution improved with the added centrifugal force [40].

2.4.4 Buoyancy Effects.

While buoyancy is a vital force in the combustion process, it is even more important to the flame migration within the UCC due to the high centrifugal load.

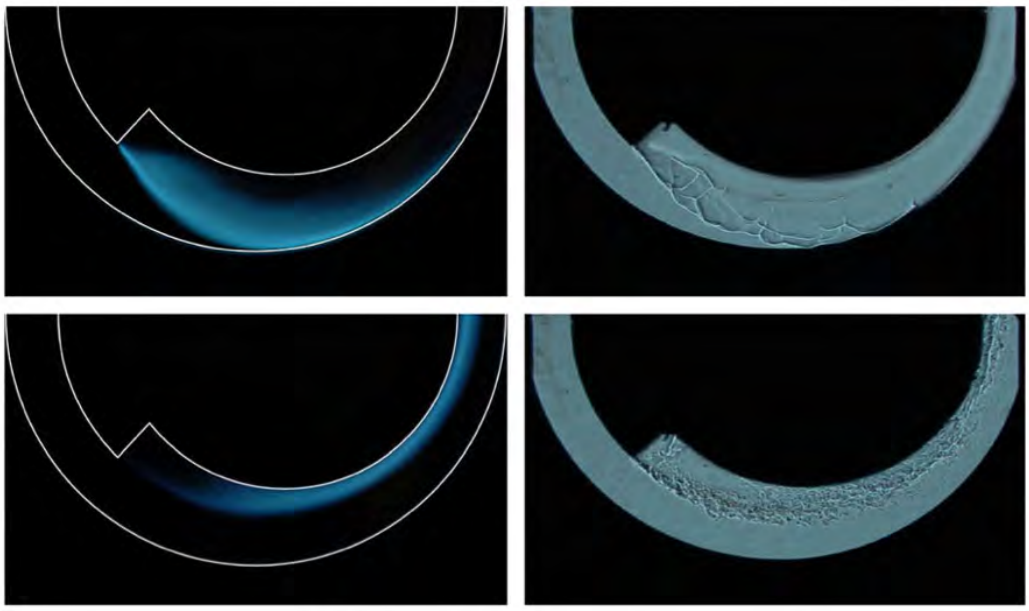

Figure 20. Typical chemiluminescence (left) and shadowgraph (right) images for negative g-load values of -28.5 g's (top) and -2850 g's (bottom) from Lapsa and Dahm [14]

Buoyancy, according to Heffernen [44], is the upward acting force that reduces an objects weight due to fluid pressure forces. Buoyancy in fluid mechanics occurs when a fluid is discharged into a medium in which a density gradient exists, according to Benhassen [20]. The standard reference for comparing the effect of buoyancy is with the Froude number, Fr, defined in Equation 12 from Heffernen [44] where U is the flow velocity, g is the gravitational acceleration, D is the diameter of the jet, ρ_a is the ambient air density, and ρ_i is the density of the buoyant jet. For the straight UCC section the gravitational acceleration is zero because the sectional model was oriented such that the flame migration from the UCC into the core flow was perpendicular to the gravitational force. However, for the curved UCC section, and also the annular UCC model, the gravitational acceleration is oriented along the radial direction, because of the rotating reference frame, and the value is the angular acceleration. The Froude number can be thought of as the ratio of inertial forces to buoyant forces. For the small-scale curved section UCC model, the Froude number is approximately 1.9

which indicates that the UCC flow is neither buoyancy dominated ($Fr < 1.0$), nor momentum dominated ($Fr > 4.0$), based on the work of Heffernen [44]. The UCC being neither buoyancy nor momentum dominated makes sense for the UCC because the buoyancy is driven by the g-load, which is driven by the momentum. However, for the straight UCC section, where there is no g-load and buoyancy is relatively constant, the flow is momentum dominated.

$$Fr = \frac{U}{\left[gD_h|\frac{\rho_a-\rho_i}{\rho_i}|\right]^{1/2}} \tag{12}$$

According to Heffernen, the effect of buoyancy on combustion has been studied extensively [44]. The work of Kolhe and Agrawal [45] observed large-scale vortical structures as a result of buoyancy induced instabilities on the flame front and noted that low frequency periodic oscillations also appeared. Heffernen [44] demonstrated that a horizontally-issuing reacting jet with negative buoyancy was characteristically similar to a non-reacting jet with positive buoyancy in both the momentum dominated and buoyancy dominated regimes. This was an important validation to the applicability of non-reacting buoyancy experiments on the characteristics of reacting flows.

Further examining the effects of buoyancy on non-reacting flows, Subbarao [46] demonstrated that a turbulent buoyant jet in co-flow produced periodic vortex rings surrounding the shear layer of the jet. Sherif and Pletcher [47] showed that increasing the gradient between the buoyant jet and cross-flow velocities resulted in increased mixing between the two flows. In Benhassen's study [20], a buoyant jet under g-load was investigated. Benhassen [20] demonstrated that high centrifugal and buoyant forces resulted in increased mixing as the g-load was increased.

The coupling of centrifugal and buoyant forces indicates that the main advantage of reaching the buoyant bubble flame regime in the UCC is not just the faster flame

speed, but also the increased buoyant forces that result from the centrifugal load. The relation for the buoyant force, from Lewis, is shown in Equation 13 where F_B is the buoyant force per unit volume, g is either the Earth's gravitational constant or the centrifugal force, ρ_a is the density of cold air, and ρ_E is the flame density [13]. Based on ratios of this relation, the buoyant force which governs the migration of flow from the UCC into the core flow will be on the order of 1000 times higher for a centrifugally loaded (buoyant bubble) flame over a non-loaded flame. This is the key to producing sufficient migration from the circumferential UCC cavity into the core flow and this is why cases with higher g-load should yield increased migration quantity.

$$F_B = \rho_a g \left[1 - \frac{\rho_E}{\rho_a}\right] \tag{13}$$

One issue with Equation 13 is that the g-load within the UCC is not constant and therefore the buoyant force is not constant. Based on Equation 11 and the AFIT sectional UCC model having a 55 mm radius yields approximately 1000 g's for a tangential velocity of about 23 m/s. Considering this radius is for the ID and the channel height of 13.5 mm, the same tangential velocity would only yield about 800 g's on the OD for an OD/ID g-load ratio of 0.8. Considering the large-scale UCC analyzed by Bohan [11], with the radius at the ID of 0.3 m and 0.35 at the OD, a tangential velocity of about 54 m/s produced 1000 g's on the ID and 860 on the OD for a ratio of 0.86. The radial variation of the g-load is a factor of the UCC radius of curvature and the channel height, but the increasing OD/ID g-load ratio shows that the radial variation of the g-load should be less significant for a large-scale UCC model over a small-scale model. In addition to radial variation, the g-load will also have angular variation for a sectional model. In a sectional model steady-state build-up throughout the circumferential cavity is not reached. Therefore, as additional mass

enters the cavity, the g-load and buoyant forces increase. Similarly, as mass migrates from the UCC into the core flow, the decreased mass in the UCC will produce lower g-loads and buoyant forces. Also, following the migrating mass from the UCC into the core flow, the mass will experience changes in the g-load and buoyant force as the mass moves inward radially due to the combined effect of the decreasing radius and the increasing angle of the mass momentum vector with the tangential direction.

III. Methodology

Establishment of sound methodology is the cornerstone to every research effort. The purpose must first be adequately articulated. In this case it is the quantitative characterization of centrifugally-loaded flame migration. A suitable research apparatus must then be determined whether analytical, numerical, or experimental. Due the nature of this research an experimental investigation using the AFIT sectional UCC was the most appropriate. Once the apparatus has been defined, appropriate measurement quantities and measurement methods must be determined. For this research, Planar Laser Induced Fluorescence (PLIF) was chosen to measure the flame structure while Particle Image Velocimetry (PIV) was selected to measure the flowfield. High-speed video was additionally used for visual flame structure and unsteadiness characterization. Finally, specific parameter values must be determined in order to provide sufficient variation range within a reasonable number of test cases. For this research UCC section curvature, radial vane height, and MFR were the key parameters of interest.

3.1 Research Purpose

The overarching objective was to characterize the centrifugally-loaded flame migration occurring within the UCC. Practically speaking, this implied first determining what parameters have a significant effect on the flame migration. The heart of the flame migration occurs at the shear layer formed between the cavity section and the main flow, and thus the strength of that shear layer was also a critical parameter. The UCC/core air mass flow ratio (MFR) and velocity ratio (VR) are used to represent the strength of the shear layer. The g-load, or the angular acceleration in terms of Earth's gravitational acceleration, is the second parameter of interest. The g-load

is a function of the UCC tangential velocity and will be most significantly changed by varying the UCC air mass flow rate. Finally, the equivalence ratio, or the ratio of the current fuel-to-air mixture to the stoichiometric mixture, is also of interest due to its direct relationship to the heat addition and its variability over an engine's operating regime. These three parameters (g-load, MFR, ϕ) are pervasive through this research. The understanding of these parameters relationship to flame migration is pivotal to geometric scaling of the UCC, specifically to a larger diameter, realizable from the results of this research. Building on previous research and utilizing the broad customizability of the AFIT sectional UCC model, potential issues with previous experimental AFIT UCC research were investigated along with an extensive parameter variation study to quantitatively determine the relationship between the aforementioned flow parameters and the flame migration from the UCC into the core flow. Specifically, three research objectives were established that each have a question to be answered, corresponding hypothesis, and methodology to prove or disprove the hypothesis. These objectives are listed, then discussed in detail below along with specification of the measurements needed, with corresponding techniques, and test conditions.

1. Why is the v-shaped flame structure eliminated when the configuration changed from the straight to the curved section?

2. Why does increased vane height reduce flame migration?

3. Why is the flame migration reduced with reduced g-load?

3.1.1 V-Shaped Flame.

The v-shaped flame investigation desired to uncover the phenomena responsible for the observed elimination of the v-shaped ambient UCC exit flame when the g-load

was added, as shown previously in Figure 13 from Drenth [9]. The hypothesis was that the v-shape, or bimodal distribution, will be well defined for 0g (straight section) and will decrease in definition as the g-load is increased until the single-mode parabolic distribution results at higher g-loads where complete breakdown of the v-shape occurs. This required that both the straight and curved UCC sections be tested at different tangential velocity conditions which generate a g-load in the curved but not the straight UCC section. It was also desired to obtain a preliminary understanding of the phenomena governing the presence of the v-shape. The UCC/core mass flow ratio was shown by Quaale et al. to influence the UCC flow velocity distribution [28], and changes in this distribution may have a significant impact on the flame shape, as such different ratio values were also tested. Thus, several test conditions were required using both the straight and curved UCC sections subjected to different g-load test conditions and MFRs. In order to verify the hypothesis, the flame shape at the ambient UCC exit had to be imaged. Single-line OH-PLIF was the obvious choice for imaging the flame shape, but visual flame images were also insightful. PLIF data was collected extensively for every case while visual flame imaging was used selectively to assess the conclusions from the PLIF data.

3.1.2 Vane Height.

The vane height investigation facilitated understanding of the scaling effect of the radial vane, shown previously in Figures 3 and 10, on the flame migration from the UCC into the core flow. The hypothesis was that, assuming the core mass flow remains the same, the core flow velocity will decrease due to an increased area associated with increased vane heights. This decreased velocity will subsequently cause the pressure gradient between the UCC and core flow to also decrease. The decreased pressure gradient will decrease the propensity of flow migration from the UCC. This investiga-

tion required additional 28 mm and 56 mm vanes be constructed for comparison with the existing 14 mm vane. While the straight UCC section was not needed for this investigation, studying a range of g-load values using the curved section was tested to determine if coupling exists between the g-load and the vane height. Changes in the UCC/core mass flow ratio were also investigated under the scaling to determine if the vane height impacted the relationship of that parameter to the flame migration. In order to measure the flame migration into the core flow, PLIF data was collected extensively in the core flow for every case. High-speed video was also collected for every case to characterize the migration trajectory and garner a qualitative sense of the migration temporal variability.

3.1.3 G-Load.

The g-load investigation desired to understand the effect of adding the g-load with respect to the flame migration from the UCC into the core flow. Clearly, as the g-load is increased the angular momentum and centrifugal/buoyant forces are likewise increased. The hypothesis was that the g-load contributed to a higher propensity for flow migration from the UCC into the core flow due to the increased magnitudes of these forces. In order to measure the flame migration from the UCC into the core flow, PLIF data was collected extensively in the core flow while high-speed video was also collected to characterize the migration trajectory. Additionally, PIV data was collected at the ambient UCC exit in order to compare the measured versus predicted g-load values. This provided an anchor of the observed phenomena at the tested conditions to the actual g-load values and was insightful to gaining a quantitative understanding of the relationship of the g-load to the flame migration.

3.1.4 Test Matrix.

Building on the results from previous research, a test matrix was specifically constructed to answer the objectives. Shown in Table 1, the test matrix varied the key parameters of straight/curved UCC section, radial vane height, g-load, UCC/core air mass flow ratio (MFR), and equivalence ratio (ϕ). The ϕ defined in the test matrix was for the UCC channel since the core ϕ was dependent on the quantity of migrating mass from the UCC into the core flow as shown in Equation 14. The ranges of these parameters was governed by previous data, specifically the stability limits set by Zelina et al. [7] which were shown in Figure 8. Conditions outside these limits were tested and shown to be unstable as expected. The nominal accuracy of the flow parameters was +/- 2% for the MFR, +/- 3% for ϕ, and +/- 9% for the g-load value based on the flow controller accuracy (see Section 3.4). Additional test cases were also added real-time during testing to answer a specific question that arose due to initial testing. These additional test points will be provided in the results chapter in which these tests helped to understand the overall objectives. Table 1 represents the base data points that were established to parameterize the initial objectives of this research.

$$\phi_{core} = \frac{\phi_{UCC}\dot{m}_{migration}}{\dot{m}_{core}} \tag{14}$$

3.2 AFIT Sectional UCC Model

The AFIT's sectional UCC models (Figures 3 & 10) were derived from the AFRL model used by Zelina et al. [2] to intentionally allow the use of non-intrusive laser diagnostics. This model was chosen over the AFRL model for numerous reason including optical access, test availability, and geometry customization. The sectional model was constructed of 316 stainless steel and consists of two parts: the core flow

Table 1. Test matrix with bolded baseline case

Case	Vane	Section	g-load	MFR	ϕ	Objective
1	2	straight	0 (500)	0.2	2	3
2	2	straight	0 (1000)	0.2	2	3
3	2	straight	0 (2000)	0.2	2	3
4	1	curved	500	0.2	2	1,2,3
5	1	curved	1000	0.2	2	2,3
6	1	curved	2000	0.2	2	2,3
7	1	curved	1000	0.1	2	2
8	1	curved	1000	0.3	2	2
9	2	curved	1000	0.2	1	2
10	2	curved	1000	0.2	3	2
13	2	curved	500	0.2	2	2,3
14	**2**	**curved**	**1000**	**0.2**	**2**	**1,2,3**
15	2	curved	1000	0.1	2	1,2,3
16	2	curved	1000	0.3	2	2,3
17	3	curved	500	0.2	2	2,3
18	3	curved	1000	0.2	2	2,3
19	3	curved	1000	0.1	2	2
20	3	curved	1000	0.3	2	2
26	2	curved	2000	0.2	2	2,3
28	3	curved	2000	0.2	2	2,3
31	2	curved	1000	0.05	2	1,2,3
33	3	curved	1000	0.05	2	2
34	3	curved	1000	0.025	2 2	2

section and the UCC section. The core flow section was previously compared to the AFRL rig in Figure 3 highlighting the location of the radial vanes of each rig. The core flow section had a channel height of 30 mm a span of nominally 14 mm (14.3 mm exactly). A detailed view of the core flow section with the curved UCC section mounted is shown in Figure 21. This figure highlights the major details of the sectional model, such as the fuel and air inlets, the radial vane, the ambient exits of both the core flow and UCC, the defined mass flow rates ($\dot{m}$) used for defining the test conditions in the test matrix (Table 1), and the coordinate system. Some of the details in Figure 21 are also shown in the top view, Figure 22, and side view, Figure 23 of the core flow section mounted with the curved UCC section.

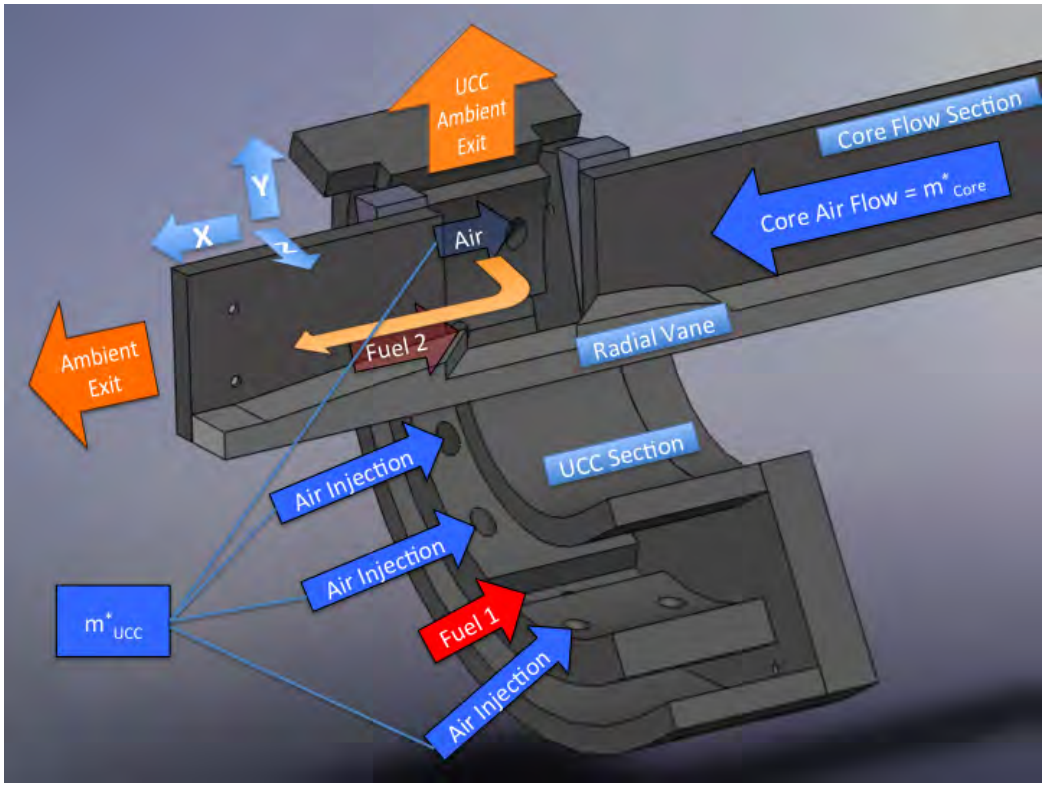

Figure 21. AFIT UCC curved section with fuel/air injection locations and coordinate axis

In order to specifically study the effect of increasing the radial vane height, two additional vanes with heights of 28 mm (28.6 mm exactly) and 56 mm (57.2 mm

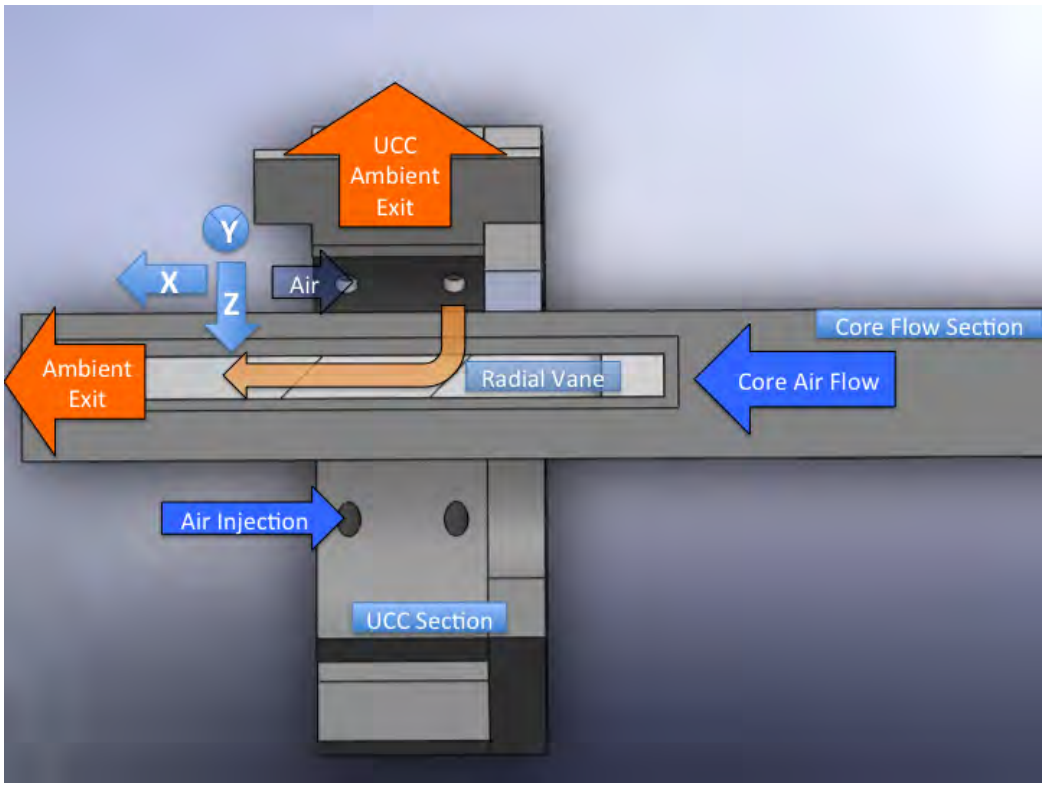

Figure 22. AFIT UCC curved section with fuel/air injection locations and coordinate axis (top view)

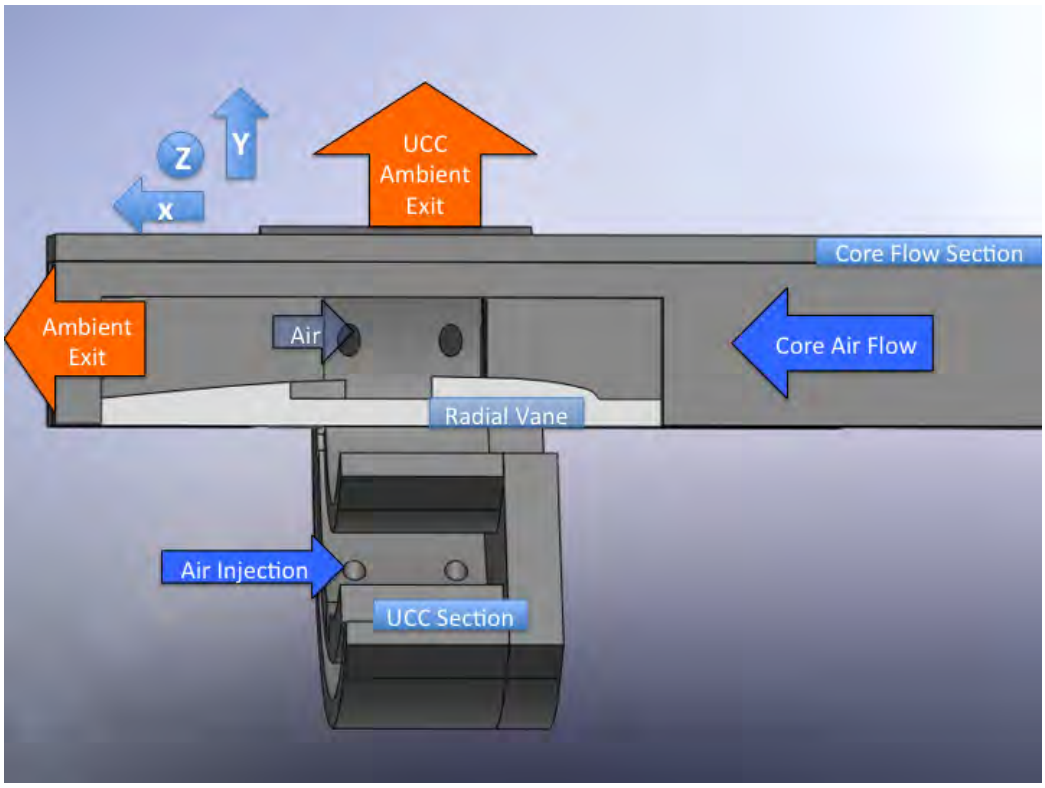

Figure 23. AFIT UCC curved section with fuel/air injection locations and coordinate axis (side view)

exactly) were constructed. Geometric scaling by factors of two and four of the existing vane height was chosen for simplicity. Figure 24 compares the 14 mm, 28 mm, and 56 mm vanes as constructed and tested. The vane ID and OD cross-section profiles were held constant through the height increase which resulted in changes in the angle of the radial vane cavity, as shown in Figure 24. This was chosen because a constant RVC angle would have impractically placed the inner RVC profile past the trailing edge of the 56 mm vane, and also to help promote flame migration farther down the span for the taller vanes. The RVC angles were 44.5, 62.5, and 75.0 degrees for the 14, 28, and 56 mm vanes respectively.

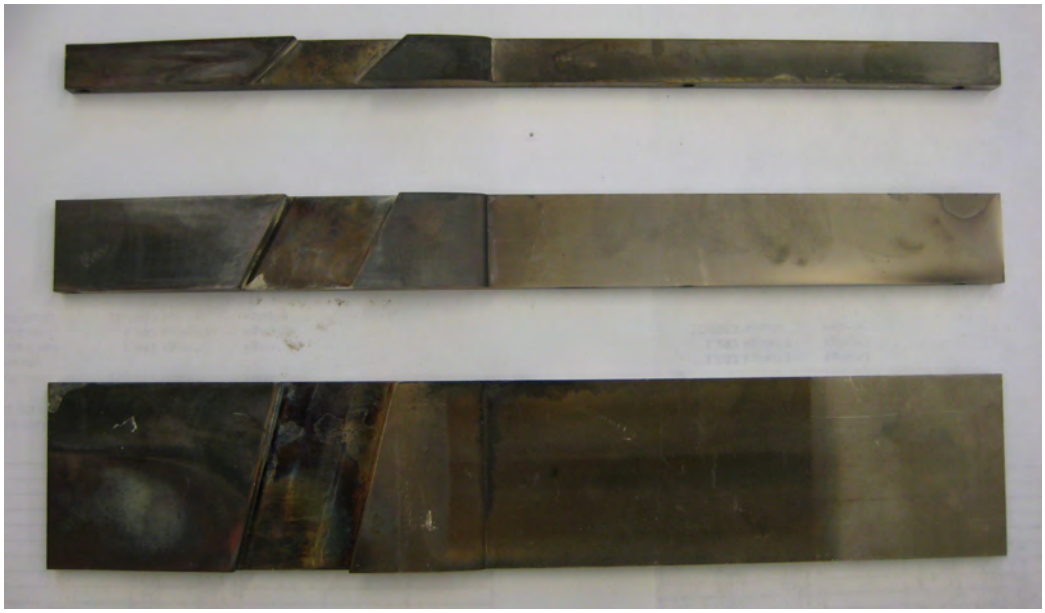

Figure 24. Comparison of the UCC sectional model radial vane heights: 14 mm vane (top), 28 mm vane (middle), & 56 mm vane (bottom)

The curved UCC section was shown in Figure 21 mounted to the core flow section. A straight UCC section also was used that closely resembles the curved UCC section simply without curvature, as shown previously in Figure 2. Both UCC sections are shown in a detailed end view in Figure 25. The curved UCC section has a radius of curvature of 55 mm, a depth of 13.5 mm and a width of 38.3 mm while the straight UCC section has an infinite radius of curvature, a depth of 14 mm and a width of 38.3

mm. This yields an exit area of 513 mm^2 and 532 mm^2 for the curved and straight UCC sections, respectively. Both UCC sections have an approximate length of 140 mm and inject air through a plenum with four pairs of 5.33 mm inlet holes at different angular locations (two pairs in between fuel injectors) with a 37 degree inclination angle, relative to radial direction, while fuel is injected inward from the outer radius through two 3.2 mm diameter injector holes into 6.1 mm square recessed cavity.

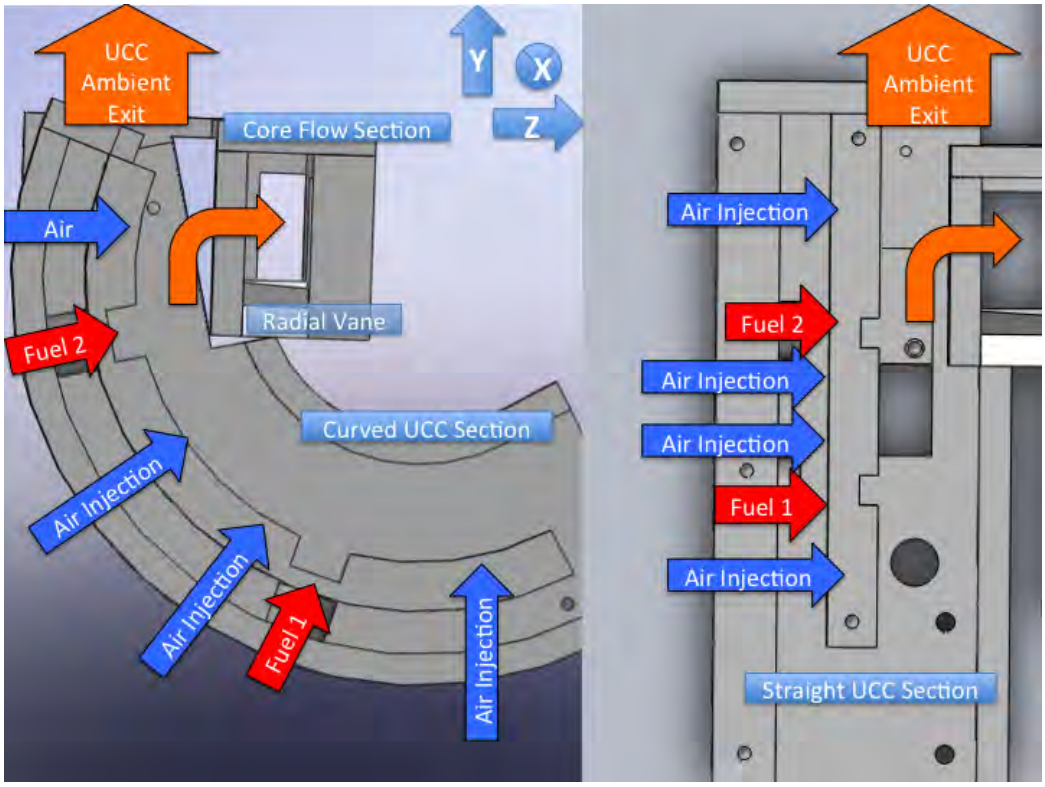

Figure 25. Sectional UCC model, end view, with curved (left) and straight (right) UCC sections

The purpose of testing both straight and curved sections was to provide otherwise identical test conditions differing only in the presence or absence of curvature and subsequently centrifugal loading. For both UCC sections the air plenum is fed from a single mass flow controller and the fuel is also fed from a single mass flow controller with the assumption that both fuel injectors receive an equal amount of fuel going to each injector. Also, the line-of-sight trajectory from the second fuel injector, neglect-

ing influence by the upstream UCC flow, impacts the OD of the radial vane, the left side of the vane for the geometry depicted in Figure 25. Considering the upstream UCC flow will only push the second fuel injector flow trajectory downstream, this would likely displace the actual trajectory downstream to the migration plane into the core flow. If the fuel flow rate was high enough, the jet from the second fuel injector could have sufficient momentum to overcome the upstream crossflow and, if using the curved UCC section, the centrifugal force. Having a fuel jet migrating with a very short residence time would yield significantly higher temperatures and downstream reactions in the core flow.

Both UCC and core flow sections were specifically designed to incorporate optical access via placement of UV-grade fused silica (quartz) using custom windows manufactured by Behm Quartz Industries and shown in Figure 26. The original window design used a step to hold straight sided windows in place but created recirculation regions underneath. Thus, windows with a 30 degree bevel were used for all modified pieces to remove the artifact recirculation region. The modified windows were only for the core flow section, except the 14 mm vane top and end windows, and did not remove the recirculation regions for the UCC section windows (see Figure 28. For all of the quartz windows a ceramic fiber based Fiberfrax was used to seal leaks around the windows and to allow for changes in thermal expansion between the steel and quartz. Figure 26 also indicates the measurement locations for the inlet and exit pressure to compute the pressure drop across the core flow and the UCC. Since the radius of curvature is fixed, the g-load was changed by varying the UCC mass flow rates. The UCC to core air mass flow ratio (MFR) was varied between 0.025 and 0.3. The equivalence ratio was changed between 1.0 and 3.0 by altering the fuel flow rate with the assumption that the changes in fuel mass flow and heat addition were negligible for these conditions.

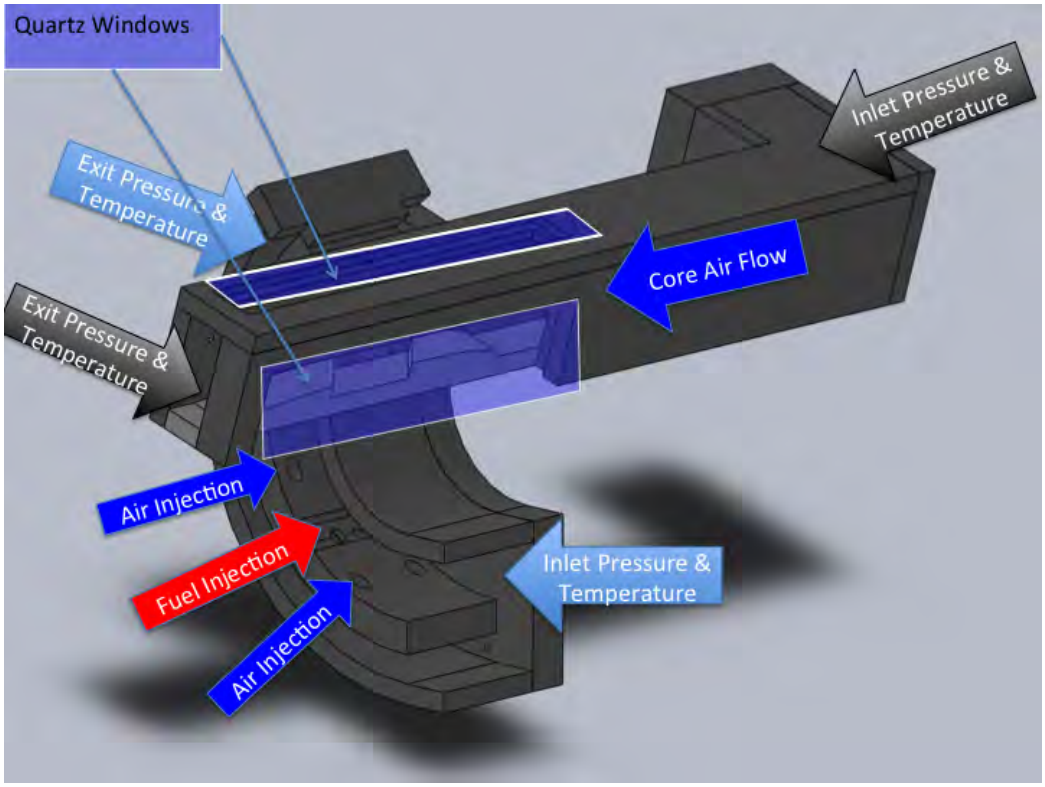

Figure 26. AFIT UCC curved section with quartz window locations highlighted

In order to address issues with previous AFIT UCC research, ramps were added to the attachment point for the curved UCC section as shown in the left image of Figure 27 to change the exit area of this section to more closely match the straight UCC section (from 233 to 513 mm^2). Figure 27 illustrates the change in the angle of the UCC flow path with the ramps (left image) from the flow path without the ramps (right image), which was equal to the ramp angle of approximately 10 degrees. This figure also illustrates that without the ramps, the UCC flow was not tangential to the core flow section, as in the annular UCC model shown previously in Figure 1. However, with the ramps added, the UCC flow direction was nearly tangential to the core flow. The ramps and wedge, used to fill the small gap underneath the core flow section created by the ramps (see Figure 27, existed for Drenth's research, but were not used because the previous mounting brackets did not fit [9] so new brackets were

made for this research.

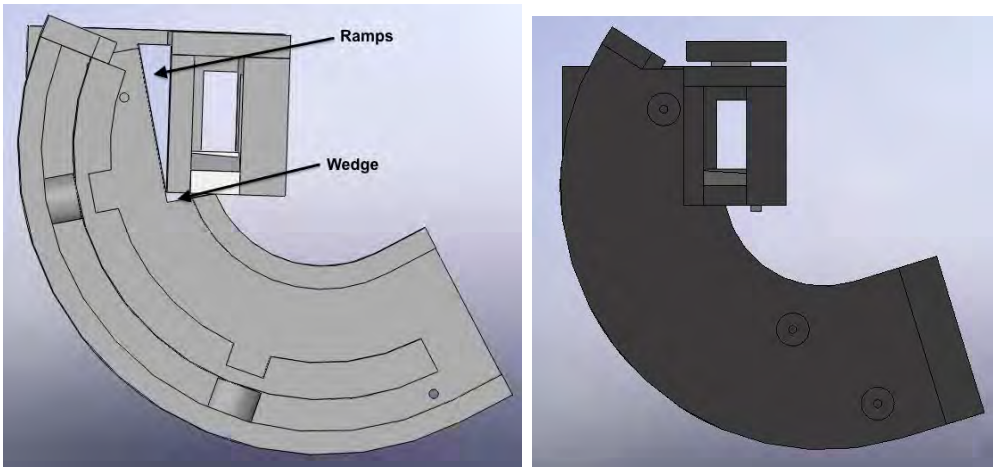

Figure 27. Images of the curved UCC section with ramps (left) and without ramps (right)

Since the g-load was a parameter of interest for variation, a means of measuring the actual g-load for a particular case was needed. Thus for this research, boxes were added to the upstream part of the UCC section to enable the addition of seed particles. This enabled the measurement of PIV particles to measure the actual g-load compared to estimations from the mass flow rates and heat addition. The boxes also served to provide more upstream flow to the UCC representative of what a full annulus would produce. A full annular model would have reacting flow at the inlet of each angular section, similar to the sectional UCC model, due to the upstream fuel and air inlets. This would also lead to a steady-state build-up, based on the specific residence lengths, where the UCC flow may exist for multiple vane passages, similar to the core flow section, as shown by Bohan [11]. The short residence length of the sectional UCC model was one area improved by the seeder box, which approximately doubled the flame residence length by moving the start of the flame (where the flame is actually held) from the first UCC section fuel injector (see Figure 25) to the seeder box fuel injector (see Figure 29). However, even with the seeder box the UCC section would have likely had a residence length of around half of the annular modelFurther

discussion about the limitations of a sectional model is in Section 3.3.

The image in Figure 28 shows the seeder box for both the straight and curved UCC sections, which differ due to the necessity of maintaining optical line-of-sight over the radial vane. If the seeder boxes were identical, viewing over the radial vane would have been blocked by the seeder box for the curved UCC section and this was not acceptable. Thus, the final design for the curved seeder box differed from that of the straight, but future work could adapt the curved seeder box design to be used with the straight section for a cleaner comparison between the two sections. The straight seeder box was identically cubic with internal side lengths of 38.3 mm while the curved seeder box had a circumferential length of 64.3 mm, a depth of 32.3 mm, and a width of 38.3 mm. Both boxes are configured with the air inlet in the circumferential direction and the fuel injector on the outward radial wall (injecting inward) but the curved UCC section seeder box has the ignitor on the windward side and the seed inlet on the leeward side while the straight box has the ignitor on the inward radial direction and the seed inlet on the windward side.

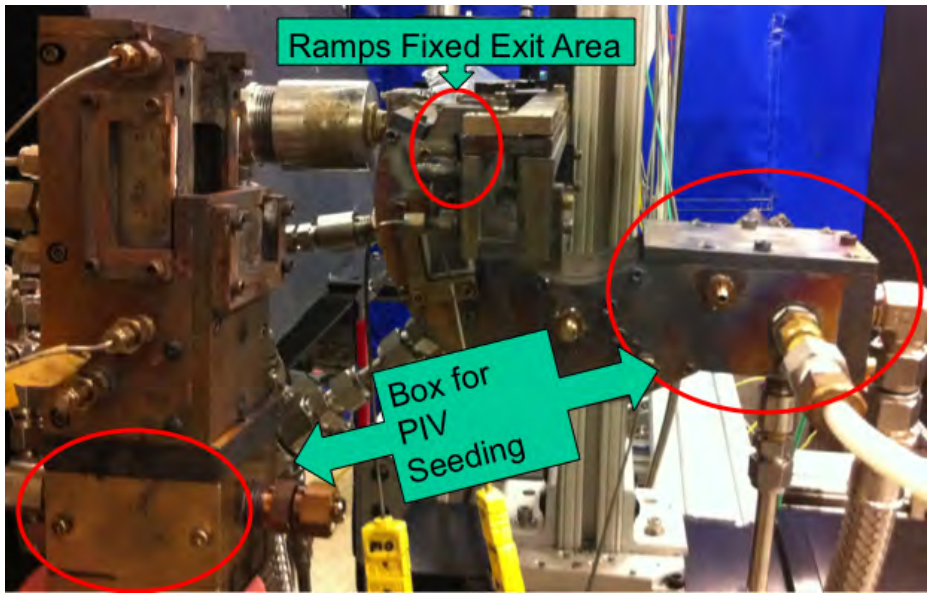

Figure 28. Picture of the sectional UCC, both straight and curved, with modifications to fix the UCC exit area and PIV seeder boxes

A detailed image of the curved seeder box is shown in Figure 29. Adding the seeder box necessarily required a change to the inlet air flow, requiring that the air to be seeded to enter on the upstream side of the seeder box. Since a large part of the UCC air flow was moved to the seeder box, an additional fuel injector was added as well as a port for the ignitor. Moving ignition into the seeder box effectively doubled the length in which flame resides within the UCC section. This increased residence length was desired to create a situation where the flow was burning longer as if resident in a full annulus. A 50/50 split was used between the fuel and air flows to the original UCC inlets and the seeder box due to the residence lengths being approximately equal. Also, increasing the residence length is believed to improve the sectional model's representation of a full annulus. The seeder box addition also allowed placement of thermocouple and pressure taps (see Section 3.4 for details) to be used to estimate the UCC flow density.

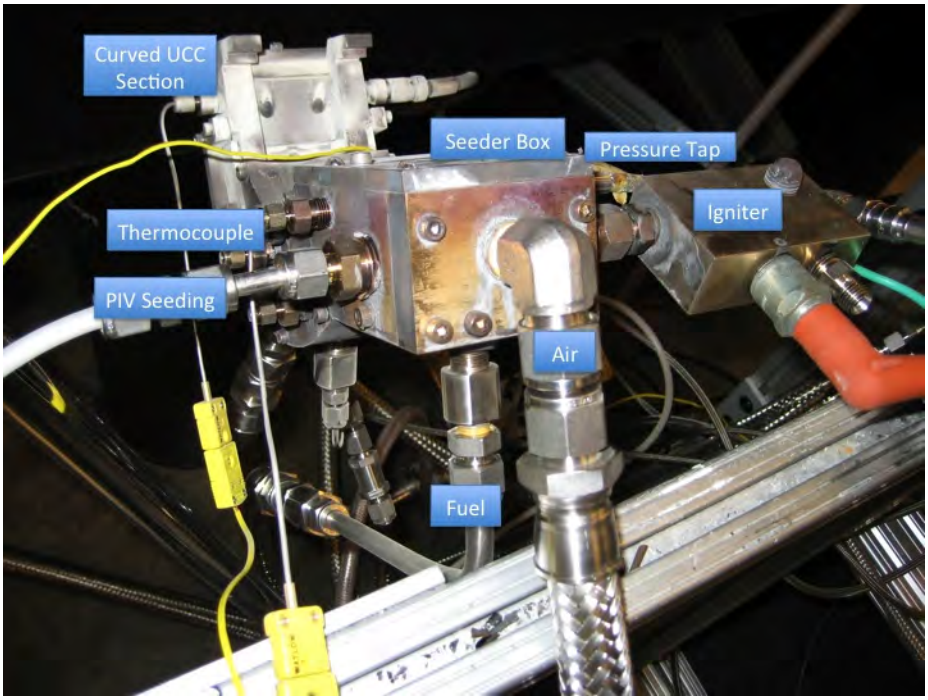

Figure 29. Curved UCC seeder box marked with fuel & air inlets, seeder port, and ignitor Port.

The vane height investigation (Chapter 5) did not use the UCC seeder box, but the v-flame and g-load investigations did (Chapter 4 and Chapter 6). However, the total fuel and total air flow rates were the same for all three investigations. The major difference was that with the seeder box the same total fuel and total air flow rates were divided between the UCC section fuel and air inlets, as shown in Figure 25, and the fuel and air inlet of the seeder box, as detailed in Figure 29. For the v-flame investigation (Chapter 4) the distribution of fuel and air was with 1/3 of the total going to the UCC section and 2/3 going to the seeder box. This distribution was accomplished using one mass flow controller for the fuel going to the UCC section (assumed to equally split between the two fuel injectors), one mass flow controller for fuel going to the seeder box, one mass flow controller setting the total air flow rate, and one mass flow controller setting the air for the UCC section. This distribution was chosen to create a large upstream reacting flow inline with the build-up that occurs in an annular model. However, under testing the mass flow controller that set the air for the UCC section caused a large enough pressure drop (not measured) such that the actual air flow rate was significantly less than 1/3 of the total air flow rate. Also, using the 1/3 and 2/3 distribution exhibited significant issues with keeping the flame attached in the seeder box and instead the flame detached from the seeder box and did not reattach until the second UCC section fuel injector. The flame holding issues created very uncharacteristic heat release and flame migration situations that are difficult to describe in words or capture illustrative images. As a result of the flame holding issues, the flow distribution was changed to be equally split between the UCC section and the seeder box. This equal distribution was accomplished similarly to the 1/3 and 2/3 distribution, but the additional UCC section air flow controller was removed with the remaining air mass flow controller split equally (by pipe sizing, like the UCC section fuel) between the UCC section and the seeder box. One additional

measure to improve the flame holding issue was that the total fuel mass flow rate for Case 14 (also Cases 15, 16, and 31), was about 34 SLPM and the equal flow split dictated 17 SLPM to the UCC section and 17 SLPM to the seeder box. However, that fuel split condition was unstable and had to be adjusted to 19 SLPM in the UCC section and 15 SLPM in the seeder box. Also, for Case 26 the total fuel required was 48 SLPM and the equal flow split dictated 24 SLPM to the UCC section and 24 SLPM to the seeder box, but this condition was also changed, for stability, such that only 21 SLPM went to the UCC section and 21 SLPM to the seeder box.

In order to simplify the overall experimental setup, the UCC rig was mounted on two translation stages as shown in Figure 30. The vertical stage was manufactured by NRC with model number 270. The horizontal stage was manufactured by Newport with model number ILS50PP. The vertical stage was manually adjusted while the horizontal stage is computer controlled via the Newport ESP300 translation stage controller. This dual-stage setup allowed fixed laser and camera alignment positions while the UCC rig was moved around that alignment. Since the majority of the data was taken using vertical planes, this eliminated the need to synchronize multiple stages as previously used by Drenth and Thomas [9; 29].

3.3 Sectional Model Limitations

In this research, a sectional UCC model was used exclusively to investigate the phenomena occurring within the Ultra Compact Combustor. However, a true application of the UCC would contain a complete annulus which resultantly has fundamental differences to the sectional model that must be discussed. These differences, while enabling the phenomena to actually be investigated which was an obvious advantage, require that limitations be placed on the results obtained. The two most distinct differences were that only part of the full annular UCC was used and that only part

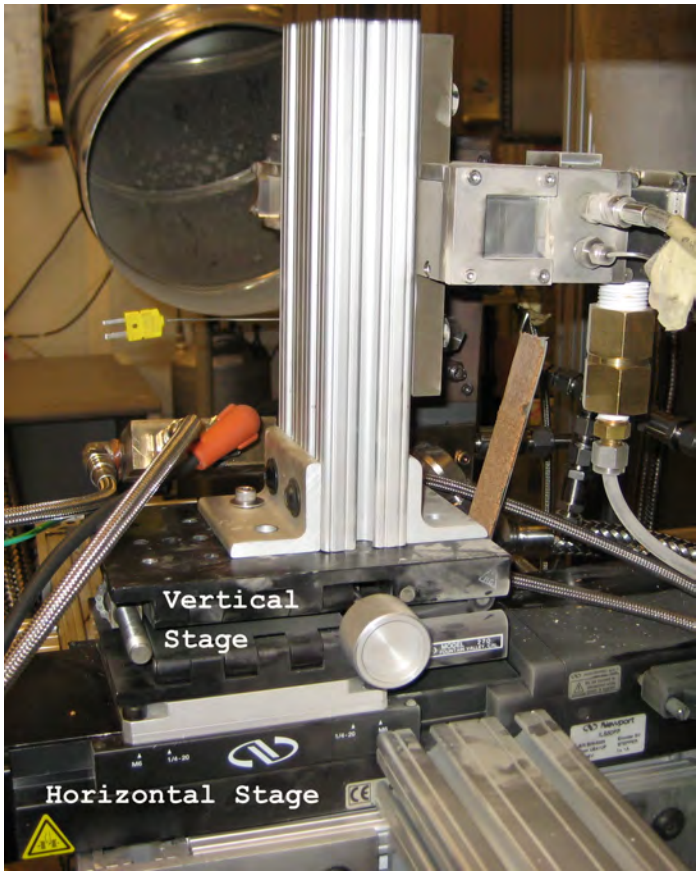

Figure 30. AFIT sectional UCC model on NRC 270 vertical translation stage and Newport ILS50PP horizontal stage

of the full core flow was used.

There are two distinct advantages of using a sectional model over an annular model. First, the sectional UCC model has significantly more optical access than the annular model. This was a major advantage for this research because multiple viewing angles were required to fully characterize the flame migration. In the annular model, viewing perpendicular to the radial vane is impossible because above every vane is the bottom of the next vane. Viewing at the UCC ambient exit is also impossible because there is no ambient exit in the annular UCC because it's a full annulus and thus no planar data in that direction can be collected. Further, the sectional model is immensely more configurable than the annular model. The annular model has a single UCC cavity, with curvature, making it impossible to even consider a straight UCC section to isolate the centrifugal force contribution. Changing the radial vane height is also impossible on the annular model because the model has a fixed radius and thus fixed inner radius for the vane height.

While the advantages of using a sectional model were critical enablers to this research, the limitations of using a sectional model are important limiting factors to the results of this research. Several notable issues arise from the use of only part of a full annular UCC. By design, the UCC creates a build-up of mass within the circumferential cavity such that at steady-state the mass flow entering the UCC must equal the mass flow exiting the UCC into the core flow. As shown by Bohan, the mass build-up occurs as mass progresses from injection around the annulus and as additional mass is injected the existing mass in the UCC moves in the inward radial direction until migration into the core flow occurs [11]. Unlike the full annular UCC, the sectional model has an inner radial wall that prevents the UCC flow from migrating until the interface with the core flow section. This will likely increase the total migration quantity into the core due to "migration ready" flow being forced to

remain in the UCC until the core flow section is reached. The opposite could also be true that at higher tangential velocity the flow may take, for example, four vane passages, as shown by Bohan [11], before migration whereas the sectional model may have less than the required number leading to lower migration levels. Eliminating the mass build up also requires a large mass flow to be added in the seeder box or along the outer radial wall. With the former, this created significant flame holding difficulties at the interface of the seeder box and UCC at the higher tangential velocities. With the latter, unrealistic injection velocities are created. Under both conditions, the sectional model may have created the undesirable situation where the flow scenario in the sectional model is unrepresentative of the scenario in the full annular model.

The majority of this research used the seeder box to replicate the upstream condition that would have been present in an annular UCC model. This flow scenario had high mass flow rates entering in from the seeder box that was used to represent two, for the g-load investigation, or four, for the v-flame investigation, upstream fuel injectors. The seeder box was used to replicate the same phenomena that Bohan documented [11] where the mass from one fuel injector resided in the UCC for four vane passages. In other words, the mass flow through a given radial cross-section was four times that of a single injector. Considering Bohan's analysis to this research, the residence length for a small-scale annular UCC model might be longer than the six vane passages that would be present. Also, under these conditions the measured g-load value was lower than predicted which indicated that higher UCC mass flow rates should be used than predicted. For an annular UCC model, the higher UCC flow rates should be used to match the measured and predicted g-loads because the density was higher than predicted. With an annular UCC model though, the total mass flow rate would be fixed and increasing the UCC mass flow would decrease the core mass flow.

Perhaps the larger issue with how the flow should be split for a sectional versus annular model, or for either independently, is that no data currently exists to give direction towards what the "right" answer should be. Bohan [11] cited residence times, which can be translated into lengths using the velocity, and noted that the tangential velocity directly impacted the residence time. However, these analyses were conducted using non-reacting conditions for g-load well over 7,500 g's simulating a condition far outside the stability limits documented by Zelina et al. [7]. Despite the fact that Bohan's analysis [11] was conducted on a non-physical condition, the analysis derived estimates for the number of vane passages for which the fuel from a given injector would reside within the UCC. Of greater interest though is the relation of the total mass flow moving through a cross section of the UCC to the inlet mass flow rate. The ratio of the inlet mass flow rate to the total mass flow moving through the UCC, which is certainly influenced by the residence time, will provide the necessary insight for determining the ideal flow conditions in a sectional model.

One additional issue exists with using a core flow section over the full geometry. This issue is that unless a full vane geometry is used, representative pressure distributions will not be created. With the model used in this research only the suction side of the vane is present without the pressure side. Inherently then the pressure distribution created will not be representative of a full vane because it is the combination of the two sides that produces the pressure distribution. Specifically, the exact measurement quantities will vary between sectional and annular models, but the fundamental interactions remain the same. It is the focus of this research to investigate these fundamental interactions and the implications of the interactions on the flame migration. It is anticipated that the trends established with the parameter variation will remain the same even though potentially significant changes in magnitude may occur.

3.4 COAL Lab Capability

COAL lab was specifically designed to investigate small-scale combustors under atmopheric conditions, such as a sectional UCC model. The lab was originally designed and built as described by Anderson [8] and validated by Koether using OH PLIF to investigate laminar premixed flame [41].

The COAL Lab uses two Ingersoll Rand air compressors to provide up to 7 kg per minute of air to the main line for the core flow and up to 2 kg /min to the secondary line for the UCC flow. Fox Thermal Instruments FT2 flow controllers with an accuracy of 1% were used to control the flow rates for each line. Smaller mass flow controllers manufactured by MKS of model ALTA 1480A were used for up to 50 SLPM of air for the igniter, 15 SLPM of ethylene (C_2H_4) for the igniter, 30 SLPM of Air for each of the two PIV seeders, 30 SLPM of nitrogen for coflow or fuel purge, and of model ALTA MC20 for up to 275 SLPM of hydrogen (H_2) or 108 SLPM of propane (C_3H_8) for the combustor. Previously, only the MKS ALTA 1480A controllers were used providing up to 50 SLPM of air (18 SLPM of propane). Four MKS ALTA MC20 controllers were purchased to increase the flow rate capability, two 100 SLPM of Air (36 SLPM of Propane) and two 200 SLPM of air (72 SLPM of propane). Both MKS flow controller models have a 1% accuracy and were powered and controlled using one of the two the MKS 247D 4-channel control boxes. Previously only one box was used to control the PIV Seeder flow, the UCC fuel flow, and the ethylene/air for the Ignitor. However, using a second seeder required another MKS 247-D control box for additional channels to control air flow for a second PIV seeder and seeder box fuel flow. The final configuration of the MKS control boxes used for the current test program consisted of box 1 controlling 18 SLPM of propane for the Hencken burner, 30 SLPM of air for core flow PIV seeding, 30 SLPM of air for UCC flow PIV seeding, with the fourth channel empty and for box 2, controlled through LABVIEW, being

50 SLPM of air for the ignitor (or Hencken burner), 15 SLPM of ethylene for the ignitor, 36 SLPM of propane for the UCC Fuel Injectors, and 72 SLPM of propane for the UCC Seeder Box Injector. The MKS mass flow controllers were calibrated similarly to Drenth [9] but with the display set to show the flow rate in SLPM instead of percent of maximum flow rate.

Previously, UCC operation was limited to either small bottled gases or liquid, which was prone to severe and hazardous pooling issues as noted by Drenth [9]. This research added the ability to use large propane flow rates from AFIT's existing liquid-gas propane vaporizer (Algas Zimmer model) from another laboratory. The Zimmer vaporizer can output up to 350 SLPM of gaseous propane and is connected to three 500 gallon liquid propane tanks, which for safety and reliability reasons are only filled to 80% and are not used below 20%. At the maximum output, corresponding to 20 gallons of liquid propane per hour, this equates to approximately 45 hours of testing time. Considering this research used at most 50 SLPM of propane this would yield around 300 hours or nearly two weeks of continuous testing. This was an immense increase over the nominal 4-6 hour limit experienced by Drenth and Thomas [9; 29] at significantly lower flow rates. Realistically, the UCC rig was only run for about 15 minutes for a specific test condition and not longer than about 30 minutes before parts of the metal rig became "red hot" and needed to cool off before testing could resume. When running a specific condition, a minimum of two minutes "on condition" was used for establishing "good data".

Thermocouples (Omega K-Type, range 73-1523K, error 0.75%) were used to measure the inlet and exit temperatures of both the UCC and the core flow to approximate the heat release with the temperature rise. Traditional pressure transducers (Dwyer model 682 with error of 0.13%) were used to measure the inlet pressure of the UCC and core flow while differential pressure transducers (Dwyer model 655-5 with error

of 0.5%) were used to measure the pressure drop across both the UCC and the core flow. Characterization of the pressure loss is important from both an efficiency and functionality standpoint of the combustor. Control over the air mass flow rates, the ignitor, and display of temperatures and pressures was accomplished using a derivative of the interface created by Anderson [8] using National Instruments LABVIEW program.

Using derivatives of Anderson's LABVIEW program allows for remote operation over the lab's gigabit ethernet network using TightVNC v1.3.10 remote desktop software. The lab's network was expanded from the existing 8-port switch to a Cisco SG200 26-port switch allowing every lab computer and camera to be simultaneously interconnected. This proved vital to improving efficiency due to every computer being able to control every other computer via remote desktop software over the internal lab network, which was immensely beneficial during camera alignment, translation stage alignment, laser alignment to the wave meter, and operation of the entire PIV system. Also, single-person operation of the lab was realized using the dedicated display computer connected to a 55" plasma TV large enough to remotely display up to six computers or five computers and one of the added Microsoft LiveCam Cinema webcams for remote viewing to determine successful UCC ignition and sustained operation. Additionally, a Data Robotics DroboPro FS network storage server was added and setup containing 16 TerraBytes (TB) on eight hard drives (Western Digital EARS20) providing 10.73 TB of usable storage with dual-redundancy (up to two drives may fail without data loss). This allows for redundant backup of all of the experimental data and each lab computer's hard drive, in case of a drive failure. Prior to the Drobo addition, two hard drive failures occurred, one total-loss and one partial loss, that required approximately two weeks to fix due to nonexistent backups of those computers.

3.5 COAL Lab Laser Diagnostics

Laser diagnostics have become commonplace in combustion research. Unlike traditional diagnostic equipment, laser diagnostics obtain measurements inside the flame while avoiding any possible disruptions in the physics due to the present of a physical object in the flow. AFIT's COAL Lab currently has the capability to perform several different types of laser-based diagnostics. The lab is already outfitted with PLIF, PIV, Tunable Diode Laser Absorption Spectroscopy (TDLAS), LII, Rayleigh scattering, and CARS. PLIF is a two-dimentional (2D) technique for interrogating flowfield species on the molecular level to measure molecular species concentration and temperature, according to Drenth [9]. According to Thomas, PIV is a technique for producing 2D measurements of the flowfield yielding velocity and turbulence statistics [29]. According to Serianne, the TDLAS technique is used to measure 1D species concentration, pressure, velocity, and temperature [48]. Laser-Induced Incandescence (LII) is a technique for imaging the planar soot particle distribution, according to Eckbreth [15]. The Rayleigh scattering technique can be used to measure 2D pressure, temperature, velocity, and species concentration, according to Muraoka and Maeda [49]. CARS is used to measure point-wise pressure, temperature, and species concentration to very high accuracy, according to Eckbreth [15]. This suite of diagnostics form a composite picture designed to be the most effective in combustion diagnostics making the COAL lab the ideal location to conduct research in optimizing the UCC design with each diagnostic having it's own unique advantages and disadvantages.

The advantages and disadvantages of each diagnostic technique were considered in the selection of the diagnostic techniques used in this research. Understanding the spatial variation was important based on the research objectives necessitating planar or 2D measurements which eliminated TDLAS and CARS from further consideration. Temperature was a key parameter of interest, but only PLIF and Rayleigh scattering

provided planar measurements. PLIF was selected over Rayleigh scattering due lacking a suitable laser for measuring Rayleigh scattering in a combustion environment. PLIF was also well documented by previous AFIT researchers investigating the UCC, specifically Koether, Hankins, Lakusta, and Drenth [41; 3; 42; 9]. Velocity was also a key parameter of interest, but only PIV and Rayleigh scattering provided planar velocity data. PIV was selected over Rayleigh scattering for velocity measurement for the same reason that PLIF was selected over Rayleigh scattering, a suitable laser for measuring Rayleigh scattering in a combustion environment was not available. LII was not chosen for this research due to soot not being thought to be a significant issue in the UCC due to the high mixing levels. While only the background literature for PLIF and PIV will be discussed in this chapter, the literature on the remaining techniques is in Appendix A.

3.6 Planar Laser-Induced Fluorescence

3.6.1 Background.

Planar laser-induced fluorescence (PLIF) is a spectroscopy technique based on the property of stimulated-emission or fluorescence, as defined by Eckbreth [15]. After a specified frequency band laser beam is sent through the sheet-forming optics, the resultant two-dimensional (2-D) laser sheet is sent into the region of interest (ROI). Photons from the laser sheet excite molecules of a particular species to a higher energy state. This higher energy state is unstable causing the excited molecules to release a photon of a particular, but different, energy so that it can relax down to a stable energy state, as stated by Hankins [3]. The photon energy, and corresponding wavelength, is dependent on the molecular species and frequency of incident light from the laser, according to Eckbreth [15]. Table 2 shows the fluorescent absorption ranges for species present in the hydrocarbon combustion process from Eckbreth [15].

Table 2. Wavelength spectral ranges for combustion species from Eckbreth [15]

Molecule	Electronic Transition (nm)
C_2	230-330 440-600
CH Radical	360-450 430-500
CO	150-240 200-250
N_2	100-500 Vac U.V.
NO	195-340 200-500
O_2	170-220 500-900
OH Radical	 240-400
CH_4	145.5-500
C_2H_2	210-237
CO_2	140-170
H_2O	145-186

While the spectra for the interested species is significantly vast, the majority of it is contained within the ultraviolet (UV) portion of the electromagnetic spectrum and typically only a single species will be interrogated for a given experimental setup, according to Eckbreth [15]. Further, because quantum mechanics governs the molecular scale, a given species will only exhibit fluorescence at discrete wavelengths contained in the corresponding ranges, according to Drenth [9]. These spectral lines are numerous for a particular species and may or may not have significant temperature variation. Fortunately, computer programs exist for the sole purpose of PLIF diagnostics, such as LIFBASE, to model the species spectra, as used by Anderson [8].

Of particular interest to applying PLIF to combustion is the hydroxyl radical (OH) because it is only present inside the flame, according to Eckbreth [15]. OH also has a very long fluorescence time, on the order of 100 ns, further adding to its attractiveness applying PLIF to combustion, according to Eckbreth [15]. Beyond the obvious use as

a flame marker, OH PLIF can also be used to measure OH species concentration and temperature by using the OH (A-X) electronic transition as shown in Figure 31 as illustrated by Hankins [3]. The figure shows both the X ground energy state and the higher A energy state with the horizontal lines representing the vibrational levels. The variations within a rotational state are shown in Figure 32 illustrating the strength of the emitted fluorescence signal versus the emission frequency (in wave numbers). Eckbreth defined the common notation for the vibrational sub-levels needed to fully specify the transition in this case is the OH (A-X) (1-0) transition, with specific rotational state specified by a letter, number, and parenthetical number of the form $Q_1(5)$ [15]. The letter and subscript, Q_1, refers to the Q_1 rotational state, while the parenthetical number, (5), refers to the fifth variation within the Q_1 rotational state. These rotational energy states are excited by specific wavelength photons and relax down to the ground state emitting longer wavelength photons due to the energy remaining in the vibrational level after fluorescence. When viewed on a frequency vs. intensity (Figure 32), the emitted wavelengths correspond to lines composing the fluorescence spectrum for the given species. In reality, the discrete wavelengths are not lines, but are typically a Gaussian or similar type distribution, according to Drenth [9].

The fluorescence spectra are the basis for PLIF spectroscopy. In particular, when using OH PLIF to measure temperature, Kostka et al. noted that only specific spectral lines are of interest [16]. There are several methods of PLIF thermometry but only two will be discussed. The first method is the excitation scan method, which also uses only a single transition line. After selecting a line of interest from LIFBASE, the incident laser is tuned in small increments through a range of wavelengths just below and above the peak, as determined by Lakusta [42]. The recorded fluorescence emission intensities, when plotted versus wavelength, show the shape of the line. This

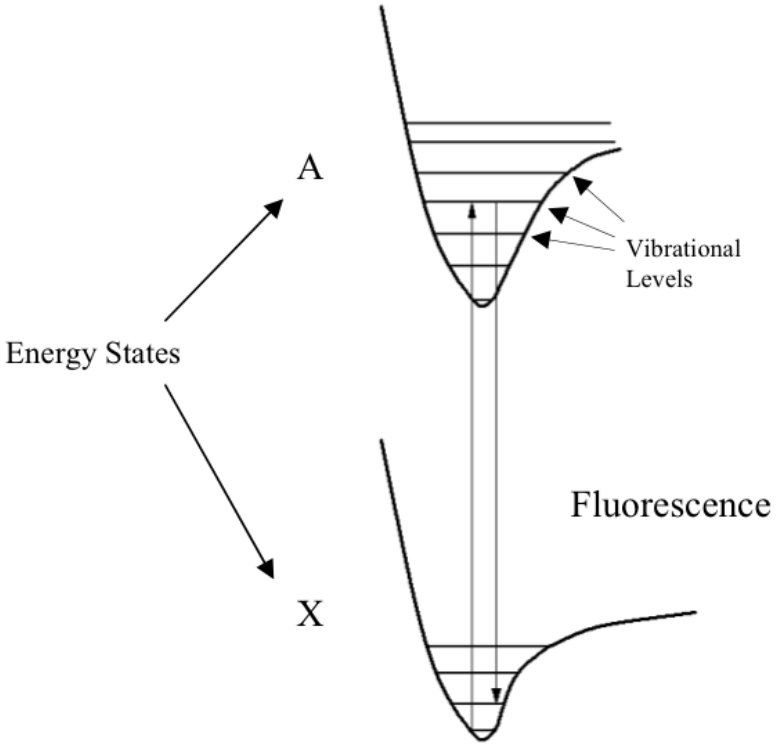

Figure 31. A-X energy levels with vibrational sub-levels shown. (Adapted from Eckbreth [15])

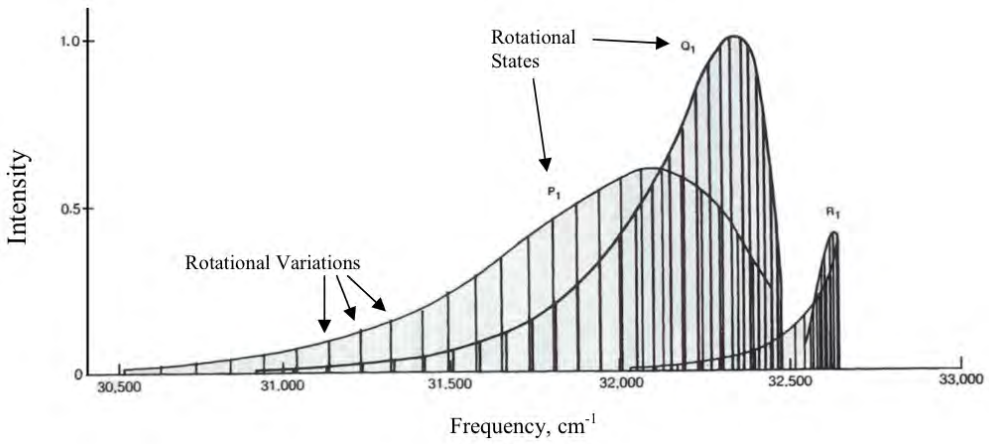

Figure 32. Illustration of the variations of a rotational state showing the emitted fluorescence signal vs. emission frequency (in wave number). (Adapted from Eckbreth [15])

line shape also depends on temperature, and thus can be correlated again with LIF-BASE data in order to determine flame temperature. Since line shape is the entity of interest for the excitation scan, a method of quantitatively analyzing these shapes must be used. The Full-Width Half-Max (FWHM) is typically used for this method as implemented by Lakusta [42]. While more accurate, the excitation scan thermometry technique requires a significantly higher data collection due to the necessity of curve-fitting the transition line, compared to the intensity-ratio method, according to Lakusta [42].

The second method, the intensity-ratio method, examines the ratio of fluorescent intensities produced by two different excitation wavelengths, as used by Drenth [9]. This method sacrifices experimental simplicity and accuracy for a reduction in necessary data collection and requires simultaneously measuring two transition lines. The two transition lines, or the line pair, are selected for their sensitivity to temperature and wavelength proximities, as determined by Seitzman et al. [50]. Hankins found that by choosing one line which is relatively insensitive to temperature and another which has an intensity varying greatly with temperature, the fluorescence intensity ratio of these two lines can be correlated with theoretical data generated by LIF-BASE in order to determine temperature [3]. Two-line PLIF thermometry using the line-peak ratio method was proposed initially by Cattolica in 1981 [51] and extensive work on the technique was continued by Lucht et al. in 1982 [52] and Seitzman et al. in 1994 [50]. The first planar data was not presented until Meier et al. in 2000 [53] and the first single-shot (not time-averaged) data by Giezendanner et al. in 2005 [54].

Seitzman et al.[50] examined three line pairs, Q2(11) - R2(5), Q2(11) - P1(7), and Q2(11) - R2(8). They measured a temperature range from 1000-3000 Kelvin (K) with as low as 5% error when using the Q2(11) - P1(7) transition pair. The

wavelengths for these lines were Q2(11) 285.16 nm, P1(7) 285.09 nm, and R2(8) 281.72 nm. Giezendanner-Thoben et al. [54] used one line pair, P1(2) - R2(13), to measure a temperature range of 1500-2200 K with an error of 4 to 7% depending on the location within the flame and the temperature. The wavelengths for these lines were as follows: P1(2) 282.66 nm and R2(13) 282.64 nm [54]. Welle et al. used one line pair, Q1(5) - Q1(14), with wavelengths of 282.75 and 286.46 nm respectively [55]. Their experimental set-up used a laser system calibrated with a premixed methane-air flame from a Hencken burner [55]. Kostka et. al. also used the Q1(5) - Q1(14) line pair (282.75 nm and 286.46 nm) in comparison of the peak intensity ratio and excitation scan thermometry methods using a Hencken burner in standard operation [16]. The Hencken burner, as shown in Figure 33 produces a nearly adiabatic laminar diffusion flame that is widely used for calibrating laser diagnostics for combustion investigations [9]. The standard operation of the Hencken burner uses separate inlets for the fuel, air, and coflow labeled on the right image in Figure 33 as H_2, Air, and N_2, respectively. However, in premixed mode, as used by Welle et al., the fuel and air are both connected, via a "T" adapter, to the inlet labeled Air in Figure 33 and no coflow is used [55].

Several varying line pairs were previously investigated by Hankins [3] and Lakusta [42] using a Hencken burner in diffusion flame configuration with hydrogen fuel. The ratios of the magnitude of these peaks were determined, both theoretically using LIFBASE and experimentally, and plotted as a function of temperature. For the experimental results, since the measured intensity is proportional to the incident laser pulse energy, the intensities are normalized by the laser pulse energy for each test, as determined by Drenth [9]. The ratios of these intensities are then compared to the ratio of peaks from LIFBASE to determine a temperature. Measurements were taken of a hydrogen flame for $\phi = 0.5 - 1.3$. The temperature measurements were compared

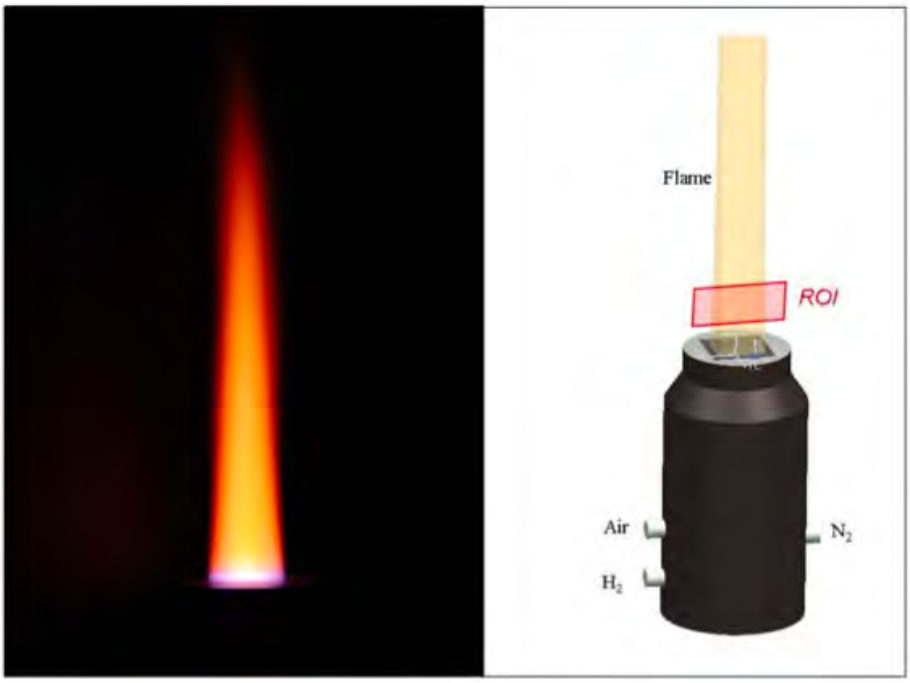

Figure 33. Image of the nearly adiabatic laminar flame from a Hencken burner (left) and sketch of the Hencken burner (right) from Kostka et al. [16]

to the theoretical temperatures and to Hancock's data [56] and as shown in Figure 34 the Q1(14)/Q1(5) ratio produced the most accurate temperature measurements with an average accuracy of 8.2%. Following the work of Hankins [3] and Lakusta [42], Drenth [9] was able to implement the simultaneous two-line intensity ratio PLIF thermometry technique at AFIT with the temperature correlation shown in Equation 15. This equation is a 5th order polynomial curve fit to the fuel-lean ratio values ($\phi < 1.0$), which were used in Figure 34, and the corresponding equilibrium adiabatic flame temperatures.

$$T = 62819 * R^5 - 116871 * R^4 + 84375 * R^3 - 29553 * R^2 + 8258.5 * R + 821.03 \quad (15)$$

There are several corrections to be considered in the application of two-line PLIF. First, the fluorescence regime must be determined. Drenth determined the OH fluo-

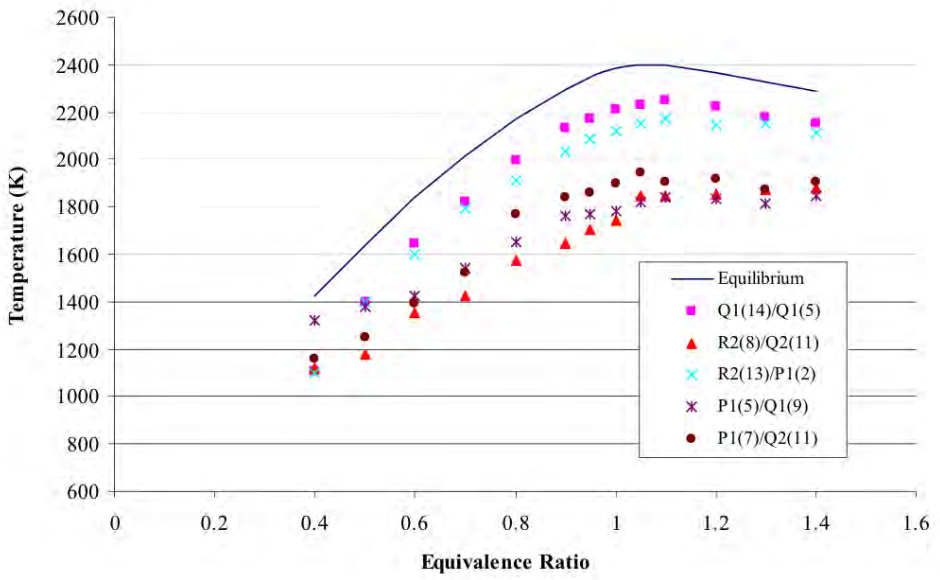

Figure 34. Intensity-ratio method temperatures vs. theoretical values from Hankins [3].

rescence was not occurring in the energy saturated regime but in the linear regime and required normalization of the fluorescence signal by the laser pulse energy [9]. The linear fluorescence regime is where the detected fluorescence is linearly proportional to the excitation energy. As noted by Kostka et al., not all fluorescence transition lines operate independently of one another, resulting in spectral overlap in the fluorescence signal of multiple lines but that the Q1(14)/Q1(5) pair had low susceptibility to this error [16]. Kostka et al. also noted the importance of correcting for collisional quenching by other species [16]. Beam quality issues can also create variations in energy distribution within the laser sheet as noted by Sietzeman et. al. [50]. Drenth also determined that the two cameras had slightly different quantum efficiencies and required a 7% correction to increase the signal captured by the Q1(14) camera for all 2-line PLIF measurements using these two cameras [9].

3.6.2 PLIF System.

The PLIF system, which was used for both flame visualization and temperature measurement, was a custom setup designed by Innovative Scientific Solutions, Inc. The system, shown in Figure 35, consists of a Spectra Physics Quanta-Ray PIV400 10 Hz dual-pulsed Nd:YAG laser with frequency conversion units to produce dual 532 nm pulses, two Continuum ND-6000 narrowband dye lasers, and two Princeton Instruments PI-Max v2 Intensified CCD (ICCD) cameras with Electrophysics 78mm F/3.8 lenses, and 295 nm long-pass filters (Lattice Optics WG295) to block UV laser scatter reflections. A LabSmith LC880 programable experiment controller was used to control the timing operation of the Nd:YAG laser and synchronize the Princeton cameras. While fully functional as two independent single-line PLIF systems, the LabSmith controller synchronizes the two systems so that measurement of each line occurs 500 ns apart. This was half of the 1 μs pulse delay that Drenth used.

Drenth also noted that a 500 ns exposure time was used to allow for a 100 ns "warm-up" time for the camera and allowing 400 ns to ensure collection of the entire 100 ns fluorescence event [9]. However, following discussions with the camera manufacturer, the start-up time was shortened to 10 ns with no visually discernible loss in signal with the reduced intensifier start-up time which then allowed the exposure time to be reduced from 500 ns to 300 ns. This allowed a shorter pulse delay to be used in the balance of necessarily needing to observe entirely separate microscopic fluorescence events while using the shortest pulse delay possible to observe the same macroscopic event. The dye lasers were tuned to output nominally 15 mJ each with wavelengths of 282.75 nm and 286.465 nm corresponding to the Q1(5) and Q1(14) transition lines. An Ophir Vega power meter with 0-30 mJ head was used to measure the laser pulse energy and a High Finesse WS7 wavemeter was used to measure the laser wavelength. For initial setup the wave meter was used for tuning the wave-

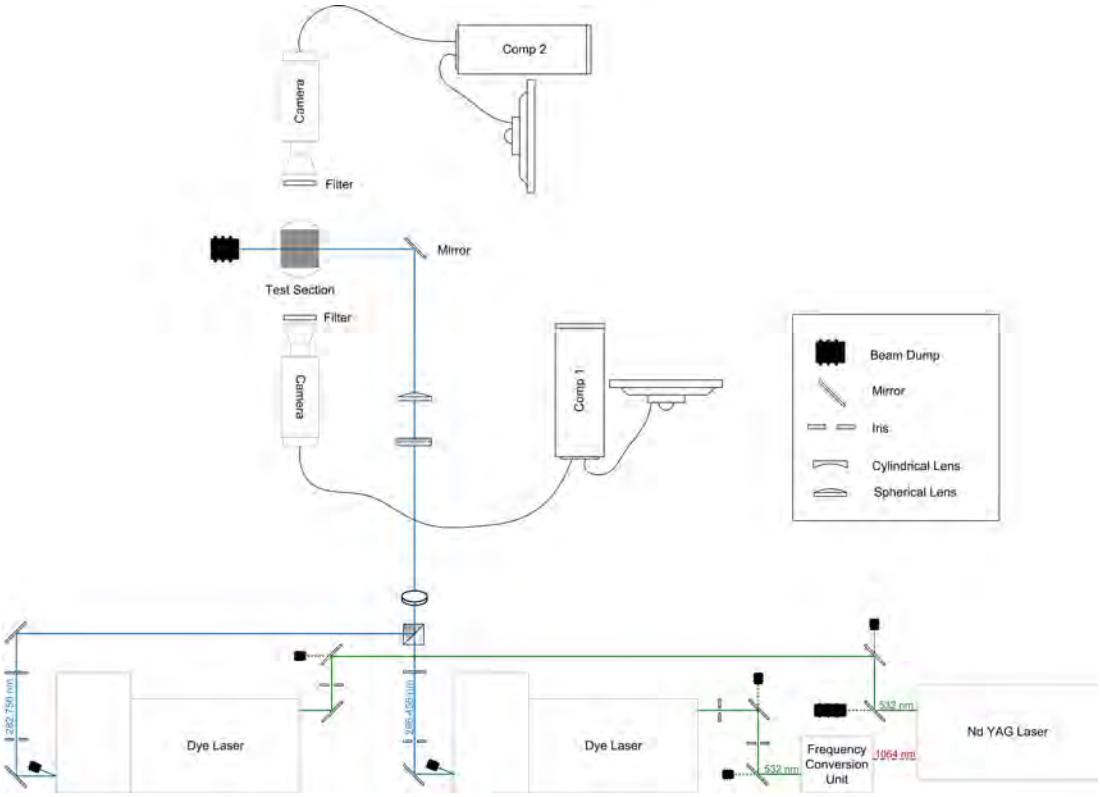

Figure 35. Schematic of the COAL lab's PLIF setup from Drenth [9]

length output of the dye laser to the excitation wavelength obtained from LIFBASE. Following the initial setup and successful collection of fluorescence signal the wavelength is fine-tuned (0.005 nm/step) to yield the maximum fluorescence signal for each transition line since this system uses the line-peak ratio method. It is important to note that the PLIF thermometry technique inherently only yields measurements in regions of OH presence. For this research, no OH is present outside of the flame and therefore no temperature is measured outside of the flame regions. This system was used to collect both single-line flame location measurements and two-line temperature measurements in the same manner as Drenth's research [9].

3.6.3 Calibration.

While previously calibrated for hydrogen flames by Hankins, Lakusta, and Drenth [3; 42; 9], it was desired to perform a new calibration using hydrocarbon fuel, preferably propane, due to its predominance in this research. The calibration was conducted using a Hencken burner which has been shown by Hancock and Welle et. al. to produce nearly adiabatic equilibrium flames [56; 55]. This burner was previously used with hydrogen-air flames by Koether, Hankins, Lakusta, and Drenth for calibration of OH PLIF measurements of this system [41; 3; 42; 9]. The burner was used to produce propane-air flames in premixed configuration, as described in Welle et. al. [55], where no coflow is used and a premixed fuel-air mixture is sent in via the air port on the Hencken burner. The air flow was constant at 7.5 SLPM and the fuel was varied to produce $\phi = 0.7 - 1.05$ with specific values of $\phi = 0.7, 0.8, 0.9, 0.95, 1.0, 1.05$ to produce a significant range of temperatures for calibration. This ϕ range was similar to the range of 0.75 to 0.975 used by Welle et al. [55]. Using propane, the peak adiabatic flame temperature of 2278.7K occurs at $\phi = 1.05$ while the temperature decreases as ϕ decreases as shown in Figure 36 using theoretical equilibrium values.

This range was chosen because the UCC has been shown by Zelina et al. to operate as a rich burn, quick quench, lean burn (RQL) combustor [37]. Based on the UCC being an RQL combustor, only values of $\phi < 1.0$ were chosen for the calibration because the measurements were taken in flames with $\phi < 1.0$, the reaction mechanism changes at $\phi > 1.0$, and every 2-line PLIF temperature measurement in the literature was calibrated to the fuel-lean side according to Drenth, Welle et al., and Kosta et al. [9; 55; 16]. The rich burn takes place within the UCC while the flame migrating into the core flow is quickly quenched into a lean burn situation where the PLIF measurements were taken. Also, measurements in the core flow showed peak fluorescence signal intensity was less than that of the signal intensity of the $\phi = 0.95$ calibration images where peak OH concentration occurs which further supported the fuel-lean assumption. Calibration data for $\phi < 0.7$ was not possible due to the flame stability limits of the Hencken burner using propane.

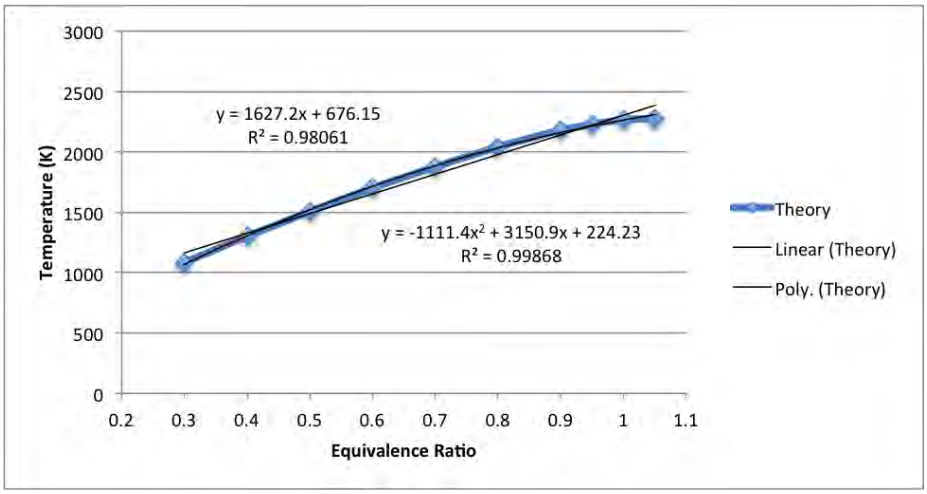

Figure 36. Plot of the equilibrium adiabatic flame temperature (K) vs. equivalence ratio (ϕ) with linear and quadratic interpolation equations

For each transition line a 200 image (20 seconds) temporal average was computed and from that a 10x10 pixel spatial average was taken at a visually determined suitable location. At this location the fluorescence signal was obtained via subtraction of the laser background image from the signal image. The fluorescence signal was

then normalized by the laser pulse energy as Drenth determined that the fluorescence signal was not saturated and thus was within the linear regime requiring normalization by pulse energy [9]. In addition to correcting for laser pulse energy, quantum efficiency differences between cameras should be accounted for. Drenth determined that the Q1(14) camera sensitivity was an approximately 7% lower in the signal detected between both cameras observing the same fluorescence event [9]. This was corrected for and the ratio of the two lines was computed. The values of the ratio with corresponding adiabatic flame temperature, based on the ϕ at the specific condition, was plotted in Figure 37. While the theoretical Boltzmann ratio is an exponential function, according to Cattolica [51], the data in Figure 37 clearly shows that a linear interpolation was reasonable over this regime. Figure 37 shows that the calibration data was reasonably interpreted by three types of interpolation functions: linear, quadratic, and logarithmic. The linear interpolation, shown in Equation 16, was used for processing the data in this research.

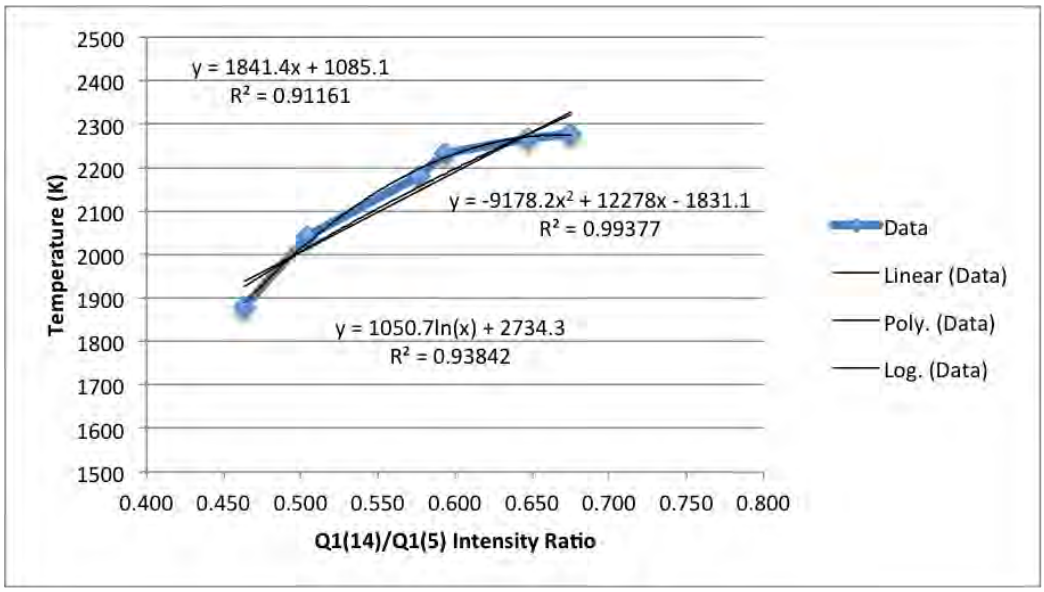

Figure 37. Experimental correlations of corrected ratio vs. temperature (K) using both linear and quadratic interpolations

$$T = 1841.4 \times R + 1085.1 \tag{16}$$

3.6.4 Error Analysis.

There are three main sources of error occur with the two-line PLIF temperature measurement that can be reasonably characterized. These three sources are the mass flow rate error, interpolation error, and repeatability error. Two mass flow controllers were used for the air and propane flows each contributing a 1% error for a combined maximum 2% error contribution. The mass flow controller error contributed to the error in setting ϕ, which was used to correlate to the temperature. As illustrated in Figure 37, there was an error associated with the linear interpolation itself. The correlation was used to compute the measured temperature which resulted in a average interpolation error of 1.85% among the calibration points when compared to the adiabatic flame temperature. Finally, in order to asses the repeatability of the measurement the $\phi = 1.0$ case was repeated three times with an average error of 7.02%. The higher repeatability error was likely due to the decreased stability of using propane in the Hencken burner, instead of the less complex fuel (hyrdogen and methane) that the burner was designed for, but propane was used since it was the dominant fuel in this research. Using the traditional root-sum-square approach yields a total error of 7.53%. This is higher than the 6% error reported by Kostka et. al. using the same line pair but this increase is expected because it was not possible to apply all of the fluorescence corrections [16]. Laser sheet energy distributions were not accounted for due to lack of equipment. Also, quenching corrections were not applied due to their requirement of a priori knowledge of the entire gas composition that, while available for the Hencken burner flame, would not be available for the UCC measurements. Spectral overlap corrections were not applied because Kostka

et. al. determined this correction was relatively insignificant for this specific line pair [16]. Figure 38 is the temperature correlation with representation of the total error resultant from the three main error sources within the calibration regime. Outside the calibration regime the error will necessarily be higher, but of unknown quantity.

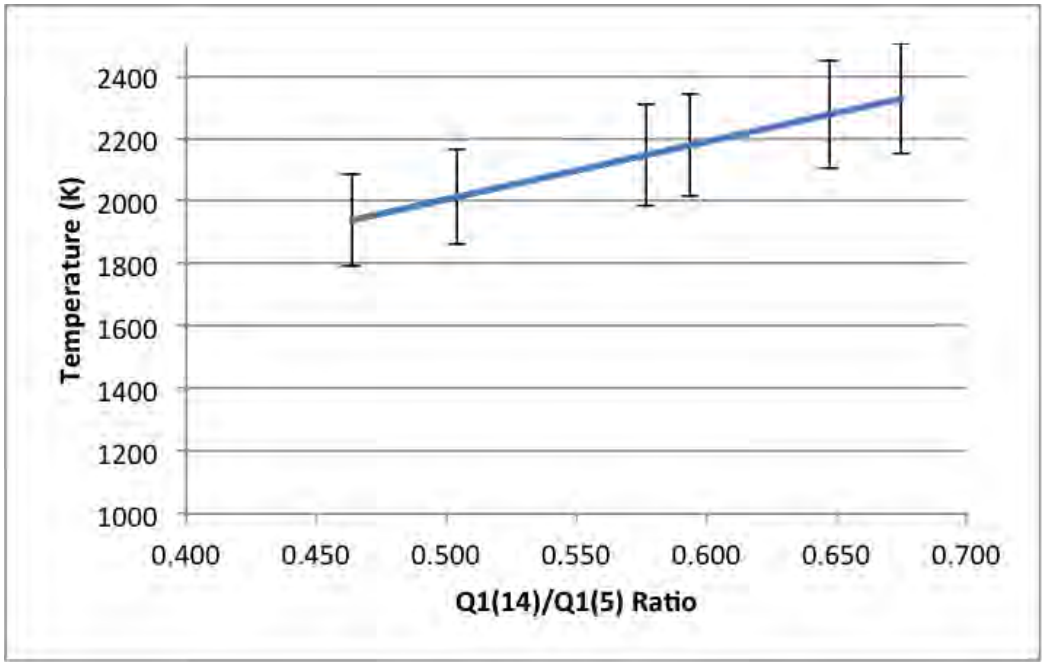

Figure 38. Two-line temperature calibration curve with error bars

In addition to the previously stated error sources (mass flow rate, data interpolation, repeatability), the fluorescence of Polycyclic Aromatic Hydrocarbons (PAH) has been problematic for certain PLIF experiments. Heffernen noted that PAH fluorescence caused significant difficulty interpreting the PLIF data from a horizontally-issuing reacting buoyant jets [44]. In order to determine if PAH was a contributing factor to this research, the excitation wavelength for the Q1(5) fluorescence line was decreased such that the OH fluorescence ceased, from 282.75 nm to 282.74 nm, as the recommended procedure by Heffernen for determining if coupling between OH and PAH fluorescence existed [44]. The images in Figure 39 illustrate the raw signal counts of OH fluorescence (top image) on the order of 1200 whereas the detuned

image (bottom) had signal counts on the order of 300, inline with the camera background intensity. According to Heffernen's results, the presence of PAH fluorescence was manifested with signal levels on the same order as OH fluorescence [44]. However, for this research, the detuned image that would have shown PAH fluorescence was on the order of the camera background, indicating PAH fluorescence was not present.

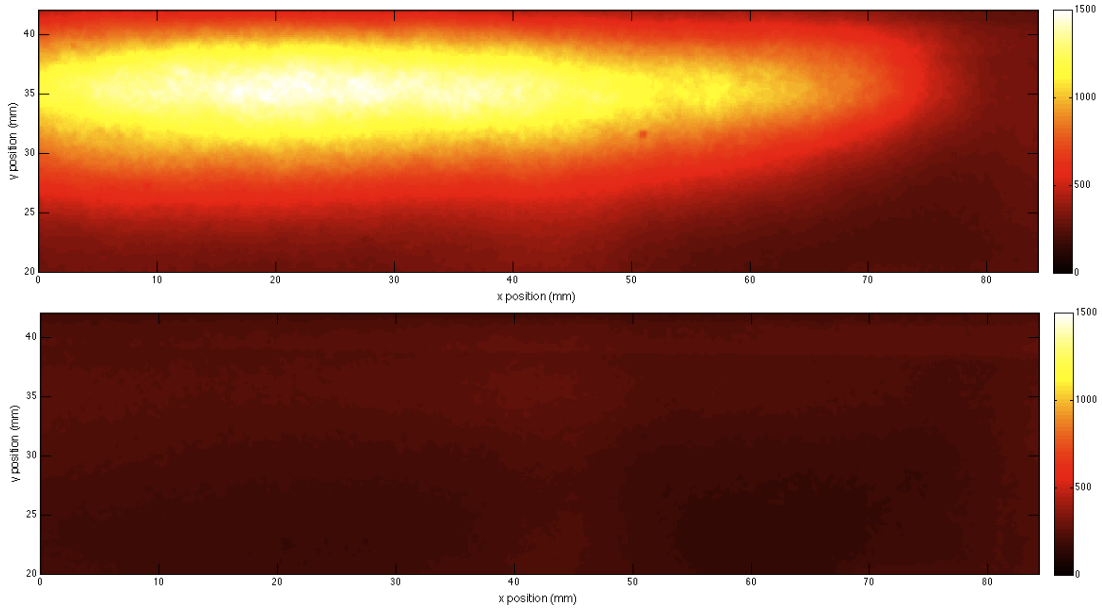

Figure 39. Test to determine coupling of OH fluorescence (top) and PAH fluorescence (bottom), note the bottom figure indicates no PAH fluorescence was present. Note the flow was from right to left and x = 0 mm refers to the exit, which is the end of the viewing window.

3.6.5 Illustrative Measurement.

This section illustrates the measurement collection and analysis procedure that was used for the single-line PLIF flame location images that were obtained for the v-flame investigation, and the two-line PLIF temperature images that were obtained for the vane height and g-load investigations. Figure 40 is the OH-PLIF spatial calibration image for the vane height and g-load investigations, and shows the UCC (behind the plane) and core flow directions, the leading and trailing edges of the radial vane, the radial vane cavity, the location of exit plane interrogation, and approximate

lengths of each feature. The image was acquired using Princeton Instruments WinView software and had a spatial calibration constant of 0.165 mm/pixel yielding a 42.24 mm by 84.48 mm total image size for the 256 by 512 pixel PLIF images. Figure 41 shows four consecutive PLIF images for the Q1(14) line (left) and Q1(5) line (right) from a representative UCC condition to illustrate the temporal variability in the flamelet location. The high temporal variability of flamelet location indicated that the time-averaged flamelet distribution must fall in the fuel-lean regime as expected. As shown in Figure 41, the images of each fluorescence line captured the same flame location independently even though there was significant temporal variation.

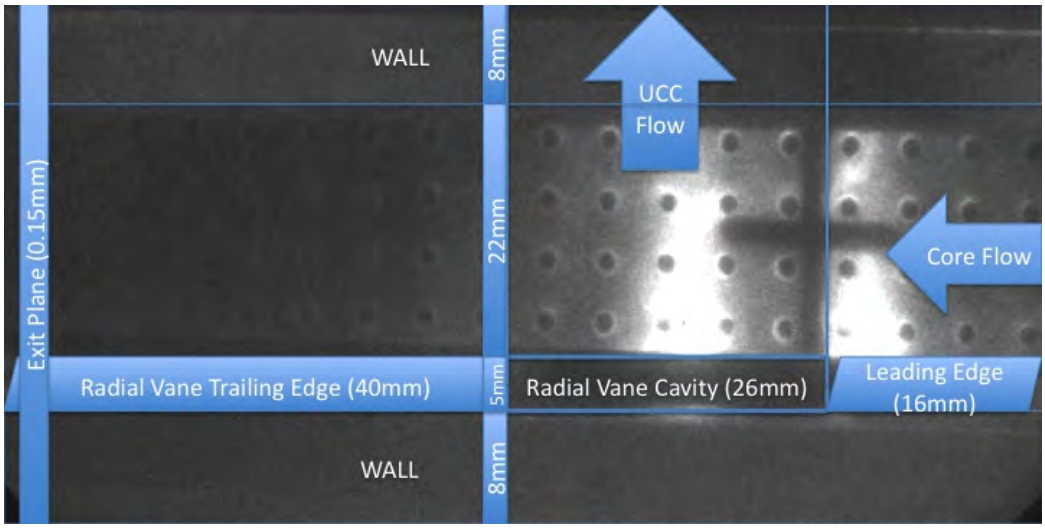

Figure 40. Spatial calibration image for OH-PLIF. Highlighted are locations of the radial vane cavity, UCC flow, core flow, and exit plane location.

A time-average of the 200 collected images, such as the images shown in Figure 41, was then taken for both the Q1(14) and Q1(5) data and produced the images shown in Figure 42 for a typical UCC condition. The selection of 200 images was based on the research of Giezendanner-Thoben et al. [54] which showed that collecting 200 images on a model gas turbine combustor reduced the time-averaged temperature error to within 1%. The raw images in Figure 42 represent the time-averaged flamelet distribution for the Q1(14) line (top) and Q1(5) line (bottom) with a 3x3 pixel average

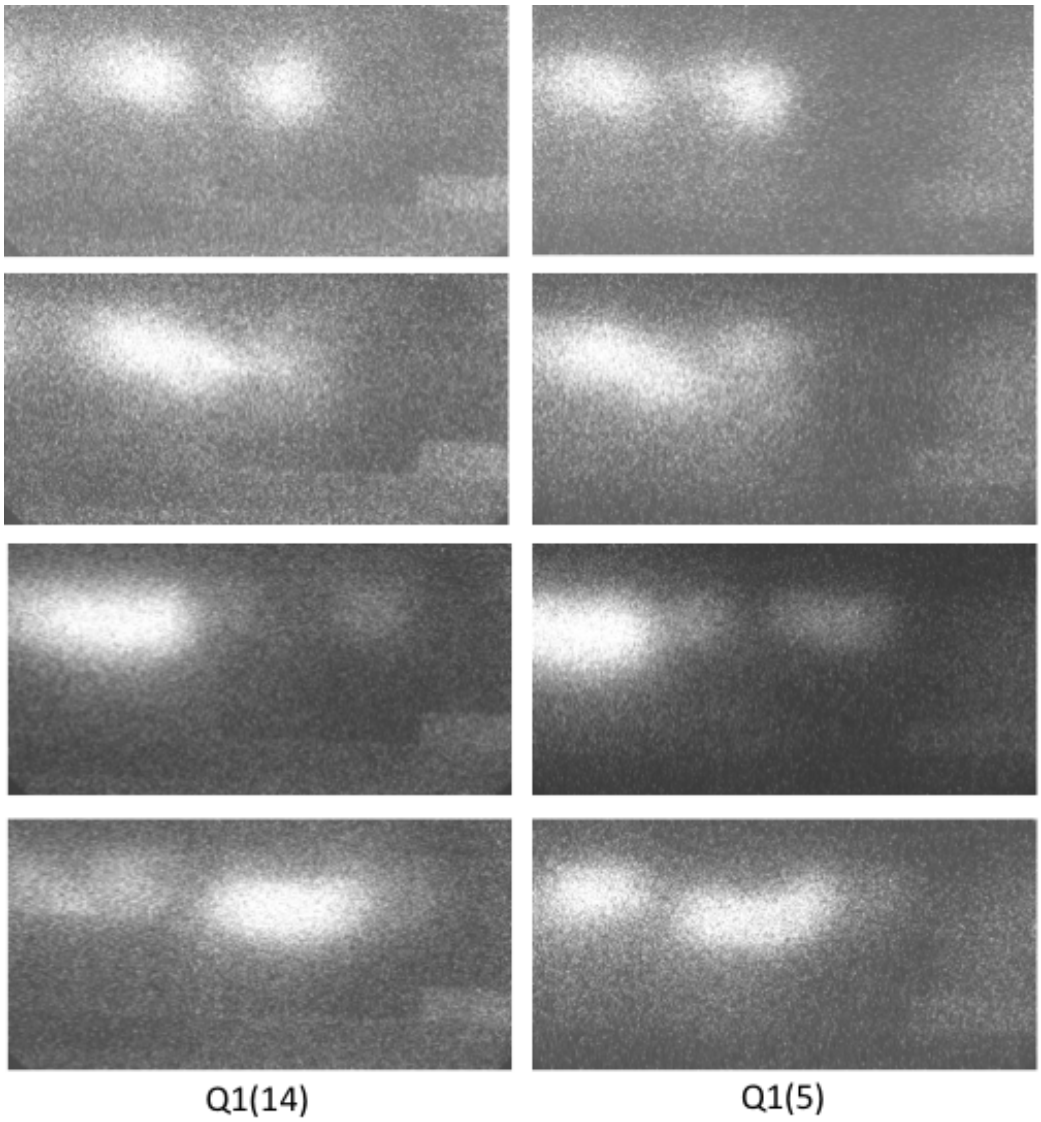

Figure 41. Raw sequence of 4 consecutive 10 Hz PLIF images illustrating flamelet temporal variability for the Q1(14) line (left) and Q1(5) line (right). The pixel intensity scale for each image was adjusted to highlight flame location.

filter applied to the images. For the v-flame investigation, the raw signal image from the Q1(5) line was used for comparison of the flame shape only, but for the vane height and g-load investigations the following additional steps were used to compute the measured PLIF temperatures.

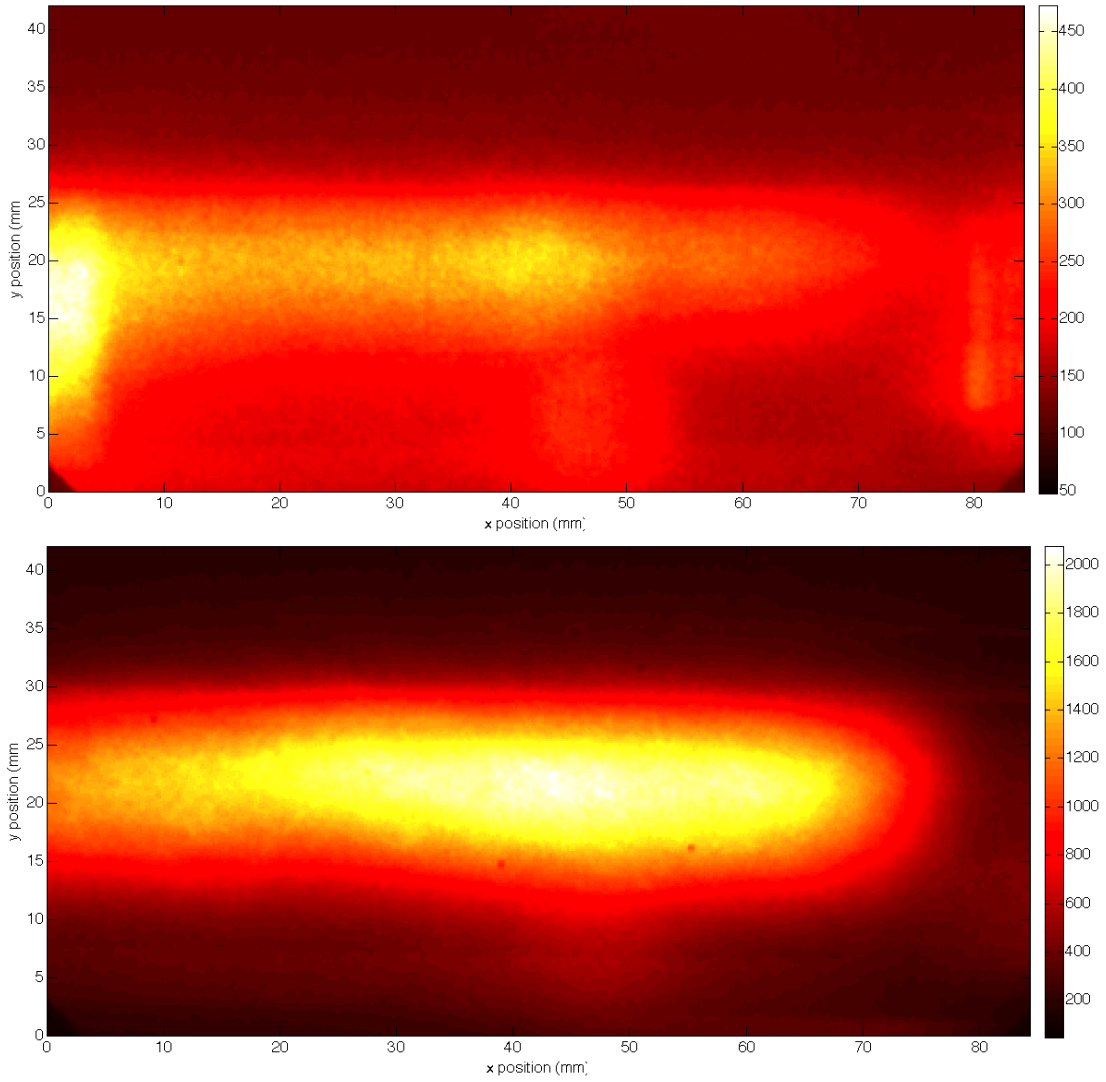

Figure 42. A raw 200 Image average of OH fluorescence signal counts for the Q1(14) line (top) and Q1(5) line (bottom)

Following the time-averaging process and proceeding to the computation of the PLIF temperature values, the laser scatter background image was subtracted from each signal image. The laser scatter background images are shown in Figure 43 for

both the Q1(14) line (top) and Q1(5) line (bottom). It was determined that the laser scatter background images were very location specific and were acquired once per setup for every data collection location. After background subtraction, each signal image was normalized by the incident laser pulse energy, typically 10-15 mJ, per Drenth's determination and then the Q1(14) signal image was then mapped onto the Q1(5) image geometry [9]. This was accomplished via MATLAB image processing tools on images of spatial mapping target, as shown in Figure 44 imaged with both the Q1(14) camera (top) and the Q1(5) camera (middle), note the circled dot position was not identical for both cameras establishing the need for the image transformation. The image transformation used a quadratic polynomial for interpolating the geometry from one reference frame to another and when there is geometric distortion of the pixels in the transformation a bilinear interpolation was used. Subtracting the transformed Q1(14) image from the Q1(5) image resulted in the bottom image of Figure 44, which showed an accurate geometry transformation resulted.

The dots in the images of Figure 44 were analyzed with functions from the MATLAB image processing toolbox to create the transformation matrix from the Q1(14) image geometry to the Q1(5) image geometry. Figure 45 shows the Q1(14) signal for the original geometry and after transformation to the Q1(5) image geometry. Once the Q1(14) image was mapped to the Q1(5) image geometry, both signal images were filtered to maintain a minimum level of signal that was greater than 25% of the maximum signal, or 10 signal counts, to ensure adequate signal levels were present for both lines before computing the ratio. The 25% value was chosen such that the minimum signal for each line used to compute a temperature was always greater than the additional 10 signal count threshold value, eliminating any biasing that could have been introduced by using a fixed value threshold. This is illustrated by the limiting condition where both lines have the minimum 10 signal counts yielding a ratio of 1.0

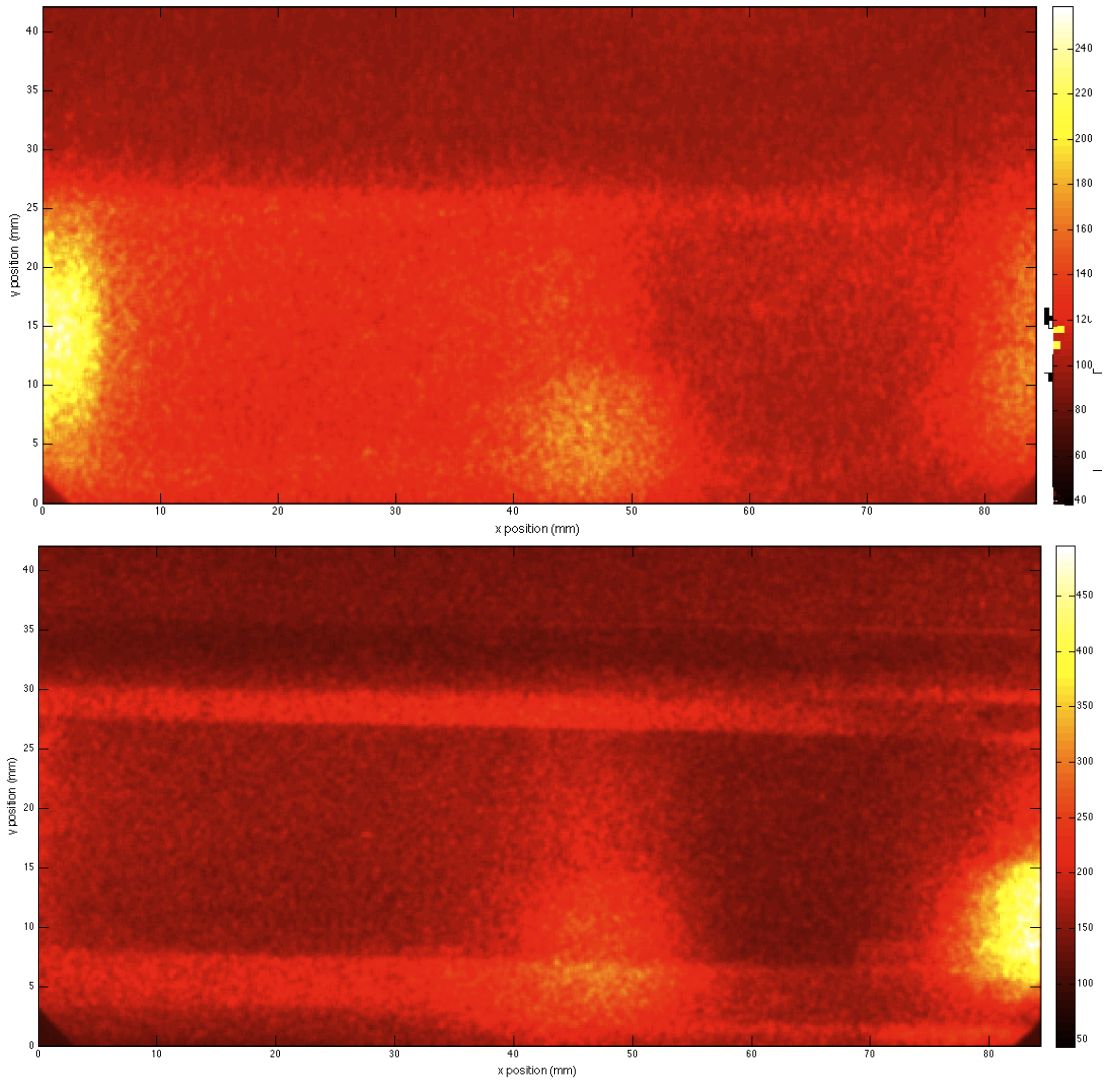

Figure 43. Background images of the laser scatter used for PLIF processing for the Q1(14) line (top) and Q1(5) line (bottom)

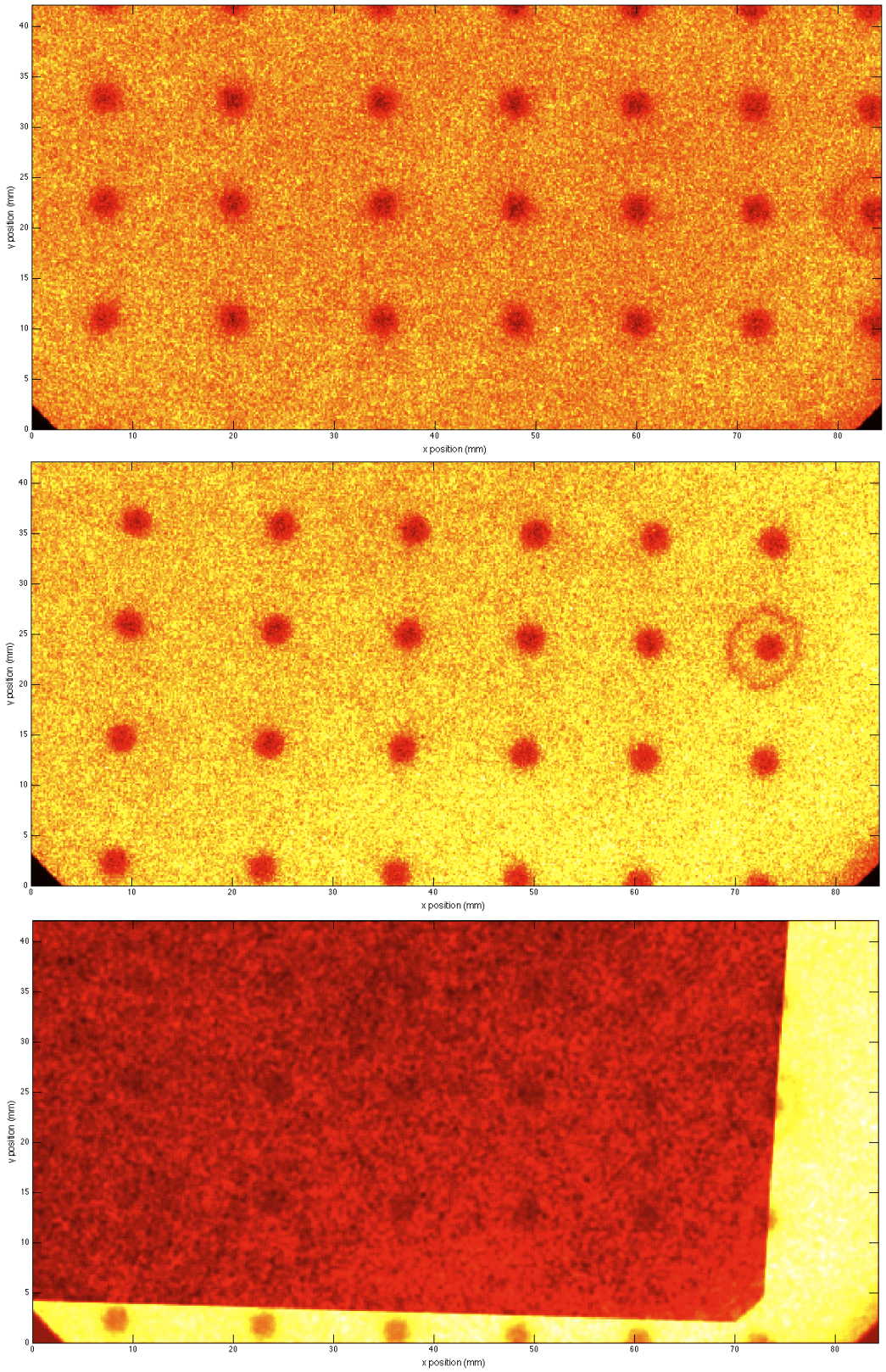

Figure 44. The target used for creating the geometric transformation between cameras imaged from the Q1(14) camera (top) and Q1(5) camera (middle), and subtraction of the top and middle images (bottom)

and producing a non-physical temperature. However, the 10 signal count threshold actually increased the threshold to about 50% for the Q1(14) line. Figure 46 shows an unfiltered temperature image to illustrate the need for the signal thresholding. In this figure, the highest temperature values would have been outside the flame where no OH existed, which produced invalid temperatures.

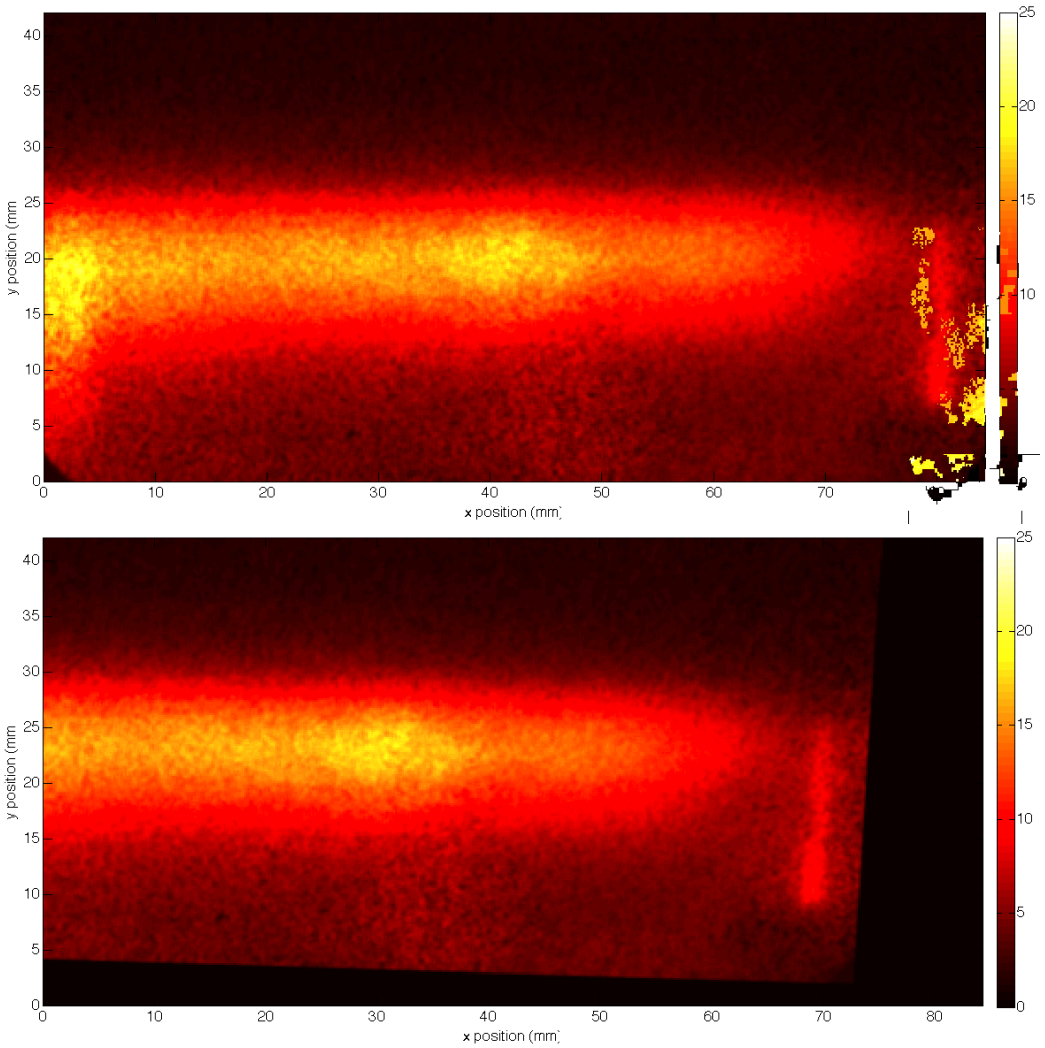

Figure 45. Q1(14) signal images from the original image geometry (top) and transformed to the Q1(5) image geometry (bottom)

Once the signal images were subjected to the low-pass filter the two images were then used to compute the intensity ratio for every pixel in the images when both contain sufficient signal levels, otherwise no ratio was computed. Finally, the temperature

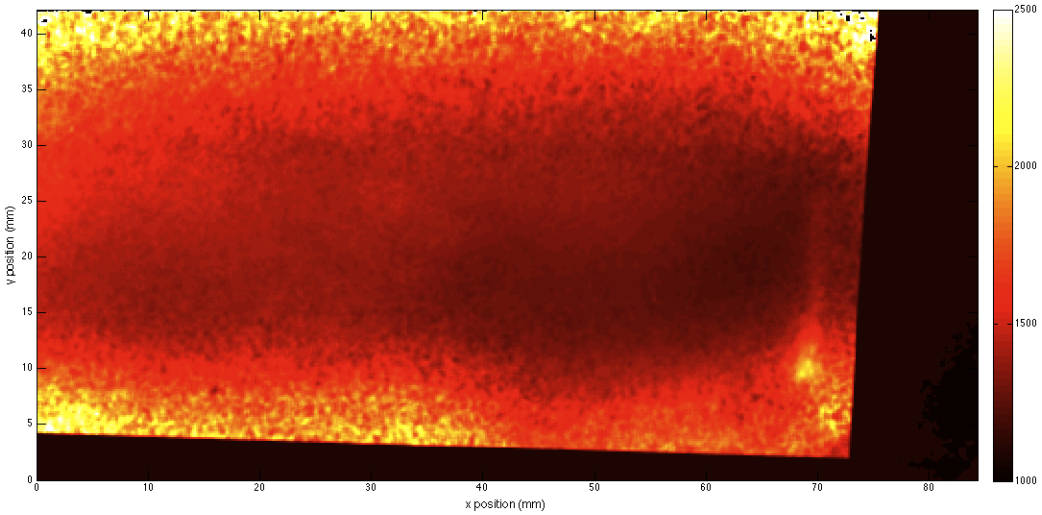

Figure 46. Planar temperature distribution from 2-line PLIF for a typical UCC test condition, without signal thresholding

correlation equation was applied to the intensity ratio values to yield a temperature measurement and produce a temperature image such as the one shown in Figure 47. The temperature distribution is insightful into the local ϕ (based on Figure 36, the mixing that occurs between the migrating flame and the core flow, and the thermal loads on the radial vane and the inner/outer diameter walls.

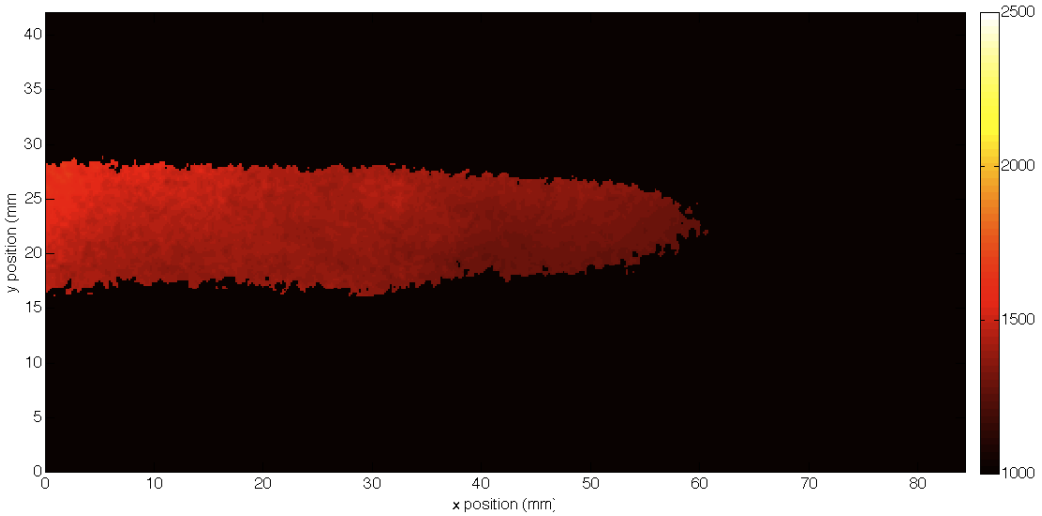

Figure 47. Planar temperature distribution from 2-line PLIF for a typical UCC test condition

3.6.6 Process Analysis.

3.6.6.1 Instantaneous Temperature.

It was important to analyze the process for computing the PLIF temperature measurements because the baseline case (Case 14) used for the illustrative measurement indicated temperatures of approximately 1400K that were significantly below the calibration range of around 1850 - 2250K. The measurement process computes the measured PLIF temperatures as the time-averaged temperatures at a given location when OH was present. Based on the images in Figure 41, it appears that OH was not present at every location at every time the PLIF signal was captured. Potentially, the temperatures were higher (within the calibration) on the instantaneous temperatures, but averaged out to be lower, outside of the calibration range, in the time-averaged temperature. Based on the development of this research effort, the PLIF system was improved from time-averaged point-wise temperature measurements to time-averaged 2D measurements, and also instantaneous 2D temperature measurements. Figure 48 shows a single image from each fluorescence line, Q1(14) on top and Q1(5) in the middle, and the resulting 2-D instantaneous temperature image on the bottom. The images in this figure illustrate reasonable instantaneous measurements resulted from the PLIF system data. However, the bottom image of Figure 48 indicated that specific regions had temperatures within the calibration range (1900K to 2300K), but the instantaneous temperatures often fell below the calibration range. Also, parts of the figure have temperatures higher than the calibration range (above 2300K) that must have resulted from low, but above the threshold, signal level. The non-physically high temperatures indicated that the threshold was set too low and should be higher for instantaneous temperature data. Figure 49 is the same data as the bottom image of Figure 48, but represented as a contour plot. This figure better illustrates the spatial temperature distribution with respect to determining which regions had temperature

values that were within the calibration range (1900K to 2300K) and outside of the calibration range, either below 1900K or above 2300K.

A comparison of the time-averaged temperature distribution from instantaneous temperature images and from time-averaged fluorescence signal images is shown in Figure 50. The images in this figure illustrate that both methods of computing the time-averaged temperature distribution produced similar results. However, the results were not completely identical as some data loss occurred between x = 30 mm and x = 50 mm for the instantaneous temperature average. The flamelets exiting the UCC, around x = 60 mm, followed a continuous path from x = 60 mm to x = 0 mm, but some of this transient information was lost in the time averaging of the instantaneous temperature images because insufficient signal events were not removed from the average.

3.6.6.2 Time Averaging.

In order to analyze data loss that occurred and the implications of the time average on the spatial variation of the OH signal, the time history of the PLIF temperature was analyzed. Figure 51 compares the temperature time history for Point 1 (x = 40 mm, y = 20 mm) and Point 2 (x = 20 mm, y = 17 mm), which were chosen because of their position in the center of the flame region (Point 1) and near the border of the flame region (Point 2). This figure shows that neither Point 1 nor Point 2 appeared to experience a significant number of insufficient signal events, but Point 2 had more insufficient signal events than Point 1. Figure 52 shows the total number of sufficient signal events at each pixel for the Q1(14) line (top), the Q1(5) line (middle), and the ratio of the two (bottom). The first two images of the figure show that the average number of sufficient signal events was around 80 but this varied from about 35 to 125 sufficient signal events out of the total 200 events. The bottom image of Figure 52

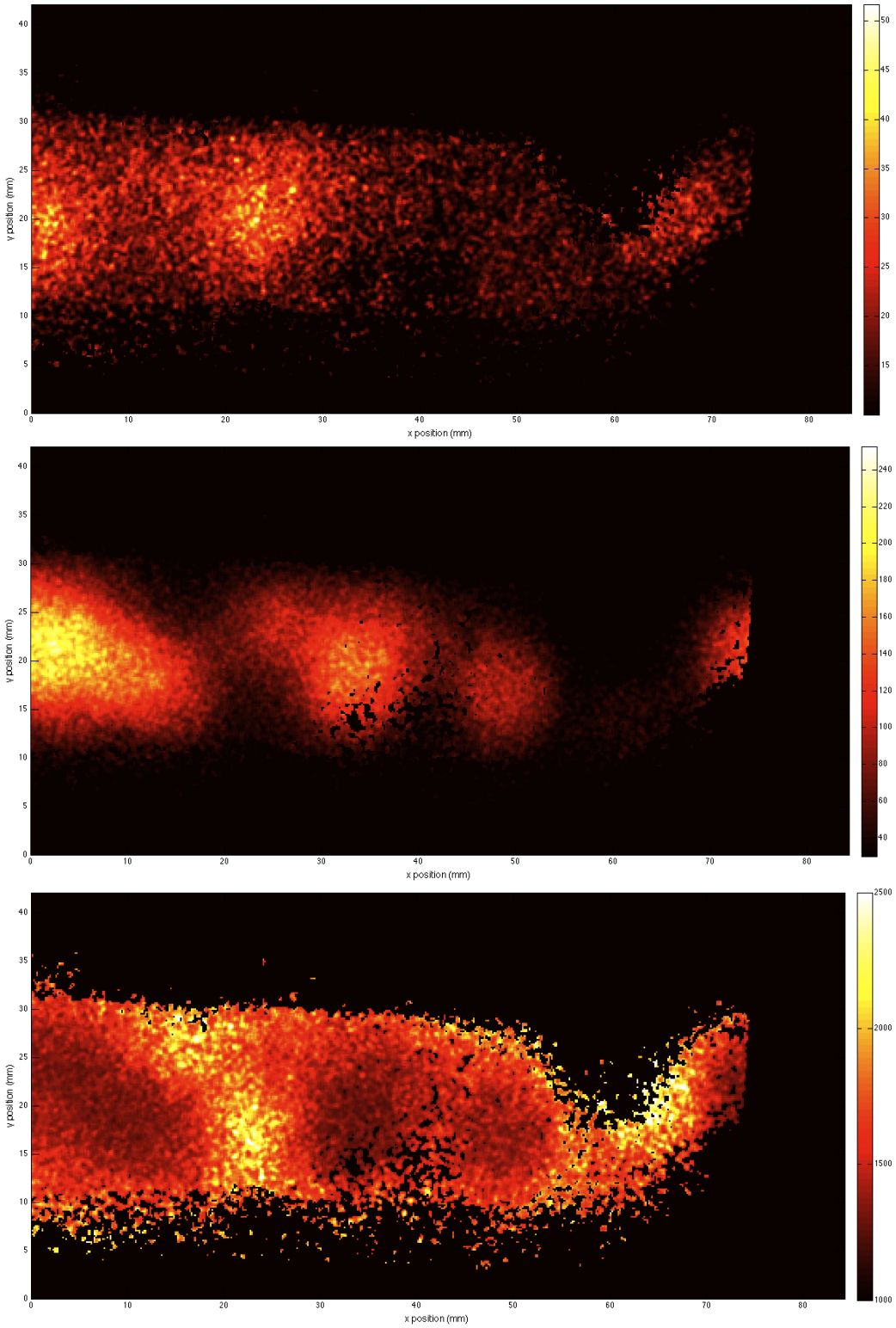

Figure 48. Instantaneous 2-D OH PLIF signal from the Q1(14) line (top), the Q1(5) line (middle), and the resulting temperature (K) image (bottom)

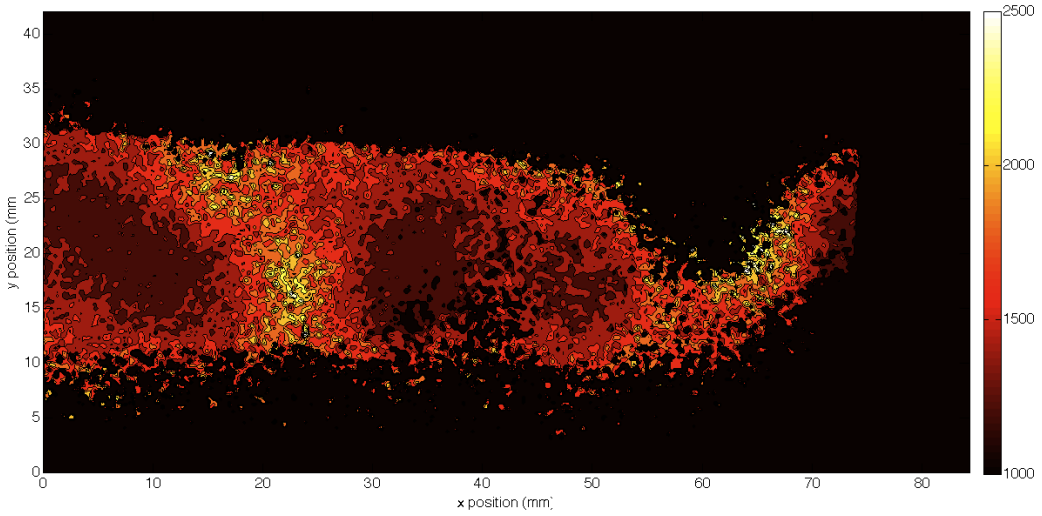

Figure 49. Contour map of instantaneous 2-D OH PLIF temperature (K)

shows that the same number of sufficient signal events was measured at each pixel for both Q1(14) and Q1(5) lines as a value less than one would have indicated a higher event count for the Q1(5) line and a value greater than one indicating a higher event count for the Q1(14) line. Since all pixels had a value exactly one, an identical number of events was observed for each pixel on both lines, pixels that did not observe any events on either line were not counted. Figure 53 shows the total number of sufficient signal events at each pixel used for computing the time-averaged temperature from the instantaneous temperature data. This figure also shows the same trend of the number of sufficient signal events compared to the total 200 events collected. With an average of less than 50% of the 200 events where sufficient signal was observed, a significant impact could have been made to the final signal levels in the time averaged when the insignificant signal events were not filtered out.

In order to quantify the impact of the insufficient signal events, the time-averaged temperature was reprocessed with the signal thresholds applied to each PLIF signal image such that insufficient signal pixels were removed from the average. The top image of Figure 54 shows the spatial temperature distribution that was computed with insufficient signal events removed from the time-averaging of each signal image

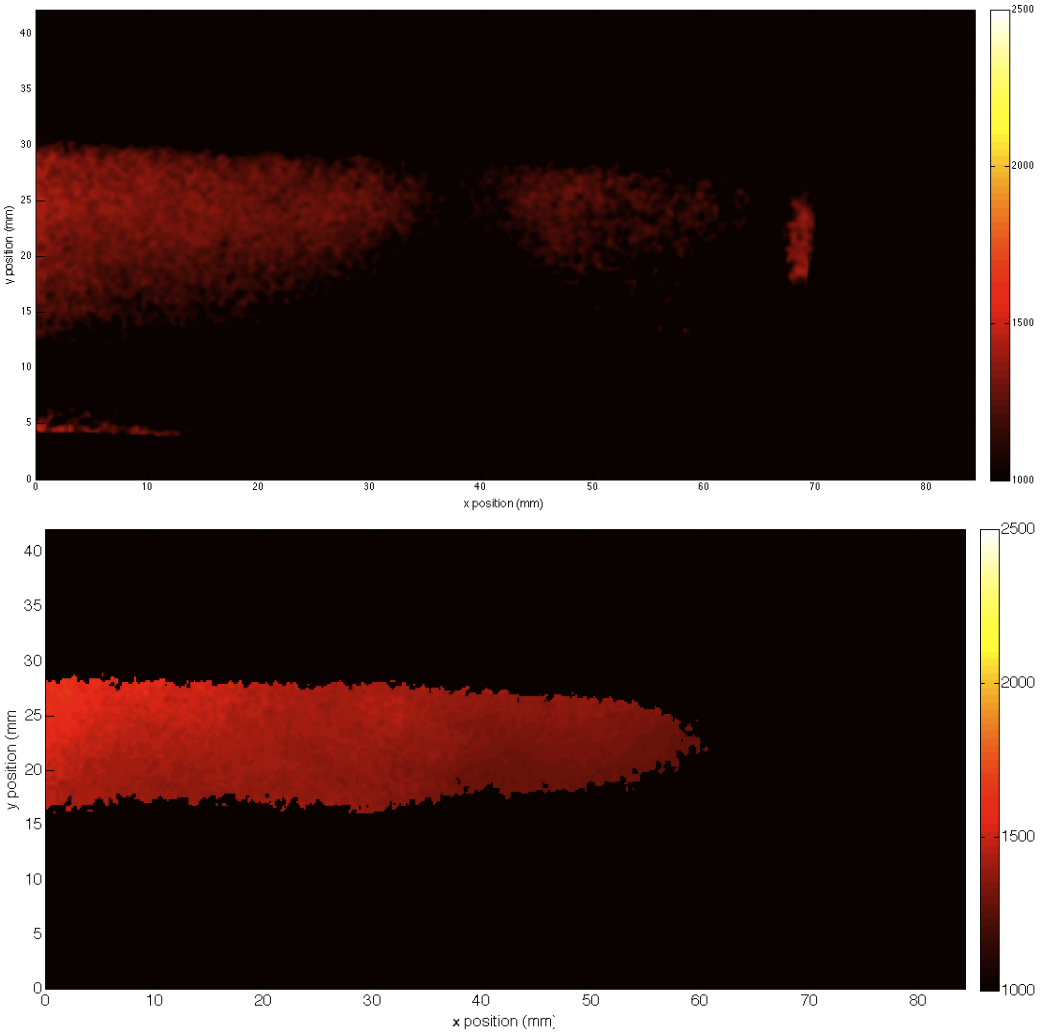

Figure 50. Time-averaged temperature distributions (K) from 2-line PLIF data computed from instantaneous temperature images (top) and from time-averaged flame location images (bottom)

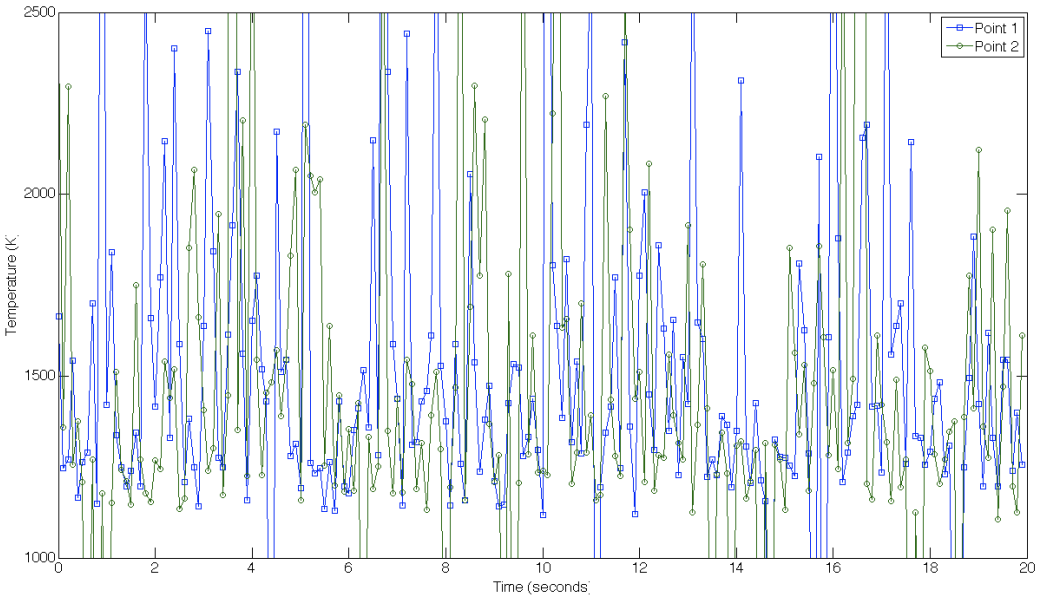

Figure 51. Comparison of the temperature time history at Point 1 (x = 40 mm, y = 20 mm) and Point 2 (x = 20 mm, y = 17 mm) vs. time (seconds)

for both fluorescence lines. This figure shows that the averaging of insufficient signal events did not significantly lower the measured PLIF temperature and yielded an increase in the average flame temperature (over the entire flame area) from about 1400 to 1500K. Applying the same method to the time average of the instantaneous temperature images resulted in the bottom image of Figure 54. This figure shows that the averaging of insufficient temperature events increased the temperature up to about 1600K, comparing the top image (average of instantaneous temperature) to the bottom image (temperature from instantaneous signal average). While 1600K is a lot closer to the calibration range than 1400K, the measured temperature values in the core flow were still significantly removed from the calibration range.

The corresponding ratio of the time-averaged fluorescence signal often fell below the smallest value obtained during calibration, around 0.47, and at times even significantly below the calibration range, as small as 0.1. As a result, the temperatures presented in this research potentially incorporate systematic errors in the relation of the fluorescence ratio to the absolute temperature value. Also, the choice of the ratio

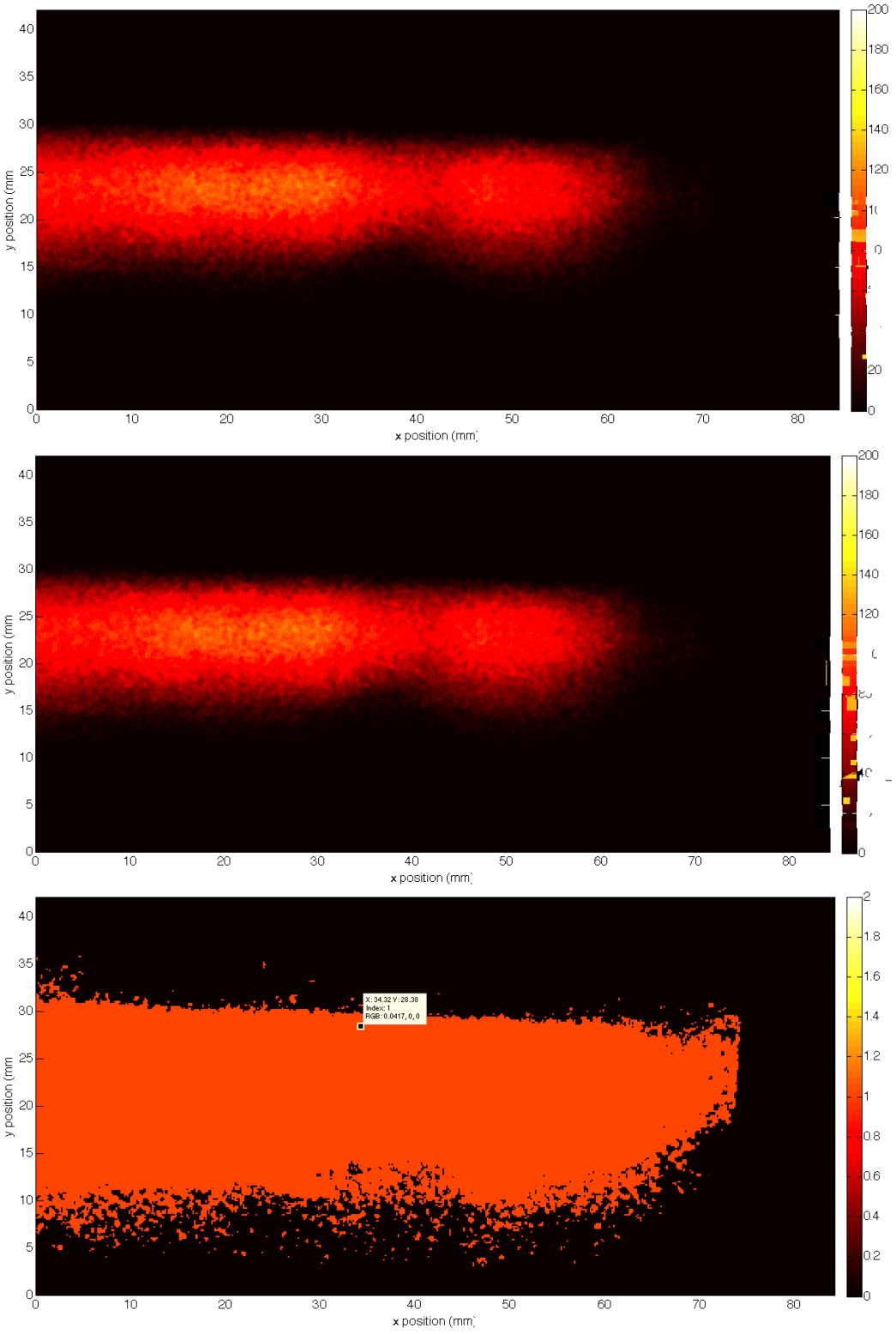

Figure 52. Spatial distribution of the number of sufficient PLIF signal events, out of 200, for the Q1(14) line (top), for the Q1(5) line (middle), and ratio of the top two images (bottom)

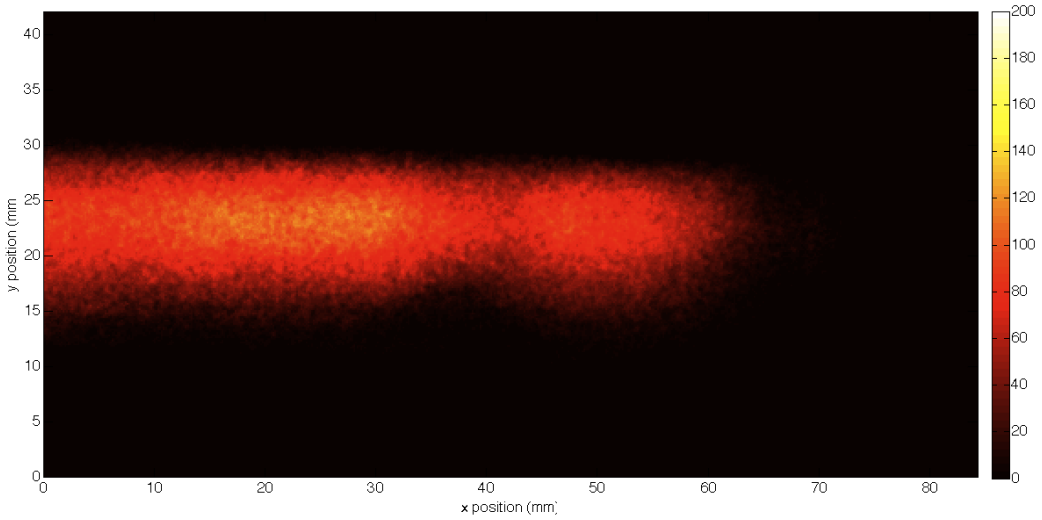

Figure 53. Spatial distribution of the number of sufficient PLIF signal events used for computing temperature

to temperature correlation has a significant impact on the represented values when data occurs outside the calibration range. For the processing in this research a linear correlation was used to compute an approximate temperature of about 1500K. However, using the quadratic interpolation the temperature would have been reported as about 300K, which is not possible with the incoming air already being at 300K and mixing with significant migrating reacting mass from the UCC. Instead, the logarithmic interpolation could have been used and would have reported a temperature of about 1000K, which could potentially be a reasonable value.

Based on the PLIF signal being processed multiple different ways to reach a temperature measurement, the values for the baseline case (Case 14) were significantly below the calibration range, yet are not unreasonable. For the majority of the testing, ϕ was 2.0, which corresponds to an adiabatic flame temperature of approximately 1600K and this must have been the maximum temperature of the migrating flame from the UCC into the core flow. With the UCC operating as an RQL combustor, the migrating mass at 1600K encountered a significantly larger mass of air at 300K causing a quick-quench to a lean-burn that would likely, but not necessarily, result in

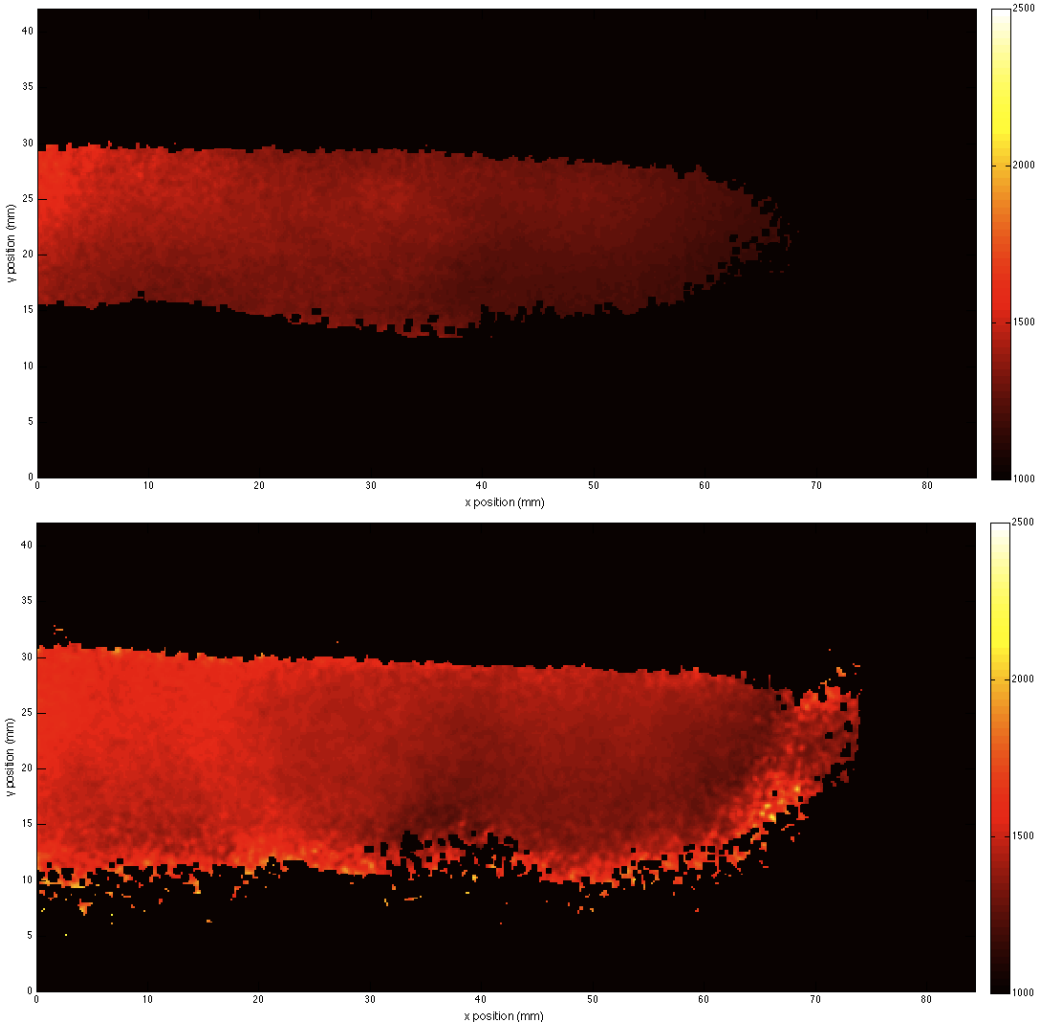

Figure 54. Time-averaged temperature distributions (K) from 2-line PLIF data computed from time-averaged flame location images (top) and time-averaged instantaneous temperature images (bottom) using signal thresholding and data loss filtering

lower temperatures. Once the lean-burn condition was reached, the migrating mass continued to react with the air releasing heat and raising the temperature. The balance of the quenching and continued heat release is the process by which the actual temperature results, and it is postulated that for the baseline condition 1600K is a reasonable expected flame temperature. However, the flame temperature and the resulting core flow temperature may not be in complete equilibrium while reactions are still occurring in the core flow. This results because the PLIF system only obtains a temperature measurement when there is a flame and OH is present, which would bias the data to a higher value, the flame temperature, versus the average core flow temperature. By theory, the fluorescence ratio indicates that higher ratio values correspond to higher temperatures, but the issue is that for ratio values significantly outside the calibration range, R from 0.464 to 0.675 or T from 1880 to 2230K, the absolute value of the temperature becomes unclear. However, comparison of the reported temperatures was illustrative of the flame migration which was of greater importance than the absolute measure of a given temperature.

3.6.6.3 SNR Threshold.

In order to analyze the choice of 25% of the max signal for the minimum signal threshold, the signal from the Q1(14) line was normalized by the maximum corrected signal in the image and then displayed in a contour map in the top and bottom images of Figure 55, respectively. The Q1(14) line was chosen to be analyzed because it has a lower SNR than the Q1(5) line. Specifically looking at the bottom image in Figure 55, the 0.30 (or 30%) line corresponds to the physical separation of where OH fluorescence occurred and where no OH fluorescence occurred. This indicated that the 25% threshold may have been slightly low for the Q1(14) line and that 30% may have been a better choice. Figure 56 shows the same data as Figure 55 for the Q1(5)

line instead of the Q1(14) line. The bottom image of Figure 56 also suggests that the threshold should be set around 30%. However, before normalization, the maximum of each line was about 19 and 115 for the Q1(14) line and Q1(5) line, respectively. These values would have put the 30% thresholds at 6 and 35 for the Q1(14) line and Q1(5) line, respectively. The 30% threshold for the Q1(5) line was well above the 10 signal count additional threshold, but the threshold for the Q1(14) line was significantly below. As such, the Q1(14) line was actually held to a threshold closer to 50% for this case, which resulted in the data loss between about y = 15 to 18 mm and y = 27 to 30 mm.

The images in Figure 57 show the original temperature image from Figure 47 with the 25% threshold (top) compared to the same data processed with a 30% threshold (middle), and with a 30% threshold without the additional 10 signal count restriction. The higher SNR threshold did not significantly change the shape of the flame area, but slight data loss occurred in the upper left region (x = 0 mm, y = 28 mm) from the top to middle images. However, comparison with the bottom image of Figure 57, which is nearly identical to the same data with the 25% threshold, shows that significant data loss occurred with the additional 10 signal count restriction in the regions from y = 13 to 17 mm and y = 28 to 32 mm. This data loss would have not impacted the reported temperature values, but would have changed the flame areas, specifically for the cases in Chapter 6. Drenth used a minimum signal threshold of 30 signal counts, which was lowered to 10 for this research, but significantly lower confidence exists for the temperatures reported using the data below the 10 signal counts.

Extending the increased SNR threshold to the instantaneous temperature data from Figure 48, Figure 58 shows the higher thresholded Q1(14) line (top), Q1(5) line (middle), and the resulting temperature image (bottom). This figure shows that the

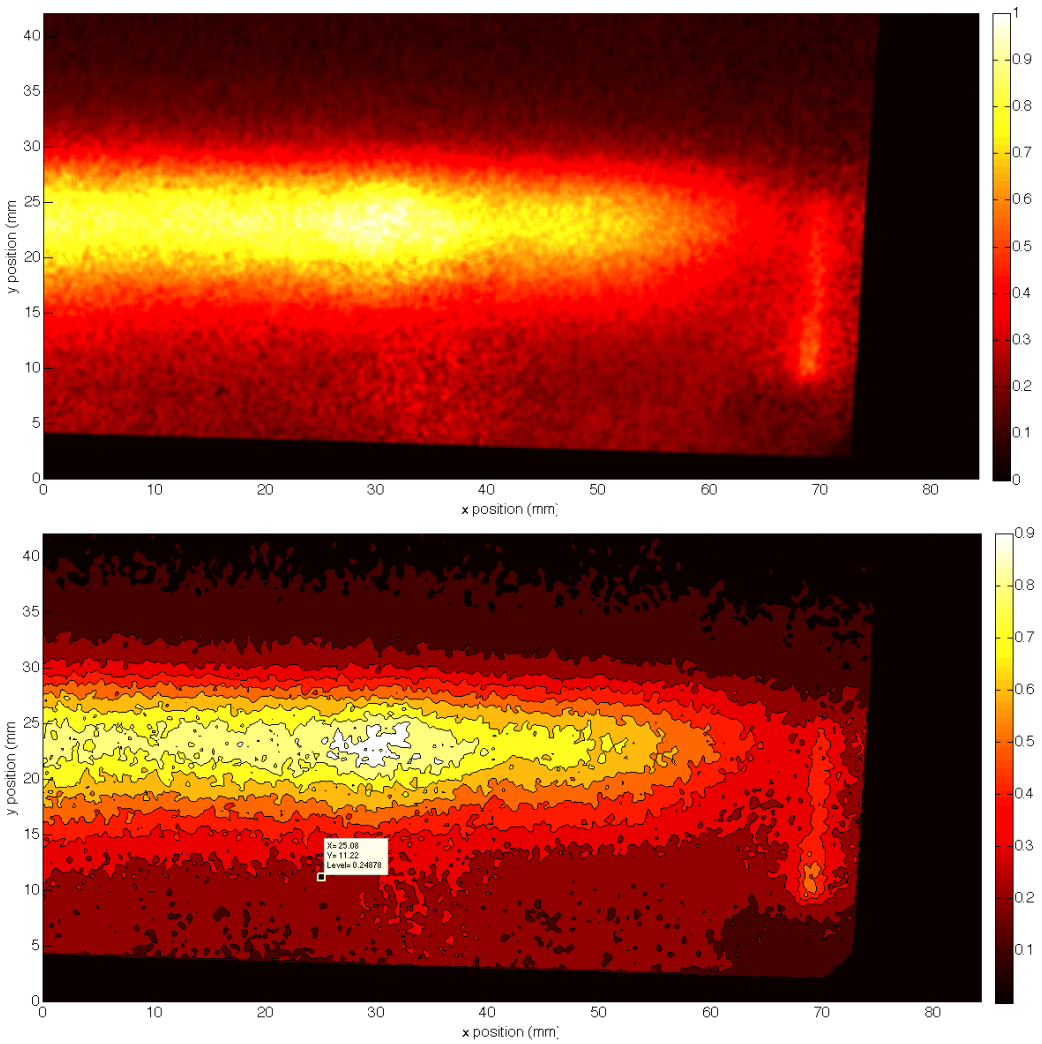

Figure 55. Normalized and corrected PLIF data from the Q1(14) line (top) and as a contour map (bottom)

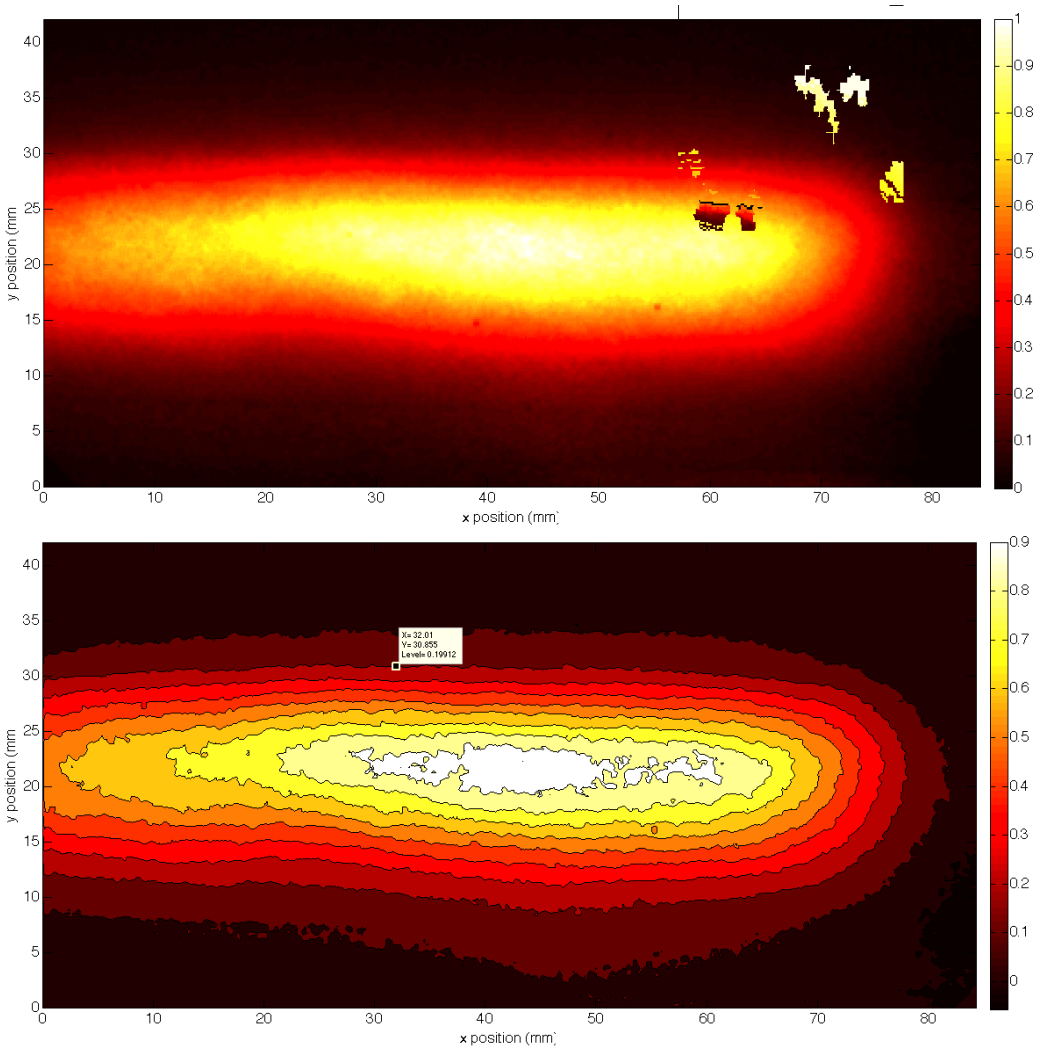

Figure 56. Normalized and corrected PLIF data from the Q1(5) line (top) and as a contour map (bottom)

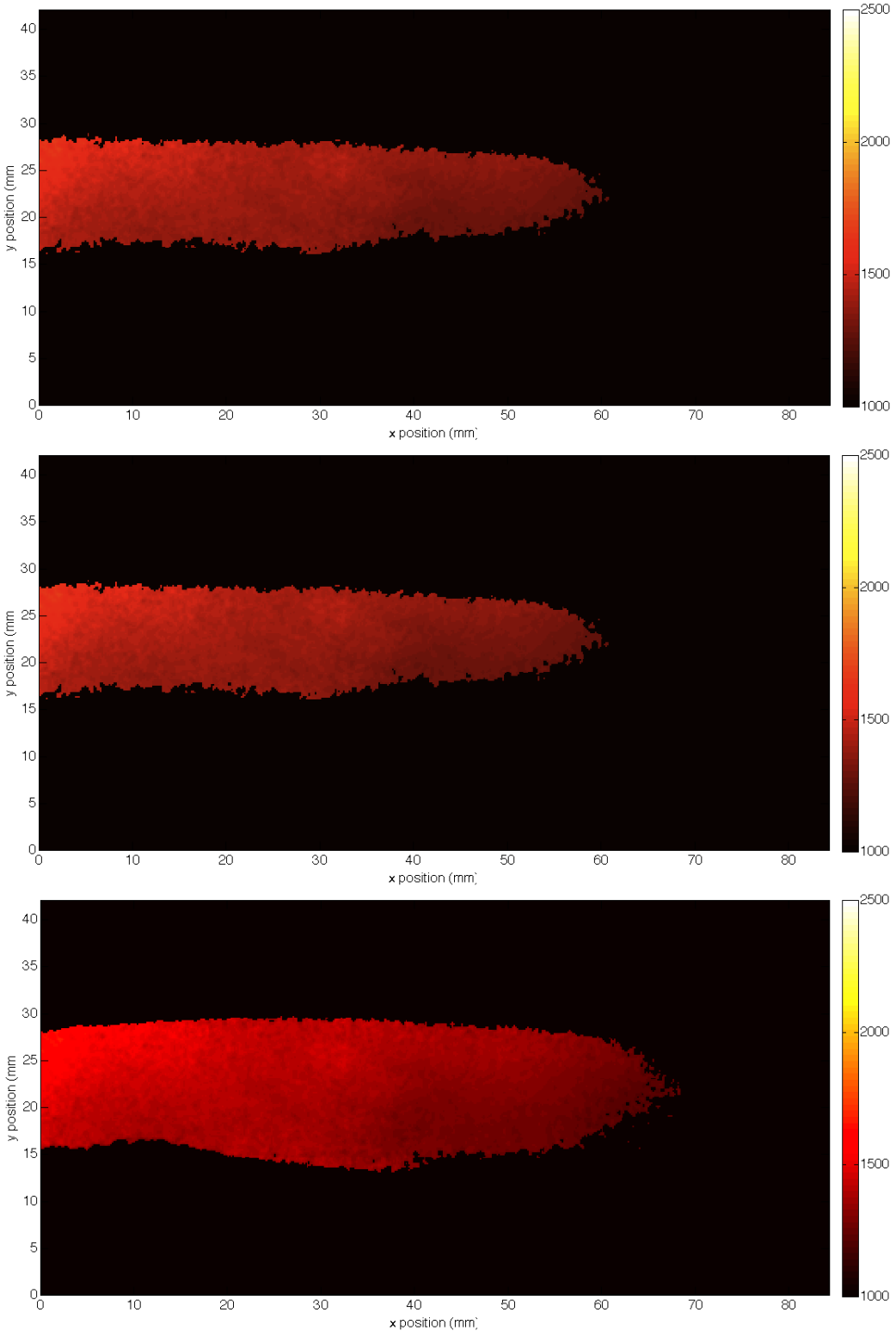

Figure 57. Planar temperature distribution from 2-line PLIF for a typical UCC test condition using the original SNR threshold (top), higher threshold (middle), and higher threshold without the additional 10 signal count restriction (bottom)

increased threshold yielded Q1(14) and Q1(5) signal images that closer resembled the raw images shown at the top of Figure 41. Also, the higher threshold improved the situation that was present in Figure 48 where the highest temperatures in the bottom image of that figure where in locations that had the lowest signal levels. However, there still appeared to be areas where low signal levels were producing the highest temperatures indicating that for instantaneous temperature data a SNR threshold higher than 30% should be used. Investigating the time history of the PLIF data, Figure 59 shows the number of significant signal events that occurred at each pixel out of the total 200 collected events with the original SNR threshold (top) and higher 30% threshold (bottom). This image shows that the higher SNR threshold reduced the maximum sufficient signal events from about 125 to about 60 and the average from about 80 to about 20 events. Further illustrating the significantly lower number of sufficient signal events, Figure 60 shows the time history of temperature at two different points with the original SNR threshold (top) and higher threshold (bottom). This figure shows that significantly less sufficient signal events occurred with the higher threshold and that the temperature points higher than 2300K, which are higher than the maximum possible temperature with propane, were removed. Carrying the instantaneous temperature into a time-averaged temperature, Figure 61 shows the resulting time-averaged temperature from the instantaneous temperature data. This figure was also improved by the slightly higher SNR threshold.

Instantaneous temperature images cannot be processed with a percentage SNR threshold like the time-averaged data because it is possible that an event could occur with no OH fluorescence signal in the entire image. This situation would allow the entire image as sufficient signal because the peak signal would be at the background level. SNR filtering of instantaneous temperature data requires the use of numerical signal count values to be used. Figure 62 shows the contour plots for the Q1(14)

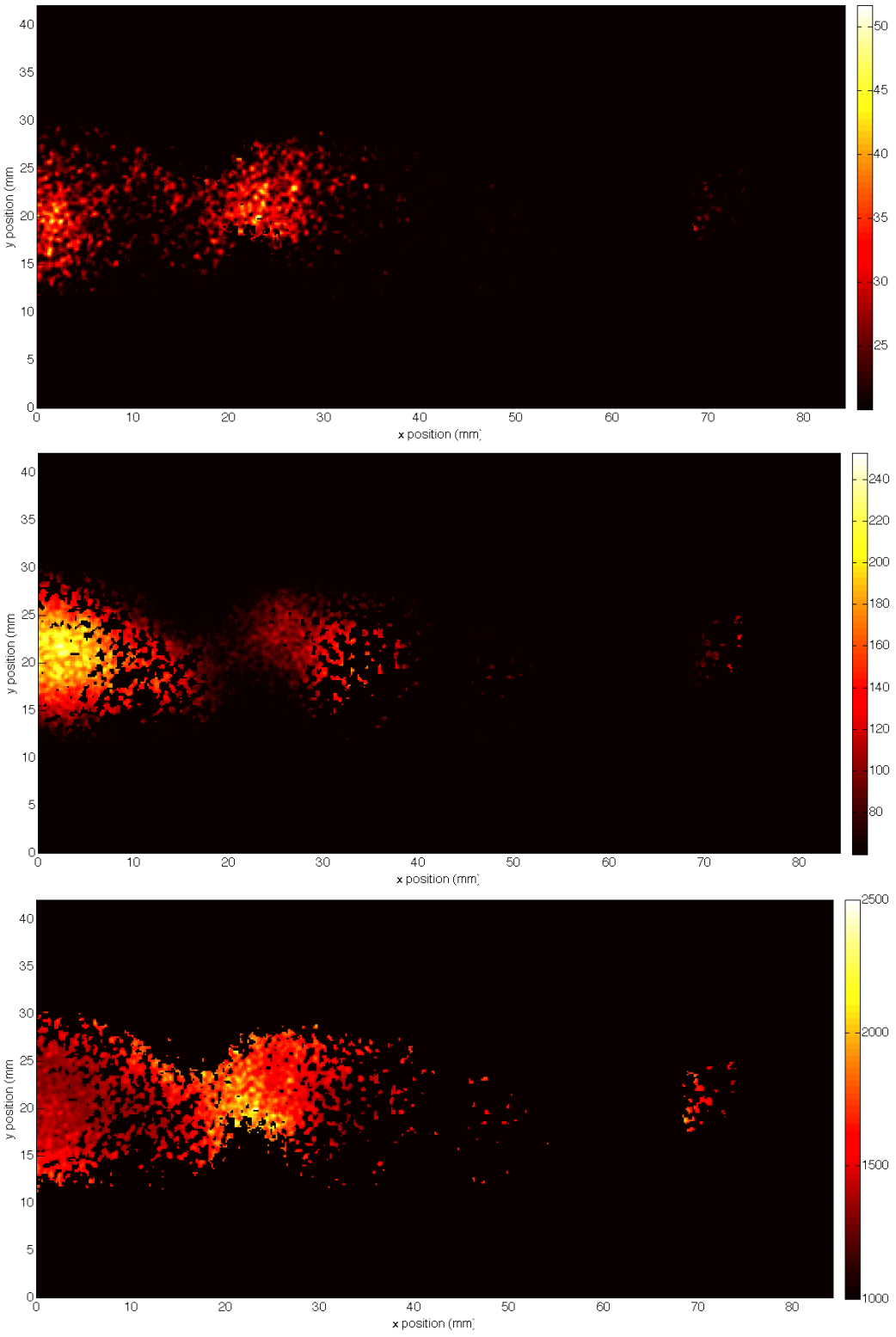

Figure 58. Instantaneous 2-D OH PLIF signal from the Q1(14) line (top), the Q1(5) line (middle), and the resulting temperature (K) image (bottom) with the higher SNR threshold

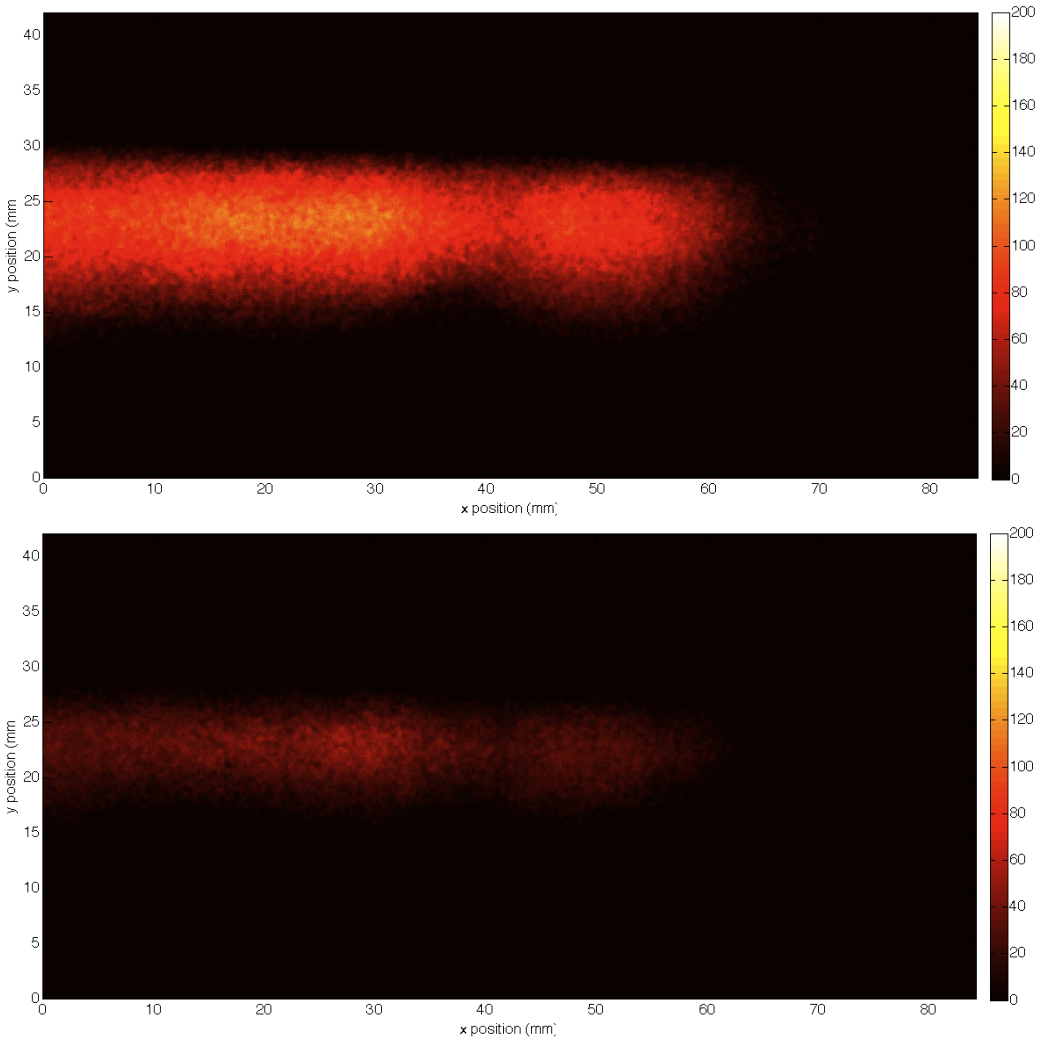

Figure 59. Spatial distribution of the number of sufficient PLIF signal events used for computing temperature with the original SNR threshold (top) and higher SNR threshold (bottom)

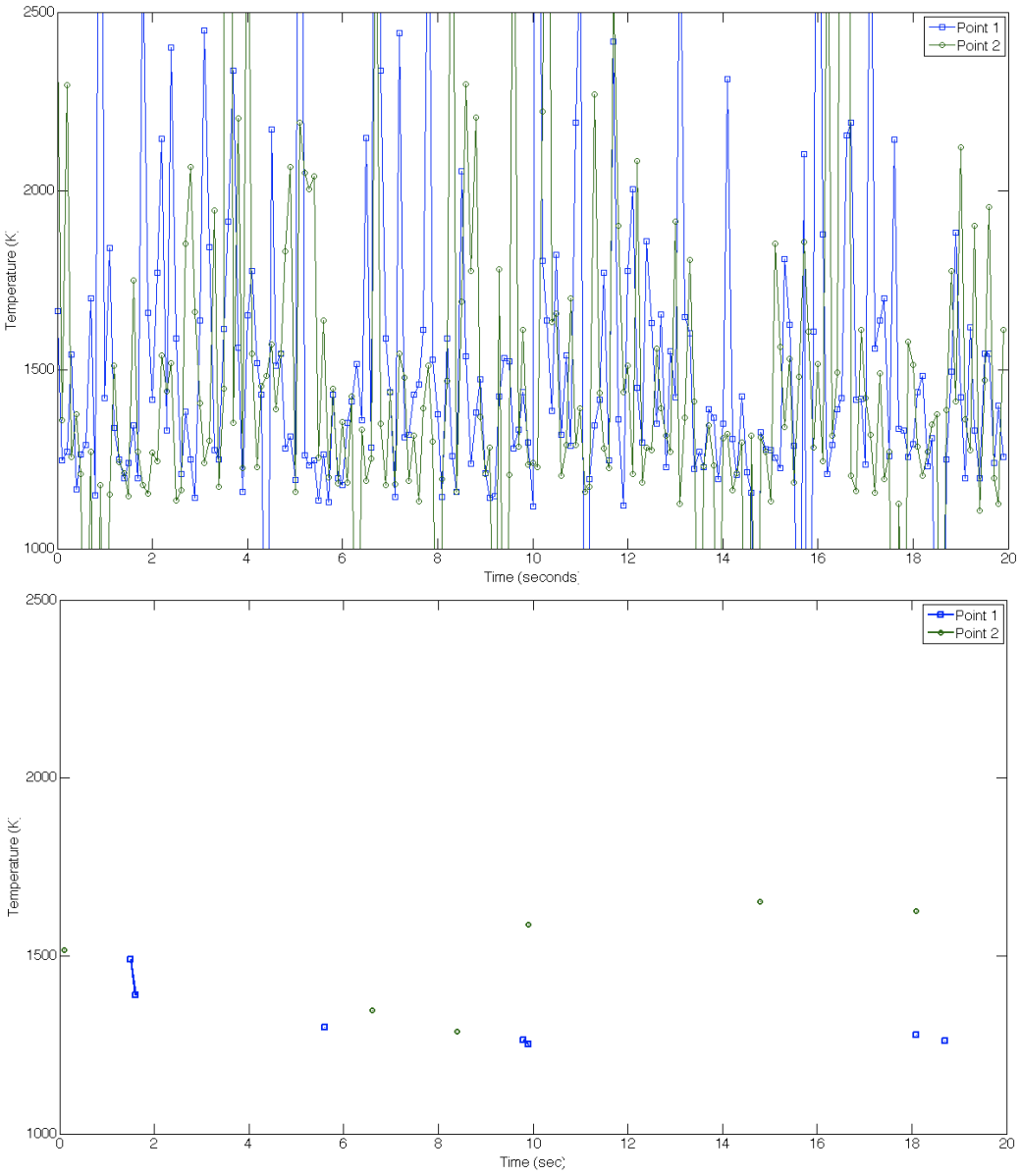

Figure 60. Comparison of the temperature time history at Point 1 (x = 40 mm, y = 20 mm) and Point 2 (x = 20 mm, y = 17 mm) vs. time (seconds) with the original SNR threshold (top) and higher threshold (bottom)

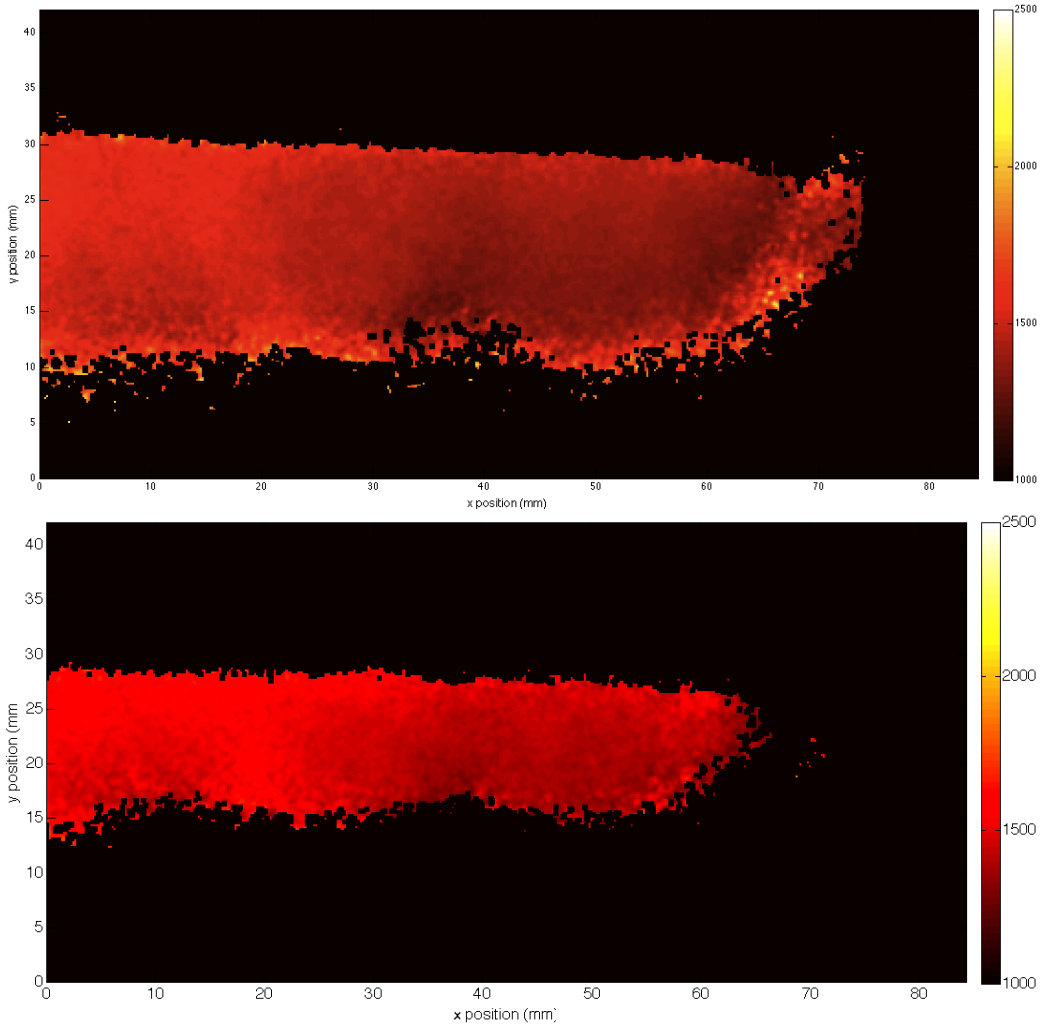

Figure 61. Time-averaged temperature distributions (K) from 2-line PLIF data computed from instantaneous temperature images using the original SNR threshold (top) and higher threshold (bottom)

line (top) and the Q1(5) line (bottom) of the processed signal counts (background subtraction, laser power correction, and geometry transformation). This figure shows that the instantaneous signal threshold should be set to about 15 for the Q1(14) line and about 50 for the Q1(5) line.

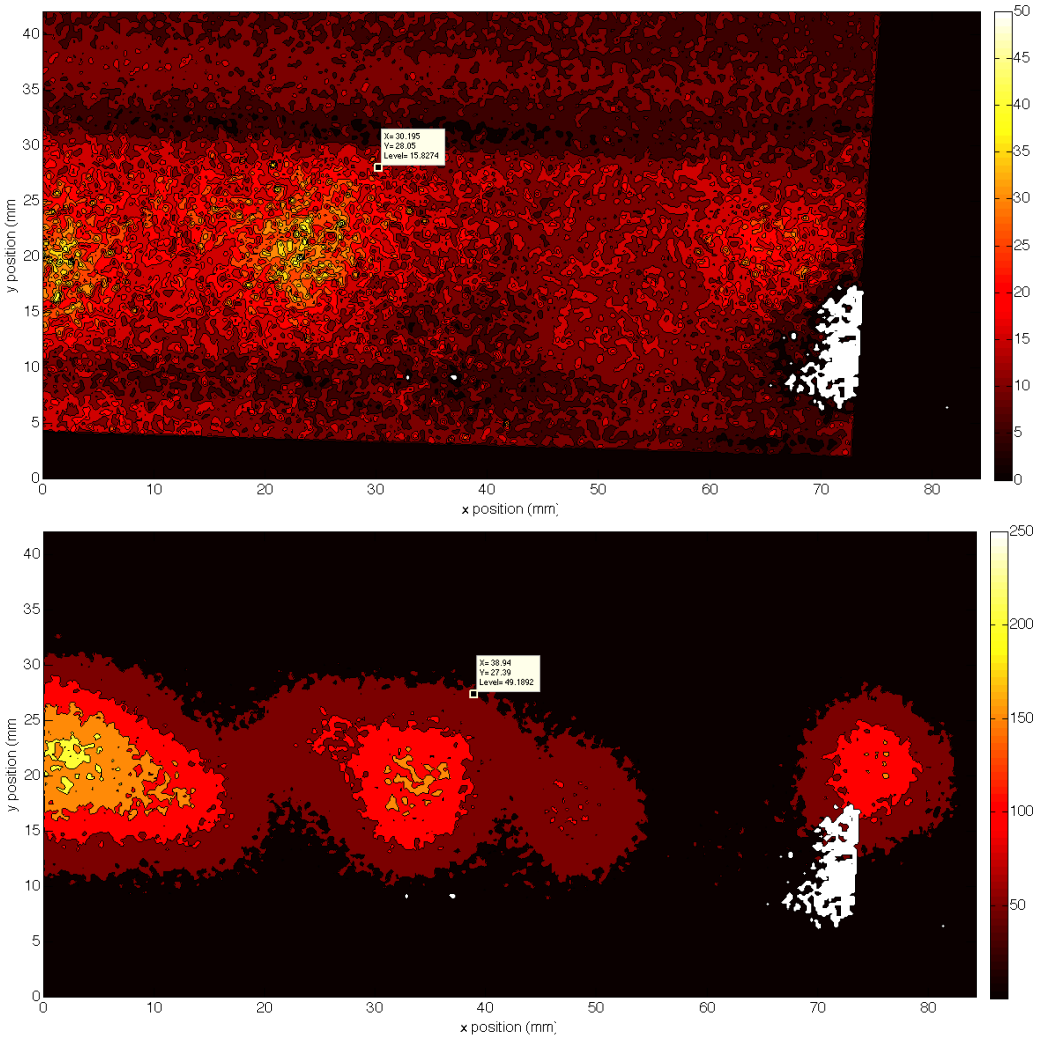

Figure 62. Contour maps of instantaneous PLIF data from the Q1(14) line (top) and Q1(5) line (bottom)

3.6.6.4 Background Images.

As Drenth documented [9], significant laser scatter issues were present for data collection in the core flow of the AFIT UCC model. Drenth used both laser and

flame off background, flame only background, and laser only background [9]. The flame background image for this research is shown in Figure 63 and ranges in pixel intensity from about 95 to 110. This figure shows that significant flame chemiluminescence was not captured even using propane, instead of the hydrogen fuel used by Drenth [9], eliminating the need to use a flame background image. Eliminating the flame background image also allowed the laser off background image to be eliminated, leaving only the laser background image.

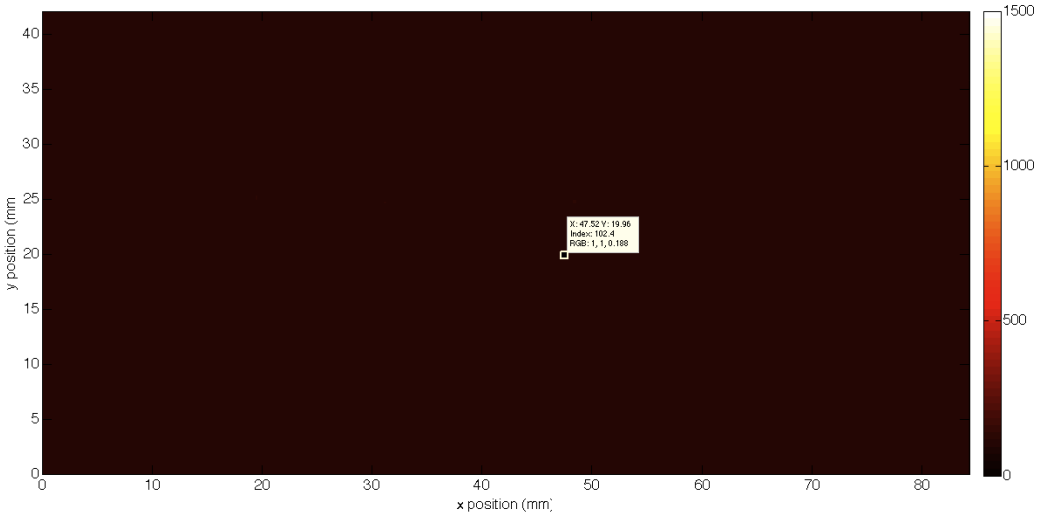

Figure 63. Spatial distribution of pixel signal for the PLIF flame background image, note no flame background signal is present

Drenth also documented significant issues with laser scatter in the laser background images where the laser background image had a higher pixel intensity than the PLIF signal image [9]. This research did not have that issue with the laser background because the UCC section typically operated with a ϕ of 2.0, instead of 1.0 for Drenth's research [9], which yielded higher PLIF signal pixel intensity. As shown in Section 3.6.5, significant laser scatter was still an issue for this research, particularly for the Q1(14) line because the SNR was much lower than for the Q1(5) line. It was also noted that the laser scattering background image varied for each location that data was collected both for the different planes within the core flow and at the

ambient UCC exit. In order to account for the variation of laser scatter, laser background images were taken for each collection location, each time the PLIF system was aligned. Day-to-day and run-to-run variations in laser scatter at a single collection location were not analyzed, but the recorded laser power values used in the PLIF data processing indicated significant variation may have existed. However, collecting run-to-run laser scattering images would not likely be practical, but day-to-day laser background images might further improve the quality of the PLIF data. This could have introduced additional error for the PLIF data collected in this research that was not directly characterized. However, during the PLIF system calibration, the $\phi = 1.0$ condition was repeated three times producing a 7% error among the three runs, as reported in Section 3.6.4. This error was likely the result of variations in the laser scatter that were not specifically characterized. Further, noticeable errors were reported over four identical runs in Section 3.6.7 that were also likely the result in variations of the laser background that was not captured in the saved background images.

In addition to run-to-run variation in laser scatter, processing instantaneous PLIF data for temperature would also introduce the laser background image to pulse-to-pulse laser power variations. Figure 64 shows the pixel-by-pixel standard deviation of the laser background image for the Q1(14) line (top) and Q1(5) line (bottom). This figure illustrates that significant pulse-to-pulse variation existed in the laser background image, as expected, both inside and outside of the core flow region. The laser background image pixel intensity varied by about 30 and 60 signal counts for the Q1(14) and Q1(5) line, respectively. Figure 65 shows the same data as Figure 64, but normalized by the mean value at each pixel. In Figure 65 the average variation in pixel intensity was about 35% and 25% for the Q1(14) and Q1(5) line, respectively. Analyzing the time history of the laser background images, Figure 66 shows the time

history of two points in the core flow (Point 1 and Point 2) and one point outside of the laser sheet, and core flow, (Point 3) for the Q1(14) line (top) and the Q1(5) line (bottom). This figure indicates that the laser background images experiences significantly less pulse-to-pulse variation in pixel intensity outside of the laser sheet, and core flow, (Point 3) than inside the core flow (Point 1 and Point 2), as expected. Figure 66 also indicates that the pulse-to-pulse variation was different for each line and varied randomly. The pulse-to-pulse variation in laser scatter makes accurate instantaneous data extremely difficult without real-time time history measurement of the laser power, laser background, and laser sheet variation, which the AFIT COAL Lab does not currently have the capability to measure.

3.6.7 Repeatability.

While the repeatability error in temperature measurement system has been characterized, it is important to understand the variability with respect to the time averaging of the transitory events being measured in the UCC. In order to characterize this variability, a typical UCC condition was repeated numerous times and investigated in the core flow, as shown previously in the spatial calibration image (Figure 40). Figure 67 shows the spatial distribution of the temperature computed from the time-averaged flamelet distribution for the same location with identical testing conditions where Runs 1-1 and 1-2 occurred on the same day while Runs 2-1 and 2-2 occurred on a different day. Each run enabled the averaging of 200 laser pulses. The images are characteristically similar but do show noticeable differences in the temperature and spatial distribution. These differences are highlighted in the exit temperature profiles shown in Figure 68 showing noticeable changes to the magnitude and shape of the exit profile. Runs 1-1 and 1-2 were fairly similar in profile while Runs 2-1 and 2-2 differed significantly between the two as well as in comparison to Runs 1-1

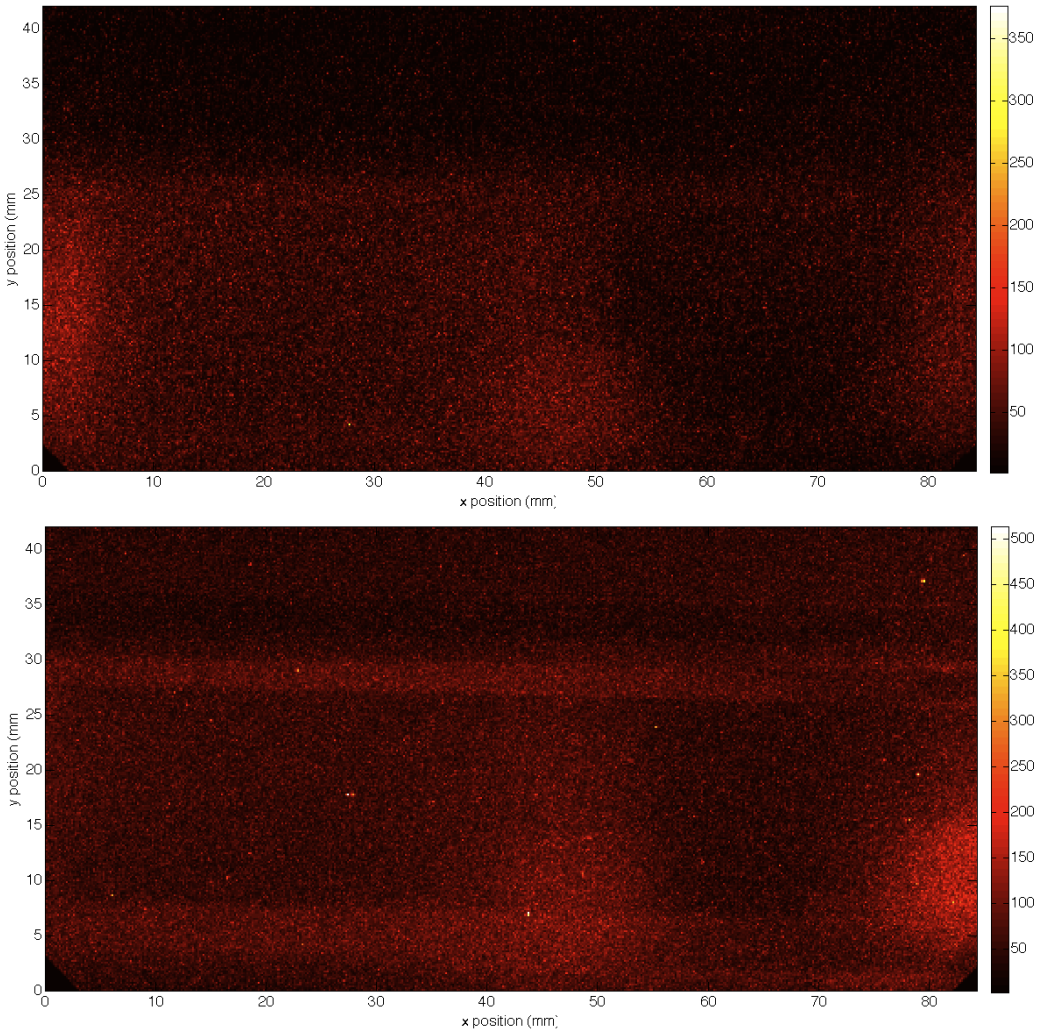

Figure 64. Standard deviation of the background images of the laser scatter used for PLIF processing for the Q1(14) line (top) and Q1(5) line (bottom)

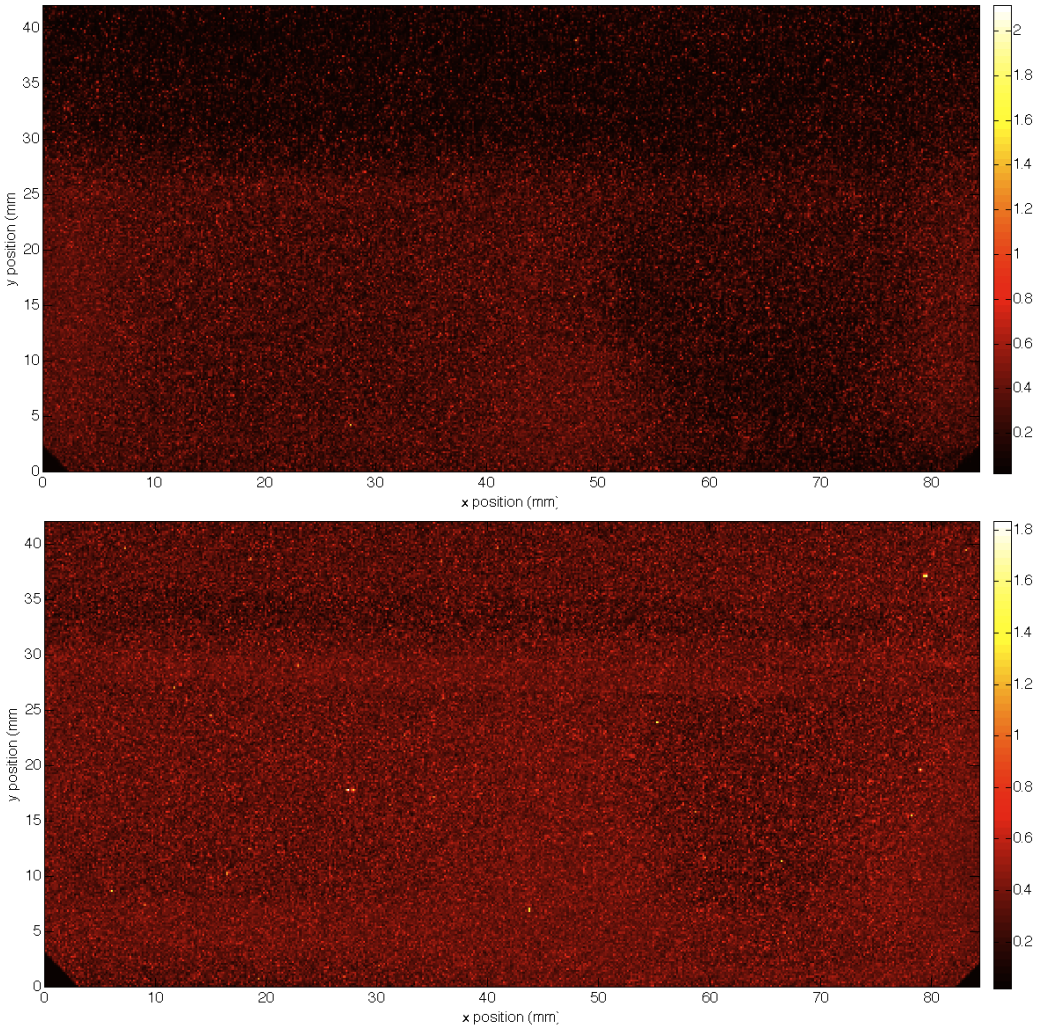

Figure 65. Standard deviation as a fraction of the mean of the background images of the laser scatter used for PLIF processing for the Q1(14) line (top) and Q1(5) line (bottom)

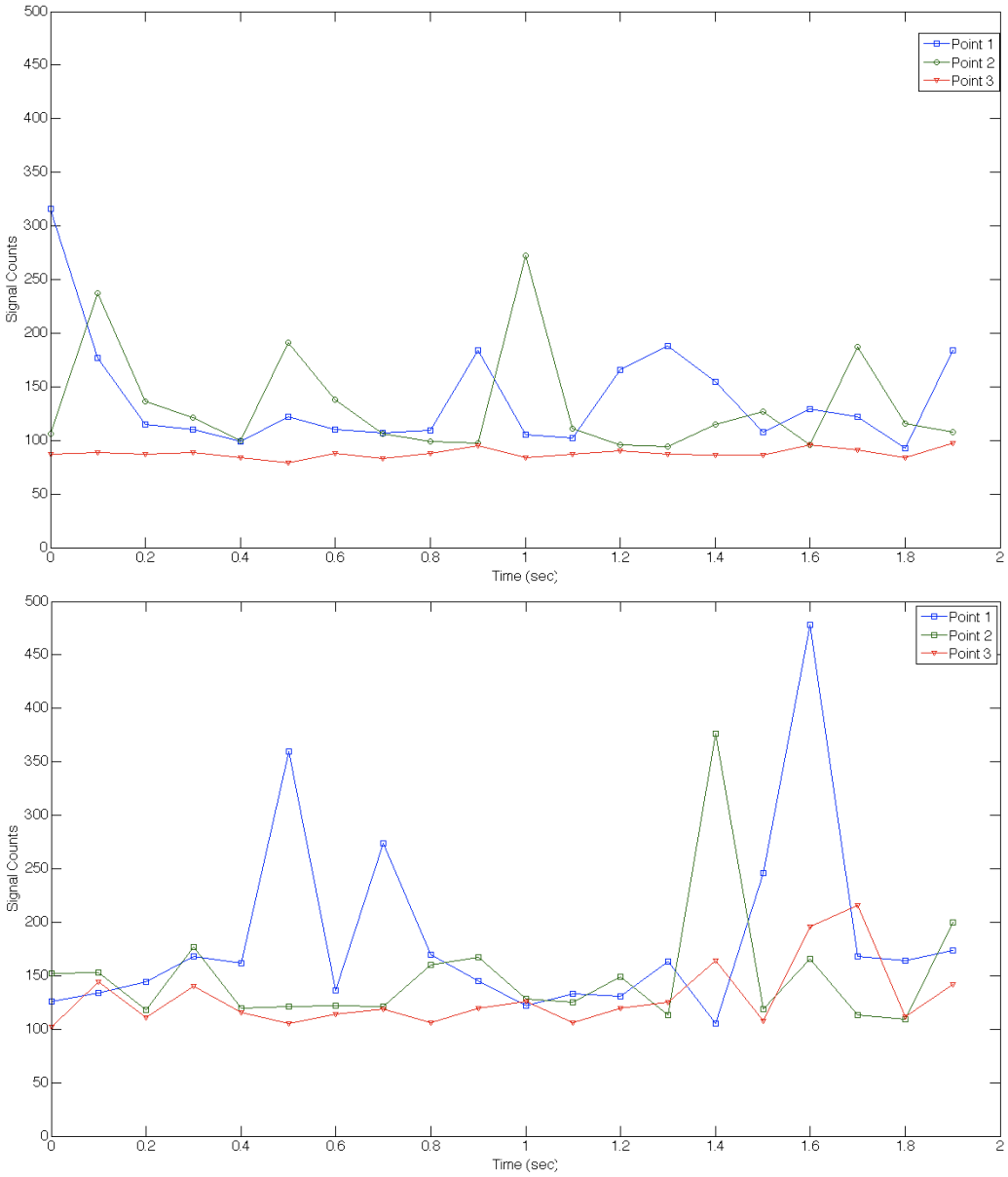

Figure 66. Time history of the background images of the laser scatter used for PLIF processing for the Q1(14) line (top) and Q1(5) line (bottom)

and 1-2. This was the result of the run-to-run and day-to-day variability and the temporal variability of the UCC-core flow interaction. Quantifying this difference with the maximum, average, and minimum measured temperature among the four runs showed average variations of 6.96%, 2.18%, and 4.16% which was well within the measurement error, but higher than the 1% error reported in a conventional combustor model by Giezendanner-Thoben et al. [54]. The higher error was likely due to the unsteadiness exhibited in the sectional UCC model that is not present in a conventional combustor model.

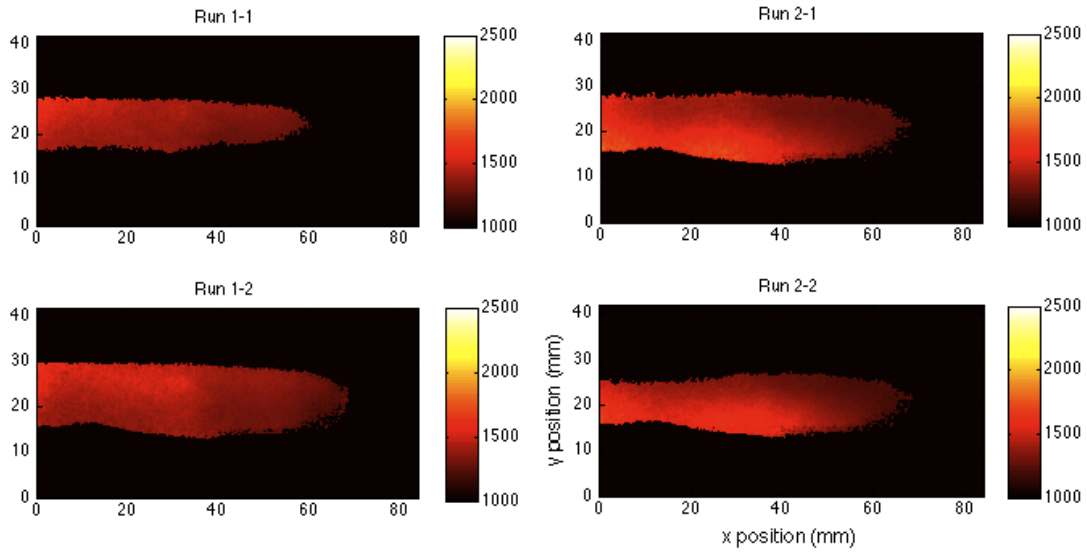

Figure 67. Repeatability study of 4 identical test conditions showing spatial distribution of temperature (K), Runs 1-1 & 1-2 on day 1 and Runs 2-1 & 2-2 on day 2

3.7 Particle Image Velocimetry

3.7.1 Background.

An illustration of the Particle Image Velocimetry process for a standard setup is shown in Figure 69. The process begins with a pulse of energy from a laser which is sent through a half-cylindrical lens to diverge the beam into a sheet and then through a spherical lens to focus that sheet to be as thin as possible at the ROI. The flow

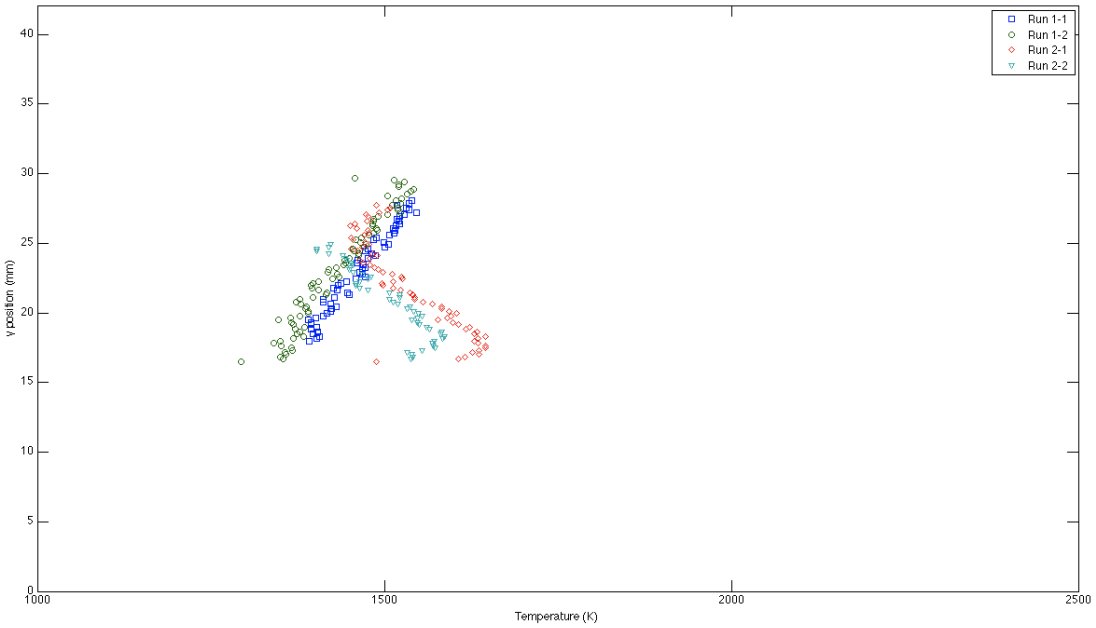

Figure 68. Repeatability study of 4 identical test conditions showing exit (x = 8 mm) temperature (K) distribution vs. y position (mm), Runs 1-1 & 1-2 on day 1 and Runs 2-1 & 2-2 on day 2

being measured is seeded with particles that are illuminated from the laser sheet, as illustrated by Dantec [17]. The sheet is imaged typically using a Charge-Coupled Device (CCD) camera and that image is divided into square subregions of four or eight pixels in length. After a short delay, called the pulse delay, a second laser pulse is similarly sent out and imaged. This pulse delay should be set according to the flow speed to yield seed particle movement on the order of 25% of the subregion size, as stated by Dantec [17]. Thomas stated that statistical relations are used to eliminate out of plane seed movement and to correlate seed particles from one image to the next and determine a velocity vector for that particle [29]. An average is computed for all the particles within a subregion and by using a calibration image, a length-to-pixels conversion is computed. The final result is a 2-D velocity field that can be used for flow visualization or in a significantly large dataset for computing flowfield statistics.

Thomas [29] used a commercial PIV system from Dantec Dynamics ®which consisted of a 10Hz dual-pulsed Nd:YAG laser with 532 nm output for each pulse, a

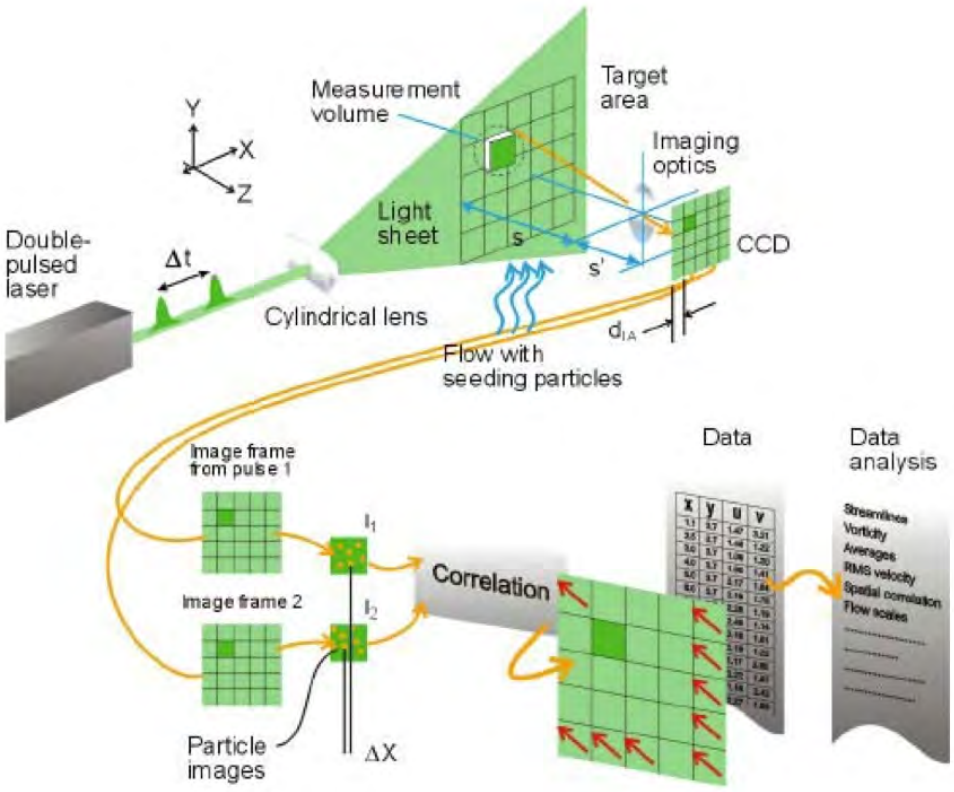

Figure 69. Illustration of the PIV process from Dantec Dynamics [17]

FlowSense 4M 2048x2048 pixel CCD camera with Nikon 60 mm F/2.8 micro lens and 75% transmission 535 nm filter with 10 nm bandwidth, and Dantec Dynamic Studio software. The maximum time resolution of the system was 7.5 Hz due to the camera frame-rate limit and the 10 Hz pulse repetition frequency of the laser. A nitrogen pressurized seeder was used to inject the seed particles [29]. Silicon carbide was chosen by Thomas [29] because of its small nominal diameter (2 micron), a low density, and low environmental hazard. A rotating drum type seeder manufactured by SCITEK Consultants Ltd. was driven by 30 Standard Liters per Minute (SLPM) of nitrogen and used to seed the core air flow.

Typical PIV systems, see Figure 69, use the de facto 10 Hz pulsed Nd:YAG laser to provide high power density for illumination of the seed particles. However, Chan stated that the PIV technique by design does not require significantly high power density [57]. As pulsed lasers have increased in repetition rate, PIV systems using these lasers have likewise increased in acquisition rates. While recent efforts have even pushed well into the MHz regime for small datasets by Murphy [58], time-resolved PIV systems are still almost exclusively based on 20 kHz pulsed lasers such as those available commercially from Dantec ®and LaVision ®. A study by Chan in 2004 was among the first to use a continuous-wave (c-w) laser for PIV but this work was relatively limited in time resolution at 490 Hz [57]. However, advances in high-speed cameras now allow for vast improvements in time resolution using a c-w laser for PIV. The advantage of using a c-w laser for PIV is that data can be taken at a wide range of acquisition frequencies. Also, the need for pulse-image triggering is eliminated which simplifies the setup further. However, c-w PIV necessitates understanding of the exposure time integration and suffers from reduced signal-to-noise due to lower laser power.

The PIV technique itself has drawbacks. Thomas stated that the particles must

be large enough to be detected, but small enough to not interfere with the flow physics [29]. Further, Anderson stated that a high enough particle density is needed to provide relevant velocity field measurements, but low enough to not disrupt the flow physics [8]. Thomas stated that an additional concern for PIV applied to reacting flows is that the injected particles should not be reactive to the combustion process [29]. Finally, pre-existing knowledge of the flow field is required to properly estimate the laser pulse delay, pulse frequency, and the corresponding camera frame-rate. It is also possible to use a continuous-wave laser with a single high-speed camera and using the pulse delay to determine an appropriate frame rate for the camera. Despite its drawbacks, PIV is an extremely useful flowfield investigation technique.

3.7.2 AFIT Time-Resolved PIV System.

The AFIT time-resolved PIV system was developed out of necessity due to the future desire to quantitatively investigate the time domain of the UCC flowfield. The system was assembled using existing lab equipment to eliminate the issue of equipment availability. The system consists of a continuous-wave Coherent Verdi V12 laser, a monochrome Phantom V12.1 camera, and dual shaker-type seeders. Each component brings advantages and disadvantages to the system over PIV systems using pulsed lasers.

The Verdi V12 is a continuous-wave laser providing 12 Watts of power at 532 nm wavelength. Due to the nature of c-w lasers, the output power over a short period of time is orders of magnitude lower than that of a pulsed laser which leads to lower signal-to-noise ratios. However, the continuous illumination allows for great flexibility in customizing the acquisition frequency allowing applicability to larger flow velocity ranges. The acquisition rate cannot be chosen haphazardly though. A priori determination of image processing parameters is required. Thomas previously determined

the optimal pulse delay for various core air mass flows [29]. According to Dantec Dynamics, that the flow velocity should displace the seed particles on the order of 1/4 of the interrogation window size over the pulse delay [17]. This becomes very situationally specific due to the factors of flow velocity, camera resolution, and interrogation window size. However, in this setup a traditional dual-pulsed laser is not used, but the pulse delay becomes synonymous with the image spacing and thus leads to a determination of the image acquisition frequency, which was 30 kHz for this system. The acquisition frequency of 30 kHz corresponds to an image spacing of about 33 μs, which corresponds to about 25 m/s flow velocity using the 1/4 interrogation window rule and the 3.3 m/s per pixel spatial calibration with the 32 x 32 pixel window size. This system uses a monochrome Phantom V12.1 camera for image acquisition. This camera is capable of 1 MHz operation at 128x8 pixel resolution or 6.2 kHz operation at 1280x800 pixel resolution. The fast acquisition frequency capability is certainly an advantage but the decreased resolution at higher frequencies could potentially become problematic depending on the flow situation. Fortunately, this camera is extremely customizable with regard to acquisition frequency and image resolution, provided the two parameters combined yield a suitable operating condition.

Previous PIV investigations by Thomas on AFIT's UCC model noted difficulty in maintaining high enough seed density in the core flow following injection from the UCC for consistent vector correlation [29]. To improve this situation, a PIV seeder box (see Figure 29) was added to the UCC flow to allow for simultaneous seeding of both the UCC and core air flows. This allowed for measurements to be taken of the UCC flow to determine the actual g-load achieved for a given condition. This also allowed for the addition of an another fuel injector in the seeder box which doubled the residence length of the flame within the UCC compared to operation without the seeder box. Two independent seeders were then required to seed the two independent

flows of the UCC and core flow sections.

In addition to the seed density issues reported by Thomas [29], large time-dependent seed density variation was observed with the rotating drum seeder. In order to improve this situation, shaker-type seeders were designed based on those in use at AFRL/RZTC by Schmidt et al. [59]. The new seeders are shown in Figure 70 are are of cylindrical shape using variable force/variable speed electric vibration motors from Vibe Co. (model SCR-100). These motors were chosen over the pneumatic driven motors in the AFRL/RZTC design for their customizability in agitation force and speed for application to the largest range of flow rates possible. Also, being electrically powered instead of pneumatic allowed for a simpler setup requiring only electrical power instead of a special air/oil mixture supply as is needed for the AFRL/RZTC seeders. Also differing from Thomas's setup was the use of mass flow controllers using air instead of nitrogen seeding gas to eliminate any issues regarding air composition and the impact of additional nitrogen on the flow velocity and velocity ratio. However, using air as the seeding gas does require minor bookkeeping to ensure the total air flow stays constant with and without the seeder. To further help with this bookkeeping the seeder flow valve was removed from the core flow section and an air bypass loop was added to each seeder, shown in Figure 70, to allow continuous flow of the seeding air that is simply directed either through the seeder, through the bypass loop, or through both flow paths allowing an additional option to adjust the particle seeding density. This additional option was not used and the entire 30 SLPM of air went through each seeder. Also, the vibration frequency was adjusted to increase or decrease the seed density as required, the frequency of each seeder was set independent of the other. To further adjust the seed density the air flow passing through the seeders can be adjusted up to a maximum of 30 SLPM of air, which was the flow rate used for this research.

Figure 70. Dual shaker-type PIV seeders

Similar to Thomas, 2 micron silicon carbide seed particles were used [29]. According to Melling, metallic seeds of this size are capable of following flowfield oscillations up to the order of 1 kHz [60]. This is important to note because while the measurement is taken at 30 kHz, resolvable flow frequencies will be capped at 1 kHz due to the choice in seed particles. However, 0.5 micron silicon carbide is capable of following flow oscillations to the order of 10 kHz and is available but was not used for this research because the decreased signal-to-noise ratio, resultant from the smaller diameter, was too low for the camera to resolve the seed particles.

The Phantom Control Center (PCC) v1.3 software was used for video acquisition while image processing used Dantec Dynamic Studio v3.2 software. Dynamic Studio v3.2 was the first version to allow image acquisition for this PIV setup within the software, but was not released until after the data collection was completed. Thus, the saved cine files from the PCC were then batch converted, using PCC, into single-image tiff files in order to be imported into Dynamic Studio for processing into vector maps.

While Dynamic Studio works extremely well for batch-processing large amounts of PIV data Thomas noted that the figure display and output capabilities are extremely limited [29]. Thus, the vector maps were then time-averaged and then exported to MATLAB for additional analysis.

3.7.3 System Validation.

While PIV systems are not typically calibrated, using a continuous-wave laser for this system instead of a pulsed laser was a stark contrast with convention. As such, the PIV system was used to interrogate three validation cases corresponding to approximately 11, 22, and 44 m/s based Equation 7 using the core air mass flow rate ($\dot{m}_{core}$, the core flow cross sectional area (A), and the ambient air density (ρ) of approximately 1.2 kg/m^3. Figure 71 compares the estimated velocity using Equation 7 with the measured velocity from the PIV system. This figure shows reasonable agreement between the estimated and measured velocities sufficient for validation of the PIV system. While the 15% overshoot is significant, Sincock showed that the actual flow rate versus the set point of the mass flow controller for the UCC and core flows exhibited up to a 20% overshoot [61]. This overshoot is a function of the Fox mass flow controller system, flow meter and pressure regulator, and is significantly higher than the manufacture specification of a 1% error. The most likely sources of this error are upstream pressure supplied to the flow controller system or due to the air compressor tanks or the downstream pressure regulators (before the regulator in the flow controller system). The main issue with estimating the error of the Fox system was that calibration of the system was possible because a validation system to perform the calibration does not (or is not known to) exist. However, the error between the estimated and measured velocities was influenced more by the Fox system error than the PIV system error. The measured velocities using PIV should be regarded with

more confidence than the estimated velocities, but the estimated velocities were used for computing the test case parameters such as g-load and velocity ratio and the estimated values may have up to a 15% bias error.

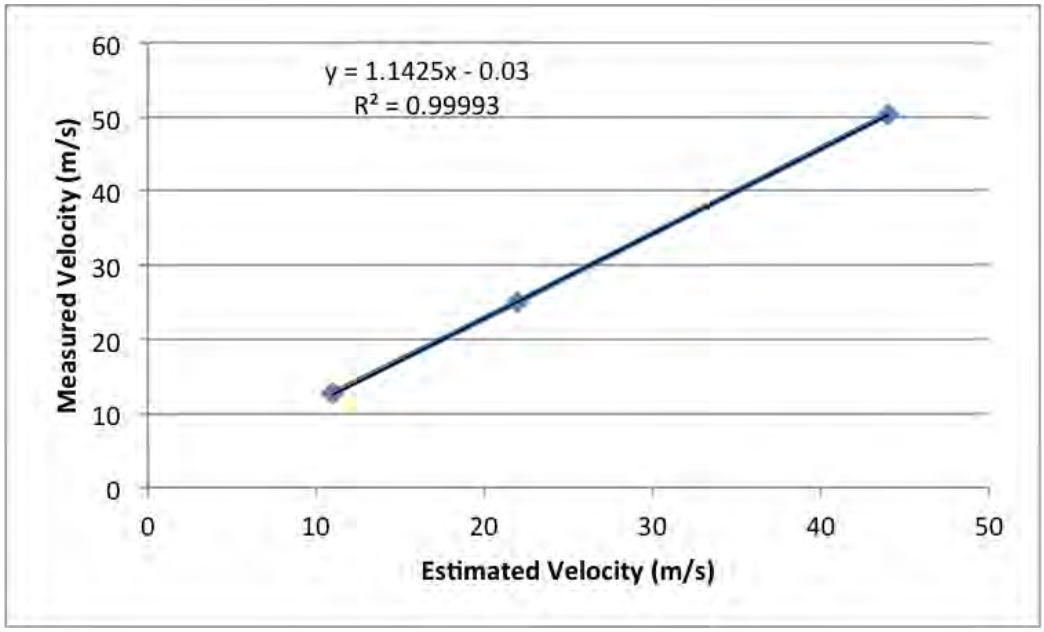

Figure 71. Relationship of the measured core flow velocity vs. estimated core flow velocity in m/s

3.7.4 Error Analysis.

Assuming an accurate spatial calibration, determination of PIV accuracy was relatively trivial. As noted by Thomas, PIV error analysis must consider the contribution of peak-locking. Peak-locking results from the limitation of finite spatial resolution for measuring the particle displacement and subsequently particle velocity. Thomas defined the peak locking error as the velocity corresponding to half of a pixel displacement, since displacement values must fall into integer pixel displacements the displacement will be off by at most half of one pixel [29]. This was considered a worst-case scenario estimate since most current processing software can estimate sub-pixel displacements. For this setup the peak-locking error was +/- 1.65 m/s based

on the spatial calibration and image time-step. From a statistical sense, error was introduced via an insufficient number of valid samples. Thomas typically used 47 samples with a resulting approximate 10% statistical error using Equation 17 [29] where U is the mean velocity, σ is the standard deviation, N is the number of samples, and Z is the confidence level which was constant at 95%. For this research 3000 samples were taken to reduce the statistical error to approximately 1.5%. A two pixel error in the spatial calibration was assumed to account for resolution of the calibration target and a 6.06% error resulted. Considering the mass flow controller used had a 1% error, not accounting for the roughly 15% overshoot bias, the average total error was on the order of 9.02% over the 10-80 m/s range, based on UCC and core flow velocity estimates, using the root-sum-square method. This total error was higher than the 8.16% error reported by Thomas [29] even with the higher number of samples due to differences in camera resolution and spatial calibration constant. The camera Thomas used had a resolution of 2048 x 2048 pixels with a calibration constant of 0.0377 mm/pixel [29] whereas this system used a camera with 800 x 200 pixels with a calibration constant of 0.11 mm/pixel resulting in nearly a three-fold increase in spatial calibration error and peak-locking error. However, the sacrifice in measurement error was necessary to gain acquisition frequency increase from 7.4 Hz to 30 kHz. Figure 72 shows this total error vs. the 10 - 80 m/s range. The curve is necessarily asymptotic in both directions due to finite error values and limitations of the appropriate velocity measurement range based on the camera resolution, image acquisition frequency, spatial calibration, and interrogation window size.

$$\%Error = 200 * \frac{Z\sigma_{rms}}{U\sqrt{N}} \tag{17}$$

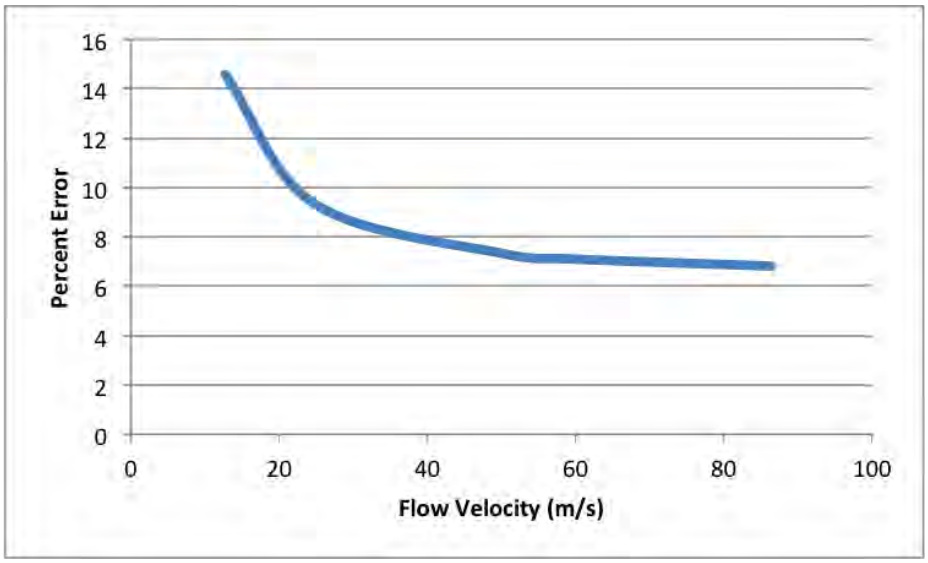

Figure 72. Measured flow velocity vs. total statistical error

3.7.5 Illustrative Measurement.

The Phantom camera was operated with a resolution of 800x200 pixels at 30kHz with an image spacing of 33.3 μs with an exposure time of 5 μs. The camera gain was increased from 1.0 to 10.0, the gamma was decreased from 2.2 to 1.0, and the sensitivity was increased from 1.0 to 4.0, otherwise the camera settings remained at the manufacture default setting. The adjustment of the camera settings was necessary for detection of the seed particles for this system. Prior to data collection a Current Session Reference (CSR) was obtained which effectively subtracted the camera background noise from the image to improve the signal-to-noise ratio (SNR). The CSR was used to reduce the increased background noise level that resulted from increasing the camera gain. The spatial calibration image for the resolution (see Figure 73) had a calibration constant of 0.11 mm per pixel with a total image size of 88 mm x 22 mm. This figure is also labeled with locations of the core flow, UCC flow, radial vane, and radial vane cavity for reference. Figure 74 shows four consecutive unprocessed images illustrating the illuminated seed particles. Also shown in this figure is the inconsistent seed density occurring at and downstream of the UCC interface. For this

reason, the PIV data was processed to only obtain inlet and outlet velocity profiles.

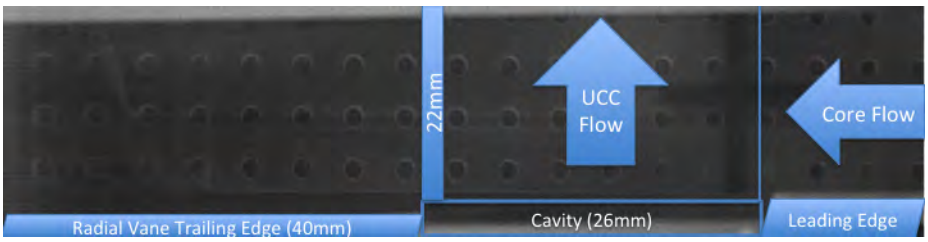

Figure 73. Spatial calibration image for PIV data collection. Highlighted are locations of the radial vane cavity, UCC flow, and core flow.

The collected images, such as the images in Figure 74, were processed with a 1-2, 2-3, 3-4, 4-5, etc. image pair sequence as was appropriate for this type of PIV system as opposed to the 1-2, 3-4, 5-6, etc. image pair sequence used for a dual-pulsed laser system. This was also the only sequencing option in the processing software for images acquired in the manner described for this system. For each test case 3,000 images were saved, corresponding to 0.1 seconds. This sample size was chosen to provide an extremely large statistical sample since Thomas noted issues with obtaining statistically significant numbers of valid samples throughout the entire measurement region [29]. A sample of the 3,000 images were used to produce 2,999 vector maps. An adaptive correlation was used with window sizes of 128x128, 64x64, and 32x32 pixels with a 50% window overlap producing a final 49x11 vector field for 539 total vectors. The adaptive correlation analyzes the data with larger window sizes first to determine rough estimates of the velocity at larger vector spacing and refines that estimate with successively smaller window sizes with smaller vector spacing, according to the Dantec manual [17]. The adaptive correlation algorithm used to compute the vector maps had a peak validation with a value of 1.2 upstream of the UCC interface, the software default, and 1.5 downstream of the UCC interface. The peak validation value was increased for the downstream location because of the seed density issues and the complex flowfield resulting from the injection of high

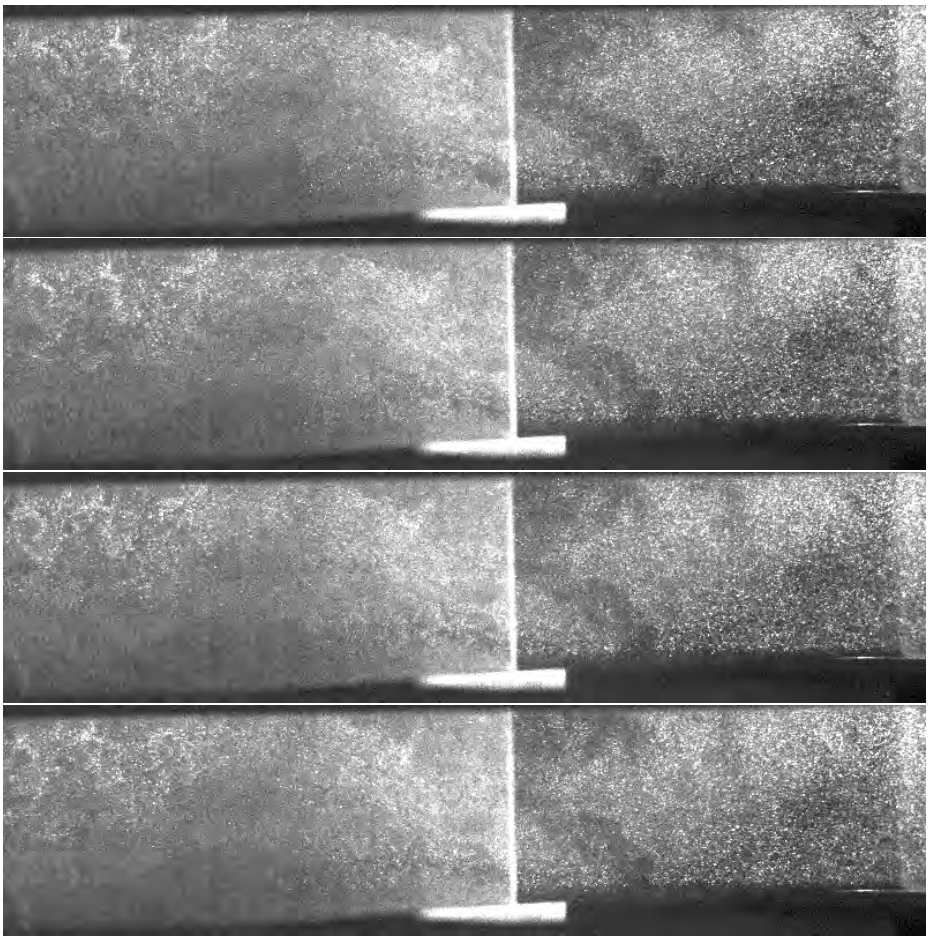

Figure 74. Sample of PIV images of taken in of a typical UCC test condition at 30 kHz

temperature UCC flow into the core. The higher peak validation value was necessary to eliminate spurious vectors obtained from the image background noise due to the low seed density.

The images in Figure 75 show a sample of four vector maps directly from the Dynamic Studio software made from five images, like the images in Figure 74, which were processed with the following sequence of image pairs 1-2, 2-3, 3-4, 4-5. The blue vectors are actual computed vectors from the correlation processing while the green vectors are substituted using a moving spatial average method during vector validation. Figure 76 shows the top images from Figures 74 and 75 with rectangles indicating regions of low seed density. The low seed density of these regions led to the uncharacteristically small or no velocity reported for interrogation windows in these regions.

Following vector validation, a time-average of the 2999 vector maps was computed using only the valid non-substituted vectors resulting in the time-averaged vector map in Figure 77. Because the bulk flow properties are of necessary determination first, only the mean flow properties were considered for the bulk of the analysis. The flow field statistics were then exported to MATLAB for further analysis. This process was repeated for both the inlet and exit regions, as marked in Figure 77. The total number of valid samples at each location is shown in Figure 78. This figure shows that the peak number of valid vectors was 2977 and the average was about 2000 for the inlet, and for the outlet the peak was about 2000 and the average was about 1200 of the total 2999 samples. An average of 1200 out of 2999 samples would have increased the statistical error contribution from 1.5% to 2.3% and would not a significant impact on the total system error.

The images in Figures 79 and 80 show the u component (x direction) of velocity and v component (y direction) of velocity for a typical UCC condition at both the

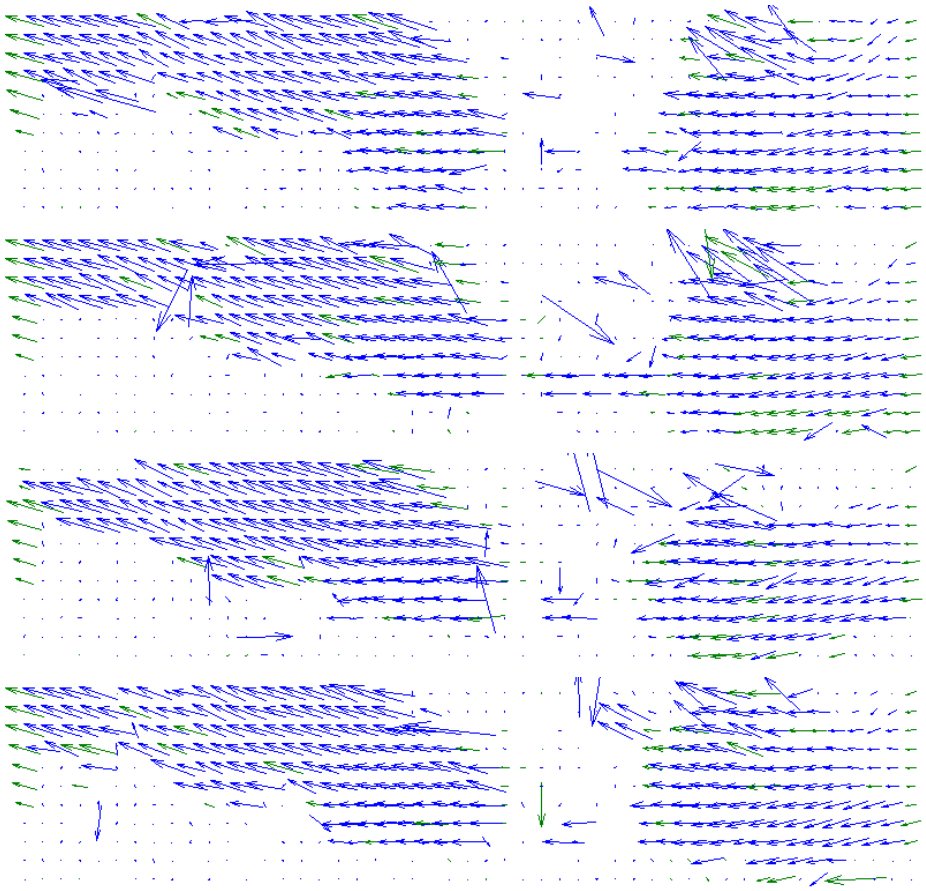

Figure 75. Instantaneous PIV vector maps at 30kHz processed with 5 images (1-2,2-3,3-4,4-5), green indicates substituted vector (from top t = 0, 33.3, 66.6, 100 μs)

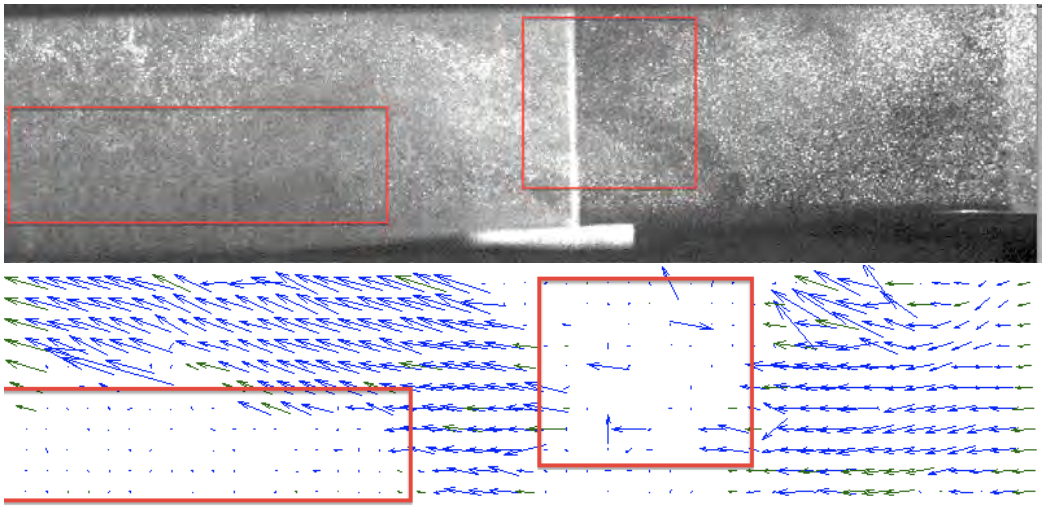

Figure 76. Raw PIV image (top) and processed vector map (bottom) with rectangles highlighting regions with low seed density

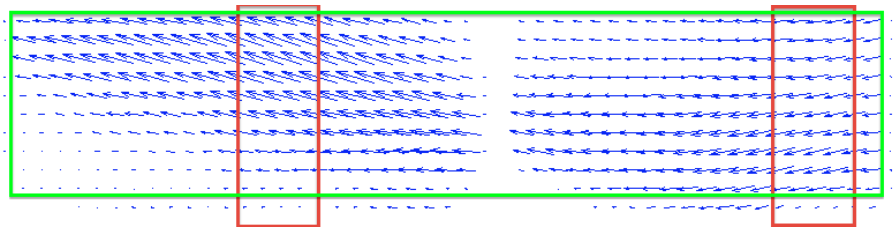

Figure 77. Time-averaged velocity vector map with red rectangles indicating the inlet (right) and exit (left) regions and the green rectangle indicating the laser sheet

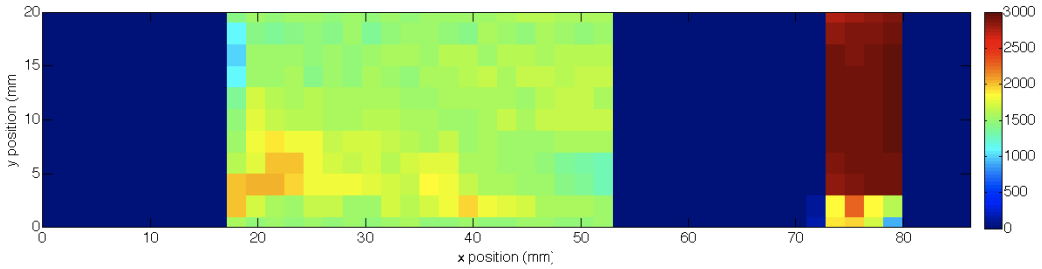

Figure 78. Spatial distribution of the number of valid vectors out of the total 2999 samples

inlet (right) and exit (left) for illustrative purposes. It is important to note that the flow is from right to left, as indicated by the vector maps in Figures 75 and 77, which yields negative u component of velocity values but in Figure 79, and for the rest of this research, the sign of the u component was changed from negative to positive. Typical inlet and exit u component velocity profiles are shown in Figure 81. The inlet and exit profiles were taken for multiple planes within the core flow, as shown in Figure 82. This figure illustrates that while reasonable profiles resulted from Planes 1-3, the results from Plane 4 were unreasonable due to very low resolved seed density particularly at this location for most cases. The reason that Plane 4 was problematic was due to the high laser scatter off of seed particles deposited on the window. Plane 2 was used for future comparison between test cases, as shown in Figure 81. Examination of this figure shows that the inlet velocity was about 16 m/s while the exit velocity was about 22 m/s. The reported values are the inferred freestream velocity based on the velocity profiles because the laser sheet did not span the entire image, which leads to lower velocity at the top and bottom of the image

(more so in the bottom), and because the downstream profiles suffered significantly low seed density that further decreased the reported velocity in that region. Further, due to the seed density issues, no comparisons are made as to the shape of the profile and discussion is limited to the inferred freestream value.

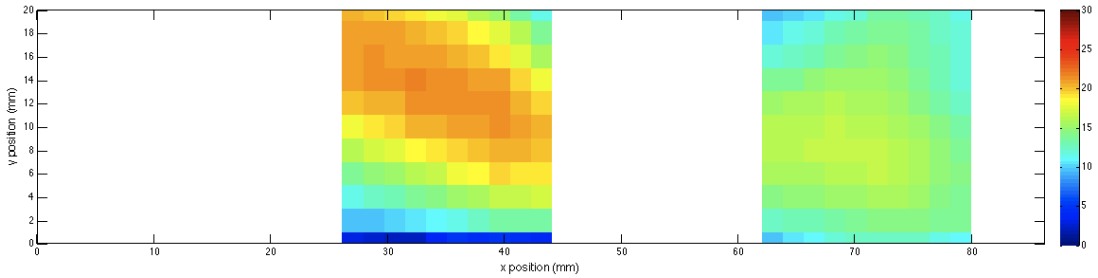

Figure 79. Typical core flow u component of velocity spatial distribution at the inlet (right) and exit (left) of a typical UCC condition

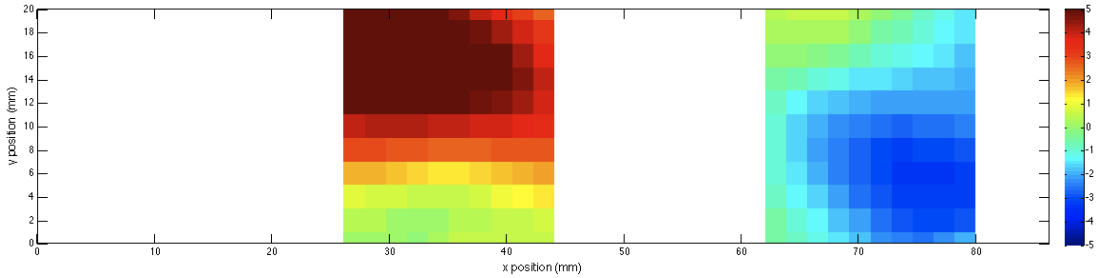

Figure 80. Typical core flow v component of velocity spatial distribution at the inlet (right) and exit (left) of a typical UCC condition

Based on the core flow inlet and exit temperatures of 296K and 633K measured using thermocouples at the locations shown in Figure 26 (y = 5 mm), this would suggest that a roughly 100% increase in the velocity magnitude should be observed. However, only about a 50% increase was measured for the u component of velocity, but based on Figure 80 a significant v component of velocity exists at the exit location an likely a significant w component (out of plane) was present that was not included in the comparison. Based on manual estimates of the velocity from the raw PIV images used for correlating this data, the 22 m/s u component of velocity was indicative of the mean flow motion of the seed particles in the plane of the laser sheet. The

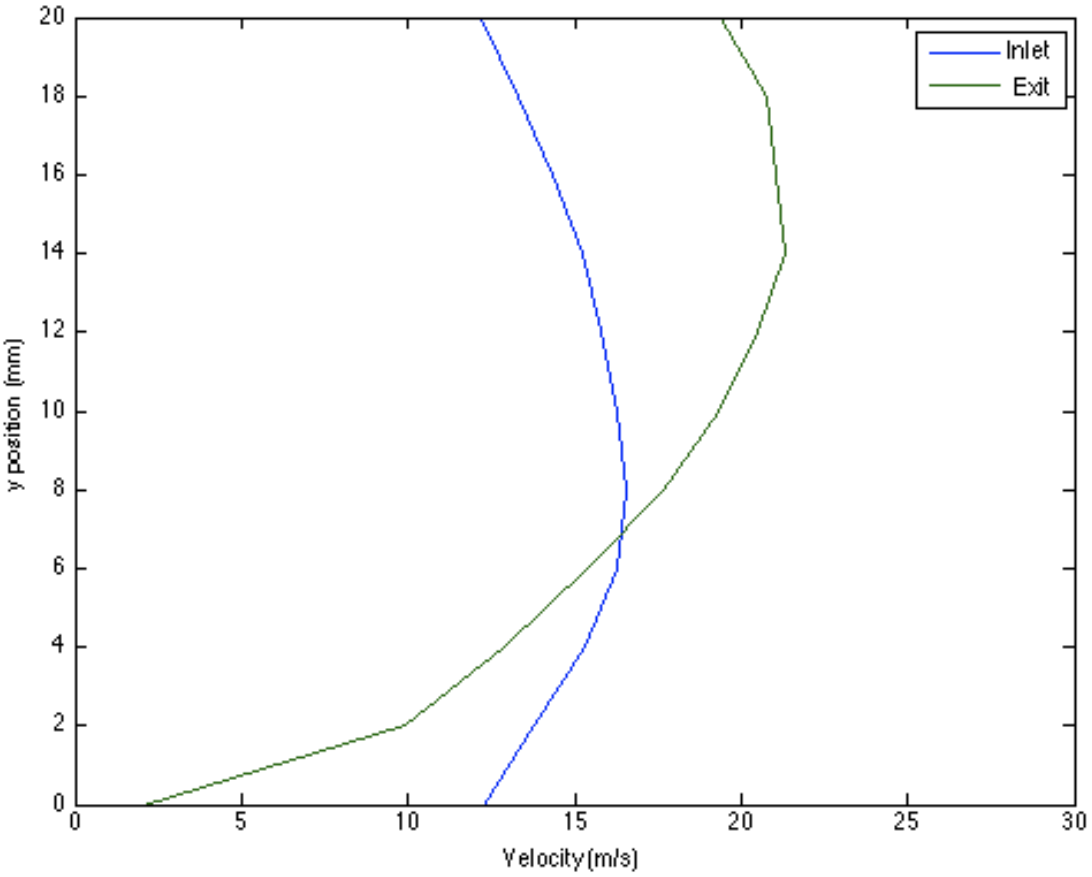

Figure 81. Typical core flow u component of velocity profiles at the inlet and exit of a typical UCC condition

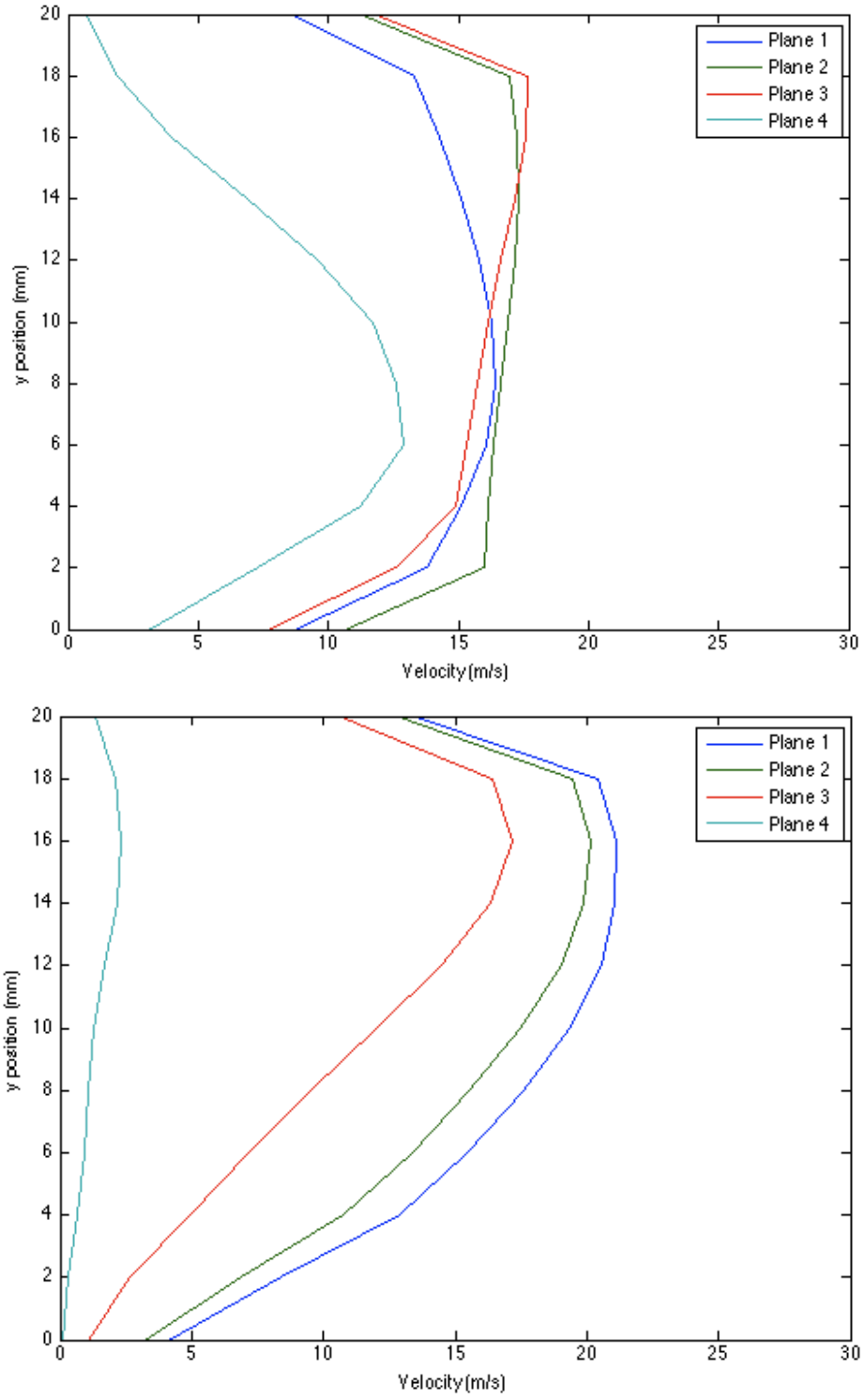

Figure 82. Typical core flow u component of velocity profiles for Planes 1-4 at the core flow inlet (top) and exit (bottom) of a typical UCC condition

data still indicates that significantly lower flow velocities were meausured in the core flow than expected for a 2x temperature increase, the situation becomes worse if the PLIF flame temperature of 1400K is uses. Accounting for the increases in the other velocity components, v and w, may explain the lower seed particle velocity than would be expected for the same temperature increase. The low downstream seed density could have also contributed to lower measured velocity values. Also, there may have been some particle lag as the core flow seed particles traversed over the large density gradient at the UCC interface that could also have contributed to the lower velocity values.

In order to analyze the unsteadiness and demonstrate the time-resolved capability of the system, the velocity magnitude was extracted from a single point from all of the vector maps (2999). The raw point velocity data in the core flow versus time is shown in Figure 83. This figure illustrates that a large percentage, upwards of 66%, of the point velocity measurements over time were determined to be invalid, based on the correlation peak criteria. However, over 1000 of the 2999 vectors were still valid, which allowed for reasonable measurements of the time-averaged velocity data. Unlike the core flow, measurements at the ambient UCC exit (see Figure 21 for the ambient exit location) yielded a significantly higher number of valid instantaneous velocity measurements, about 2400 over the 1200 in the core flow, and reasonable point-wise velocity versus time data resulted. The point-wise velocity values for the ambient exit were plotted against time as shown in Figure 84 which was enlarged to show more detail in Figure 85. In these figures, the average velocity was consistently around 20 m/s with significant temporal variation.

The Power Spectral Density (PSD) was computed in order to analyze the frequencies present in the velocity signal. In order to compute the PSD, as described by Mathieu and Scott [62], the total velocity was assumed to consist of the average

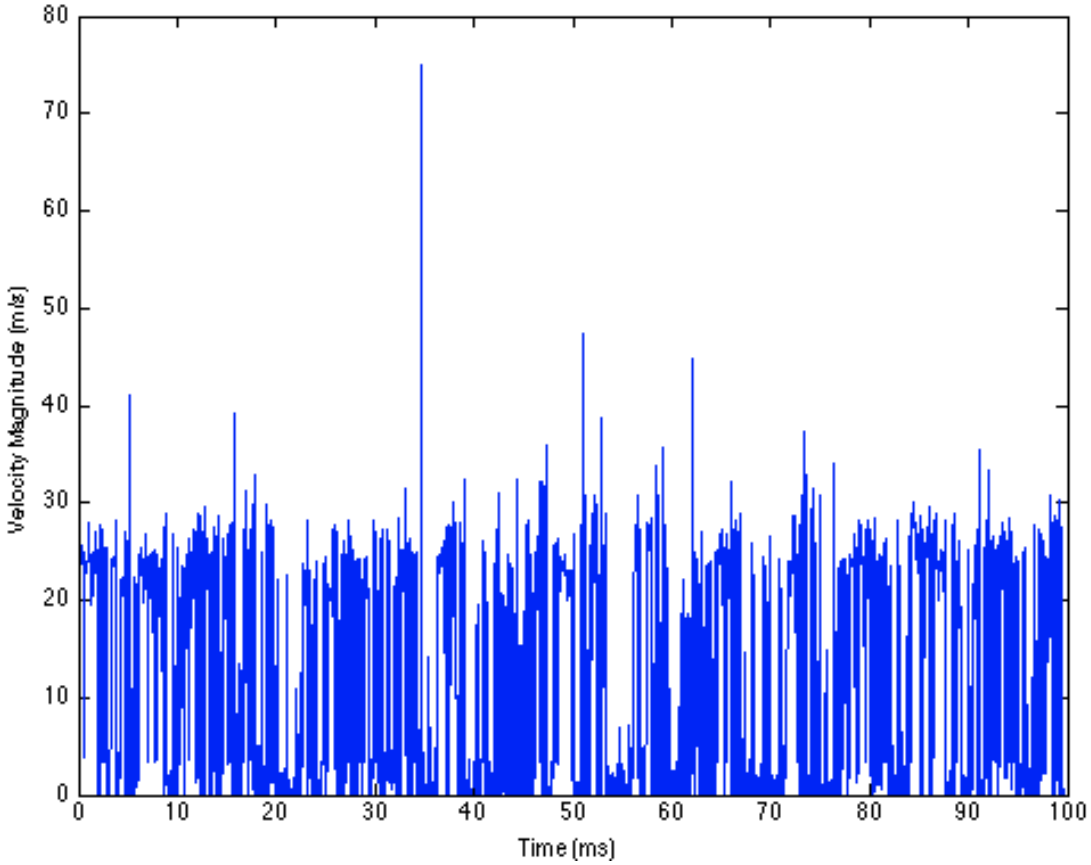

Figure 83. Typical velocity magnitude (m/s) vs. time (ms) in the core flow, downstream of the UCC interface

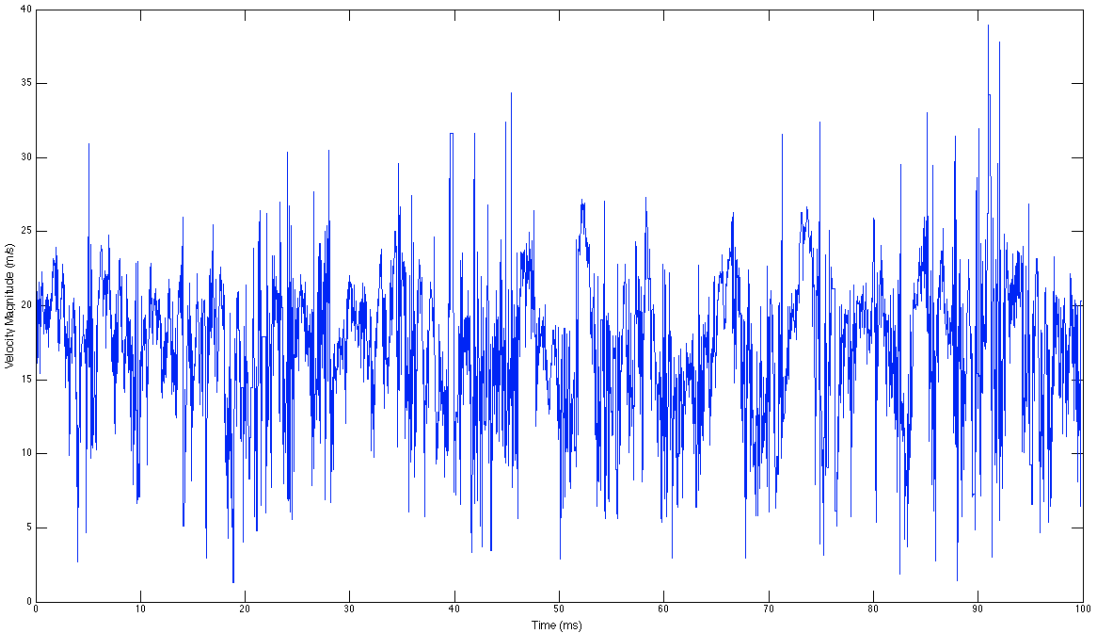

Figure 84. Typical velocity magnitude (m/s) vs. time (ms) at the ambient UCC exit

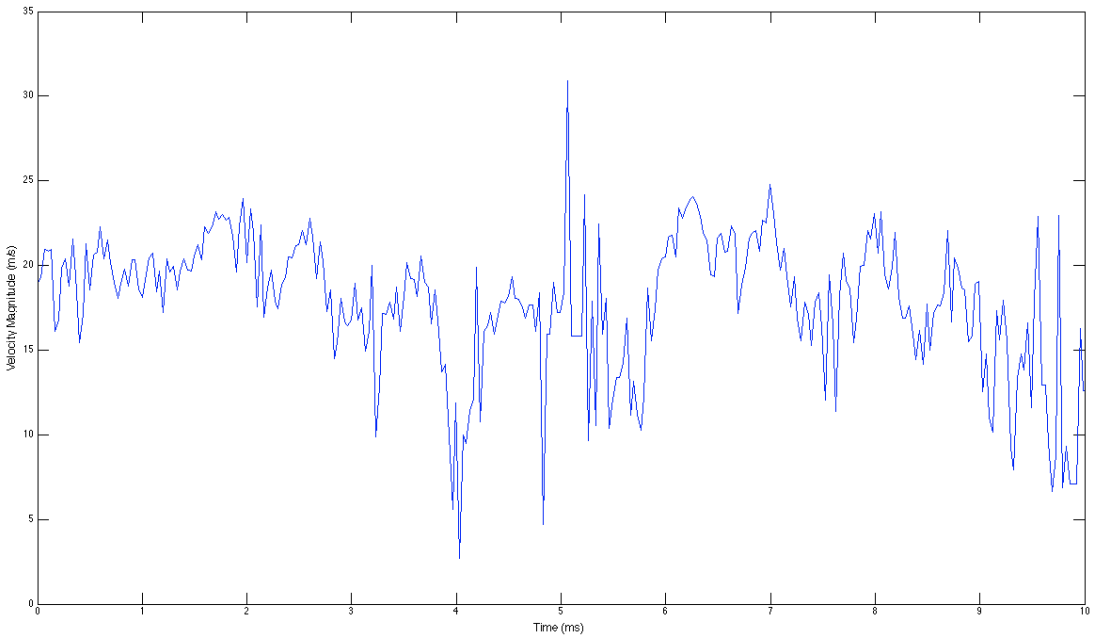

Figure 85. Typical velocity magnitude (m/s) vs. time (ms) at the ambient UCC exit, enlarged to show the first 10 ms of data

component and the fluctuating component as shown in Equation 18. Then, a Fast Fourier Transform (FFT) was taken of the fluctuating velocity component for analysis in the frequency domain. Since the resulting FFT was complex, the FFT was multiplied by the complex conjugate of the FFT to yield the PSD according to Equation 19. According to Mathieu and Scott, the PSD of the fluctuating velocity component (normalized per unit mass) has units of velocity squared or power per unit frequency (W/Hz) like the Reynolds stress tensor used in turbulence modeling and is useful for studying the temporal variability of turbulent flows [62]. A PSD was computed of the point velocity data, Figure 84, which was taken at the ambient UCC exit. The PSD, shown in Figure 86 was created by analyzing the velocity magnitude at the given point for all 2999 vector maps. This created a frequency range for the PSD of about 10 to 15,000 Hz. However, examining Figure 86 shows the dominant frequency peaks occurred below 1,000 Hz, which was the limit based on the seed particle size and was also in the reportable range for the HSV data. In order to more closely examine

the dominant peaks, a "zoomed" PSD is shown in Figure 87 which showed the most dominant peaks were around 130 and 260 Hz for this case.

$$V(t) = \bar{v} + \acute{v}(t) \tag{18}$$

$$PSD = \text{FFT}(\acute{v}) * \text{conjugate}(\text{FFT}(\acute{v})) \tag{19}$$

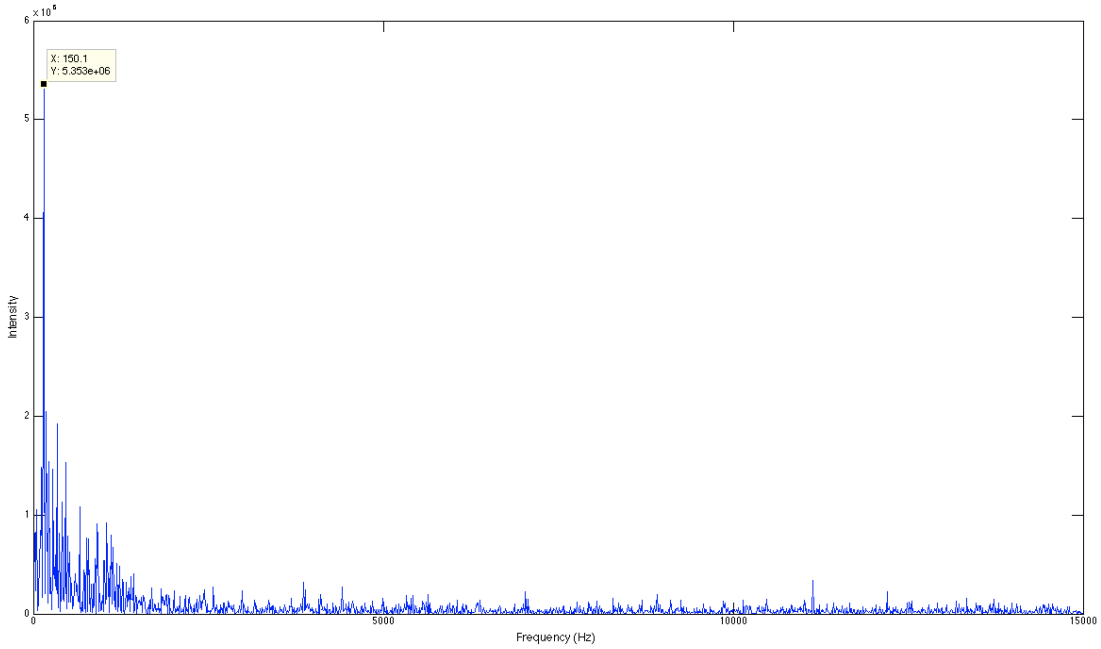

Figure 86. Typical Power Spectral Density (PSD) at the ambient UCC exit

3.7.6 Process Analysis.

In the previous section, Case 14 was used for the illustrative measurement. However, will be shown in Chapter 5, this case is subjected to migrating flame that easily traverses the entire radial vane span, reverses, and likely traverses back to the OD endwall. The significant span-wise velocity component that must have been present would likely be much higher than the 4 m/s estimated in Chapter 6. Even at 4 m/s though, a seed particle would have traversed the thickness of the laser sheet, about

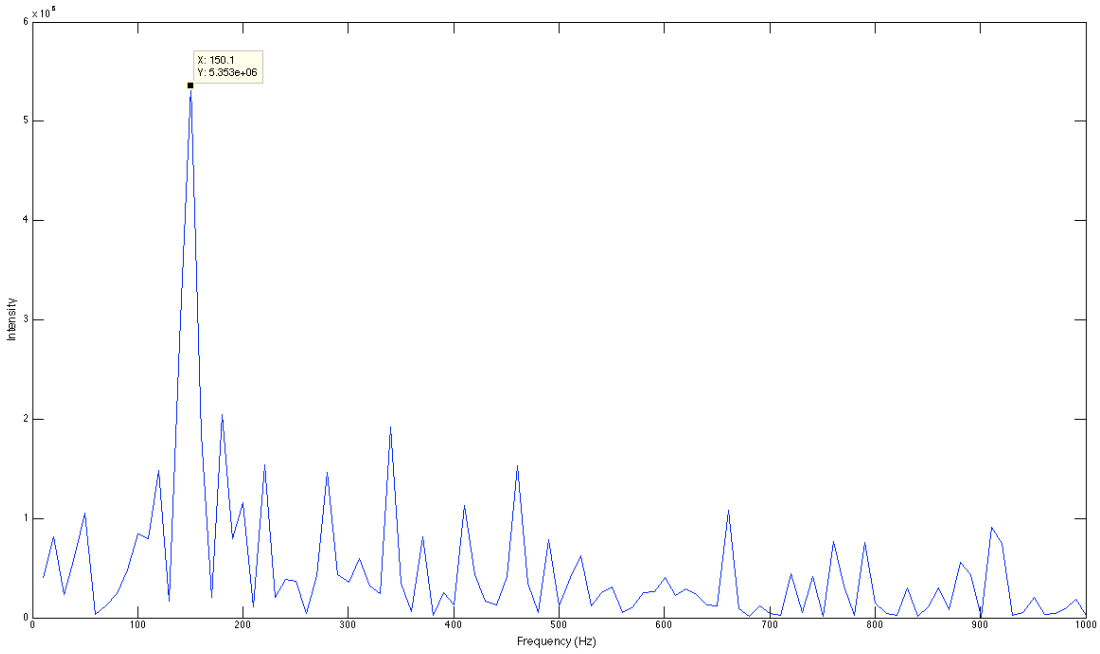

Figure 87. Typical Power Spectral Density (PSD) in the core flow at the ambient UCC exit, enlarged to show frequencies up to 1,000 Hz

0.5 mm, in three frames (about 100 μs). Three frames is likely the best case scenario because of the complex 3D nature of the core flow interface with the UCC and realistically the seed particles would have had around two frames within the laser sheet. Two frames is the minimum requirement to produce a velocity vector, which leaves the PIV system with significant trouble detecting particle motion downstream of the UCC interface for this particular case. However, decreasing the MFR and VR improved this issue.

Examining Case 15, with MFR = 0.1, instead of Case 14, with MFR = 0.2, better results were obtained. Figure 88 shows four raw images from the dataset for that case. This figure shows that improved seed density was observed for this test case over Case 14, but significant issues were still present in the immediate vicinity of the UCC interface, as expected. Figure 89 shows the four resultant vector maps from the first five raw images (only images one through four were shown in Figure 88). This figure shows that less data loss occurred in the region downstream of the UCC

interface due to improved seed density in that region. Figure 90 shows the resultant time-average of the total 2999 instantaneous vector maps and confirmed that data loss downstream of the UCC interface was less of an issue for Case 15 over Case 14, as expected. Figure 91 shows the inlet and exit velocity profile for Case 15. This figure shows that while the raw images and vector maps appeared to produce better data for Case 15 than Case 14, the issues with interpreting the velocity profiles persisted for this case as well. The most plausible explanation was that the out of plane motion still plagued the PIV system, mainly in the ability to image the particles moving with significant out of plane velocity.

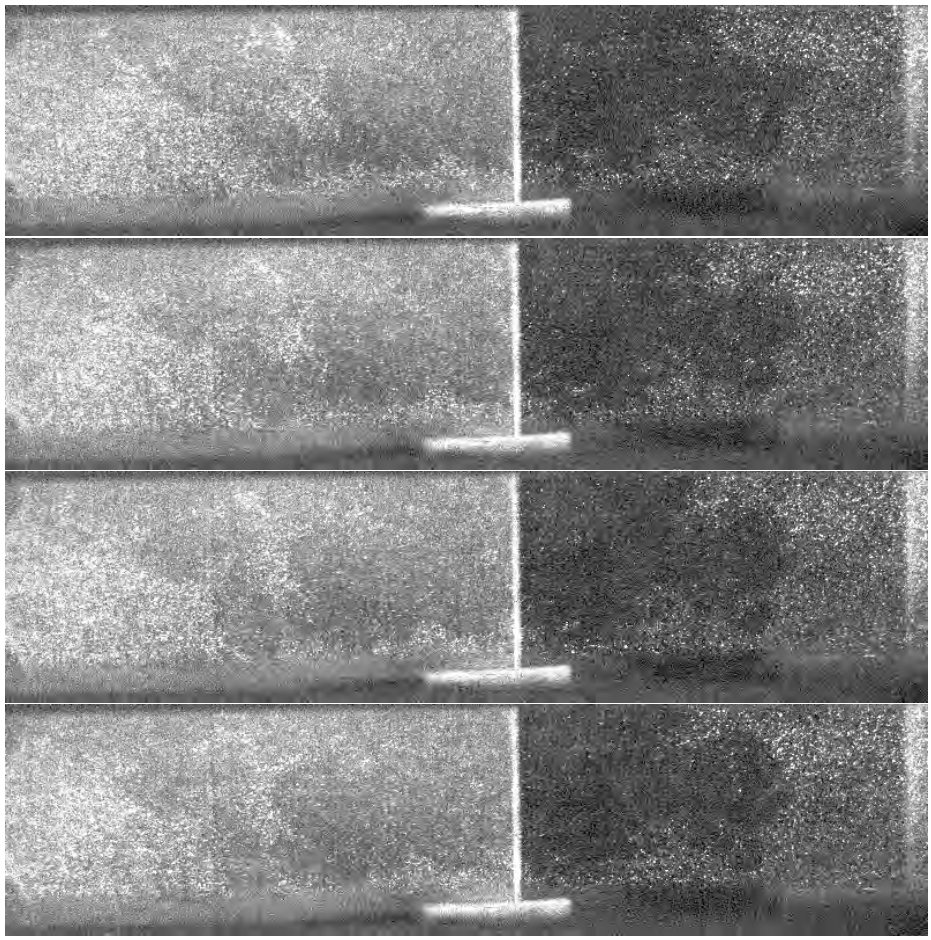

Figure 88. Sample of PIV images of taken in of a typical UCC test condition at 30 kHz (Case 15)

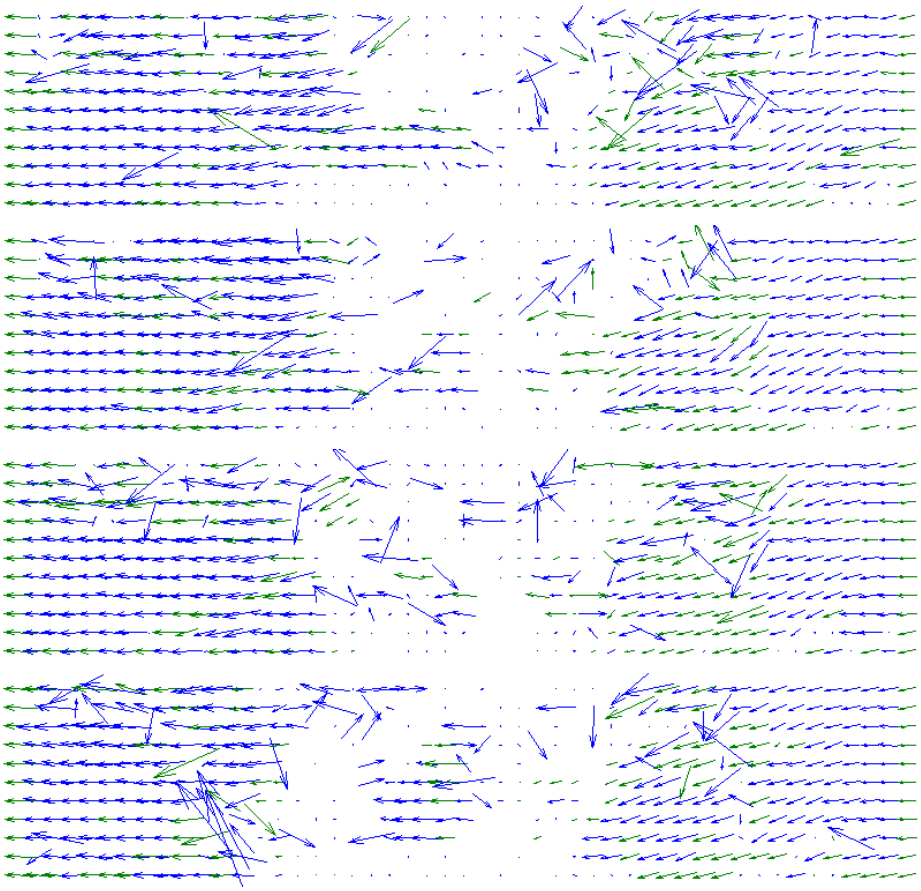

Figure 89. Instantaneous PIV vector maps at 30kHz processed with 5 images (1-2,2-3,3-4,4-5), green indicates substituted vector (from top t = 0, 33.3, 66.6, 100 μs) from Case 15

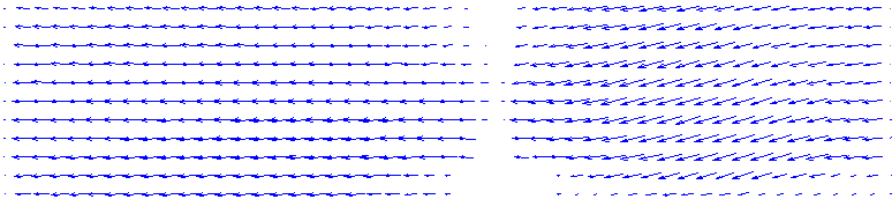

Figure 90. Time-averaged velocity vector map for Case 15

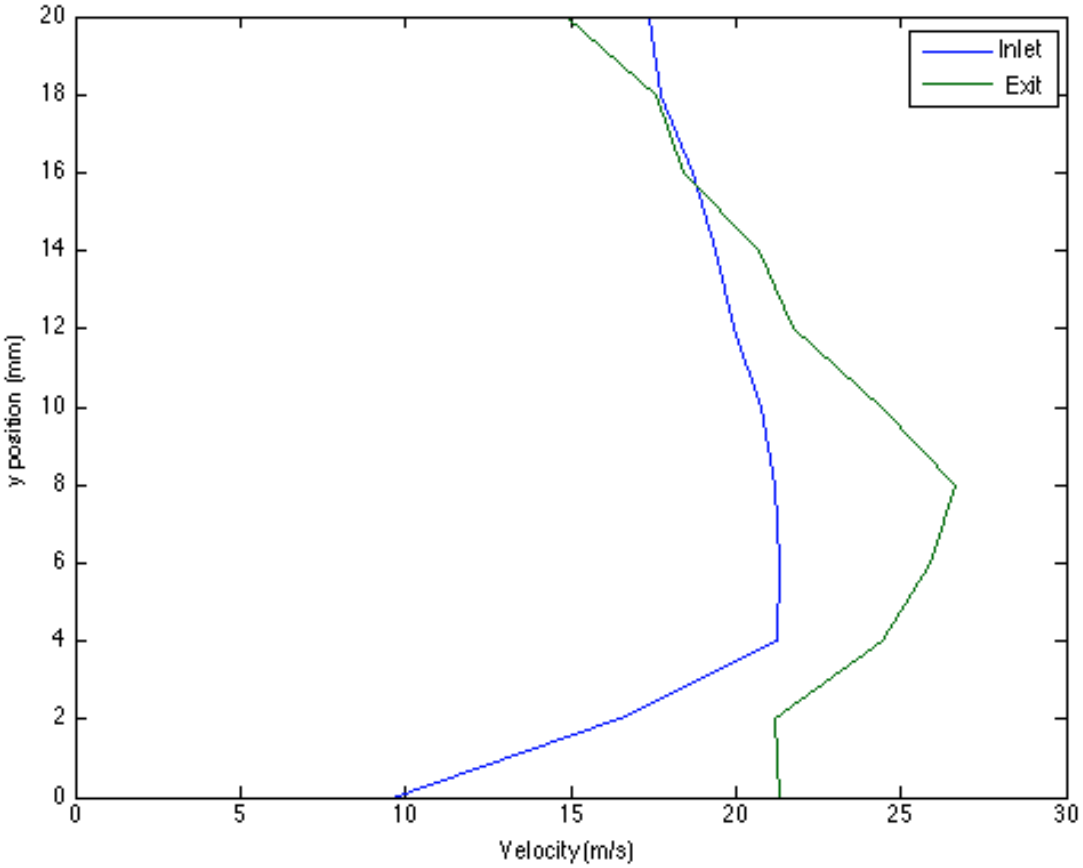

Figure 91. Typical core flow u component of velocity profiles at the inlet and exit of a typical UCC condition (Case 15)

3.7.7 Repeatability.

While the repeatability error in velocity measurement has been characterized, it is important to understand the variability with respect to the time averaging of the transitory events being measured. In order to characterize this variability, a typical UCC condition was repeated numerous times. Figure 92 shows four u component velocity profiles at the inlet (top) and exit (bottom). This figure illustrated good repeatability at the inlet, characteristic of the measurement repeatability, while the exit velocity profiles showed about 5 m/s variation at a given y location. This was likely a result of the noted seed density issues from the raw PIV images.

3.8 High-Speed Video

High-Speed Video was collected using a Vision Research Phantom V12.1 Color camera which was similar to the monochrome camera used for PIV. This camera is capable of 1 MHz operation at 128x8 pixel resolution or 6.2 kHz operation at the full chip resolution of 1280x800 pixels. The high acquisition frequency capability was certainly an advantage, but the decreased spatial resolution at higher frequencies could potentially become problematic depending on the flow situation being investigated. For this research, HSV was used for flame migration trajectory and flowfield unsteadiness. As such, the spatial resolution was the driving requirement, not the acquisition frequency, so this was not an issue. For the HSV analysis the camera was operated at 1280x800 pixels with a 2kHz acquisition frequency for the vane height investigation and at 800x200 pixels with a 5kHz acquisition frequency for the g-load investigation. The acquisition frequency was increased to reduce the exposure time and eliminate pixel saturation that was observed in the vane height investigation. Simply reducing the exposure time from 400 to 190 μs would have eliminated the pixel saturation, but the acquisition frequency was also changed to demonstrate an

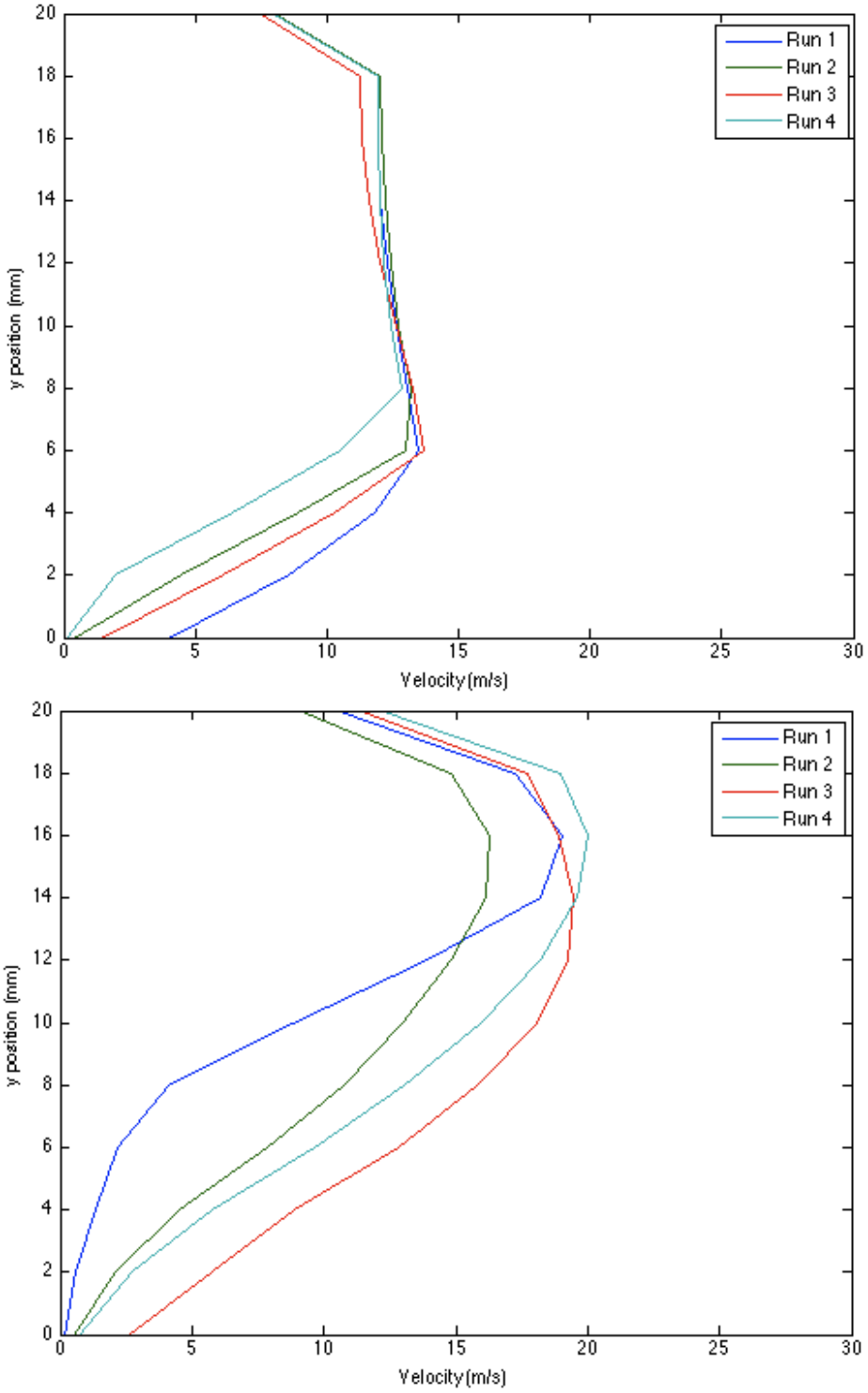

Figure 92. Comparison of the inlet (top) and exit (bottom) u component velocity profiles of 4 runs with identical test conditions

improved time resolution capability. The spatial resolution was the same for both investigations, but the g-load investigation did not need the full 1280x800 resolution because only the 28 mm vane height was used. For both investigations one second of data was collected corresponding to 2000 and 5000 images for the Vane Height and G-Load investigations, respectively.

3.8.1 Illustrative Measurement.

The Phantom Control Center (PCC) software was used for image acquisition. The camera gain was increased from 1.0 to 10.0 and the gamma was decreased from 2.2 to 1.0 but all other settings remained at the default setting. The gain was increased to increase the light detection sensitivity while the gamma was decreased to maintain a linear relationship between the detected light and the reported pixel intensity, according to the manufacturer. Also, a CSR was taken each day before data collection, which lowered the background intensity to zero. An illustrative five image sequence of HSV data is shown in Figure 93 for a typical UCC test condition.

While HSV readily supplies immense knowledge about the qualitative flame migration, quantitative data was required for accurate characterization of parameter variation. First, it is evident from Figure 93 that the angle at which the flame migrates into the core flow was clearly defined and did not appear to vary significantly with time (+/- about 5 degrees). Termed the flame injection angle, this was the angle at which the flame migrates into the core flow with respect to the core flow freestream direction and is illustrated in Figure 94. In Figure 94 the flame injection angle was approximately 60 degrees. For all of the flame angle measurements, great care was taken to distinguish between the flame that was observed in the radial vane cavity and the bulk flame moving from the UCC into the core flow directly. The measured flame angle is for the latter condition, where the flame moves directly from the UCC

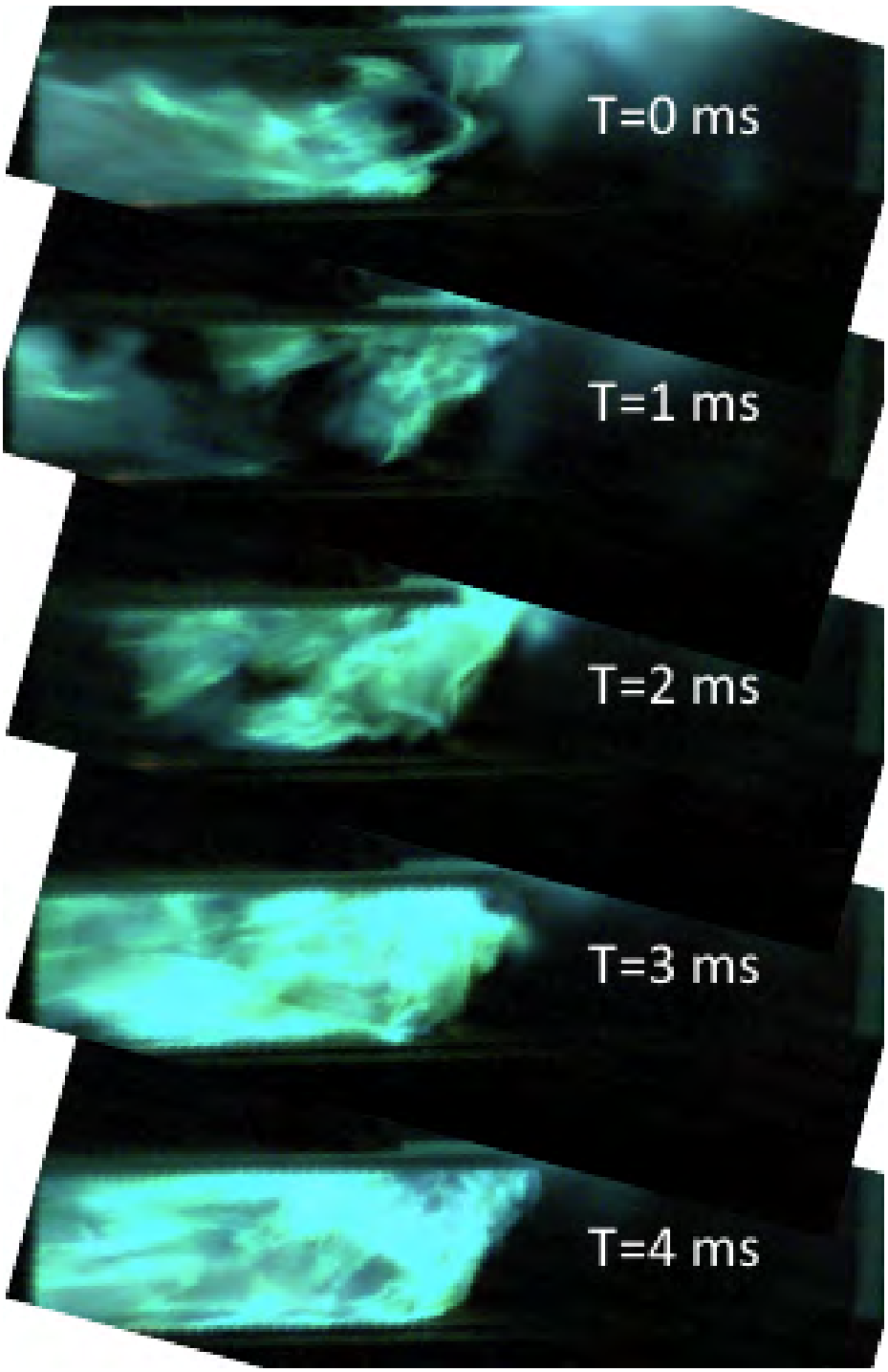

Figure 93. Illustrative High-Speed Video (HSV) image sequence taken from above the radial vane

into the core flow and not through the RVC. The angle of this flame geometry with the freestream was the flame angle and the vertex of the angle was not held constant.

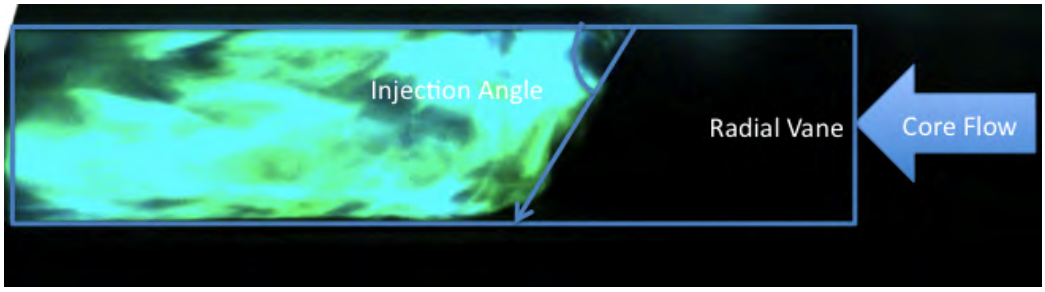

Figure 94. Illustration of the measurement of the flame Injection angle

In order to quantify the time-averaged flame angle and the temporal variability, the HSV data was processed using MATLAB. Figure 95 shows an instantaneous HSV image (top), a 1000 sample time-averaged image (middle), and a 1000 sample pixel-by-pixel standard deviation (bottom). The high intensity region in the upper right hand side of the images in this figure was flame from the ambient UCC exit that moved over top of the core flow section, not inside the core flow. The top image in Figure 95 shows the same flame angle, approximately 60 degrees, as the unprocessed HSV image in Figure 94. The middle image of Figure 95 indicates the time-averaged flame angle was also around 60 degrees. Examining the bottom image of Figure 95 indicated that the flame angle fluctuated between about 55 and 65 degrees, or +/- 5 degrees from the average, based on the highest standard deviation values in the flame angle measurement region. Quantification of this angle was insightful about the flow geometry occurring at the UCC interface.

Similar to the PIV data, the HSV data was also used to measure the flowfield unsteadiness. Figure 96 shows the variation of pixel intensity over time for a typical case in the core flow, downstream of the UCC interface (x=45 mm, z=14 mm). This figure illustrates that there was significant temporal variation of the pixel intensity due to the unsteady flame migration from the UCC into the core flow. Figure 97 shows

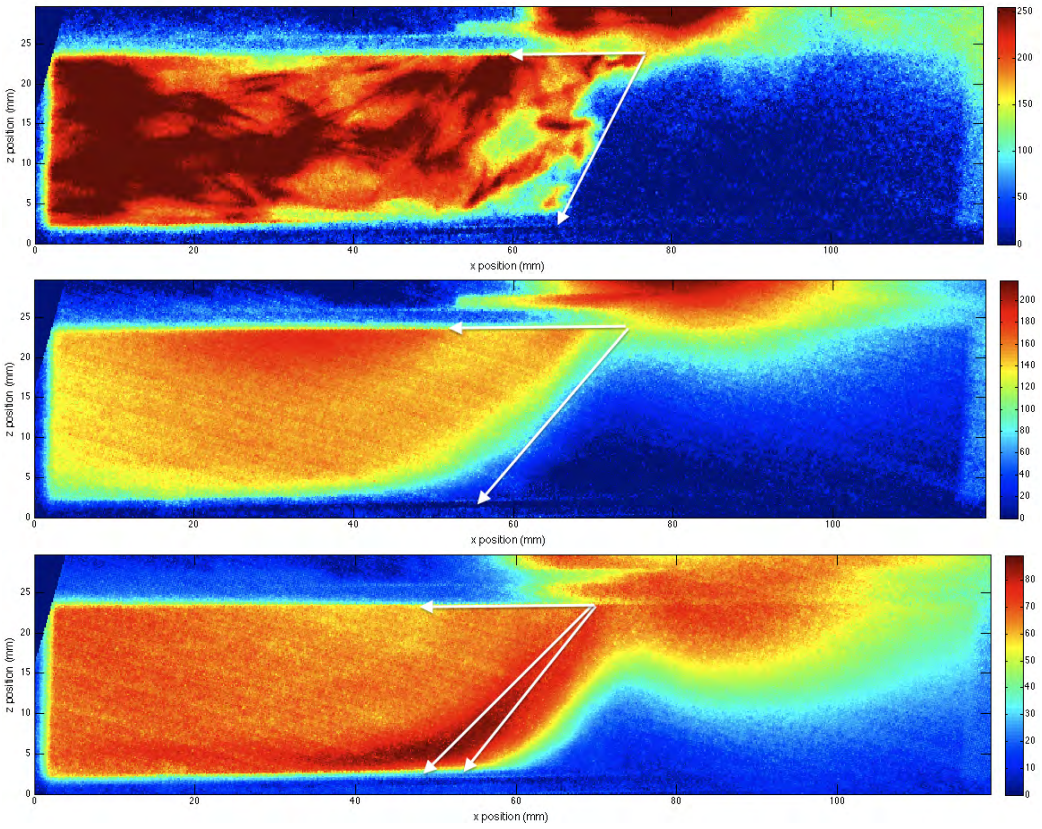

Figure 95. MATLAB processing for flame angle, the angle between the horizontal core flow arrow and the flame angle arrow, of an instantaneous HSV image (top), time-average of 1000 HSV images (middle), and standard deviation of 1000 HSV images (bottom)

the same data as Figure 96 but enlarged to show detail. The PSD was computed from the time-dependent total pixel intensity data similar to Equation 19, but without the time-averaged component removed. The PSD from the point-wise HSV data, shown in Figures 98 and 99, determined the flame migration unsteadiness was dominated by 130 and 260 Hz modes, similar to the results of the PIV analysis.

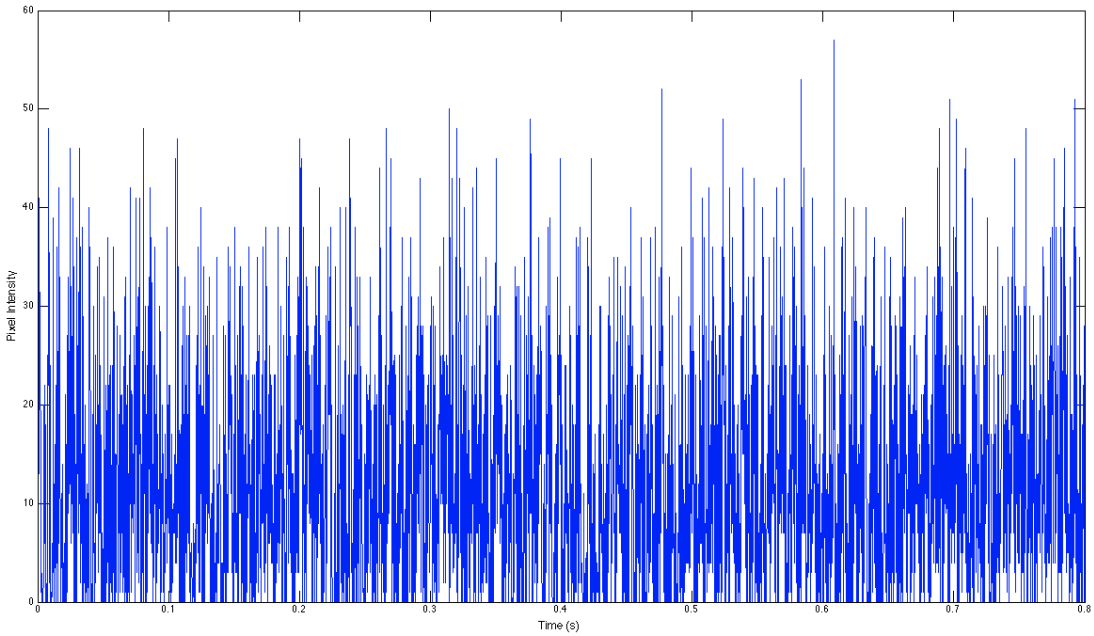

Figure 96. Typical HSV pixel intensity vs. time downstream of UCC interface (x=45 mm, z=14 mm)

In addition to computing the PSD at a single location, a 2D FFT was used on a synthesized 2D Time Image with one dimension of spatial information and the second image of temporal information. This was done in order to capture the global frequencies that may vary significantly from point to point depending on the chosen location. Figure 100 illustrates the process where a single line from each HSV image was taken to form a new Time Image, time vs. span-wise (z) position, containing both spatial and temporal information as used by Cross et al. [18]. A sample Time Image from this process is shown in Figure 101. In this figure, only the lines from 500 images are shown for illustration, but 4000 images were used in the analysis. The

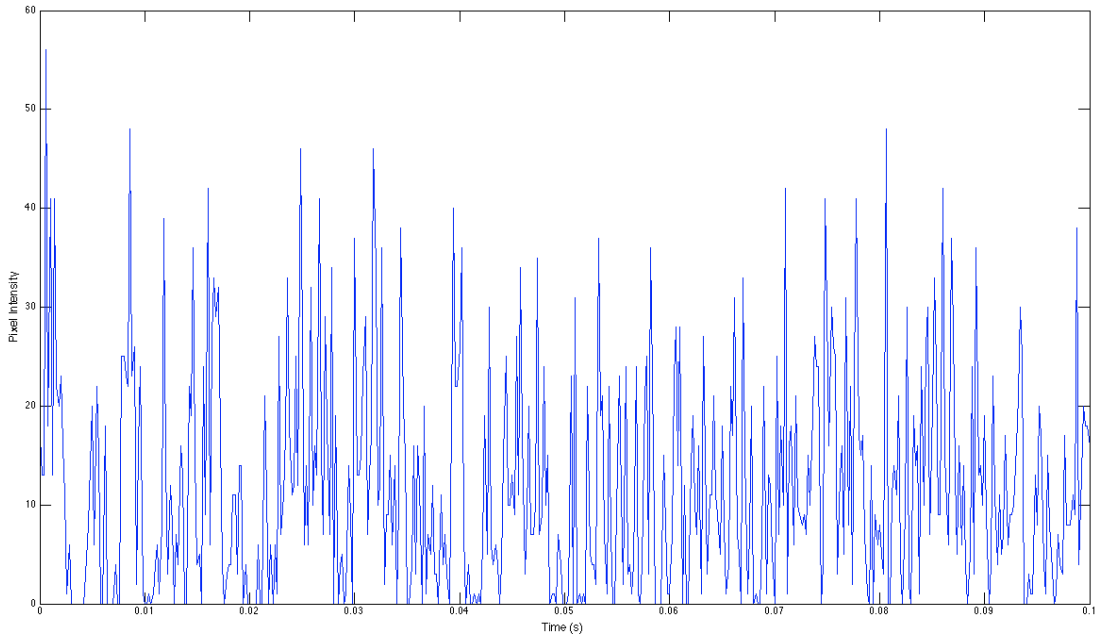

Figure 97. Typical HSV pixel intensity vs. time downstream of UCC interface (x=45 mm, z=14 mm), enlarged to show detail

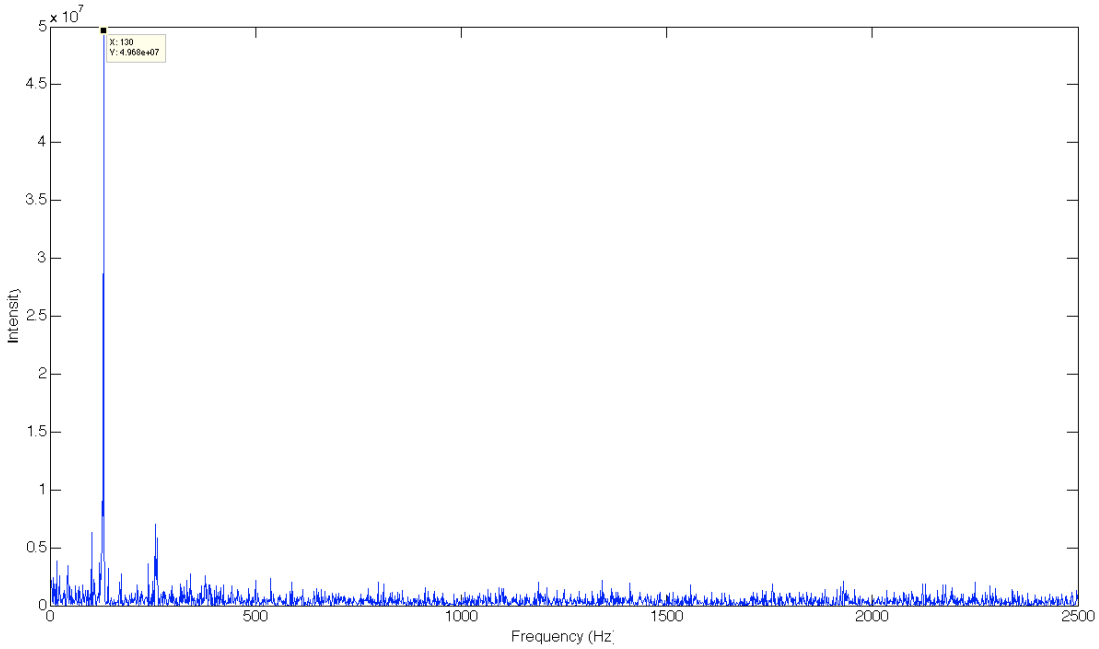

Figure 98. Typical HSV PSD in the core flow, downstream of UCC interface (x=45 mm, z=14 mm)

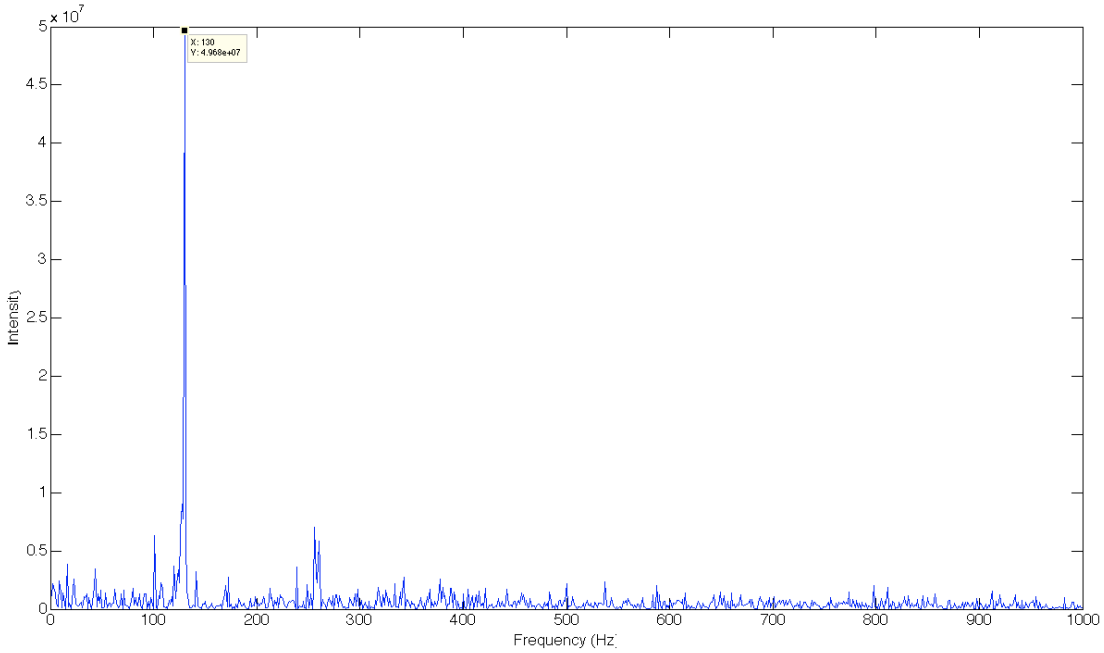

Figure 99. Typical HSV PSD in the core flow, downstream of UCC interface (x-45 mm, z=14 mm), enlarged to show detail

reason only 4000 images of the 5000 collected images were used was due to the total image limit of 4471 for a multi-page TIFF file and as such 4000 images were used as a round number. Using 4000 images limits the discernible frequencies to being between 1.25 and 2,500 Hz due to the sampling frequency and total sampling time.

Once the Time Image was created, a 2D FFT was computed of the image which results in a Frequency Image (frequency vs. span-wise position) as illustrated in Figure 102 from Cross et al. [18]. In order to asses the global frequency content, the Frequency Image was then averaged in the spatial direction which resulted in Figure 103. This figure shows that there were two dominant frequencies less than 1,000 Hz. In order to show these frequencies more clearly, Figure 104 shows the same data isolating the frequencies less than 1,000 Hz. In this figure a dominant shedding frequency around 130 Hz was observed with a secondary peak around 260 Hz, which was the same result as the point-wise PSD analysis of both the HSV and PIV data. It is likely that these two peaks were manifestations of the same phenomenon at a

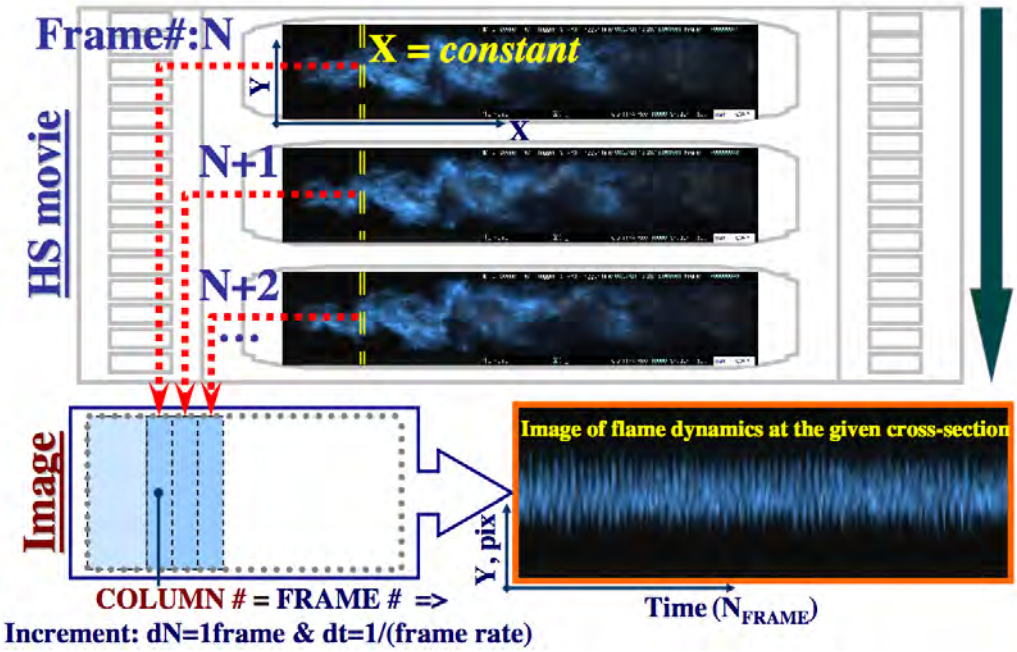

Figure 100. Illustration of the creation process for the 2D time images from Cross [18]

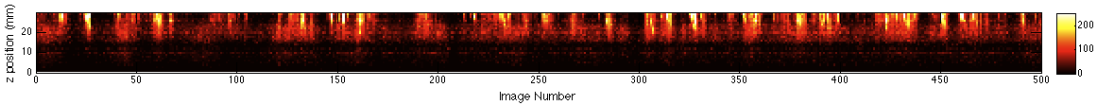

Figure 101. Typical 2D time image, enlarged to show the first 500 images

primary and secondary harmonic frequency.

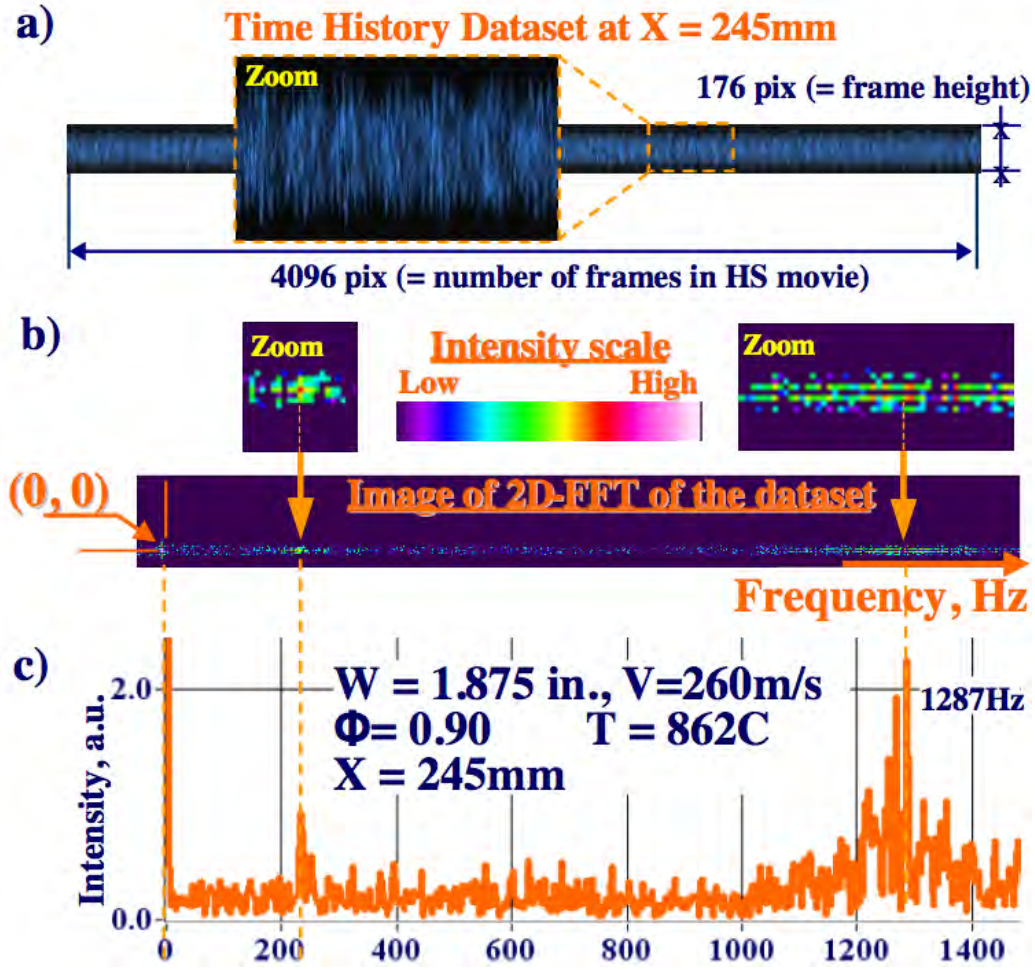

Figure 102. Illustration of the 2D FFT process for HSV data from Cross [18]

3.8.2 SNR Threshold.

While a SNR threshold was not used for processing the HSV data, future processing would benefit from established SNR thresholds to eliminate insufficient signal events from the time-averaging, like those established for the PLIF data. Figure 105 shows contours of an instantaneous HSV image (top) and the time-average of 4000 images (bottom). This figure shows that the 40 pixel intensity contour differentiated between regions with flame and regions without flame present for both images. Also

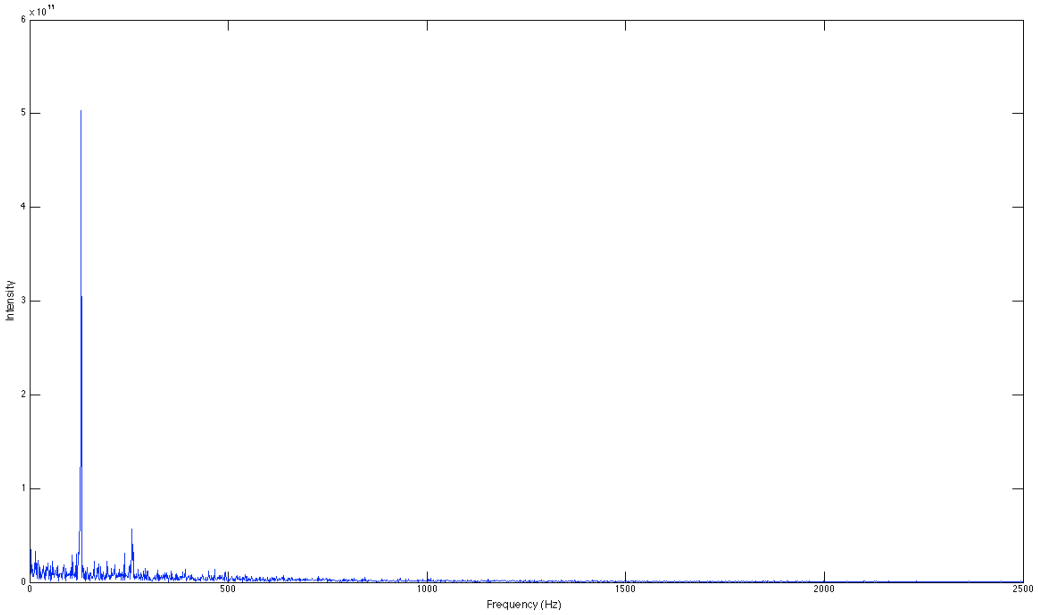

Figure 103. Typical HSV frequency spectrum in the core flow, downstream of UCC interface

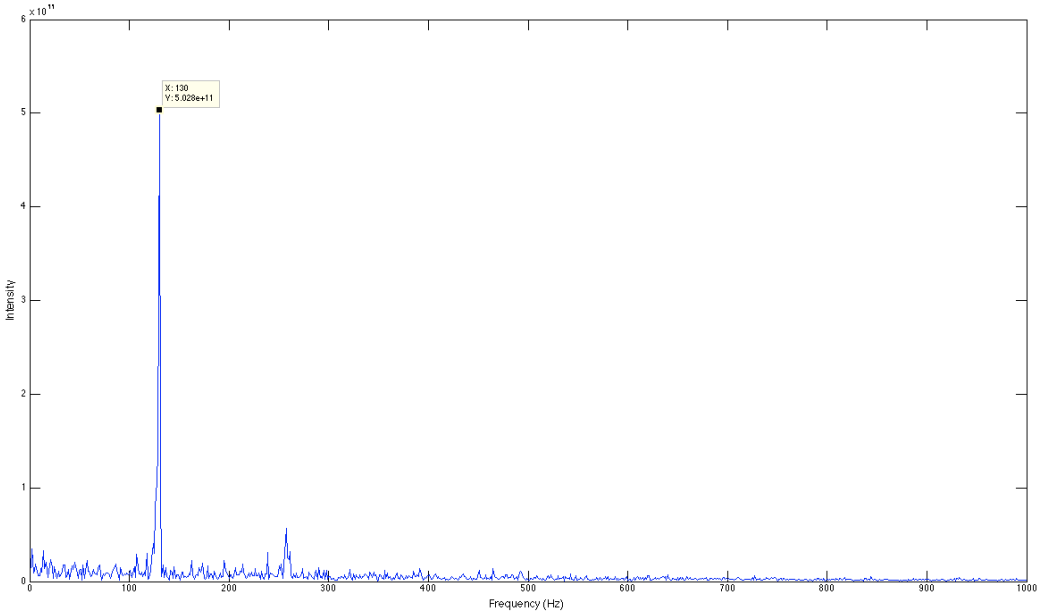

Figure 104. Typical HSV frequency spectrum in the core flow, downstream of UCC interface, enlarged to show frequencies up to 1,000 Hz

in Figure 105 was the flame from the ambient UCC exit which moved over top of the core flow section, not inside the core flow, and this flame was imaged in the upper right hand side of the images in the figure. Figure 106 shows the spatial distribution of the number of sufficient signal events out of the total 4000 events. The average number of sufficient signal events was about 1200 while the maximum was about 3900 events out of the total 4000 events. This showed that on average the signal was present about 30% of the time, which was inline with the PLIF measurements that showed 40% for the original threshold and 10% for the higher threshold.

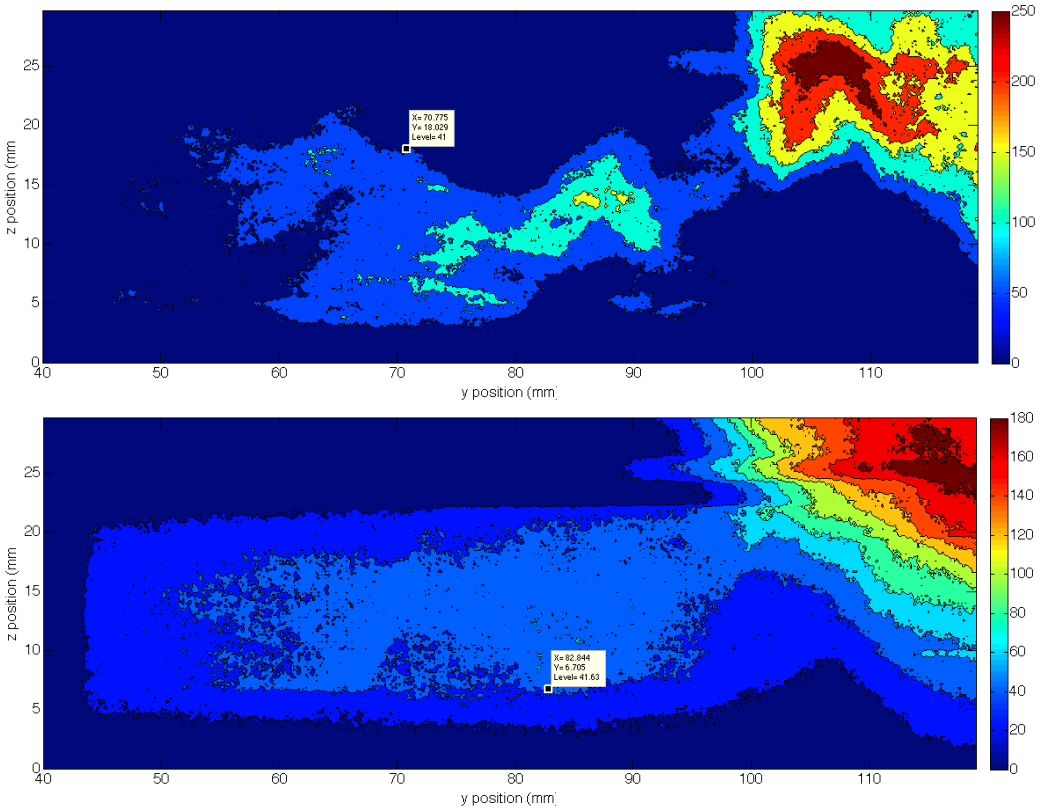

Figure 105. Contour plot of instantaneous HSV image (top) and time-average of 4000 images (bottom)

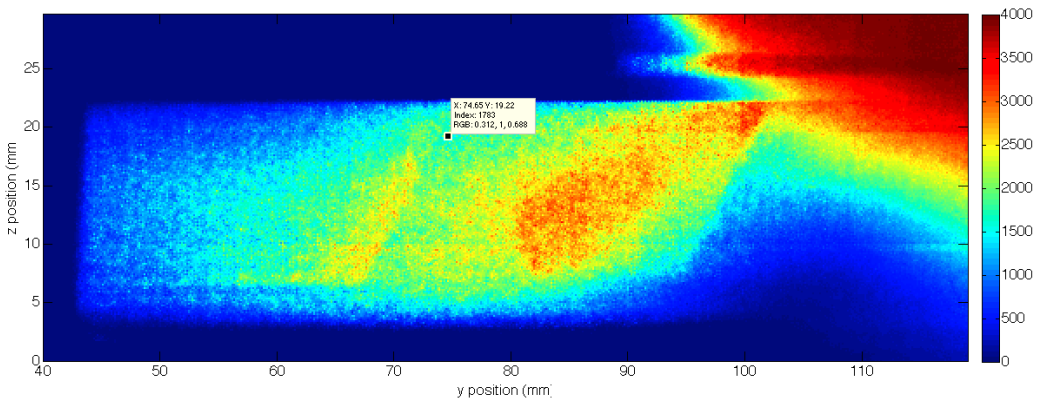

Figure 106. Spatial distribution of the number of sufficient HSV signal events out of the total 4000 events

3.9 Measurement Synthesis

While each of the aforementioned diagnostics contributes vital information about the physics within the UCC and the interaction with the core flow, no single measurement provides the complete picture. This made the synthesis of the different measurements even more important. However, each measurement must be acquired independently and each has its own acquisition frequency (10 Hz for PLIF, 30 kHz for PIV, 5 kHz for HSV). This necessitates a comparison based on the time-averaged values of each measurement since, as shown qualitatively by HSV and quantitatively in the PLIF and PIV repeatability, there was significant temporal variation. While an in-depth analysis of the time-dependent nature could be conducted on any single measurement, as recommended for future work in Chapter 7, it was more important to gain a clear and consistent understanding of the time-averaged phenomena using multiple measurements to establish a solid framework for the basis of future research. Despite the inability to couple time-dependent data, temporal analysis was conducted on the PIV and HSV data and both were compared for global unsteadiness characterization.

In order to establish this framework and determine a quantitative characterization

of the centrifugally-loaded flame migration within the UCC three main issues were addressed. First, as shown by Drenth [9] a fundamental change in the flame shape at the ambient UCC exit was observed under centrifugal loading. The non-loaded flame had a V-shape and this shape change was studied under the v-shape flame investigation discussed in Chapter 4. Further, scaling the UCC as a viable combustor technology for the AFRL VAATE program necessitated that scaling issues with the radial vane height be investigated. Significant increased in the radial vane height were studied under the vane height investigation discussed in Chapter 5. Also, the fundamental function of the UCC relies on the relationship of the centrifugal load and the flame migration from the UCC into the core flow. This relationship was studied in the g-load investigation discussed in Chapter 6. These three investigations as a whole address basic issues concerning the past and future of the UCC concept, the synthesis of the results from each investigation into the larger picture of the UCC flame migration is then discussed in Chapter 7.

IV. V-Shaped Flame Investigation

The first objective sought to understand why the v-shaped flame from the ambient exit of the straight UCC section that was not exhibited with the curved section. The corresponding hypothesis was that while the v-shape was not present with the curved section at Drenth's test conditions, the shape would return and become more defined as the g-load was decreased. Drenth discovered this phenomenon while testing a flow condition that corresponded to about 40 g's with the curved UCC section, shown previously in Figured 13, and presumed that the flow structure changed due to the curvature addition resulting in disappearance of the v-shape [9]. This presumption was inline with the physics suggested by Lewis in the creation of a stream-wise propagating vortex creating the bubble velocity [13]. However, Drenth also noted a factor of 2.4 decrease in the exit area from the straight to the curved UCC section as another potential cause of the change in flame shape [9]. The first step of the investigation was to adjust the exit area of the curved UCC section to match that of the straight section, in order to determine the underlying cause of the change in flame shape. Then, Drenth's test conditions were repeated to determine if a relationship between the flame shape and curvature existed or if the change was the result of the change in exit area. Once the cause of the shape change was determined, several test conditions were analyzed to understand the structure of the v-shape itself. The flame shape was measured extensively using OH-PLIF with volume-integrated chemiluminescence images taken for select cases.

4.1 Test Setup

The test matrix was specifically designed to investigate the existence of the v-shaped flame. Using Drenth's conditions as a starting point [9], Table 3 was created

to investigate the origin behind the v-shape. Hydrogen fuel was used with the UCC equivalence ratio, ϕ, held constant at 1.0 for the V Cases, since that was the fuel used by Drenth [9], and Propane was used with a $\phi = 2.0$ for the global Test Cases 13-15. For Test Cases 13-15, the fuel and air were split with 1/3 of the total UCC flow of each (fuel and air) being injected along the outer radius of the UCC section and the other 2/3 entering into the seeder box, shown in Figure 29, similarly to the V Cases. This fuel and air distribution was chosen to try to make the sectional UCC model more representative of the annular model, which would have even higher quantities of fuel and air entering upstream. The parameters of interest were determined to be the UCC flow velocity, the core flow velocity, and the positions of the fuel injectors, in addition to changing between the straight and curved UCC sections (in other words - the g-load itself).

Table 3. V-shaped flame test matrix using both straight (S) and curved (C) UCC sections with $\phi = 2.0$, G=39 (curved only) & 0 (straight only), and the fuel was hydrogen

Test Case	UCC Section	UCC Air Mass Flow (kg/min)	Core Air Mass Flow (kg/min)	MFR	Seeder Box Fuel Flow (SLPM)	Injector 1 Fuel Flow (SLPM)	Injector 2 Fuel Flow (SLPM)
V1	**S/C**	**0.1**	**1.0**	**0.0167**	**0**	**15**	**15**
V2	S/C	0.1	1.0	0.0167	20	5	5
V3	S/C	0.1	1.5	0.011	20	5	5
V4	S/C	0.1	0.5	0.033	20	5	5
V5	S/C	0.1	0.167	0.1	20	5	5
V6	S/C	0.1	0.167	0.1	0	15	15
V7	S/C	0.1	0.167	0.1	30	0	0
V8	S	0.1	0.167	0.1	0	30	0
V9	S	0.1	0.167	0.1	0	0	30
V10	S	0.1	0	∞	0	15	15

The curved section exit area was changed via addition of ramps to the attachment point of the UCC section to the core flow section. The ramps were designed to increase the exit area from the origin 243 mm^2 to 544 mm^2, equivalent to the area of the straight section, and to orient the UCC flow in the curved section to be tangent

to the core flow at the interface, as was the case in the full annular design. Single-line OH-PLIF was used to determine the flame shape using a 1 second time average (20 images) at three vertical planes of the UCC's ambient exit as shown in Figure 107. Multiple planes were chosen to determine if spatial variation existed and could be used to understand the structure of the v-shape. This figure also illustrates the viewpoint of the camera used for OH-PLIF imaging. For convention, the right-hand-side (RHS) of the UCC, as viewed from the PLIF camera, was referred to as the windward side and the left-hand-side (LHS) of the UCC, as viewed from the PLIF camera, was referred to as the leeward side.

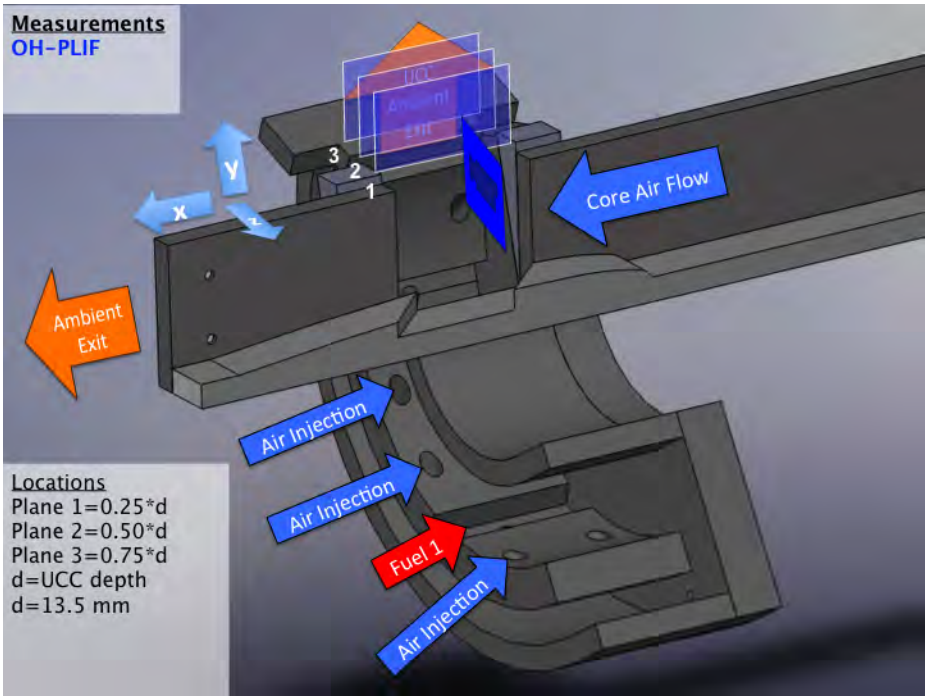

Figure 107. Illustration of the 3 data planes used for the v-flame investigation

4.2 Results

Identical conditions (Case V1 in Table 3) to Drenth's data were tested [9] using the curved UCC section. Figure 108 shows the flame shape of both the straight and curved sections of the baseline case V1 at Plane 2. It is clearly evident from this

figure that the v-shape is now present with the curved section following the exit area fix. However, the v-shape is less pronounced at this plane than at the same plane for the straight section. Investigating the shape at all three planes, as shown in Figure 109, reveals noticeable spatial variation in the flame shape that was not seen with the straight section. However, taking a visual flame image from the same camera viewpoint as the PLIF camera (shown in Figure 107), the left side of Figure 110 clearly confirms the presence of the v-shape with the parallel plane image.

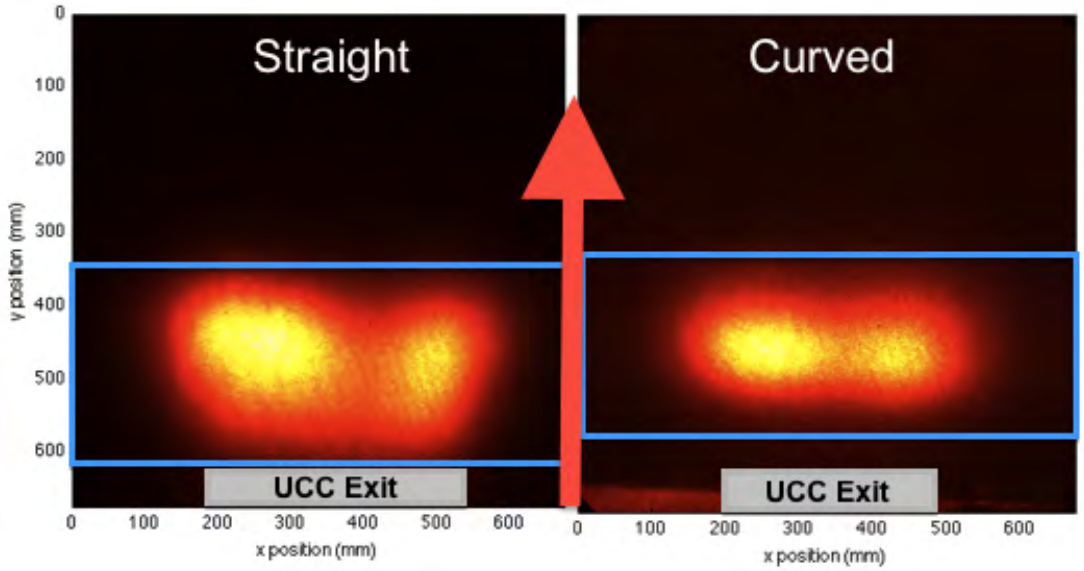

Figure 108. Flame location data for Case V1 with the straight (left) and curved (right) UCC sections at Plane 2. The red arrow indicates thef low direction, the blue rectangle illustrates the placement and height of the laser sheet, and the grey rectangle indicates the location of the ambient UCC exit.

Examining the perpendicular plane image taken from the upstream core flow direction (top right of Figure 107), the right side of Figure 110 provides insight into the appearance of spatial variation of the flame shape with the curved section in Figure 109. As shown in Figure 110, the high spatial variation with the curved section was the result of the inclination of the flame to the outward radial direction. Due to the centrifugal loading with the curved section that was intentionally not present in the straight section, an additional force acted on the flame within the UCC section

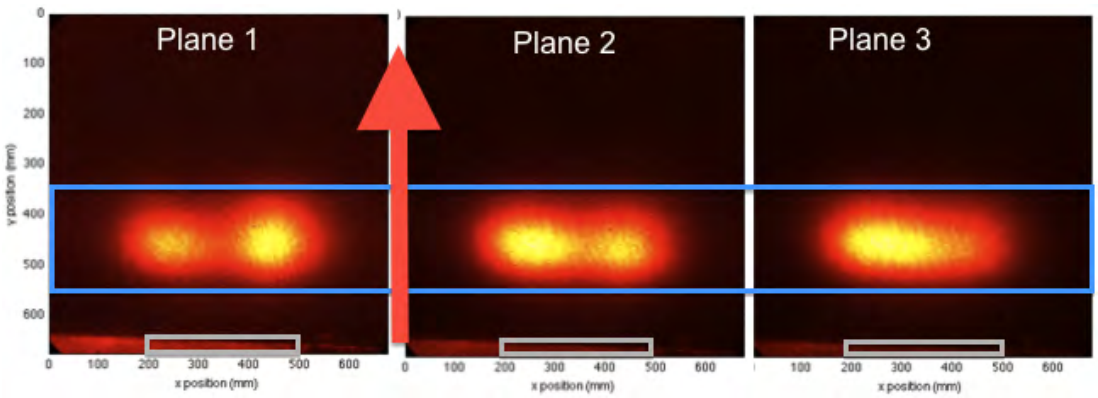

Figure 109. Flame location data for Case V1 with the curved UCC section at Plane 1 (left), 2 (middle), and 3 (right). Note the red arrow indicating the flow direction, the blue rectangles indicating the height of the laser sheet, and the grey rectangles indicating the location of the ambient UCC exit.

in the outward radial direction. Upon reaching the ambient UCC exit the OD wall was no longer present to contain the flame inside the OD and the outward radial momentum was then dissipated in the ambient mixing process. This was manifested in the approximately 20 degree inclination angle of the flame to the outward from the tangential direction. Zelina et al. reported a 23-27 degree inclination angle from the tangential direction was present in the UCC flow based on numerical studies of the full annular UCC [7]. In conclusion, once the exit area of the curved section was increased to the same order as the straight section, both UCC sections displayed the v-shape at identical conditions demonstrating the shape was independent of the addition or removal of the g-load, even though the orientation of the shape changed.

The presence of the v-shape with both UCC sections essentially negates the original objective and hypothesis but raised the issue of what actually caused the v-shape. It was then hypothesized that the shear caused by the interface with the core flow caused the v-shape. This hypothesis was tested using Cases V1, V6, and V10 where the core flow was decreased by a factor of two from Case V1 to V4 and the core flow was removed entirely in Case V10. Figure 111 shows visual flame images for Case V1 (left), V6 (middle), and V10 (right). Comparing Cases V1 and V6 shows that

Figure 110. Visual flame images for Case V1 with the curved UCC section from Plane 1-3, parallel, viewpoint (left) and perpendicular (right)

v-shape was present at the reduced core flow. However, comparing Cases V1 and V6 with V10 shows that the v-shape was eliminated when the core flow was eliminated and the hypothesis was proved to be correct.

Figure 111. Visual flame images with the curved UCC section (averaged over Planes 1-3) of Cases V1 (left), V6 (middle), and V10 (right) with MFR=0.0167, 0.1, ∞, respectively

With the cause of the v-shape determined, the contribution of each fuel injector on the combined flame shape was investigated to gain insight into the shape's composition. In order to do this, injectors 1 and 2 (see Figure 107) were isolated individually for cases V8 and V9, respectively. Figure 112 shows the flame shape for each injector. These cases indicate the propensity for the flame to move to the windward (right) side with injector 2 producing more OH at this location due to the shorter residence length. This figure also showed that the fuel injector flow situation within the UCC was similar to a jet in cross-flow. Also shown in Figure 112 was that the fuel injected

upstream of the core flow interface, from injector 1, resulted in creation of a weak v-shape resultant from interaction at the interface with the core flow which injector 2 was not subject to. Examining the combined shape with both injectors Figure 113 shows the combined shape was instead weighted to the leeward (left) side. With both injectors vying for the windward side, injector 1 had preference due to being farther upstream in the flow path forcing injector 2 to fill the leeward side. This was confirmed by the higher intensity on the leeward side due to the shorter resident length of injector 2.

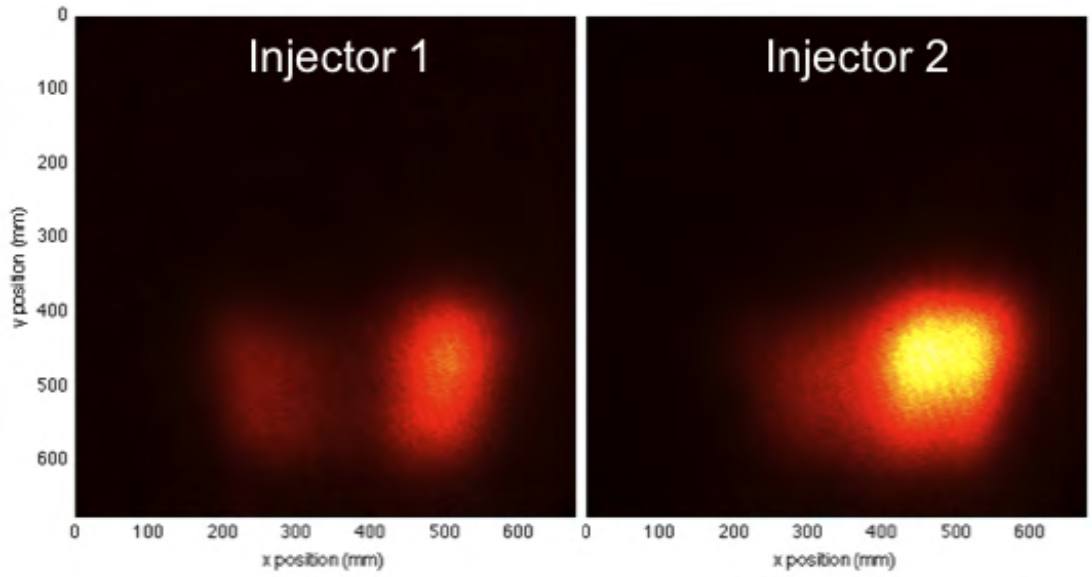

Figure 112. Flame location data with the straight UCC section at Plane 2 for Injector 1, Case V8, (left), and Injector 2, Case V9, (right)

On the inward radial direction, the distribution was bimodal and heavily weighted to the windward side. However, moving outward in the radial direction, from Plane 1 towards Plane 3, the distribution was bimodal with a more even distribution between the modes at Plane 2 while Plane 3 was bimodal with weighting to the leeward side. The shear caused by the increasing core flow was assumed to cause a recirculation zone on the upstream side of the UCC channel, similar to the classical backward facing step. As the shear strength increases, the migration of flow from the UCC into

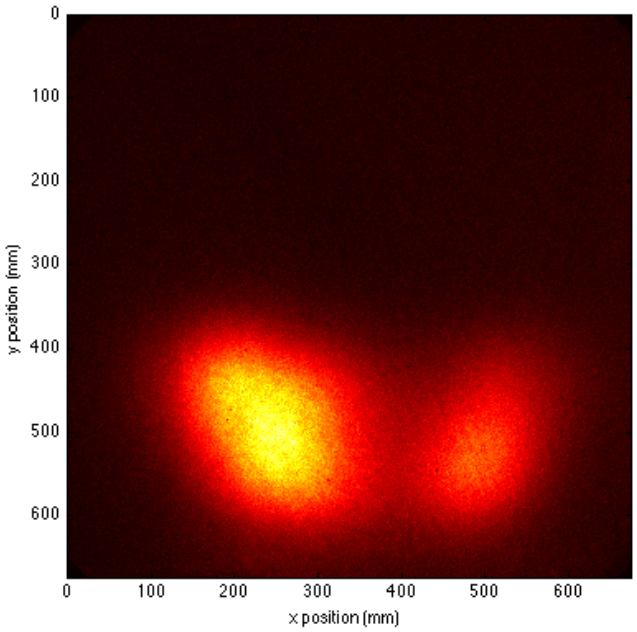

Figure 113. Flame location data for Case V6 with the straight UCC section at Plane 2

the core flow increases, due to the increased pressure gradient, resulting in more of the mass to move into the core flow. Due to the injection order, the inward radial mass must be the mass from injector 1. Therefore, injector 1 must be the major component of the windward side of the flame shape or the right-hand-side of the V, whereas the flow from injector 2 (see Figure 107) enters last and must fill the leeward side. An illustration of these flow paths is shown in Figure 114. This figure also attempts to illustrate the injection order with injector 1 followed by injector 2 which resultantly occupy the inner radial wall towards outward radial wall in that order.

An additional factor that may have contributed to the formation of the v-shape was the recirculation regions created behind the windows of the UCC sections. Illustrated in Figure 27 and discussed in Section 3.2, the existing window design created recirculation regions on the inside of the windows. The UCC section windows were not upgraded to the new bevel window design, shown in Figure 26, and could have also contributed to the formation of the v-shape, in addition to the direct link estab-

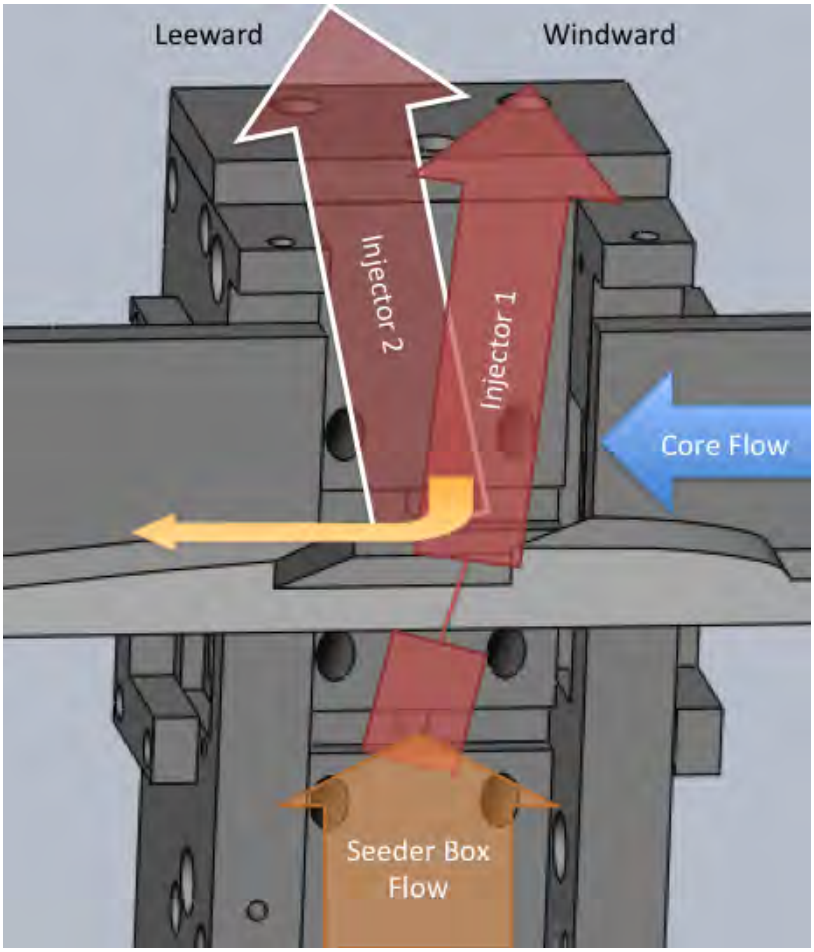

Figure 114. Illustration of the v-shape flame formation

lished with the core flow. Upgrading the UCC section windows to the new beveled design would determine if a connection does exist between the small recirculation regions behind the current windows and the v-shape.

V. Vane Height Investigation

The second research objective was to characterize the effect of radial vane height on the flame migration from the UCC into the core flow. A fighter-size UCC would require a radial vane with a height of 50-60 mm, but the previous UCC research by Drenth and Thomas [9; 29] used vanes in the 14 mm range used. Thus, two new vanes of height 28 mm and 56 mm were designed and built to test in conjunction with the 14 mm vane to characterize the effect of radial vane scaling. Only the curved UCC section was used as the intent was to isolate the vane height scaling effect. OH PLIF was used with HSV for measurement of temperature and flame geometry. The goal of this objective was to understand the parameters that impact how the flow exits the UCC and how the radial migration across the span of the radial vane can subsequently be controlled as the UCC concept is applied to larger engines which in turn use taller radial vanes.

5.1 Test Setup

In order to test the effect of radial vane scaling, two additional vanes were required. In order to simplify the scaling, the existing radial vane height of 14 mm was simply doubled and quadrupled to produce the 28 and 56 mm vane heights. As shown previously, Figure 24 compares the 14 mm, 28 mm, and 56 mm with a noticeable change in the angle of the radial vane cavity (RVC). This was intentional in order to create identical root and hub vane profiles to promote migration through the RVC across the entire span. Additional parts were also required to expand the vane passage to accommodate the increased vane height. Only the curved UCC section was used with each vane passage. The g-load was estimated using the air mass flow, exit area, and radius of curvature with an assumed density, per Equations 11 & 7.

Then, the main air mass flow was varied to change the UCC/core air mass flow and velocity ratio. Comparisons were made between matching the core mass flow rate and the core flow velocities. This alters the flow migration out of the combustion cavity. The cavity/main air mass flow ratios used were 0.1, 0.2, and 0.3 for each vane while additional cases were added for constant UCC/core velocity ratio. The equivalence ratio (ϕ) was held constant at $\phi = 2.0$ in the UCC section. Figure 115 shows pictorially the data collection locations of PLIF and high-speed video, which were taken at 10 Hz with the two Princeton cameras and at 2 kHz with a color Phantom V12.1 respectively. Table 4 shows the exact locations of each data collection location along the span of each vane.

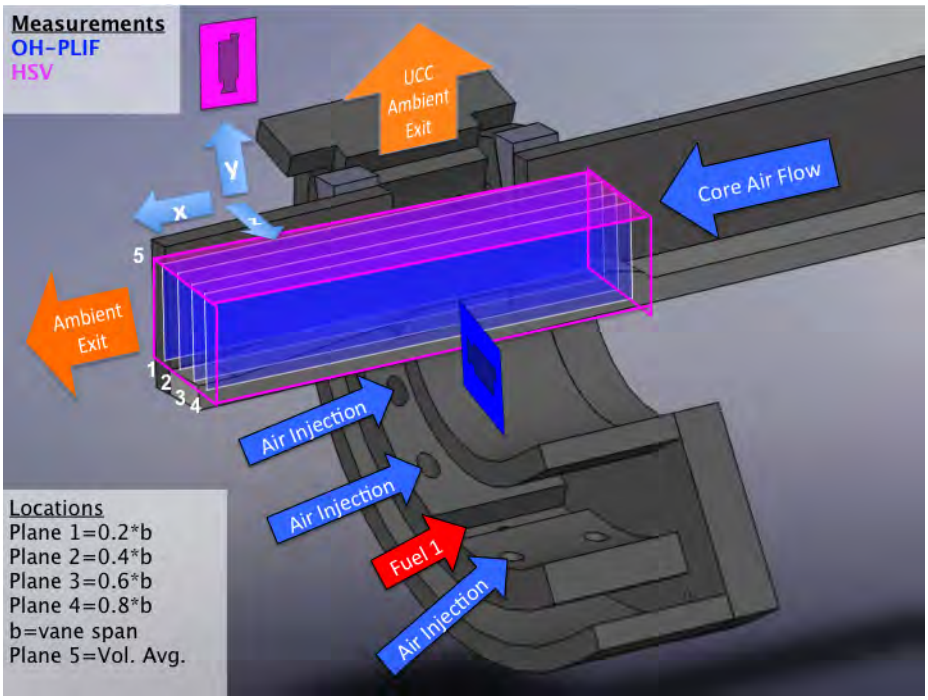

Figure 115. UCC data collection locations for the vane height investigation

From the global test matrix, Cases 4-28 were examined as well as three additional test cases with all cases using the curved UCC section. These cases are listed in Table 5 and provided identical comparison of constant core flow velocity across the increased vane heights. These cases were added due to the fact that matching the

Table 4. Data collection planes (distance from UCC interface)

Vane Height	Plane 1	Plane 2	Plane 3	Plane 4
14 mm	3 mm	6 mm	9 mm	
Frac. of Span	0.21	0.42	0.63	
28 mm	6 mm	12 mm	18 mm	24 mm
Frac. of Span	0.21	0.42	0.63	0.84
56 mm	6 mm	12 mm	24 mm	36 mm
Frac. of Span	0.105	0.21	0.42	0.63

MFR resulted in a decreased core flow velocity and subsequently decreased shear layer strength. Adding constant core flow velocity cases provided a means to address the impact of vane scaling independent of flow velocity changes.

Table 5. Additional test cases used for the vane height investigation

Case	**Vane**	**Section**	**g-load**	**MFR**	ϕ
31	2	curved	1000	0.05	2
33	3	curved	1000	0.05	2
34	3	curved	1000	0.025	2

All of the test cases examined for this investigation did not used the seeder box, shown in Figure 29 and discussed in Section 3.2. The total fuel was split between the two outer radial fuel injectors, only injector 1 is labeled in Figure 115 but both injectors are shown in Figure 21, and the total air flow entered into a plenum, which fed all of the air injection ports. Testing without the seeder box would have resulted in higher fuel and air inlet jet velocities, about 40 m/s for both fuel and air without the seeder box versus about 20 m/s with the seeder box, than the same test case run with the seeder box, which was used for the results in Chapter 4 and Chapter 6.

5.2 Results

This investigation clarified the effects of three main parameters on the radial migration of the hot gases as they exit the UCC flow path and enter the core flow path. These parameters were the g-load, the UCC/core air mass flow ratio, and the

radial vane height. The baseline condition that was established for this study was Test Case 14. This case represented nominal values of 28 mm for the radial vane height, 1000 for the g-load, and 0.2 for the UCC to core air mass flow ratio (MFR). Figure 116 shows five HSV images with 1 ms time steps. Immediately apparent in this figure is the high temporal variability of the quantity and intensity of the flame exiting the UCC. An example of the time-averaged PLIF data was shown previously in Figure 47 where the ratio of time-averaged PLIF signal for each fluorescence line was used to compute the time-averaged temperature. Also shown is the temporal consistency of the flame migration angle. This angle is illustrated in Figure 117 and was resultant from the shear layer at the UCC interface with the core flow. Also illustrated is the flame migration spanning almost the entirety of the 28 mm vane passage. Before an investigation into the temporal variability can be considered an understanding of the mean flow must be established. As a result, only the time-averaged results were considered in order to establish a baseline of the bulk flame migration properties.

The images in Figure 118 show the planar temperature computed from the time-averaged flamelet distributions for each span-wise location. As indicated in these figures, significantly high temperatures were measured across the entire span. This was the result of the high UCC/core velocity ratio created at this MFR allowing high mass flux from the UCC into the core flow, as evident by the fact that hot gases have easily traversed the 28 mm and have not been swept significantly downstream by the core flow (less than 10 mm of axial distance from the exit of the UCC). The high span-wise velocity was further confirmed by the visualization of the red hot ID endwalls that were observed during testing of MFRs greater than 0.2.

Also apparent was the thermal distribution's weighting towards the upper wall of the vane passage in Figure 118. The PLIF data indicated concentrations of OH decreased down the span consistent with a reduction in ϕ as the fuel-rich flamelets are

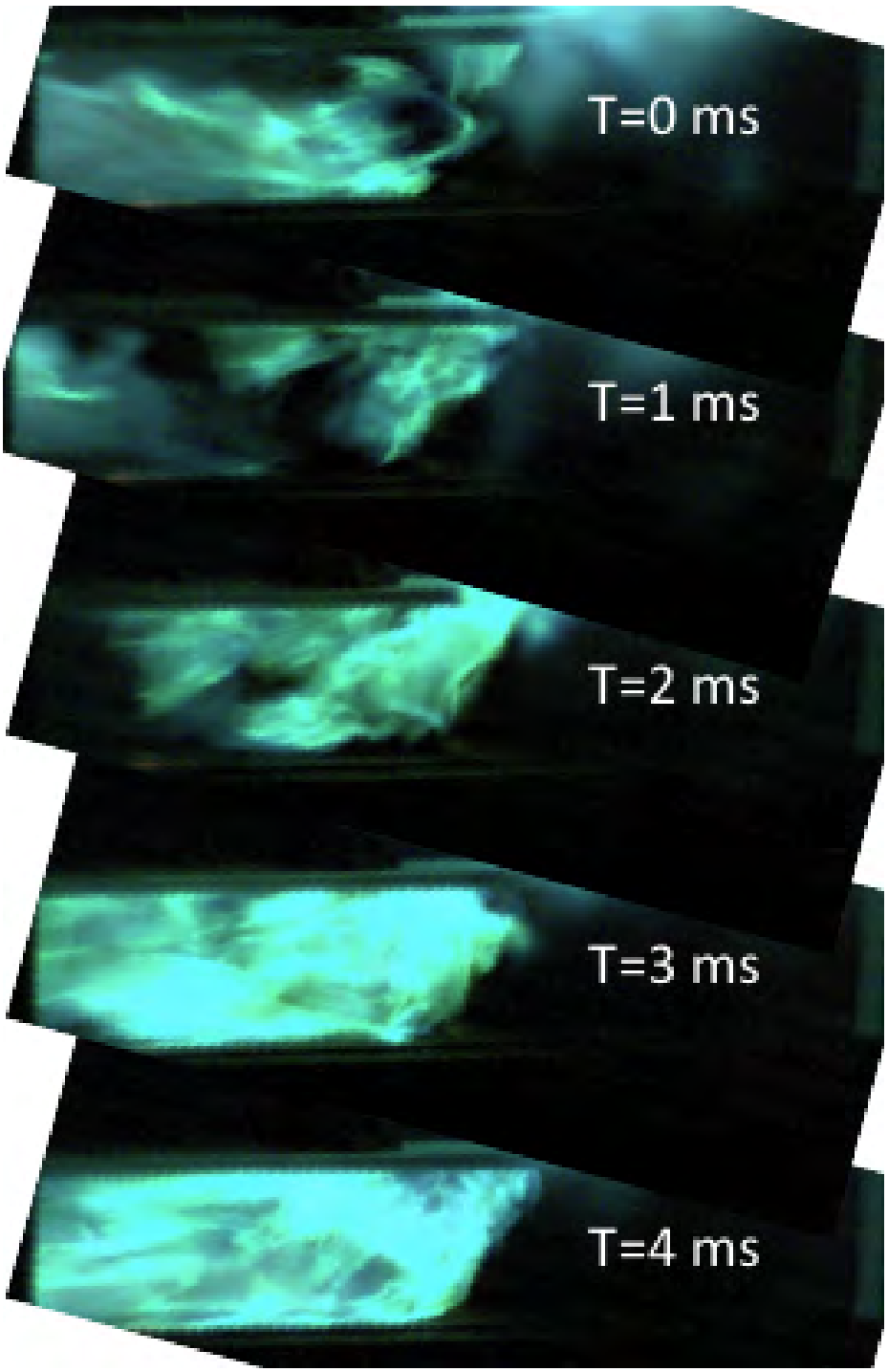

Figure 116. High-Speed Video (HSV) image sequence above radial vane of 28 mm vane, 1000g, MFR=0.2, $\phi = 2.0$ (Test Case 14)

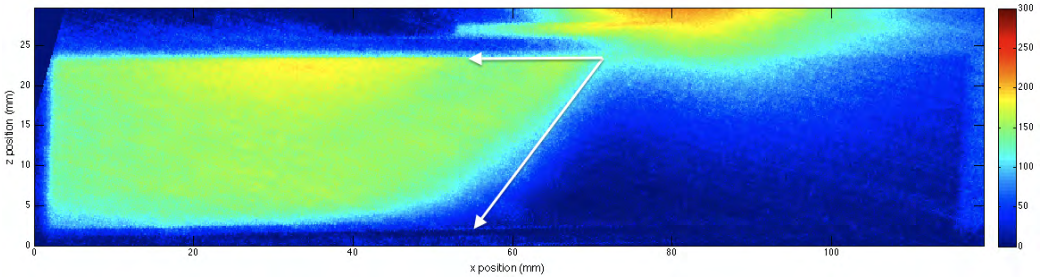

Figure 117. Time-averaged High-Speed Video (HSV) data from 1000 images above the radial vane of 28 mm vane, 1000g, MFR=0.2, $\phi = 2.0$ (Test Case 14)

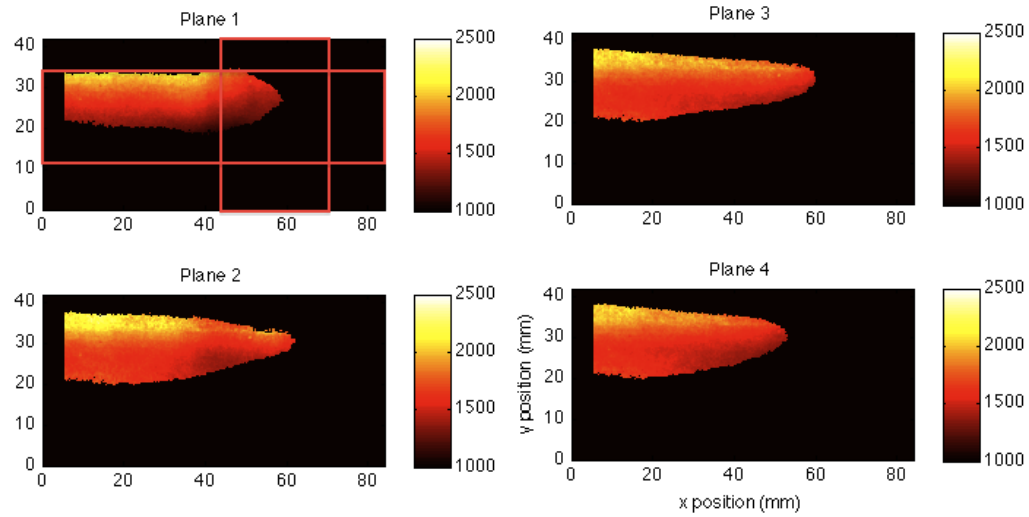

Figure 118. Temperature (K) for 28 mm vane, 1000g, MFR=0.2, $\phi = 2.0$ at 0.2, 0.4, 0.6, and 0.8 span from UCC interface (Test Case 14)

quenched by the pure air in the core flow. From this data, exit temperature profiles, taken at x=10mm, were plotted in Figure 119. These profiles represent the pitch-wise temperature distribution at the four radial spans. These profiles are limited by where OH existed in the flow, thus the sharp drop offs in temperature at the edge of the flame (Y = 20 and 35 mm). These figures confirm the relatively even thermal distribution span-wise but also indicate that the highest temperatures are towards the upper wall of the vane passage (farthest from the radial vane). This was the result of the flamelet vertical momentum (y direction) upon mixing with the core flow. This might be expected to cause high thermal loading on the pressure side of the adjacent vane. In other words, the high temperature flow followed what would be the pressure side of the adjacent vane (upper core flow wall) and the radial vane cavity would not be expected to play a significant role as the bulk of the hot gases move in the opposite direction (away from the vane cavity) towards what would be the pressure side of the adjacent vane. The upper wall of the core flow section used for this research was a flat wall rather than what would be the curved geometry of the adjacent radial vane.

Investigation of Test Cases 13, 14, & 26 revealed the impact of the g-load on the visual flame migration and on the temperature distribution. The higher g-loading was achieved by increasing the flow rate in the UCC cavity as indicated in Table 1 while keeping the MFR constant. As shown in Figure 120 increased flame migration was indicated with increased g-load, particularly for the 2000g case where the ID wall glowed from the increased heat transfer to it. Also in Figure 120, the injection angle appears unchanged as the g-load was increased. Investigating the injection angle further, Figure 121 quantifies the injection for all of the cases with a MFR of 0.2. For any given radial vane height the injection angle was relatively insensitive to the g-load of the UCC. However, apparent in this figure is that each vane height resulted in a different injection angle. Since the MFR was held constant for each of these cases, as

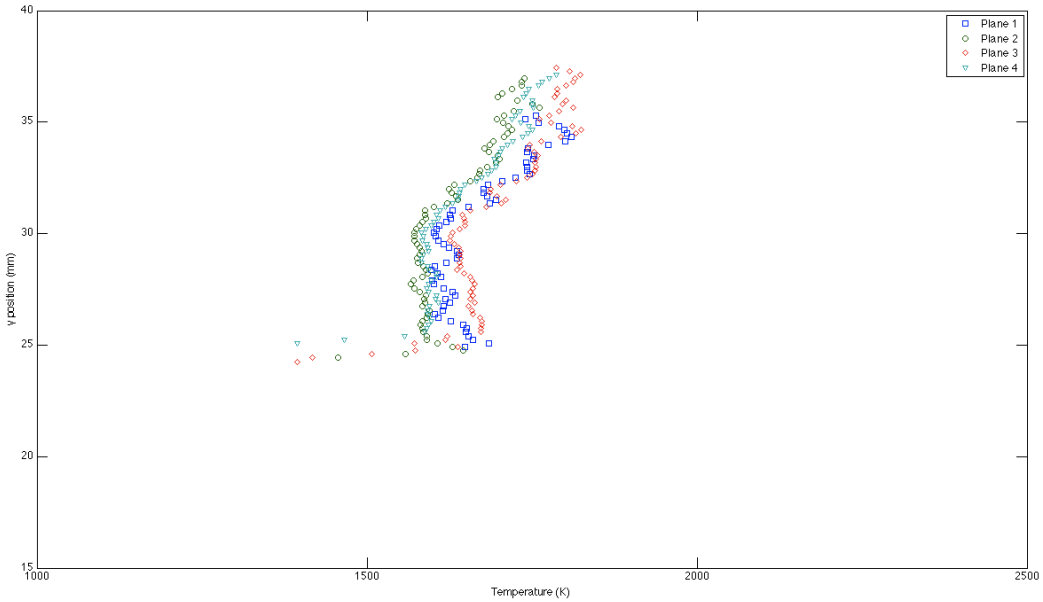

Figure 119. Exit temperature (K) vs. y position (mm) for 28 mm vane, 1000g, MFR=0.2, ϕ = 2.0 at 0.2, 0.4, 0.6, and 0.8 span from Cavity (Test Case 14) at x 8 mm

the vane height increased, the core flow velocity decreased and the UCC/core velocity ratio increased. The increased VR resulted in a deeper penetration of the UCC flow into the core flow and thus a higher injection angle. The images in Figure 120 also indicated an increased migration quantity as the g-load was increased. As shown in Figure 122, at 6 mm from the UCC interface the peak temperature increased with increased g-load as indicated first by the deeper penetration of the combustion gases in going from 500 to 1000 g's. Then as 2000 g's was achieved the intensity of the flame increases further and the flamelet distribution becomes very compacted due to the increased span-wise momentum at the interface of the UCC and core flows for the same MFR (and VR).

Varying the MFR was accomplished by altering the core flow rates at constant UCC flow rates to maintain the same g-load. Test Cases 31, 15, 14, and 16 changed the core air mass flow rate by a factor of 6, which represents the realistic flow rate range an Ultra Compact Combustor may experience in application. Figure 123 shows

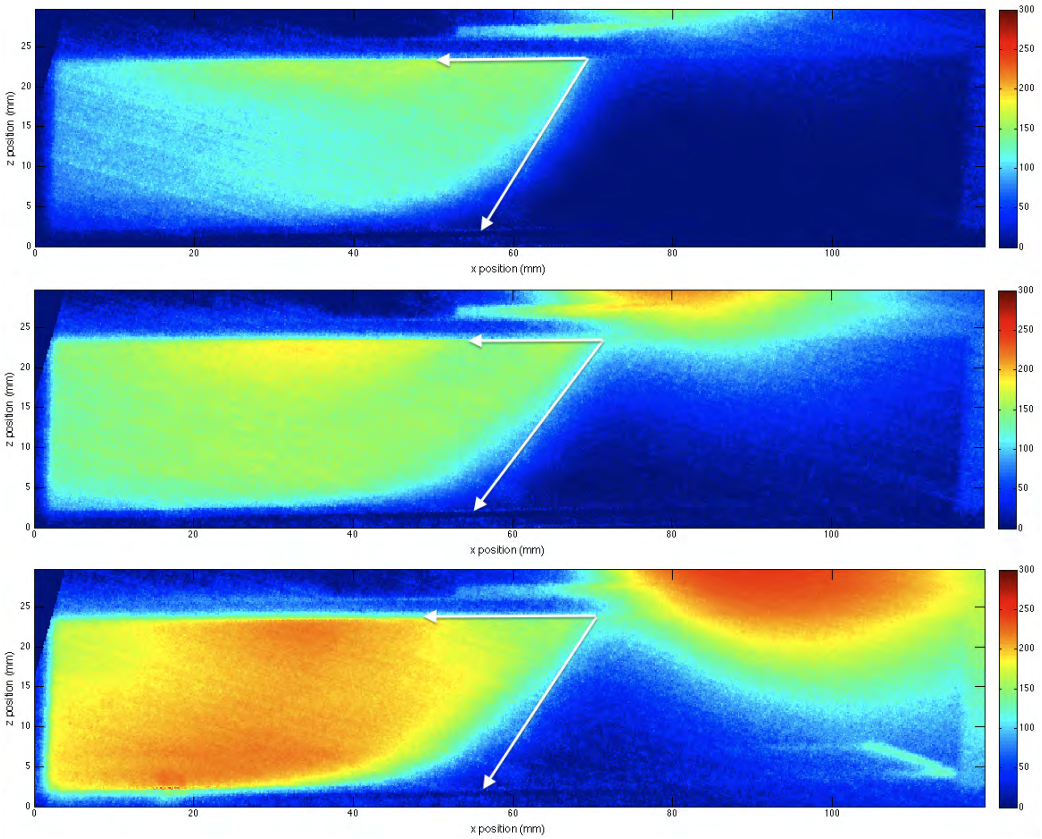

Figure 120. Time-averaged High-Speed Video (HSV) data from 1000 images above radial vane of 28 mm vane, MFR=0.2, $\phi = 2.0$ at 500g (top), 1000g (middle), and 2000g (bottom) (Test Cases 13,14,26)

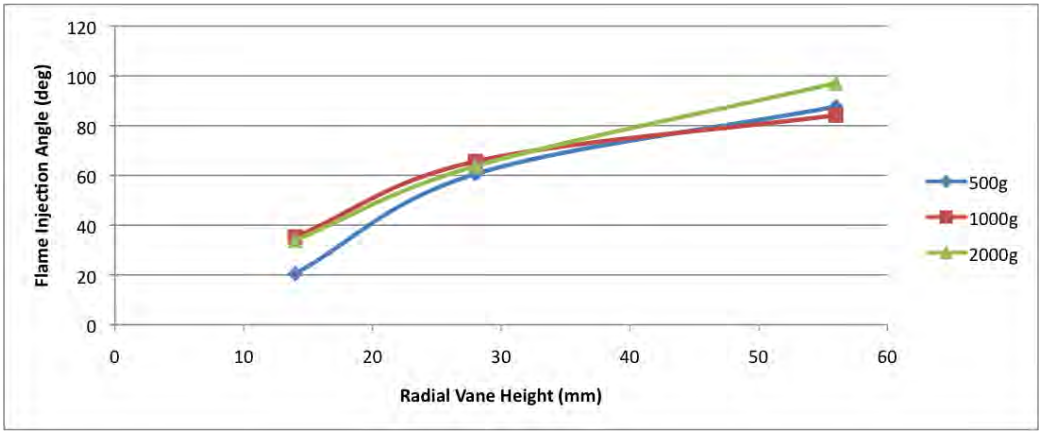

Figure 121. Flame injection angle from UCC interface for MFR=0.2, $\phi = 2.0$, at 500, 1000, and 2000g for each 14, 28, and 56 mm vanes

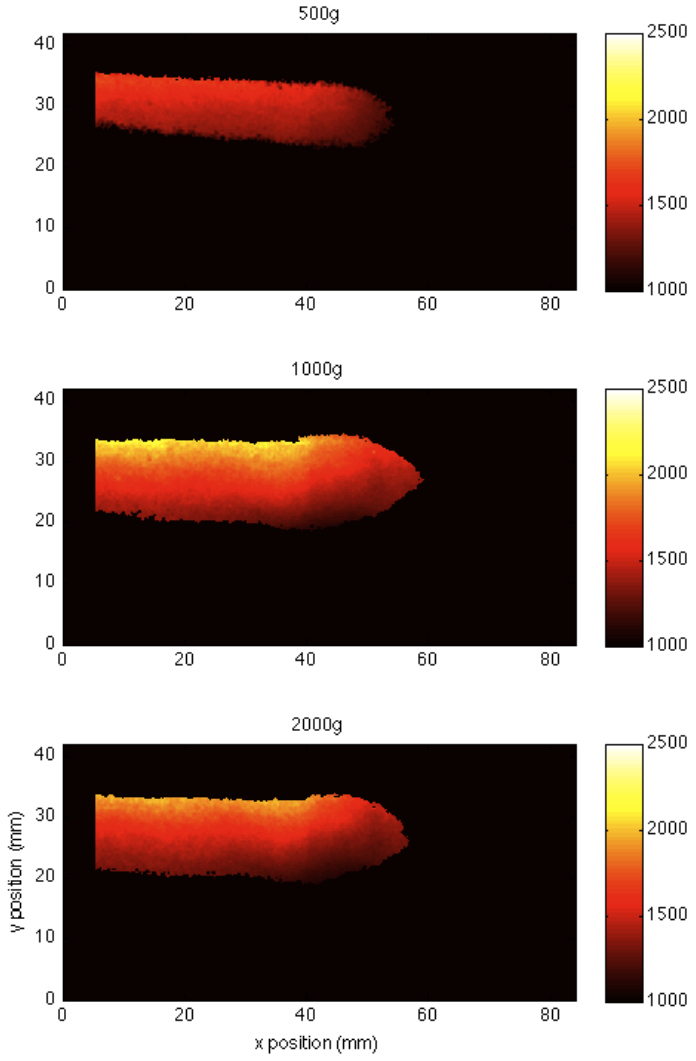

Figure 122. Temperature (K) for 28 mm vane, MFR=0.2, $\phi = 2.0$, 6 mm from UCC, at 500, 1000, and 2000 g's (Test Cases 13, 14, 26)

representative HSV images for each MFR variation case. This figure shows an increasing flame injection angle as the MFR was increased. The increased flame angle led to significantly deeper penetration of the migrating flame even to the point of causing significant heat transfer to the ID wall causing it to glow red and rolling back towards the OD wall. The MFR = 0.3 condition (Case 16) indicated migrating flame impacted the ID endwall and rolled back across the entire span of the core flow. The trajectory impacting the ID endwall and rolling back into the OD endwall is not an easy situation to control from a temperature distribution standpoint or from a vane cooling standpoint. Clearly the MFR was a key parameter to enabling the flow to exit the UCC and traverse across the span of the vane. By tailoring the MFR the exit temperature profile can be adjusted for a particular vane span. Over the MFR range tested (0.05 - 0.3) the value of 0.2 appeared to produce the most uniform flame distribution without the detrimental aspects of the 0.3 case. Figure 124 plots the x location of the flame entrance into the core flow over the range of MFRs. This figure shows that significant variation in the entrance location was observed, as would be expected for decreasing the MFR that the additional core momentum would force the flame migration from the UCC to enter further downstream and that a higher quenching would occur due to the increased air flow. Examining the top image of Figure 123 indicated that the flame did not traverse the entire 28 mm vane span. Verifying this indication with the PLIF data, see Figure 125, confirmed that no OH reached Planes 3 and 4 resulting in no reported temperature signal in the right images of the figure.

Similarly to the g-load variation cases, the variations in injection angle as a function of MFR is displayed in Figure 126. This figure highlights that the MFR is a key parameter for dictating the angle that the combustion products exit the UCC. This linked with the g-load effect (shown previously) will determine how far across

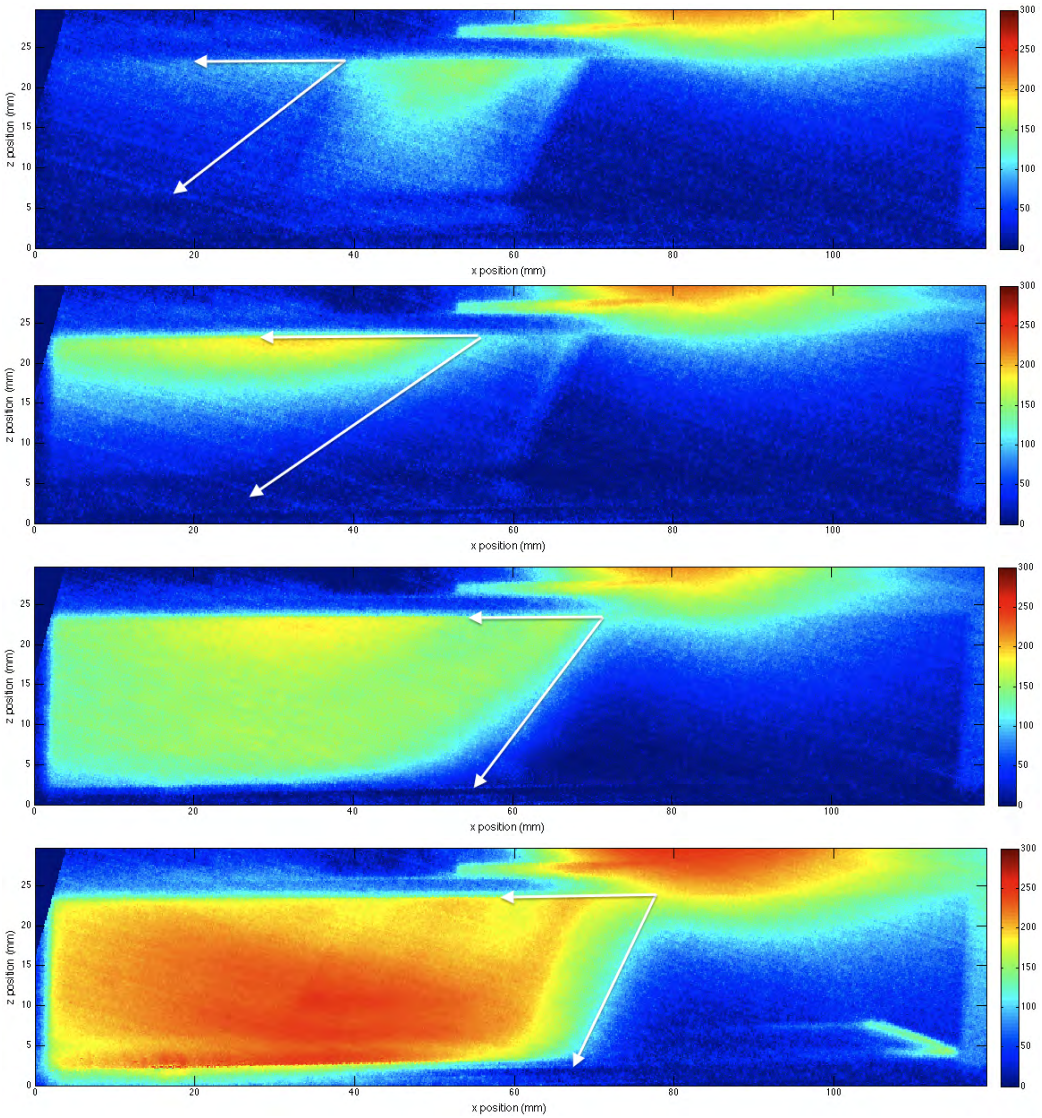

Figure 123. Time-averaged High-Speed Video (HSV) data from 1000 images above radial vane of 28 mm vane, 1000g, $\phi = 2.0$ at MFR=0.05 (top), 0.1 (middle top), 0.2 (middle bottom), and 0.3 (bottom) (Test Cases 31,15,14,16)

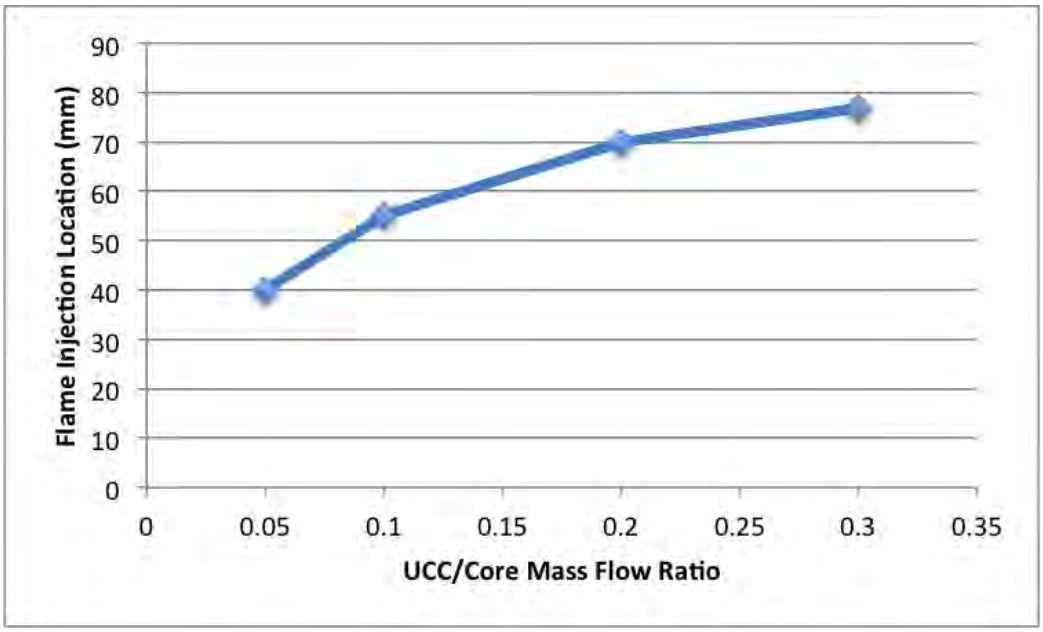

Figure 124. Plot of the flame injection location vs. UCC/Core MFR over the range of 0.05 to 0.3

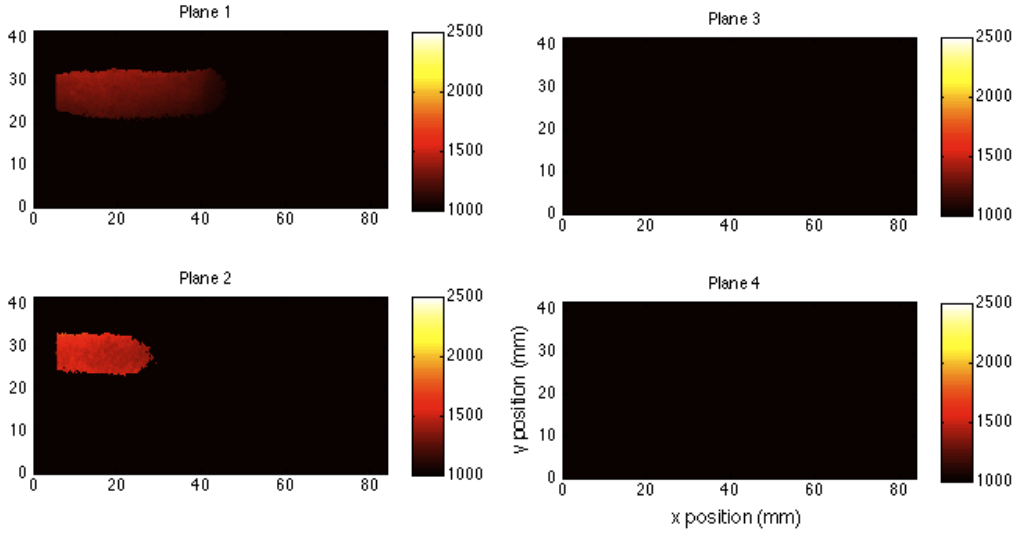

Figure 125. Temperature (K) for 28 mm vane, 1000g, MFR=0.05, $\phi = 2.0$ at 0.2, 0.4, 0.6, and 0.8 span from UCC interface (Test Case 31)

the span the hot gases will migrate. It's important to note that the angle varied significantly from the RVC angles of 44.5, 62.5, and 75.0 degrees for the 14, 28, and 56 mm vanes respectively. The independence of the flame angle from the RVC angle indicated significant bulk flame migration occurred outside of the RVC, which was intended to promote flame migration. The significant bulk migration paired with the PLIF data indicating higher temperatures on the upper wall, opposite the radial vane, indicates the vane orientation should be reversed such that the suction side is on the upper wall instead of the lower wall. Figure 127 quantifies the variation for Test Cases 5, 15, and 33 which maintain the core velocity at 13.1 m/s for the same vane heights. The flame injection angle was nearly constant at 40 and 60 degrees for the 6.55 m/s and 13.1m/s cases when the velocities (and velocity ratios) were maintained. The 26.2 m/s cases indicate a very loose, at best, relationship between vane height and flame injection angle. These results are expected as the shear was the same for the respective cases, but what was indicated from a migration standpoint was that the intermediate reacting species may not in bulk be able to traverse the entire span of the taller vanes. Maintaining the MFR constant resulted in a larger injection angle that was able to fill more of the span of the taller vanes. Plotting the same data as a function of VR reveals that the flame angle was nearly constant for cases with the same VR.

The images of Figure 129 revealed changes in the temperature distribution as the MFR was varied from 0.05 to 0.3. Similar results were determined for the other vane heights (not shown). Also, as the MFR was increased, so was the UCC/core velocity ratio which in turn resulted in increased radial momentum after equilibration of the flamelet with the core flow. Figure 130 provides the span-wise distribution of the spatially averaged temperatures within the flame region only for a set of images such as those in Figure 118. As evident from this figure, a possible "sweet spot" appeared

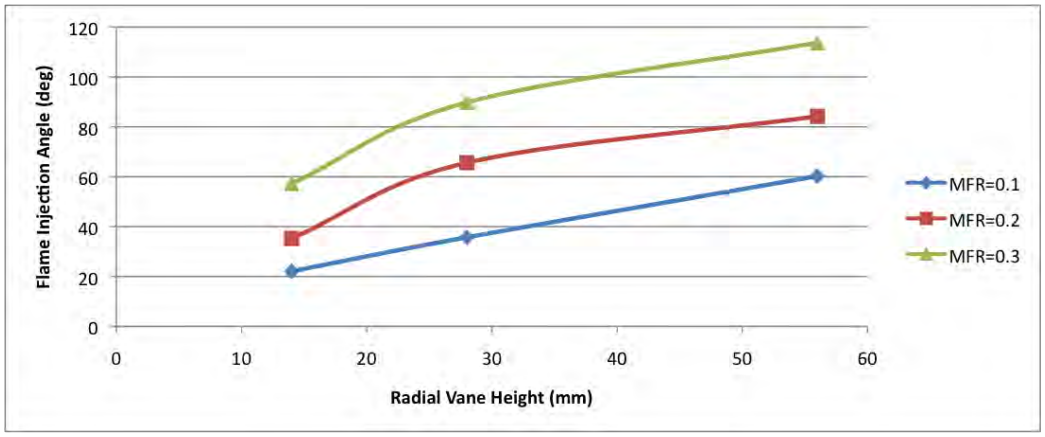

Figure 126. Flame injection angle from UCC interface for 1000g, $\phi = 2.0$, and MFR=0.1, 0.2, 0.3 for each 14, 28, and 56 mm vanes

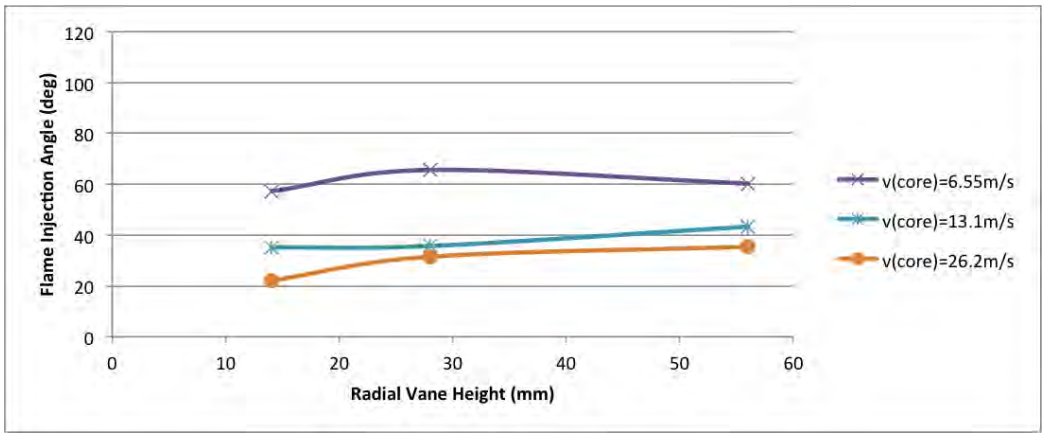

Figure 127. Flame injection angle from UCC interface for 1000g, $\phi = 2.0$, V_{core}=6.55, 13.1, 26.2 m/s for each 14, 28, and 56 mm vanes

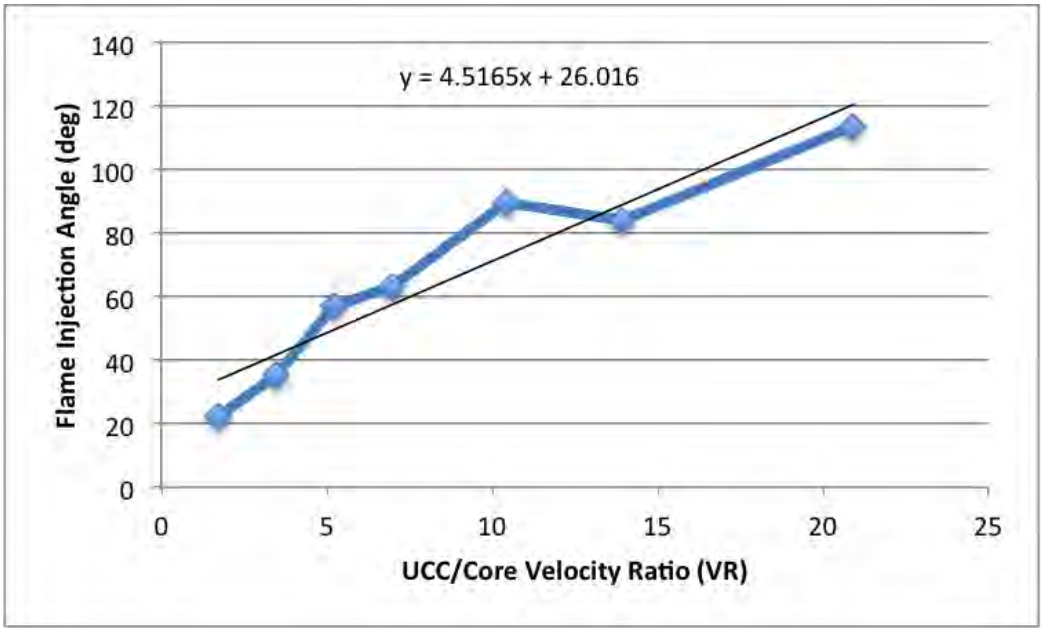

Figure 128. Plot showing the relationship between the UCC/Core Velocity Ratio (VR) and the flame injection angle (degrees)

to be around MFR=0.2 for the 28 mm vane such that a nearly uniform spatially averaged temperature distribution resulted. This is a more ideal exit condition for a typical combustor yielding a turbine inlet temperature profile more consistent with typical turbine durability requirements. While MFR values higher than 0.2 produced reasonable temperature profiles, the HSV data indicated adverse heating of the ID endwall and a roll-back of the migrating flame to the OD endwall. Conversely, for the case with MFR = 0.05 the flame did not propagate over the entire vane span, as indicated by PLIF temperatures only being reported at the 0.2 and 0.4 span-wise locations in Figure 130.

For the smaller vane height of 14 mm, the ideal MFR also appeared to be around 0.2 as evident in Figure 131. Similarly, Figure 132 shows the tallest vane height of 56 mm, which resulted in an ideal MFR also around 0.2 to achieve a uniform temperature across the span. This was expected since a constant MFR over increasing vane heights yielded decreasing core flow velocity and increasing UCC/core velocity

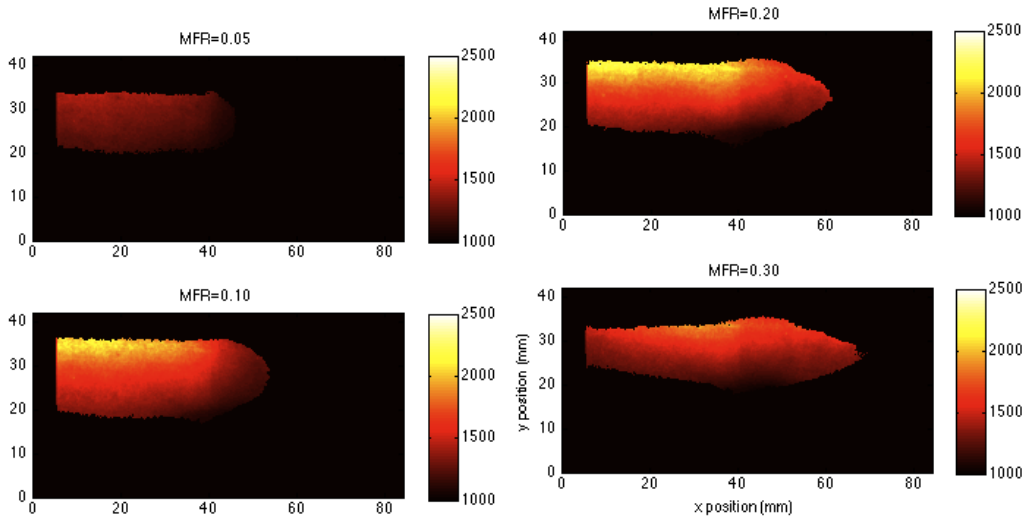

Figure 129. Temperature (K) 28 mm vane, 1000g, $\phi = 2.0$, 6 mm from UCC, at MFR=0.05, 0.1, 0.2, and 0.3 (Test Cases 31,15,14,16)

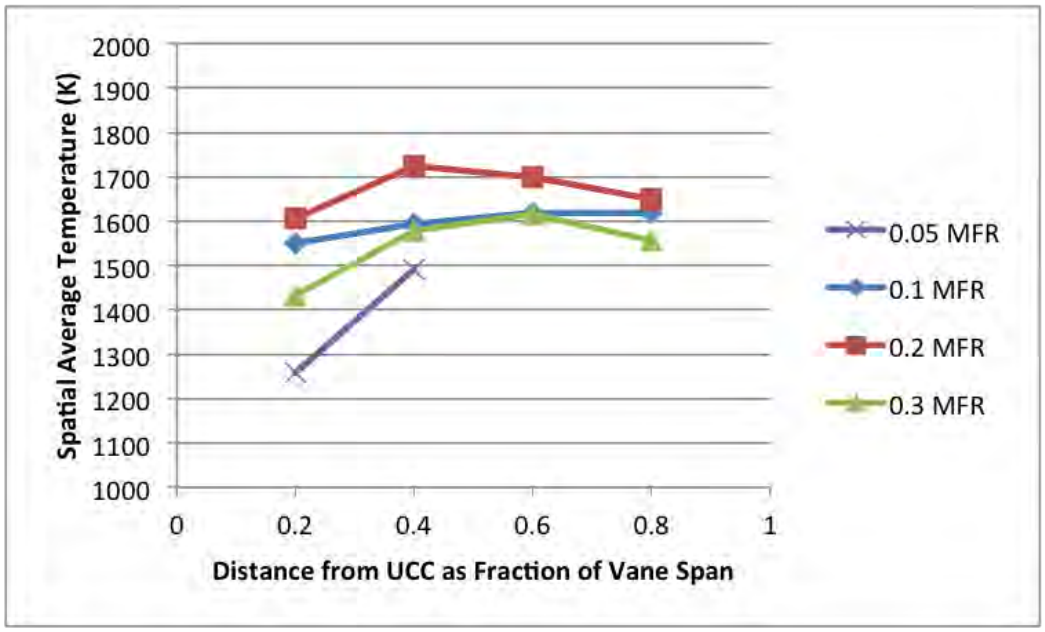

Figure 130. Span-wise spatial average temperature of 28 mm vane, 1000g, $\phi = 2.0$ at MFR=0.05, 0.1, 0.2, and 0.3

ratio. Increasing the VR increased the flame injection angle allowing the migration to spread over the larger span. Similarly to the MFR = 0.05 case with the 28 mm, the flame did not propagate over the entire span, as indicated by PLIF temperatures not being reported beyond the 0.4 span-wise location in Figure 132.

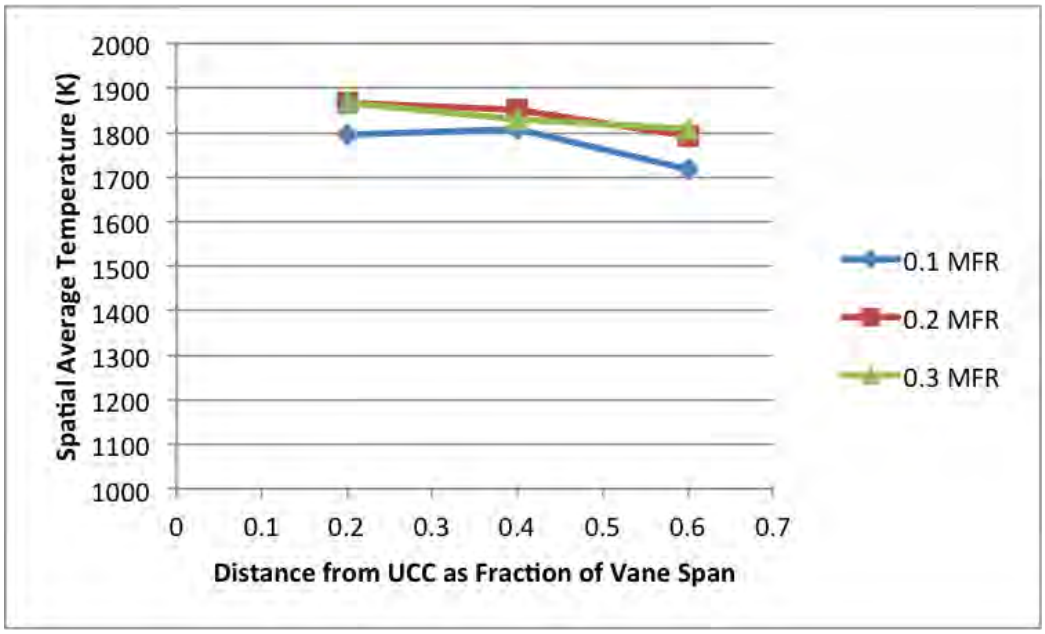

Figure 131. Span-wise spatial average temperature of 14 mm vane, 1000g, $\phi = 2.0$ at MFR=0.1, 0.2, and 0.3

Looking specifically at the effect of the vane height, Figure 133 shows the temperature contours at 6 mm from the UCC for the 1000g and MFR of 0.2 cases with vane heights of 14, 28, and 56 mm, respectively. This figure shows a change in the flame injection angle similar to varying the MFR with the vane height held constant. These three cases all had the same mass flow ratio, but at 6 mm from the cavity the smallest vane has a significantly wider flame regime and more spatial variation in the temperature distribution due to confinement within the smaller core flow channel volume. This was more evident in interrogating the exit temperature profile for these three cases. As shown in Figure 134, at this distance from the circumferential cavity, the flame extended nearly 16 mm pitch-wise from the upper wall for the shortest

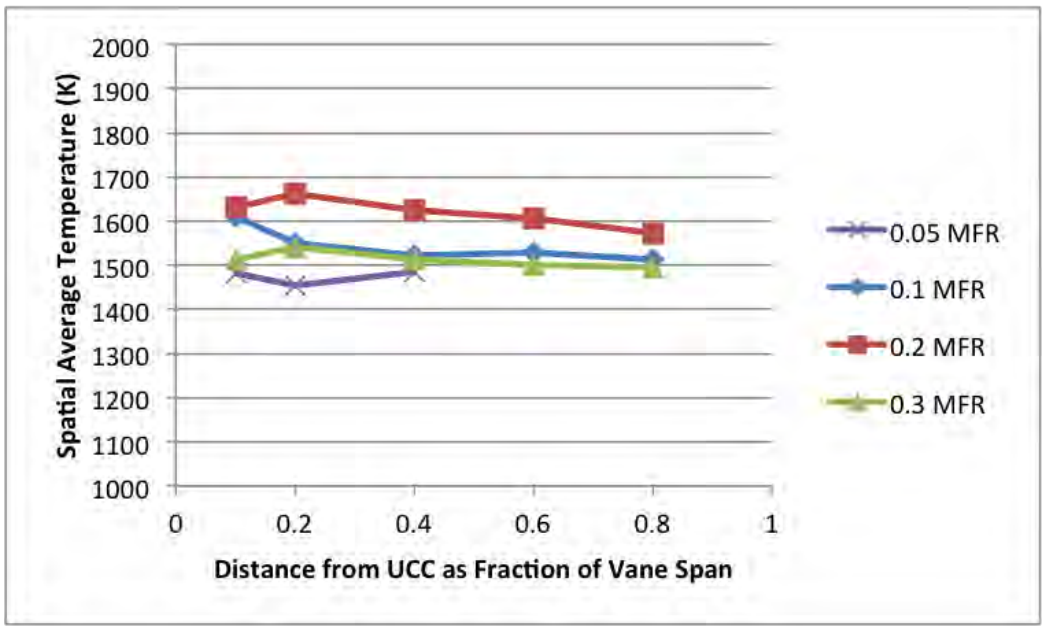

Figure 132. Span-wise spatial average temperature (K) of 56 mm vane, 1000g, $\phi = 2.0$ at MFR=0.05, 0.1, 0.2, and 0.3

vane, which is the entire height of the channel. This reduced to 14 mm and then 10 mm from the upper wall for the 28 mm and 56 mm vane, respectively. While the MFR was held constant, the increased vane height decreased the core flow velocity resulting in higher UCC/core velocity ratios, similar to increasing the MFR with the vane height held constant. The flow that exited the UCC from the taller configuration had a higher momentum relative to the core flow and stayed more cohesive as it entered the core and continued reacting. Figure 135 shows the span-wise temperature distribution for each vane height. This figure shows lower temperatures with increasing vane height which must result from decreased flame migration due to the increased velocity ratio since the MFR was held constant and the core flow velocity decreased with increasing vane height, which increased the VR.

Examining the core flow pressure drop, which occurred due to the changing VR as the vane height was changed, Figure 136 illustrates that the pressure drop decreased as the vane height and VR increased for both reacting and non-reacting conditions.

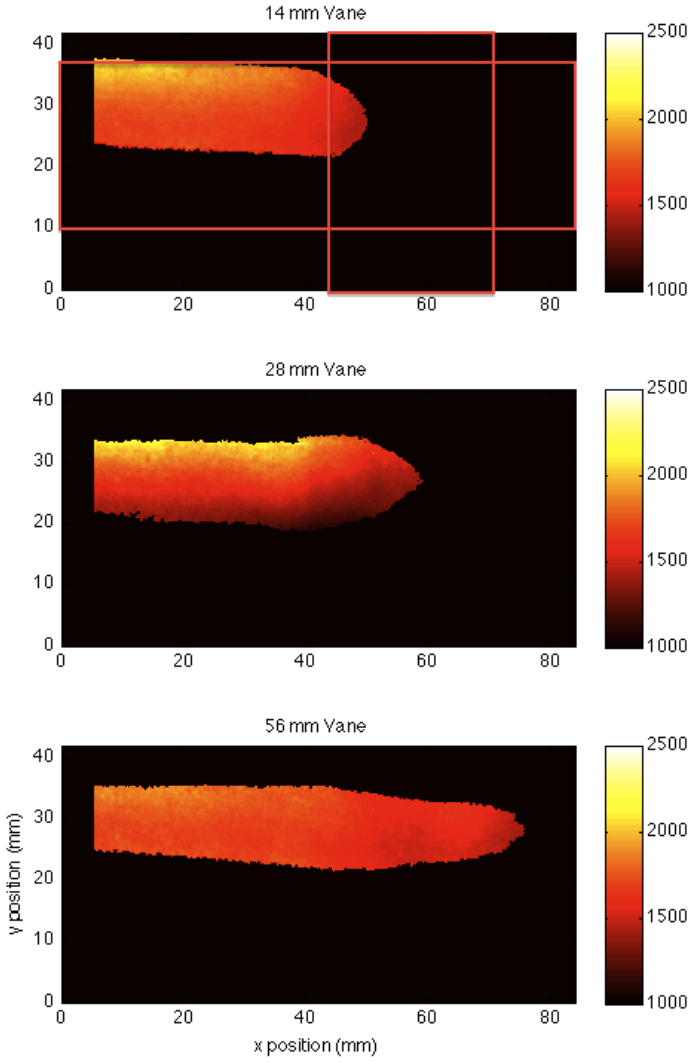

Figure 133. Temperature (K) for 1000g, MFR=0.2, $\phi = 2.0$, 6 mm from UCC, at 14, 28, and 56 mm vanes (Test Cases 5,14,18)

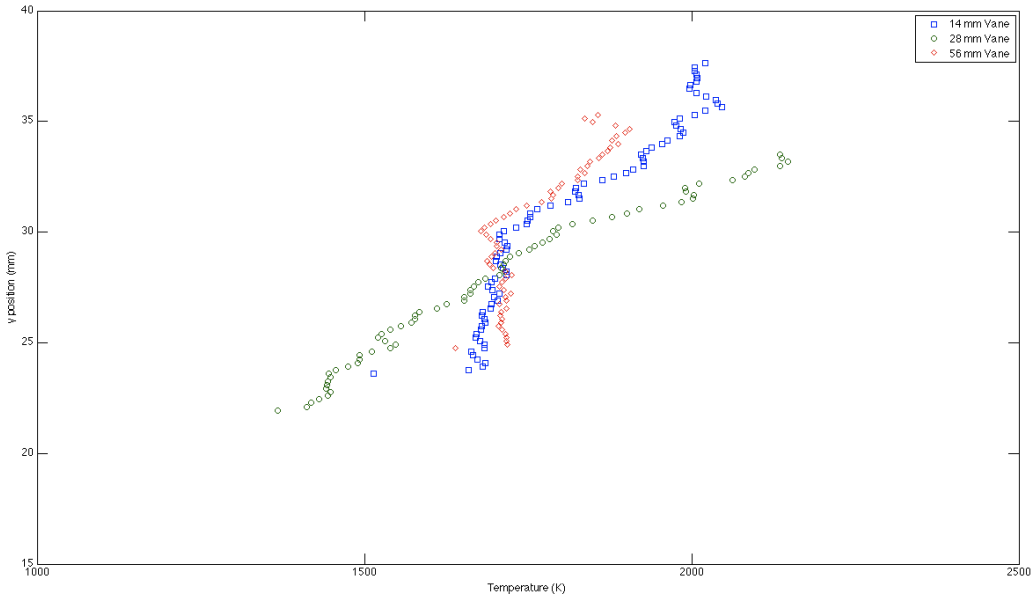

Figure 134. Exit temperature (K) vs. y position (mm) for 1000g, MFR=0.2, $\phi = 2.0$, 6 mm from UCC, at 14, 28, and 56 mm vanes (Test Cases 5,14,18) at x 8 mm

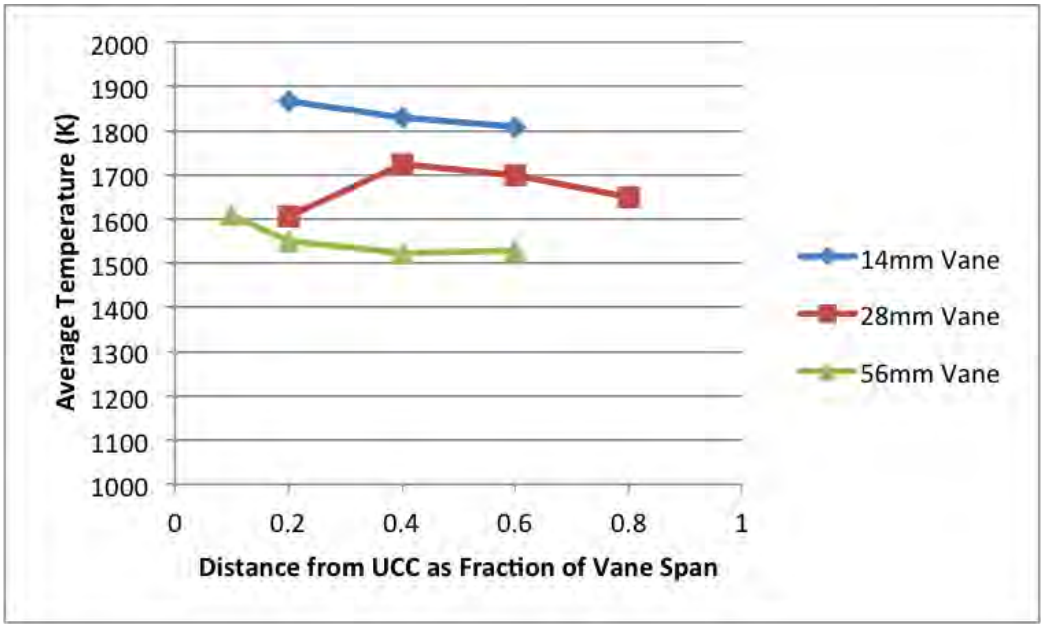

Figure 135. Spatially averaged span-wise temperature profile (K) for 1000g, MFR=0.2, $\phi = 2.0$, for the 14, 28, and 56 mm vanes (Test Cases 5,14,18)

The decrease in the flame migration from the UCC into the core flow was a result of the decreased pressure drop in the core flow. A numerical analysis by Anisko [39] on increasing the radial vane height also revealed the same result. In comparison to Figure 136, which showed the pressure drop for the constant MFR cases, Figure 137 shows the pressure drop for the cases with constant VR (Cases 5, 15, 33). As indicated in the figure, the pressure drop was relatively constant, within the measurement error, between the three cases with constant VR (Cases 5, 15, 33). The constant pressure drop for constant VR as the vane height was increased was expected because the flow velocities set the drop in the non-reacting conditions, which in turn influence the flame migration, which influences the pressure drop for the reacting conditions. This was an interesting result because it indicated that the same flame migration quantity occurred for the three cases, even though the measured core flow temperatures decreased as the vane height increased. However, keeping the VR constant required increasing the core mass flow rate proportional to the vane height increase, which led to the migrating flame encountering a larger air mass to react with, producing a lower core ϕ and resultant lower core temperature.

One question that arose was whether the radial vane height caused an effect due to the height itself or due to the slowing of the core flow velocity at the same MFR. To investigate this, Test Cases 5, 15, and 33 were run with the core flow maintained at 13.1 m/s which fixed the UCC/core velocity ratio at 1.773. Figure 138 provides the temperature distribution in the core flow for these cases at 6 mm from the UCC. Noticeable was both the significant reduction in the flame width (pitch-wise) and temperature for the 56 mm vane height. This reduction for the largest vane height was experienced for all span locations for the 56 mm vane and at higher spans for the 28 mm vane (not shown). Further, the leading edge of the flame aligns for each case reinforcing the dependence of the flame injection angle on the core flow velocity.

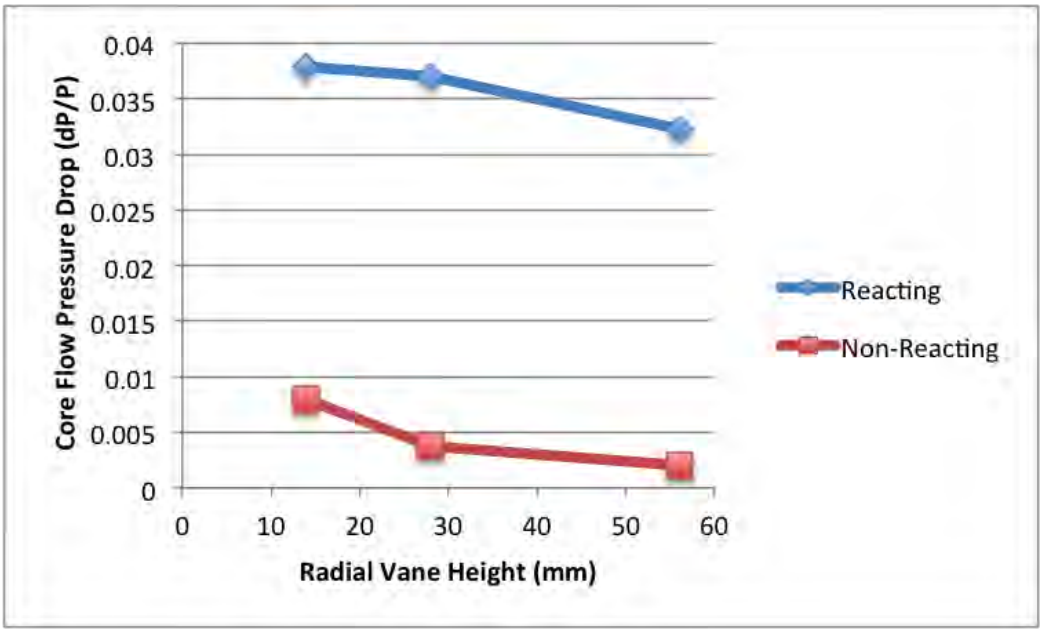

Figure 136. Comparison of reacting and non-reacting core flow pressure drop (dP/P), vs. radial vane height (mm) for Cases 5,14,18 (constant MFR = 0.2)

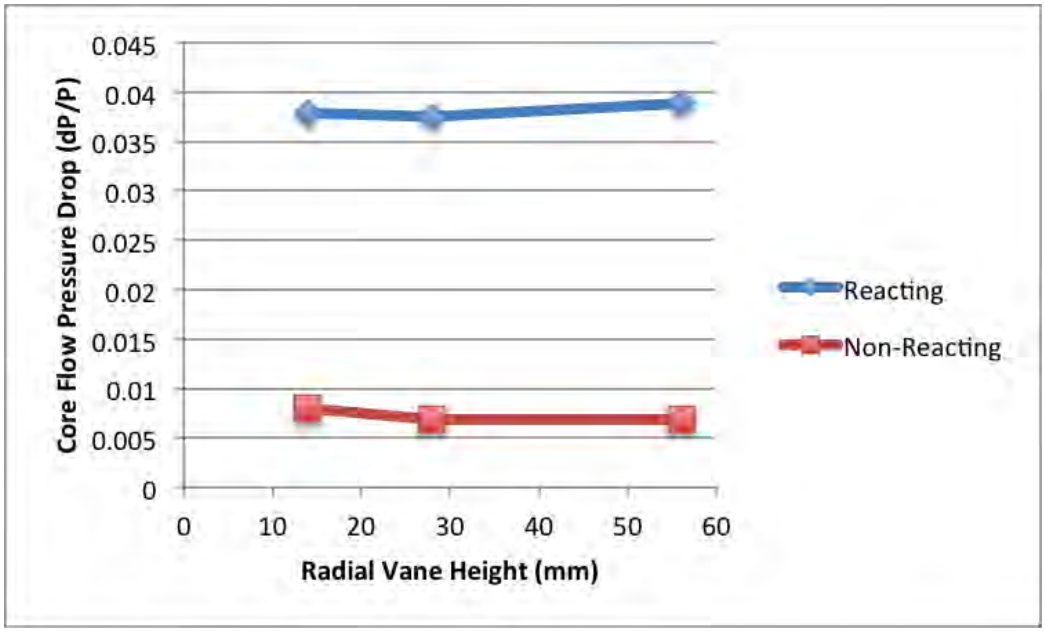

Figure 137. Comparison of reacting and non-reacting core flow pressure drop (dP/P), vs. radial vane height (mm) for Cases 5,15,33 (constant VR = 1.773)

Clearly maintaining the core flow velocity (and velocity ratios) minimized the reaction as the vane height was increased. However, matching the VR led to increasingly unfavorable temperature distributions as predicted numerically by Anisko [39].

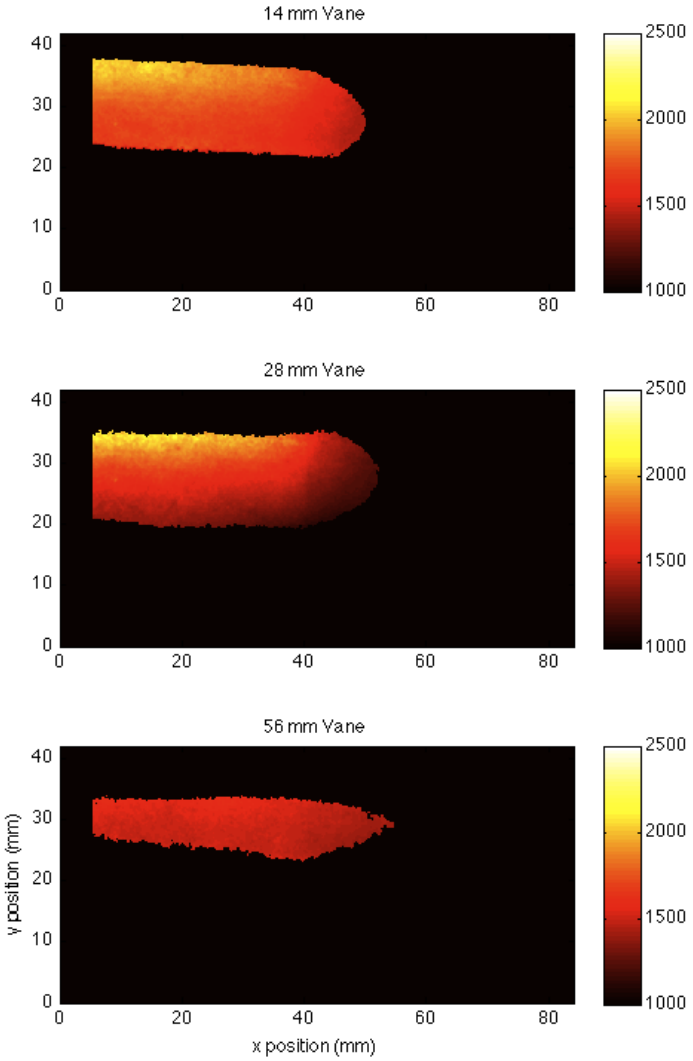

Figure 138. Temperature (K) for 1000g, $V_{core} = 13.1$m/s (VR=3.49), $\phi = 2.0$, 6 mm from UCC, at 14, 28, and 56 mm vanes (Test Cases 5,15,33)

Similarly to Figure 117, Figure 139 illustrates the flame injection angle for Test Case 15 while Figure 140 shows the same for Test Case 5. Comparing Figure 117 (Test Case 14) with Figure 139 (Test Case 15) for a single vane height with two different core flow velocities yielded an injection angle change from around 65 to 35 degrees.

This result was identical for a fixed core mass flow rate over two different vane heights such as Test Cases 14 and 5 (Figures 117 and 140) because doubling the vane height at the same mass flow rate halved the core flow velocity. However, matching core velocity over two different vane heights (Figures 140 and 139 for Test Cases 5 and 15, respectively) yielded identical flame injection angles around 35 degrees. Even though the flame angle was the same, the results were strikingly similar for all vane heights and core flow velocity variations.

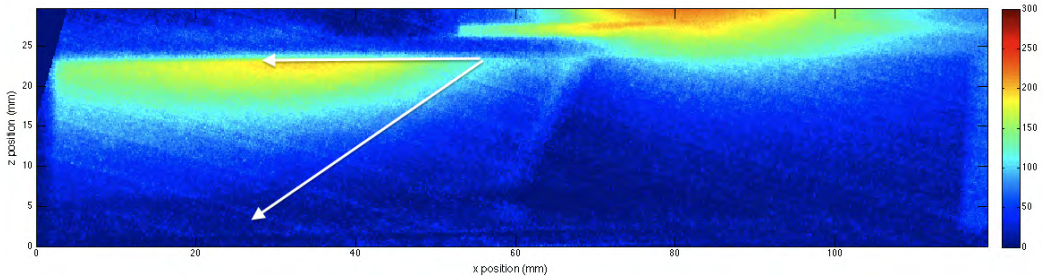

Figure 139. High-Speed Video (HSV) image above radial vane of 28 mm vane, 1000g, MFR=0.1, $\phi = 2.0$ (Test Case 15)

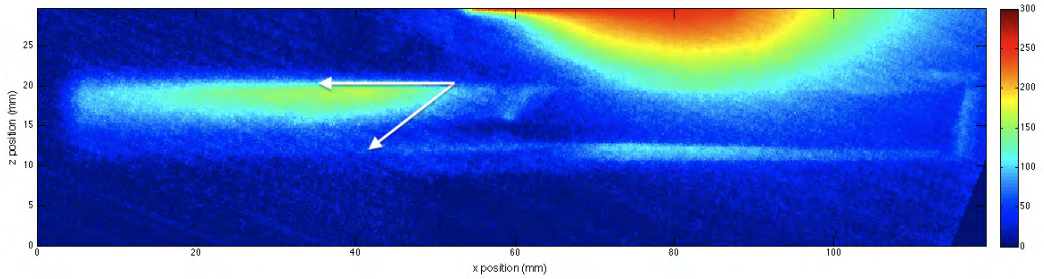

Figure 140. Time-averaged High-Speed Video (HSV) data for 1000 images above the radial vane of 14 mm vane, 1000g, MFR=0.2, $\phi = 2.0$ (Test Case 5)

VI. G-Load Investigation

The third research objective was to characterize the effect of centrifugal loading, or g-load, on the flame migration from the UCC into the core flow. It is important to first understand the effect of adding centrifugal forces to the combustor. Further, implementation of the UCC in an actual engine will likely yield significant g-load variation over the engine operating envelope. Based on the vane height investigation, the HSV and PLIF data indicated higher flame migration at higher g-loads. In order to isolate the contribution of the g-load, both the straight and curved UCC sections were used to provide identical test conditions differing only in the presence of centrifugal loading. Additionally, the g-load was measured and compared to the predicted values. Only the 28 mm vane was used as the intent was to isolate the effect of the g-load. OH PLIF, PIV, and HSV were used for measurement of temperature, flowfield parameters, and flame geometry. Pressure transducers and thermocouples were also used to measure the pressure and temperature at specific locations. The goal of this objective was to understand how the presence and variation of the g-load impacts the migration from the UCC into the core flow.

6.1 Test Setup

As shown previously, Figure 2 shows both straight and curved UCC sections for comparison. These two sections were purposefully built to be nearly identical aside from the obvious change in the radius of curvature being infinite for the straight section and 55 mm for the curved section. This enabled the same tangential velocity to be created in each cavity with the difference being that the straight section created no g-load thus isolating this effect for investigation purposes. The nominal predicted g-load value used was 1,000 g's with additional tests at 500, 1500, and 2000 g's. The

g-load was predicted using the total UCC air mass flow rate with the previously shown relations for the g-load (Equation 11) and mass flow rate (Equation 7) with the density assumed to be 0.7346 kg/m^3. The nominal UCC/core air mass flow ratio was 0.2 with additional tested ratio values of 0.025, 0.05, and 0.1. The equivalence ratio (ϕ) was held constant at $\phi = 2.0$ for the majority of the tests with additional tested ϕ values of 1.5 and 2.5. Figure 141 shows pictorially the data collection locations of PLIF, PIV, and high-speed video. The two-line PLIF measurements were taken at 10 Hz with the two Princeton PI:Max 2 cameras interrogating Planes 1-4. The PIV measurements were taken at 30 kHz with the monochrome Phantom V12.1 interrogating Planes 1-4, and 6. The HSV was acquired at 5 kHz with the color Phantom V12.1 collecting the volume-average from Plane 5, as previously depicted in Chapter 3. The location of Planes 1-4 were in the core flow section perpendicular to the radial vane span at 6 mm, 12 mm, 18 mm, and 24 mm from the UCC interface, corresponding to approximately 0.2, 0.4, 0.6, and 0.8 (0.21, 0.42, 0.63, 0.84 exactly) of the total vane span of approximately 28 mm. Planes 5, which was used for HSV only, was located in the core flow section, parallel to the radial vane span and the data collected was volume-averaged over the entire core flow channel height of 30 mm. Plane 6 was located at the ambient exit of the UCC section approximately in the middle of the channel depth of 13.5 mm.

In addition to the g-load investigation cases from the global test matrix (Cases 1-3, 13-16, 26 in Table 1), several additional test cases were considered. These cases, listed in Table 6, provided necessary variation in both the tangential velocity and in the MFR (or VR) to estimate the contributions of both parameters on the migration from the UCC into the core flow. The straight section was used exclusively with these cases because the total UCC velocity could not be measured due to the curved section flame being inclined to the outward radial direction and variations of this angle with

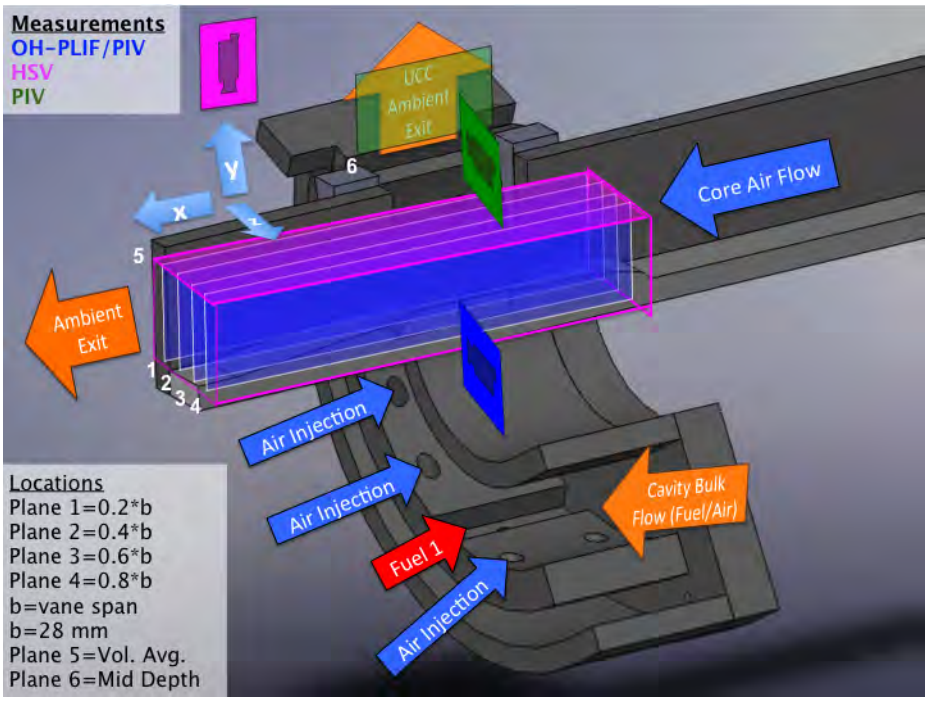

Figure 141. Illustration of the sectional UCC with locations of PLIF, PIV, and HSV data collection for the g-load investigation

the g-load was not investigated.

The test cases studied in this investigation used the UCC seeder box, shown in Figure 29 and discussed in Section 3.2. For the conditions in this investigation, significant flame holding issues were observed particularly for the 2000g case (Case 26), but also intermittently for the 1000g case (Case 14). The specific issue was that the flame would not stay back into the seeder box and would become detached from the seeder box interface and attach downstream of next fuel injector. As a result of the flame holding issues, the fuel and air into the UCC was split equally with 1/2 of the total fuel and air entering from the outward radial wall of the UCC section, shown in Figure 141, and 1/2 entering in from the UCC seeder box. The 1/2 and 1/2 split was different than the fuel and air distribution used for the v-flame investigation (Chapter 4), which was 1/3 and 2/3 of the total fuel and air entering from the outward radial wall of the UCC section and the UCC seeder box, respectively. The 1/2 and 1/2 split

Table 6. Additional test cases used for the g-load determination investigation

Test Case	**Predicted V_{tan} (m/s)**	**Corresponding G-Load (g's)**	**UCC/Core MFR**	**UCC/Core VR**	ϕ
S1	16.42	500	0.2	6.97	2
S2	16.42	500	0.1	3.49	2
S3	16.42	500	0.05	1.74	2
S4	16.42	500	0.025	0.87	2
S5	23.23	1000	0.2	6.97	2
S6	23.23	1000	0.1	3.49	2
S7	23.23	1000	0.05	1.74	2
S8	23.23	1000	0.025	0.87	2
S9	28.45	1500	0.2	6.97	2
S10	28.45	1500	0.1	3.49	2
S11	28.45	1500	0.05	1.74	2
S12	28.45	1500	0.025	0.87	2
S13	32.85	2000	0.2	6.97	2
S14	32.85	2000	0.1	3.49	2
S15	32.85	2000	0.05	1.74	2
S16	32.85	2000	0.025	0.87	2
S17	23.23	1000	0.2	6.97	1.5
S18	23.23	1000	0.2	6.97	2.5

was used for all cases, straight and curved, in this investigation and would been less accurate in representing an annular UCC model as the 1/3 and 2/3 distribution. The change in the fuel and air distribution may have also changed the actual g-load value that resulted from running the same test condition with a different distribution, but no data existed to infer what that impact was or if there even was an impact. The change in the distribution of fuel and air between the UCC section and the UCC seeder box significantly improved the flame holding issues, but it did not entirely resolve the issue for Case 26. In order to establish adequate flame holding for Case 26, the curved ramp was removed at the interface between the curved UCC section and the UCC seeder box, shown in right image of Figure 142. The removal of the ramp left a backward facing step at the interface that was able to establish stable flame holding. The ramp was removed for all of the curved UCC section data collected for this investigation, but not for the v-flame investigation, where the fuel and air distribution was different, or the vane height investigation, which did not use the seeder box at all. The straight section testing with the seeder box did not experience the same flame holding issues that the curved section did and the flame remained stabilized within the seeder box.

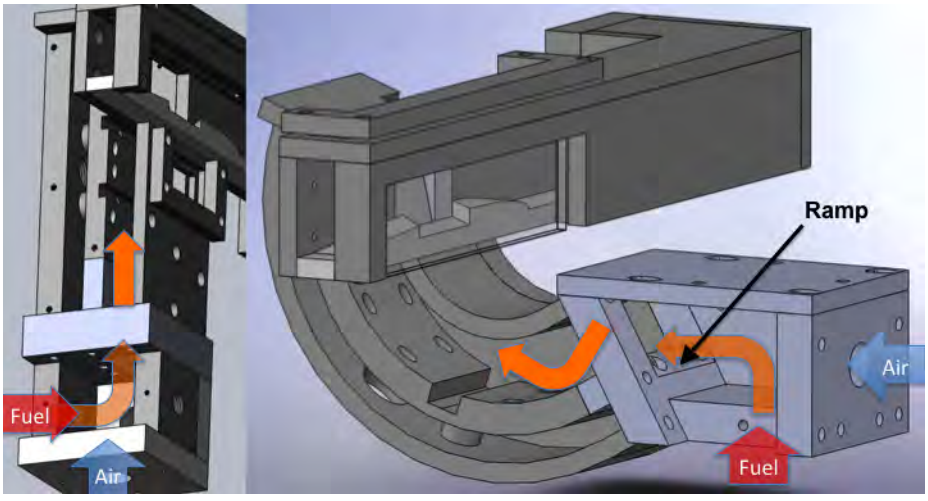

Figure 142. Illustration of the seeder box interface with the straight (left) and curved (right) UCC sections with the turning ramp on the curved interface (right)

6.2 Results

The goal of this investigation was to understand the effects of the presence and variation of the g-load on the radial migration of the hot gases exiting the UCC flow path and entering the core flow path. While the main parameter of interest for this study was obviously the g-load, its coupling with the UCC/core air MFR was also of interest. The g-load investigation was conducted in two parts. Initial results were obtained concurrently on Test Cases 13, 14, and 26, from Table 1, with the vane height investigation using PLIF and HSV to investigate the core flow temperatures and flame migration trajectory, see Chapter 5. These cases indicated increasing flame migration with increasing g-load. However, it was desired to investigate the same 500-2000g range using both the straight and curved UCC sections to isolate the contribution of the centrifugal load to the flame migration. For the first part of the investigation, Cases 1-3, 13, 14, and 26 were investigated for a comparison of the test conditions with and without the g-load. To determine the centrifugal force contribution, PLIF was used to measure the core flow temperature distribution, PIV was used to measure the velocity distribution in the core flow, and HSV was used to measure the flame migration trajectory and characterize the flame migration unsteadiness. For the second part of the investigation, Cases S1-S18 were investigated with the straight UCC section using PIV at Plane 6 to measure the tangential velocity at the ambient UCC exit for comparison to the predicted values and the estimated values from the pressure and temperature data.

6.2.1 Straight vs. Curved Comparison.

In order to specifically isolate the g-load effect both straight and curved sections were tested with identical flow conditions. Cases 1-3, 13, 14, and 26 corresponded to the predicted 16, 23, and 33 m/s tangential velocity conditions for the straight and

curved UCC sections respectively with the MFR = 0.2, ϕ = 2.0, and using the 28 mm radial vane. Figure 143 qualitatively illustrates the similarities and differences between the straight and curved UCC sections for the 23 m/s tangential velocity condition using HSV at Plane 5. In this figure, the flame migration into the core flow is of noticeably lower pixel intensity with the straight section suggesting a lower amount of mass flux into the core flow and resultantly lower temperature than with the curved section. The flame migration appears to be of lower intensity for the straight section than with the curved section. Despite these differences, the flame injection angle qualitatively appears to be about the same for both sections. This further demonstrates the flame angle does not depend on the g-load, which further solidifies the previous conclusion that the flame angle was a function of the VR alone. While the VR sets the geometry of the migration, the g-load influences the quantity of the migration independently of the geometry based on significantly higher image pixel intensity with the curved UCC section over the straight. This can be thought of in vector terms where the VR determine the direction (the flame angle) while the tangential velocity only influences the magnitude of the migration mass. This was due to the increased buoyancy, which acts in the migration direction, resultant from the added g-load, as quantified by Lewis [13].

Further analysis of the flame injection angle at more g-loads confirmed the similarity between the straight and curved section. Figure 144 shows the injection angle was independent of the g-load. It also indicates that removing the g-load completely (the straight section cases) had no impact on the injection angle. This was not unexpected but was an important confirmation of the injection angle dependence on the VR alone rather than a multi-parameter dependence. This also further confirmed that the g-load does not alter the direction of the flame migration, only the magnitude.

A closer examination of the temperature distribution using PLIF confirmed the

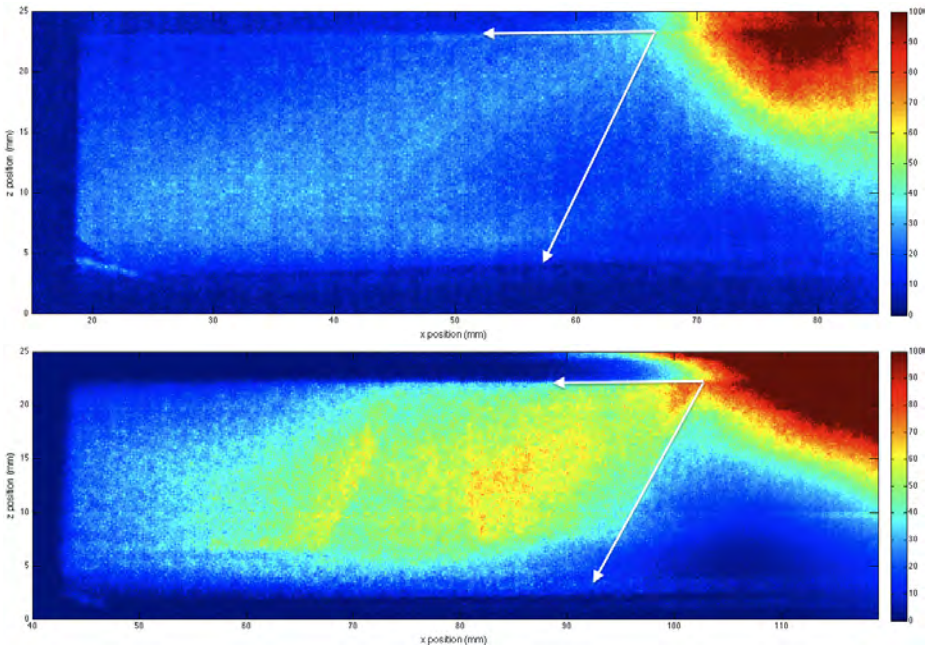

Figure 143. HSV images of the Vtan=23 m/s, VR=6.97 (MFR=0.2), $\phi = 2.0$ for the straight (top) and curved (bottom) UCC sections at Plane 5

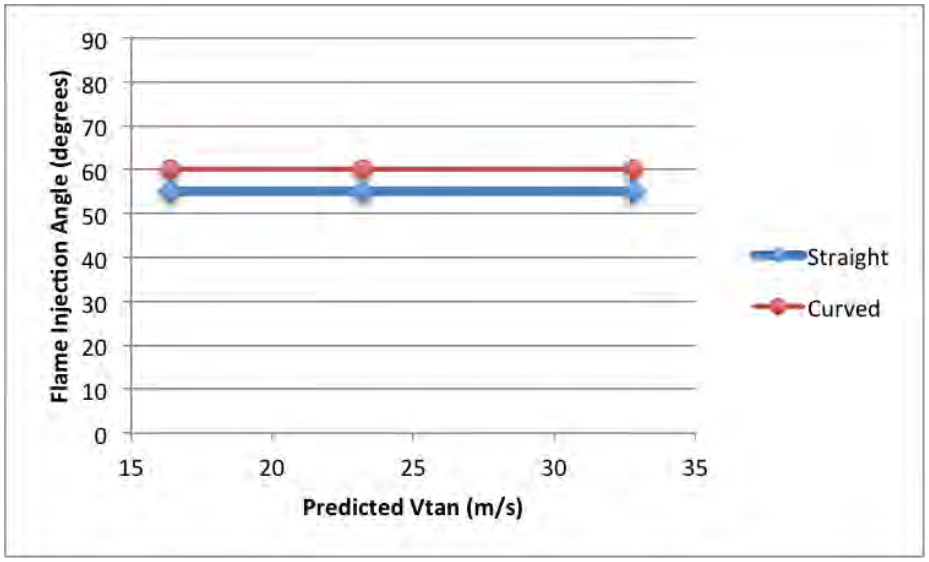

Figure 144. Flame injection angles vs. UCC tangential velocity (m/s) with VR=6.97 (MFR=0.2) $\phi = 2.0$ for the straight and curved UCC sections

indication that the migration from the straight section yielded lower core flow temperatures. This is shown qualitatively with the planar distributions for the 1000g conditions specifically in Figure 145 which also show a characteristically smaller flame area at the same span-wise location. Only three of the four data planes are shown due because quality data was not obtained for Plane 4. The flame areas of the images in Figure 145 did have similar shape which was further evidence that the g-load did not affect the flow geometry, only the quantity of flame migrating from the UCC into the core flow. Quantitatively investigating the spatially averaged span-wise temperature distribution for the three g-load conditions is shown in Figure 146. This shows that the reduced core flow temperature distribution for the straight section was common for all three tangential velocity conditions. Also, the temperature distribution increased more significantly as the tangential velocity was increased for the curved section than the straight section. Since these measurements are the temperature computed from the time-averaged flamelet distributions, higher temperatures are the result of higher flamelet concentrations for a given region and thus higher quantities of flame migration into the core flow. This was an obvious deduction since the temperature measurement was based on the presence of OH resulting from reactions with migrated UCC flow into the core flow. The higher flame migration with the core flow was inline with predictions from Moenter's computational study [40].

Investigating the effect of the flame migration on the flowfield, Figure 147 illustrates that similar velocity profiles existed in the core flow upstream of the UCC interface for both the straight and curved UCC sections. However, there were slight variations in the inlet velocity on a case by case comparison. The core mass flow rate was set identically between the straight and curved cases, but the slight variations could have been the result of mass flow controller oscillations, as documented by Sincock [61]. Figure 148 shows that the curved UCC section has higher velocity

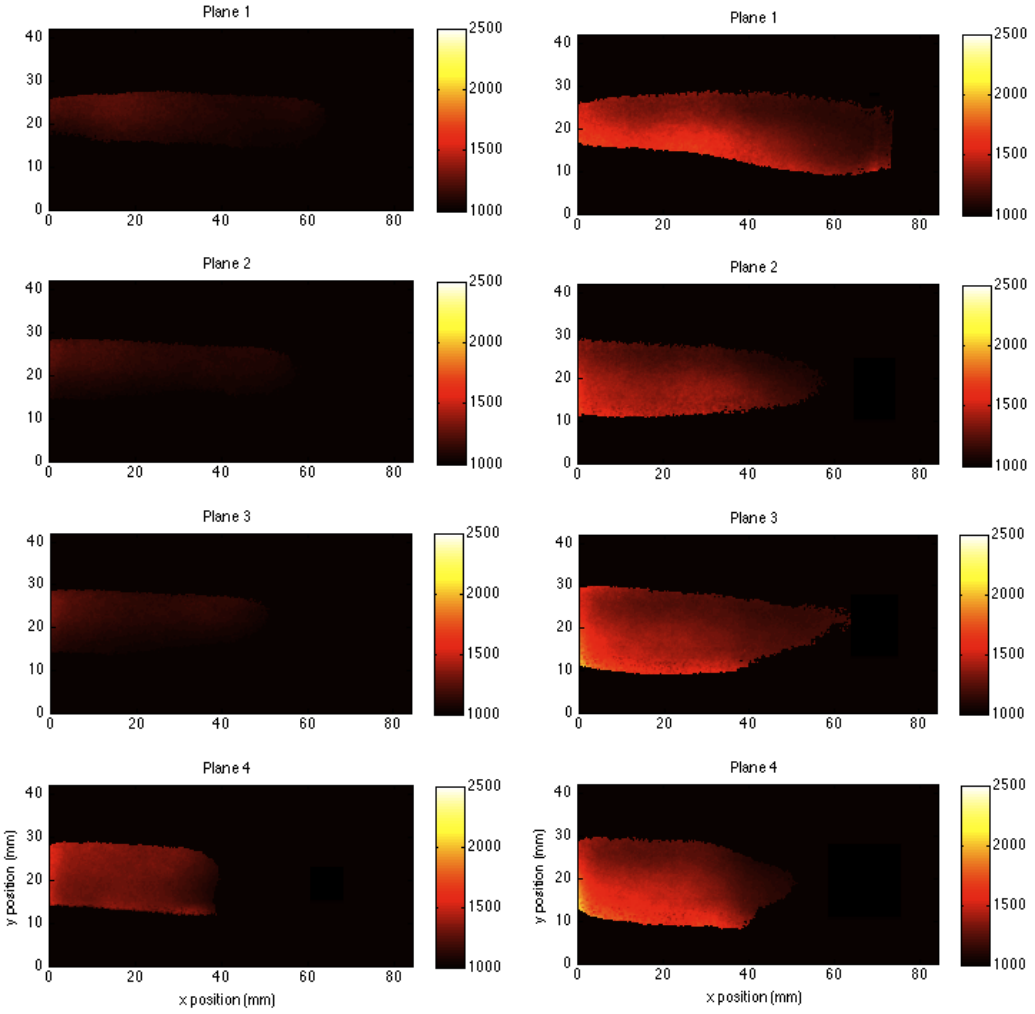

Figure 145. Planar temperature distribution of Planes 1-4 for the Vtan=23 m/s, VR=6.97 (MFR=0.2), $\phi = 2.0$ for the straight (left) and curved (right) UCC sections

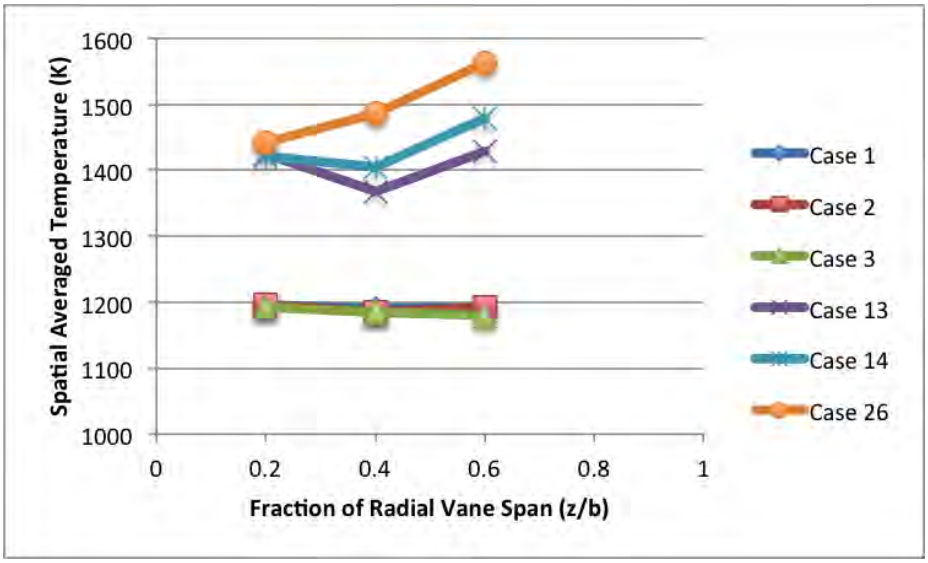

Figure 146. Span-wise average temperature distribution of the Vtan=16, 23, 33 m/s conditions with VR=6.97 (MFR=0.2), $\phi = 2.0$ for the straight (Cases 1, 2, 3) and curved (Cases 13, 14, 26) UCC sections

profiles in the core flow downstream of the UCC interface despite the slight variations in the inlet profiles. The resulting increase in the flow velocity for the curved section indicated a higher mass flow downstream of the UCC interface than with the straight section. This increased mass flow in the core resulted from the increased migration of mass from the UCC into the core flow, as indicated by the HSV and PLIF data.

In order to characterize differences in the unsteadiness between the two UCC sections, both HSV and PIV were used. Examining the HSV data in detail, the pixel intensity at location (x= 45 mm, z= 12 mm) was plotted vs. time for both Case 2 (top) and Case 14 (bottom) in Figure 149. This figure indicates that the pixel intensity for the straight section case (Case 2) was significantly lower than for the curved section case (Case 14). Figure 149 also indicates that the pixel intensity was relatively constant, between 50 and 120 signal counts, for the straight section case, but varied significantly for the curved section case, between 50 and 250 signal counts. Expanding the analysis from a point to examining the history of an image strip over time, the time images, processed as illustrated previously in Figure 100, for the straight and curved

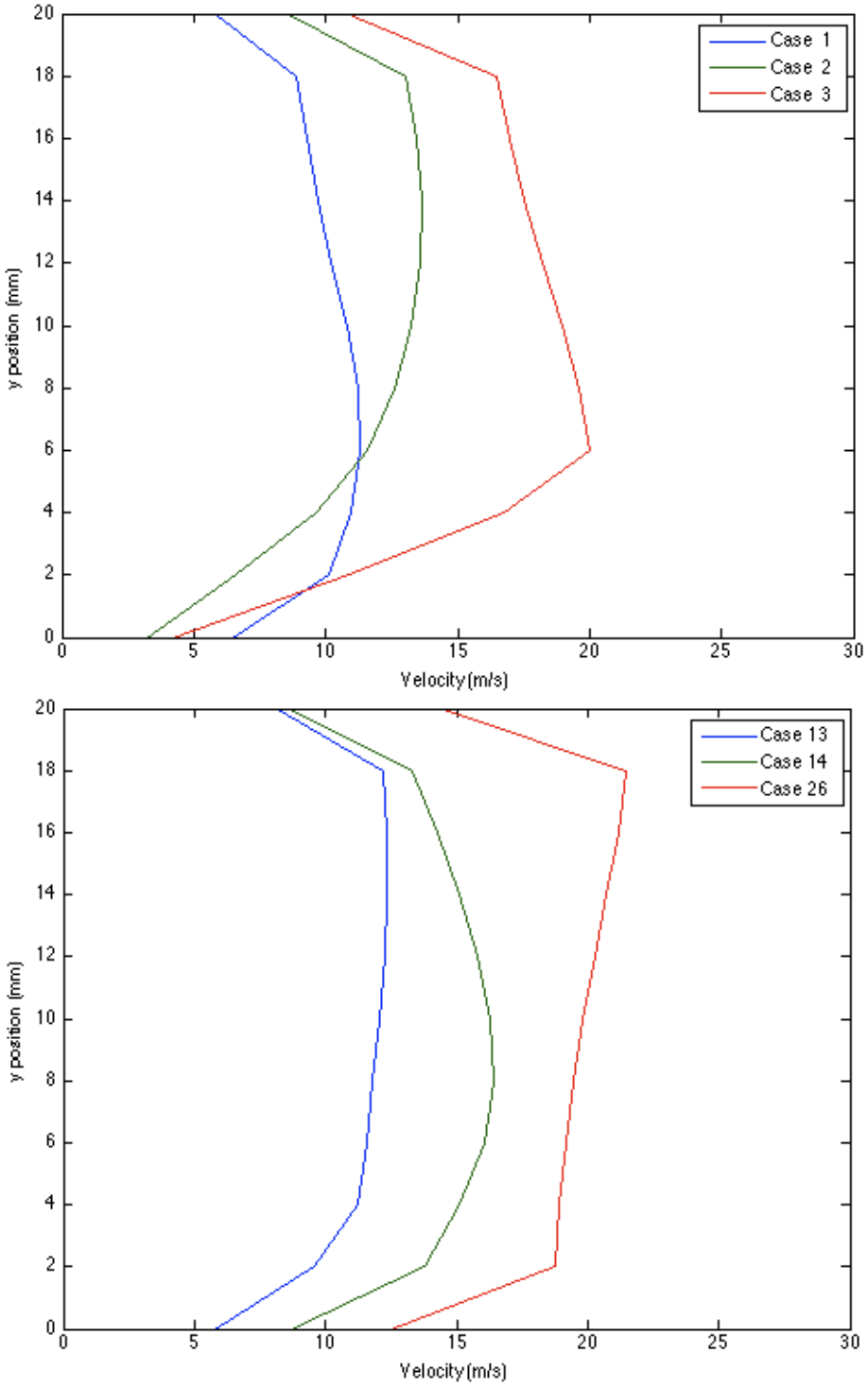

Figure 147. Inlet u component velocity profiles for the straight (top) and curved (bottom) UCC sections with VR=6.97 (MFR=0.2), and $\phi = 2.0$

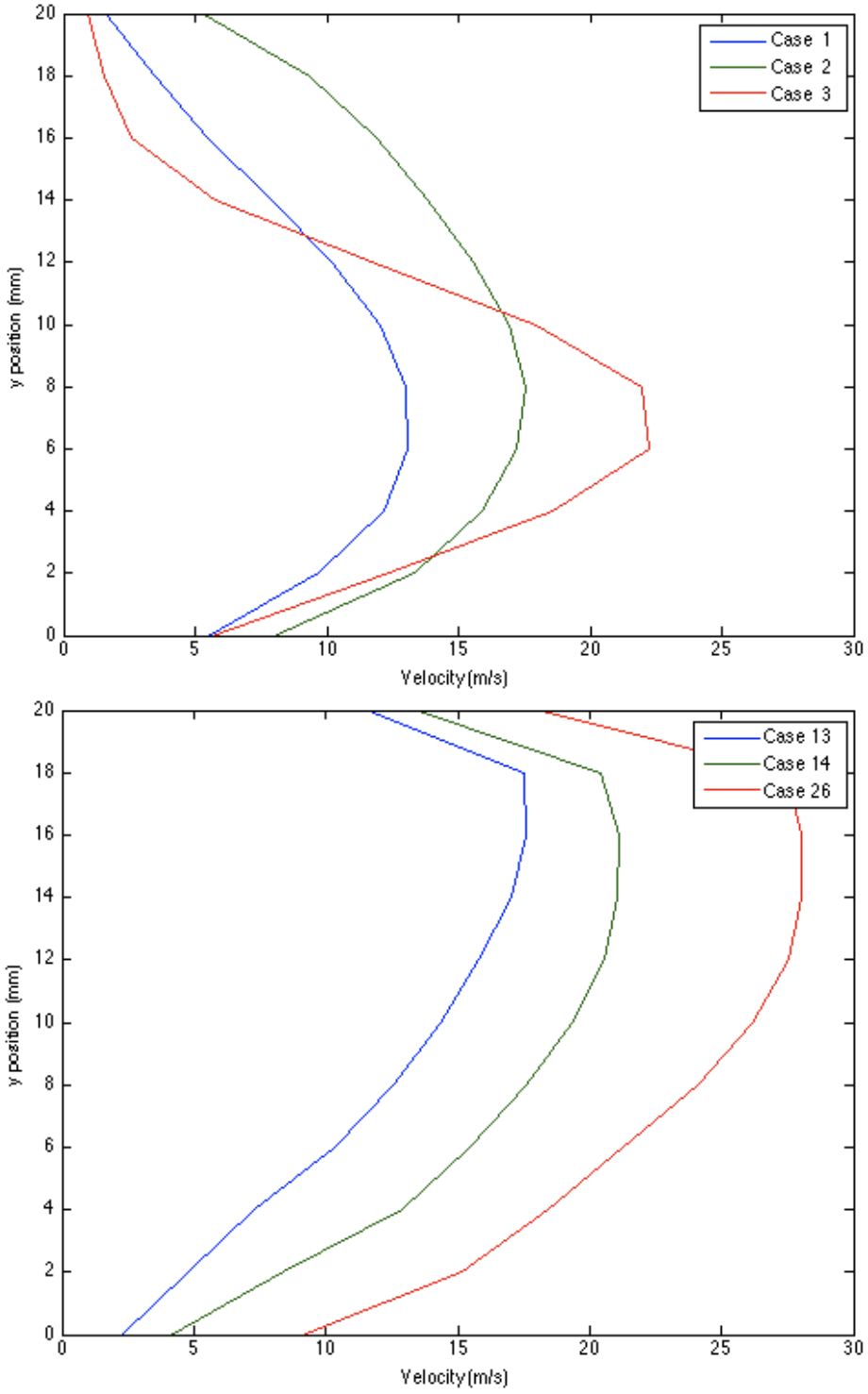

Figure 148. Outlet u component velocity profiles for the straight (top) and curved (bottom) UCC sections with VR=6.97 (MFR=0.2), and $\phi = 2.0$

cases are shown in Figure 150. These images more clearly illustrate the temporal consistency in the pixel intensity for the straight section and the periodicity of the intensity for the curved section. The trend of relatively consistent pixel intensities for the straight section and periodic oscillations for the curved section was observed over the entire tangential velocity range.

Continuing the HSV unsteadiness analysis, the frequency spectrum from the 2D FFT was computed from the time images in Figure 150 for straight (Case 2) and curved (Case 14) section cases. The time images were processed as illustrated previously in Figure 102, with the resulting power spectra shown in Figure 151. This figure indicates that while the curved section had a single dominant peak at 130 Hz with a secondary peak near 260 Hz the straight section had several dominant peaks in the 15 to 30 Hz range and also near 55, 75, and 175 Hz. Also, the intensity of the peaks for the curved section were two orders of magnitude higher than the peaks for the straight section, 5×10^{11} versus 5×10^{9}. The 130 Hz dominant frequency with the curved UCC section aligned well with the frequency measured by Lewis [13] of approximately 125 Hz for flames subjected to a centrifugal load while non-loaded flame frequencies were several orders lower in magnitude, the same trend was observed for the non g-loaded flames using the straight UCC section. Lewis postulated this was due to the stream-wise propagating vortex induced by the g-load [13].

Examination of the unsteadiness from the PIV data was conducted at the ambient UCC exit (Plane 6) for Case 2 (straight section) and Case 14 (curved section). As a starting point, Figure 152 shows the velocity magnitude at this location plotted versus time and enlarged to show the first 10 ms of data (300 samples). This figure shows that similar mean velocity values were measured for both points but higher fluctuation levels were present with the straight section. In order to analyze the frequency of these fluctuations, the PSD was computed for each case and is shown in

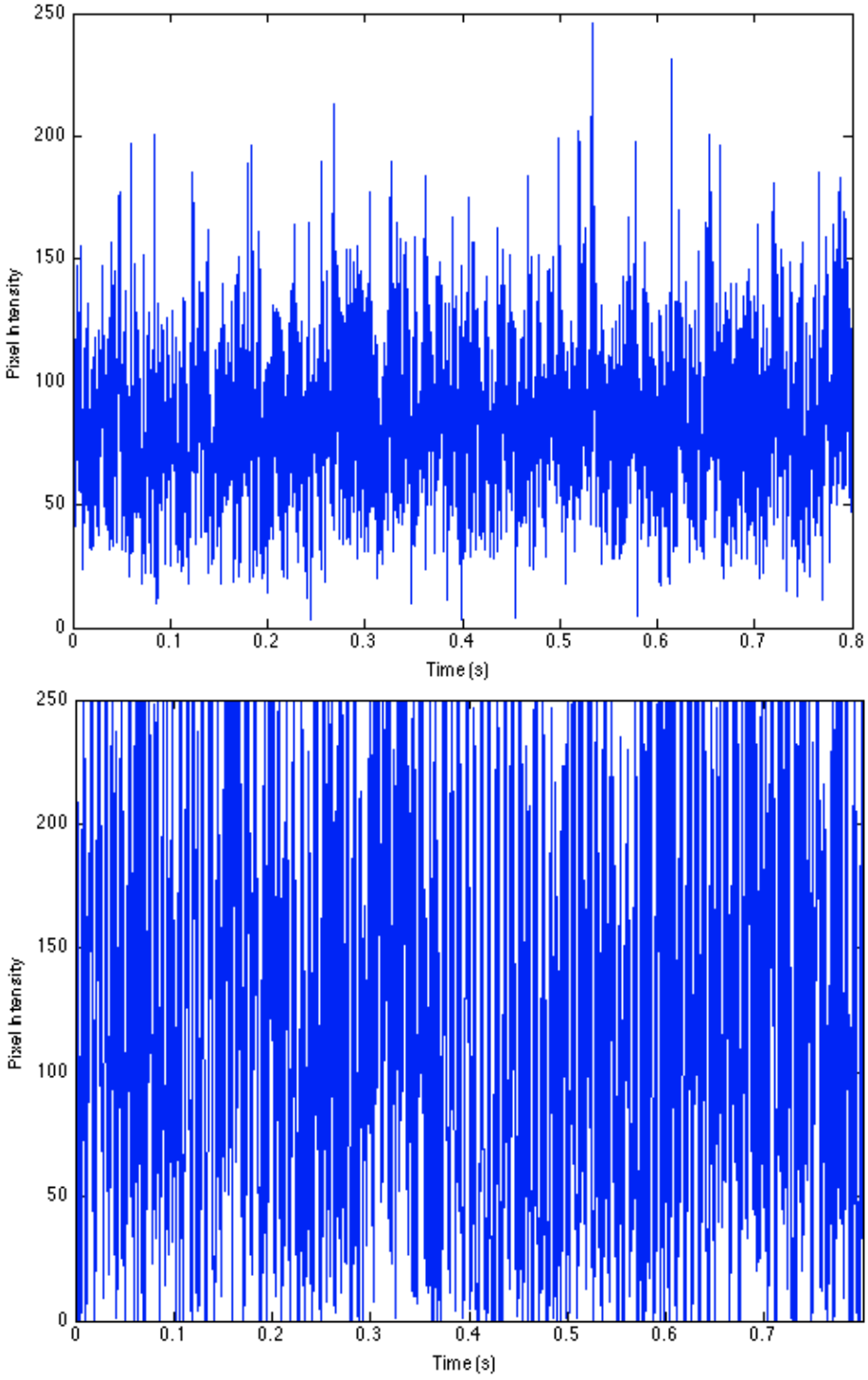

Figure 149. HSV pixel intensity vs. time (s) at (x=45 mm, z=12 mm) of the Vtan=23 m/s, VR=6.97 (MFR=0.2), $\phi = 2.0$ for the straight (top) and curved (bottom) UCC sections at Plane 5

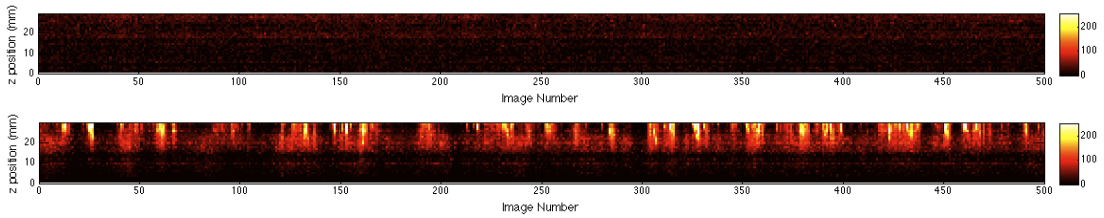

Figure 150. HSV data showing the time history of location x=45 mm vs. time (image number) for the straight section, Case 2, (top) and curved section, Case 14, (bottom)

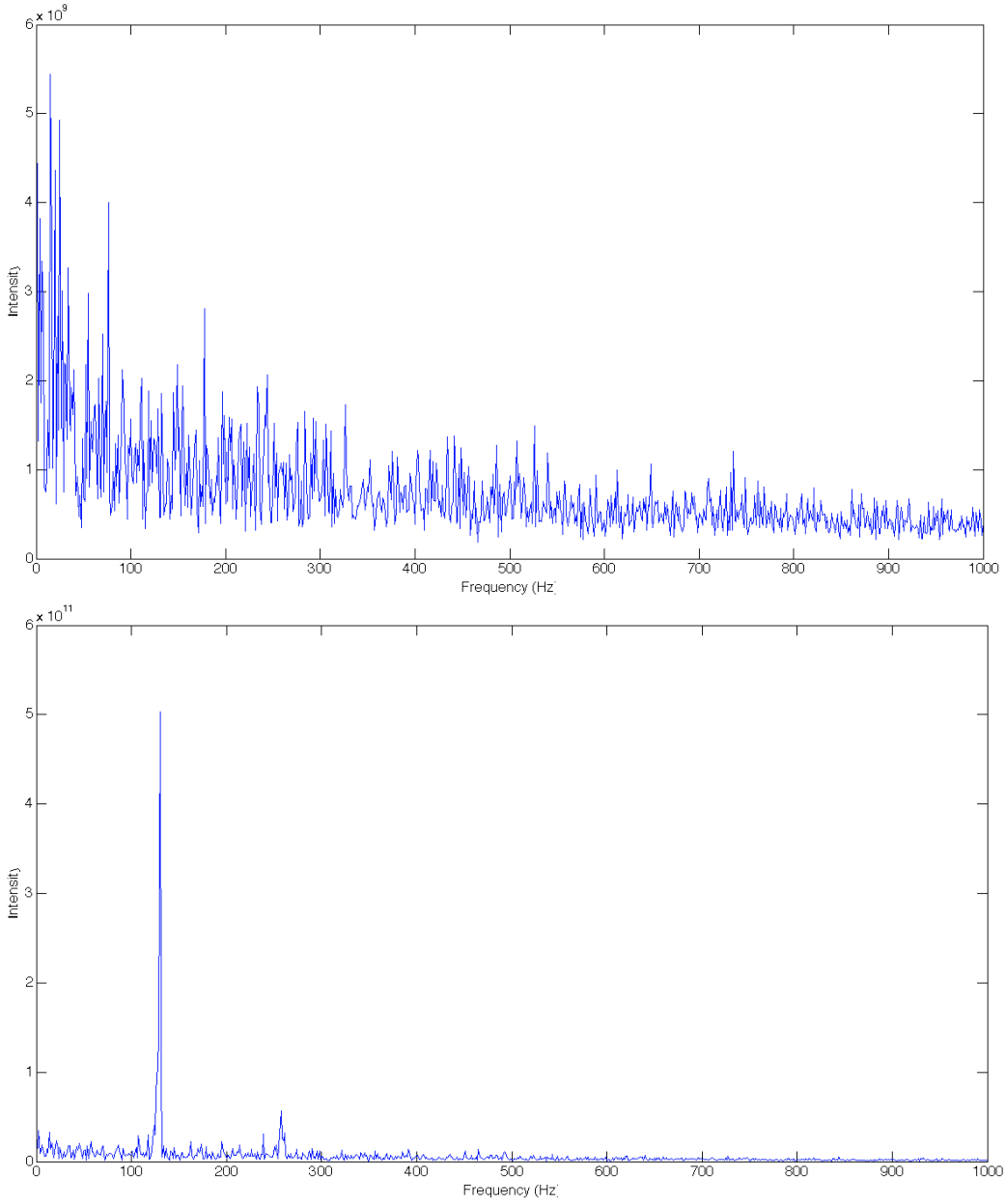

Figure 151. HSV frequency spectrum for the Vtan=23 m/s, VR=6.97 (MFR=0.2), $\phi = 2.0$ conditions for the straight (top) and curved (bottom) UCC sections

Figure 153. This figure shows that the curved section had higher intensity fluctuations than the straight section for both the HSV and PIV data. The straight section did not have a single dominant peak, but several competing frequencies around 150, 210, and 510 Hz. The curved section had a single dominant peak around 150 Hz that was of much higher intensity than the peaks with the straight section. The 150 Hz peak with the curved section was likely the result of the same phenomena as the 130 Hz peak of the HSV data as the flame migrated from the UCC into the core flow. This also indicates a higher level of unsteadiness with the curved section that could be detrimental to the turbine rotor. Also, prior to this frequency characterization, no data existed for estimating the time period used for creating the time-averaged data. Particularly for the PLIF and PIV data, as shown previously in Figures 67 and 92, slight variations existed among multiple runs of the same test condition. The measured flow frequencies could have been a major contributing factor in these variations.

The correlation of the frequency spectrum for the curved section at the ambient UCC exit with the core flow was an important result. This correlation indicates that the g-load induces a fundamental frequency into the UCC flow in the 130-150 Hz range. This fundamental frequency results in a pressure build-up and relieving effect that occurs as the flame migration into the core flow oscillates. It was also interesting that the fundamental frequency was insensitive to changes in the g-load (unexpected) and the VR, based on the HSV data (not shown). This insensitivity appears to be analogous to the scenario in highly turbulent flow where the integral scale becomes insensitive to changes in the Reynold's number. It was expected that the frequency would change with changes in the g-load value, assuming the frequency was indicative of the bubble velocity proposed by Lewis [13]. It was not likely that the 130 Hz was related to the bubble velocity since that same frequency dominated over varying g-

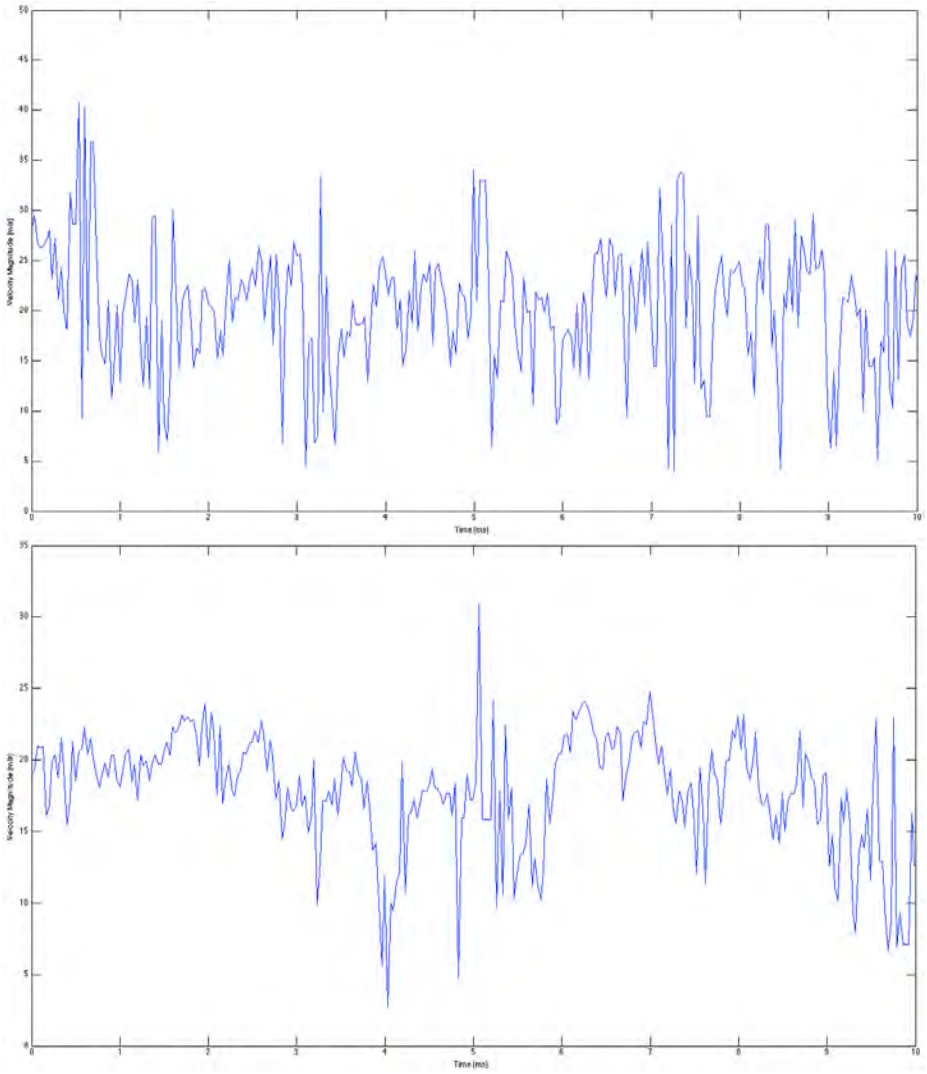

Figure 152. Velocity magnitude (m/s) vs. time (ms) at Plane 6 for the Vtan=23 m/s, VR=6.97 (MFR=0.2), $\phi = 2.0$ for the straight (left) and curved (right) UCC sections

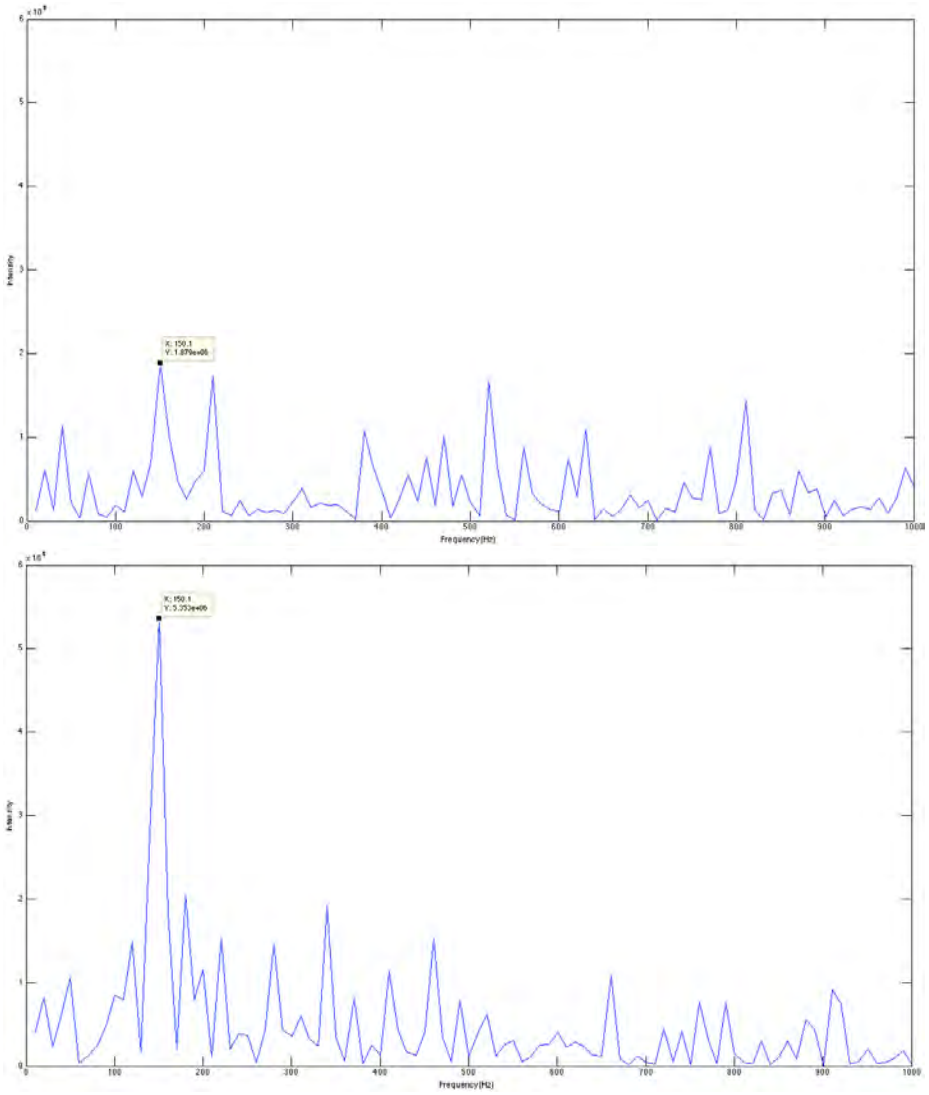

Figure 153. Power Spectral Density (PSD) vs. frequency (Hz) at Planes 6 location for the Vtan=23 m/s, VR=6.97 (MFR=0.2), $\phi = 2.0$ for the straight (left) and curved (right) UCC sections

load values, but this frequency was then likely to be some sort of acoustic resonance in the curved section geometry that was activated by the g-load.

6.2.2 G-Load Determination.

The relation for computing the g-load was shown in Equation 11. In the test case determination, the tangential velocity was predicted using the total UCC air mass flow rate (both injected circumferentially and in the seeder box) in the classical mass flow rate relation shown previously, Equation 7. There were a couple options of which density to chose. One option was to use the equilibrium flame density of 0.17624 $\frac{kg}{m^3}$ which would have resulted in the predicted g-load to be well over 17,000 g's for the 1000g test condition of Case 14. Another choice was the unreacted density of 1.293 $\frac{kg}{m^3}$ which would have resulted in the predicted g-load to be around 300 g's for the same conditions. Each of these values either grossly over-predicts or under-predicts, respectively, the g-load value and instead the density used for g-load prediction was 0.7346 $\frac{kg}{m^3}$, which was in reasonable agreement with later estimations using a chemical kinetics program (ChemKin), which yielded approximately 0.6 kg/m^3. Once the seeder box was added, the UCC flow could be seeded and the actual tangential velocity could be measured using PIV at the ambient UCC exit location (Plane 6 in Figure 141).

Examining the 23 m/s tangential velocity conditions (Case 2), the spatial distribution of the tangential velocity is shown in Figure 154. As illustrated in this figure there was noticeable spatial variation in the tangential velocity. In order to quantify this spatial variation, a tangential velocity profile was plotted at y = 20 mm (approximate center of the 30 mm laser sheet height). This tangential velocity profile, shown in Figure 155, shows a parabolic distribution with slight weighting to the left hand side. In order to assign a single tangential velocity value for this test condition the

average of the velocity profile was used. This assumption assumes that the velocity distribution in the z direction (radial), which was not measured, was similar to the distribution in the x direction (channel width), which was measured. It is possible that significant variations in the velocity distribution exist in the z direction, but no data was obtained to confirm nor deny the assumption.

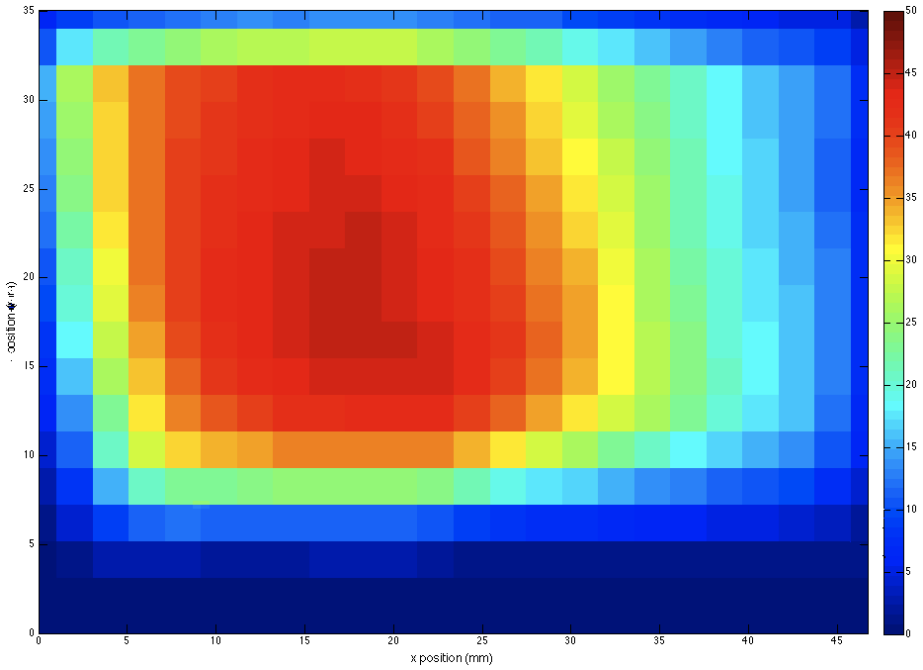

Figure 154. Spatial distribution of the tangential velocity at Plane 6 for Case 2 (straight UCC section) with predicted Vtan=23 m/s, VR=6.97 (MFR=0.2) & $\phi = 2.0$

Figure 156 compares the measured tangential velocity using PIV with the predicted tangential velocity for the straight section (Cases 1, 2, 3) and the curved section (Cases 13, 14, 26). This figure shows that for both UCC sections the measured tangential velocity did not always increase with the increased inlet mass flow rate of the higher predicted tangential velocity cases. For the straight section, Figure 156 shows that the predicted density produced tangential velocity estimates significantly lower than measured. The predictions were in much better agreement than using the unreacted or equilibrium flame densities and reasonable without previously existing data. The higher measured tangential velocity than predicted indicated that

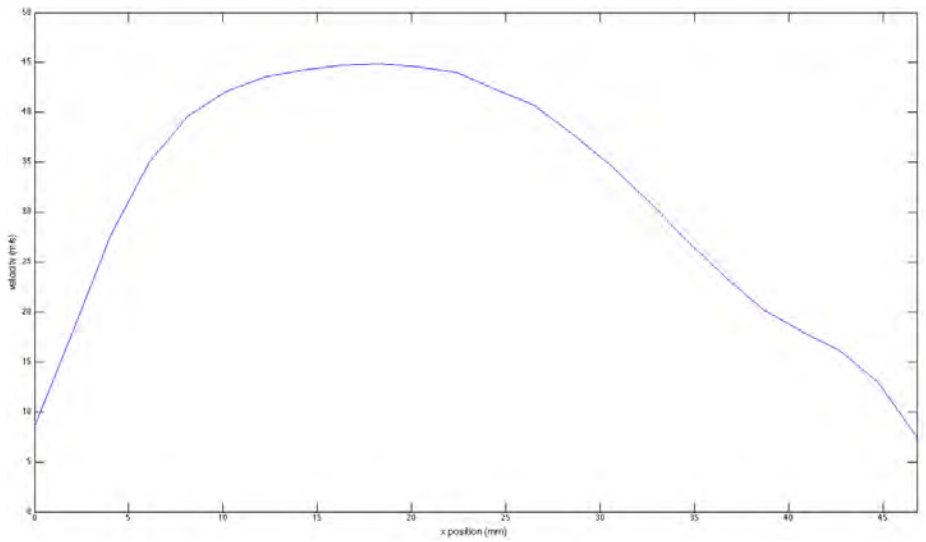

Figure 155. Tangential velocity profile at Plane 6 for Case 2 (straight UCC section) with predicted Vtan=23 m/s, VR=6.97 (MFR=0.2), & $\phi = 2.0$

the assumed density was higher than the experimental density. Also, the measured tangential velocity values indicated an asymptotic behavior towards 36 m/s which would correspond to approximately 2500 g's, whereas the predicted Vtan was around 23 m/s which corresponded to 1000'g. This was due to the increased migration of flow from the UCC into the core flow as g-load increases, as previously demonstrated. Therefore less flow remains in the circumferential cavity resulting in lower flow velocity in the UCC after the core flow interface with increasing g-load due to increased migration of mass from the UCC into the core flow. While the measured tangential velocity was hoped to provide a better density estimate, the asymptotic nature of the measured tangential velocity would require an almost exponentially increasing density with increasing mass flow rate, which would be non-physical.

Contrasting the straight section data with the data from the curved section showed that the curved section had a higher measured tangential velocity than the curved for the predicted 16 m/s condition, but at higher predicted Vtan conditions the straight section had a higher measured Vtan. There are two contributing factors that would have influenced the trend reversal. The first factor stems from the inclination

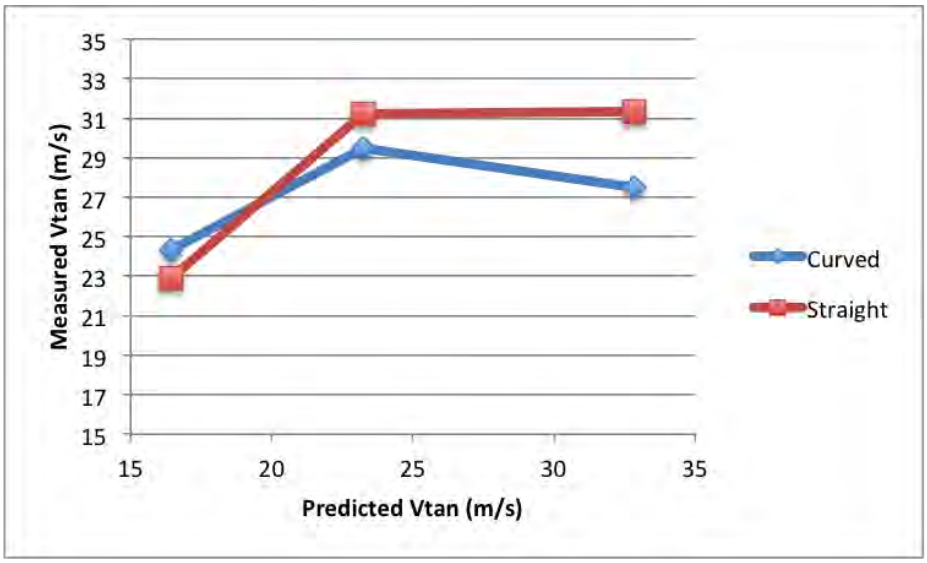

Figure 156. Comparison of the span-wise migration velocity (m/s), using PIV, and the predicted value for the straight and curved UCC sections

angle of the ambient exit flame to the outward radial direction with the curved UCC section. The flame inclination angle, see Figure 157, may increase with increased Vtan causing a decreased ratio of the tangential velocity to the total velocity. No data was collected to either quantify the inclination angle or quantify variations in the angle. The second factor was that as Vtan was increased, the quantity of mass migrating from the UCC into the core flow increased significantly at the higher Vtan conditions, which resulted in less mass and lower velocities in the UCC at the ambient exit. Both of these factors may have been influential, but the migration factor was supported by Lewis's research [13] that the centrifugal force does not become dominant until approximately 800 g's, or Vtan = 22 m/s. While measuring Vtan at the ambient UCC exit revealed distinctions between the straight and curved UCC sections, the actual tangential velocity at the core flow interface was not revealed.

The addition of the seeder box also allowed the UCC static temperature and pressure measurement location to be moved from the UCC air plenum to the interface of the UCC and seeder box of the curved section, as shown previously in Figure 29, to

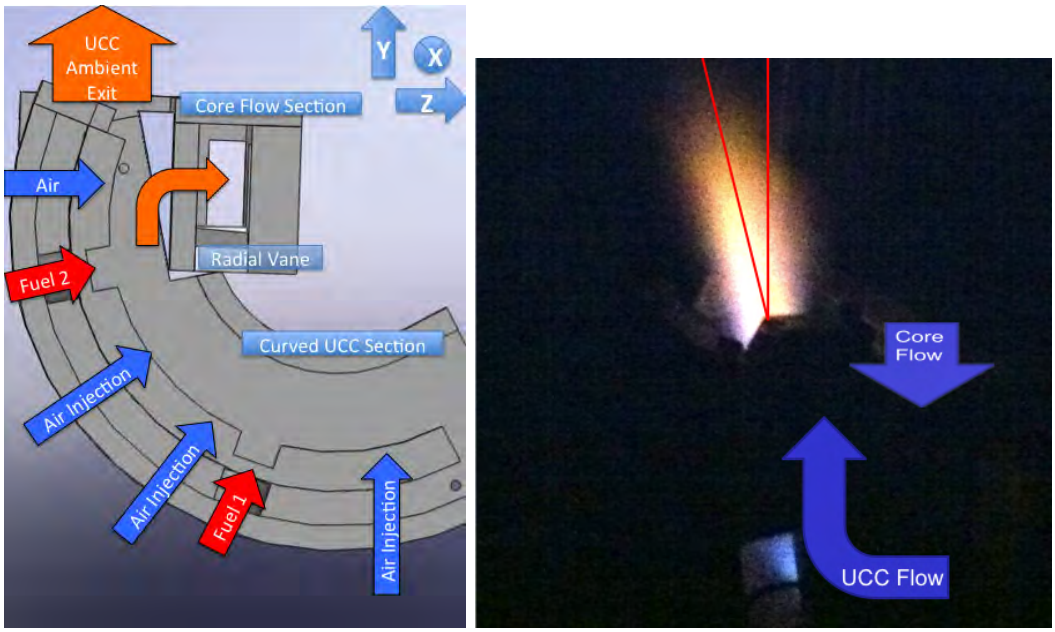

Figure 157. End view of the curved UCC section (left) and visual image of the ambient UCC exit flame inclined to the outward radial direction (right)

further improve g-load estimation. It was assumed that the measured density in the UCC seeder box was the same for both straight and curved section which is reasonable because both sections have the same inlet conditions. The pressure and temperature measurements in the seeder box were used to estimate the density using the classical Ideal Gas Law shown in Equation 20. In this equation the value of R was determined from theoretical equilibrium data to be 352 J/kg-K for $\phi = 2.0$. Because the flame within the UCC was not premixed, the value of R will vary spatially due to the discrete locations for fuel and air inlets. However, within the seeder box the value was assumed to be close to the equilibrium value, although no data currently exists to support or deny the assumption. These measurements estimated the average density to be approximately 0.37 kg/m^3 over the tested g-load range, but the actual values were 0.417 kg/m^3 for the predicted 500g condition, 0.376 kg/m^3 for the predicted 1000g condition, and 0.368 kg/m^3 for the 2000g condition. Using the measured density with the mass flow rate relation (Equation 7) the resulting estimated tangential velocity is

plotted against the predicted tangential velocity along with the measured values, from the PIV data, in Figure 158. The plot of the estimated tangential velocity from the computed density scales linearly with predicted tangential velocity and subsequently inlet air mass flow rate, as expected. Further, in the lower range there is relatively good agreement between the estimated and measured tangential velocity values with the estimated value always being higher.

$$P = \rho RT \tag{20}$$

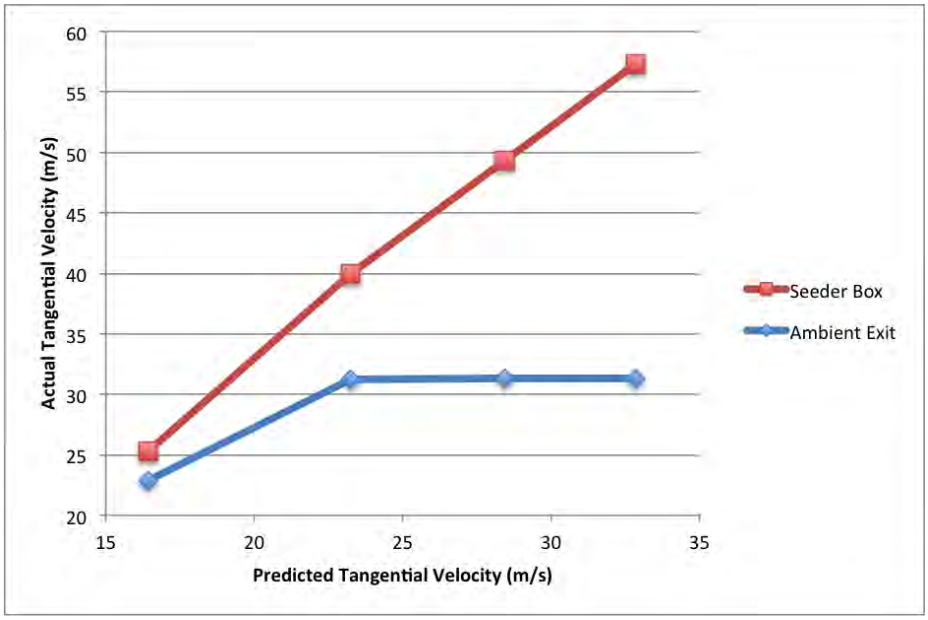

Figure 158. Comparison of the estimated tangential velocity (m/s), from pressure/temperature data, and the measured value, from PIV, versus the predicted value

Using two assumptions, the values from Figure 158 were used to estimate the g-load with the curved section. The first assumption was that the estimated flow velocity values were the total velocity values and not the tangential velocity component, which would be the case for the curved UCC section but not the straight section. The second assumption was that the flow velocity within the UCC progressed at a similar tangent angle as the tangent angle discussed by Zelina et al. for flow within that UCC

model, which was reasonable considering the observed inclination angle at the ambient UCC exit (Plane 6) was similar in value (around 25 degrees) to the angle reported by Zelina et al. (around 27 degrees) [7]. With these assumptions, the g-load was estimated and compared to the predicted values as shown in Figure 159. This figure indicates reasonable agreement between the predicted and estimated values based on experimental data with the predicted values being consistently higher. The predicted g-load values of 500, 1000, and 2000 actually yielded g-loads of about 308, 768, and 1582. The predicted g-load values were higher than the measured g-load values due to the combined effect of higher total velocity values than predicted and the presence of the 27 degree tangent angle of the UCC flow that was not used in the predictions. Using the estimated g-load values, the Froude number, the ratio of momentum forces to buoyant forces, was computed for both the straight and curved UCC sections using the previously shown Equation 12. For the straight UCC section, since g = 0 based on the UCC section orientation, the Froude number would approach infinity, which indicated the straight section flow was momentum dominated. Figure 160 shows that the Froude number was relatively constant, around 2.0, for the curved UCC section, which indicated the flow was neither momentum nor buoyancy dominated because the angular momentum generated the dominating buoyant force. However, roughly the same momentum existed for both sections, since the flow velocity was the same for both the straight and curved UCC sections, the decrease in Froude number for the curved section could only have resulted from the increased buoyancy for that section, which was generated by the g-load. This was an important result because it was postulated that the increased buoyancy, from the g-load, with the curved section was the dominant factor that led to increased flame migration for the curved over the straight UCC section.

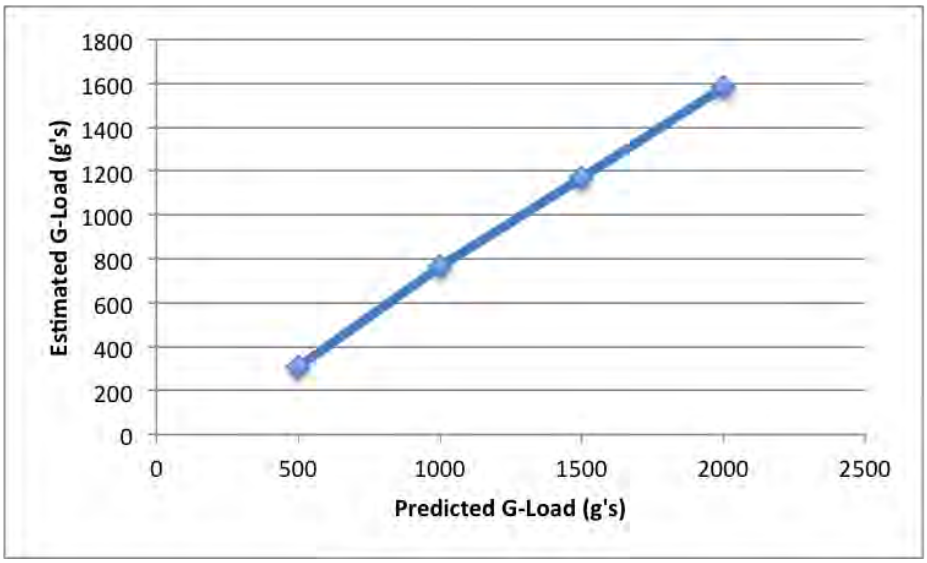

Figure 159. Comparison of the estimated g-load, using pressure/temperature measurements, and the predicted g-load using the curved UCC section

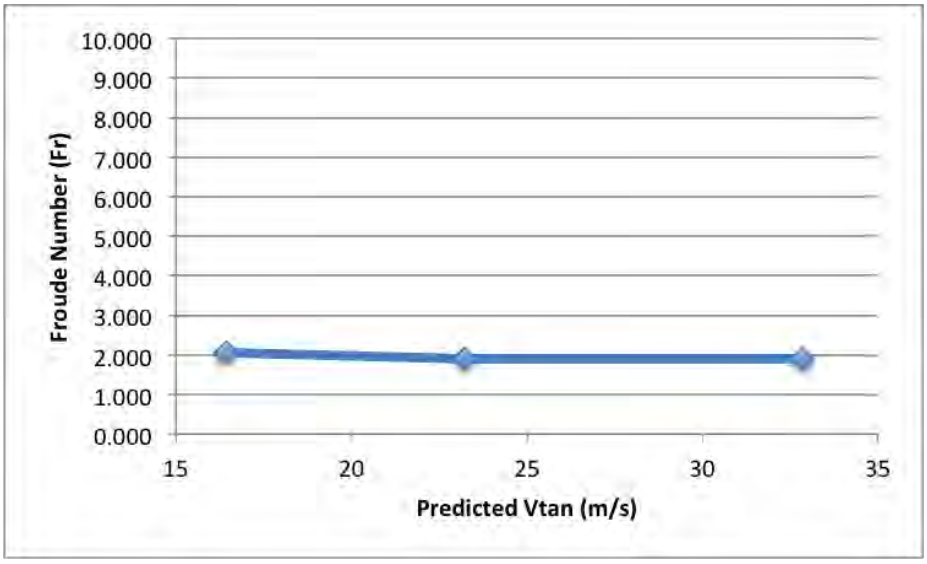

Figure 160. Plot of of the Froude number (Fr) with the predicted Vtan (m/s) with the curved UCC section

6.2.2.1 Migration Estimation.

For this sectional model, almost all of the UCC mass flow enters the UCC upstream of the core flow interface. The flow velocity, and subsequently g-load, will necessarily decrease after this interface due to migration into the core flow. Thus, the estimated tangential velocity value, from temperature and pressure data, functions as an upstream condition while the measured value, from PIV data, serves as the downstream condition. These two conditions can then be used to estimate the quantity of mass flow into the core flow using a simple mass balance and assuming a constant density and velocity distribution. These profiles were created for all of the additional cases and were used to estimate the mass flow into the core flow versus the estimated tangential velocity is shown in Figure 161. This illustrates a parabolic scaling of the migration mass into the core with the g-load for a constant MFR (and VR) that was reasonably approximated with a linear interpolation. Using the migration mass quantity with the area of the UCC/core flow interface yielded approximations for the span-wise (z direction) velocity component. Figure 162 compares the span-wise migration velocity with the buoyant force in the curved UCC section, using Equation 13. This figure showed that a linear relationship existed between the span-wise migration velocity and the magnitude of the buoyant force, which was the dominant factor in yielding higher flame migration with the curved UCC section over the straight section.

Estimating the migration quantity using the same relationship among all the constant VR cases (S1-16), Figure 163 illustrates a nearly linear relationship existed at all VRs. The image in Figure 163 also shows the trend that the flame migration increased with decreasing VR. Coupling this trend with the previous PLIF measurements, which showed decreasing core temperatures with decreasing VR, indicated that the higher core mass flow (lower VR at same Vtan) had a larger effect on the

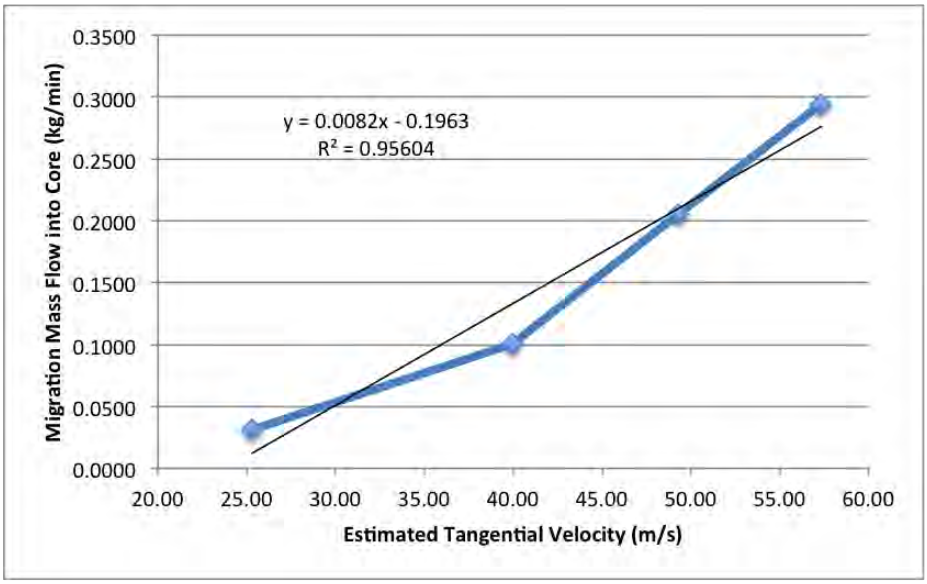

Figure 161. Estimation of the migration mass flow (kg/min) from the UCC into the core flow (ϕ) versus estimated tangential velocity (m/s) for $\phi_{UCC} = 2.0$ and VR=6.97 (MFR=0.2)

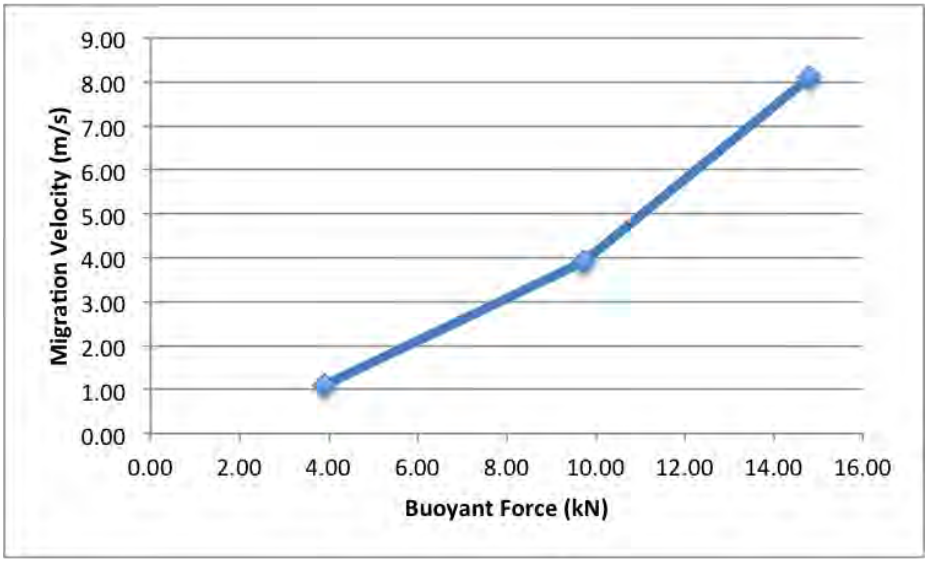

Figure 162. Comparison of the span-wise migration velocity (m/s) and the buoyant force (kN) for the curved UCC section

core flow temperature, and core flow ϕ, than the increased flame migration quantity. In other words, the increase in core mass flow responsible for decreasing the VR did not yield a proportional increase in the flame migration quantity leading to lower core ϕ and lower core flow temperatures. Figure 164 estimates the resulting core flow ϕ, computed using the previously shown Equation 14, accounting for the increases in migration relative to the total core flow. Assumed in the computation of core flow ϕ was that while the flamelets are quickly quenched upon entrance into the core flow, the flamelet ϕ was equal to the UCC ϕ which likely overestimates the core ϕ. Additionally, these estimates are for the 28 mm vane as estimates based on a different vane height will change the MFR for the same VR resultantly changing the core ϕ as shown previously in Equation 14. As expected, the higher VRs produced higher ϕ's, and resultantly higher temperatures not because the migration quantity was higher, but because the migration quantity relative to the core flow produced a higher core flow ϕ.

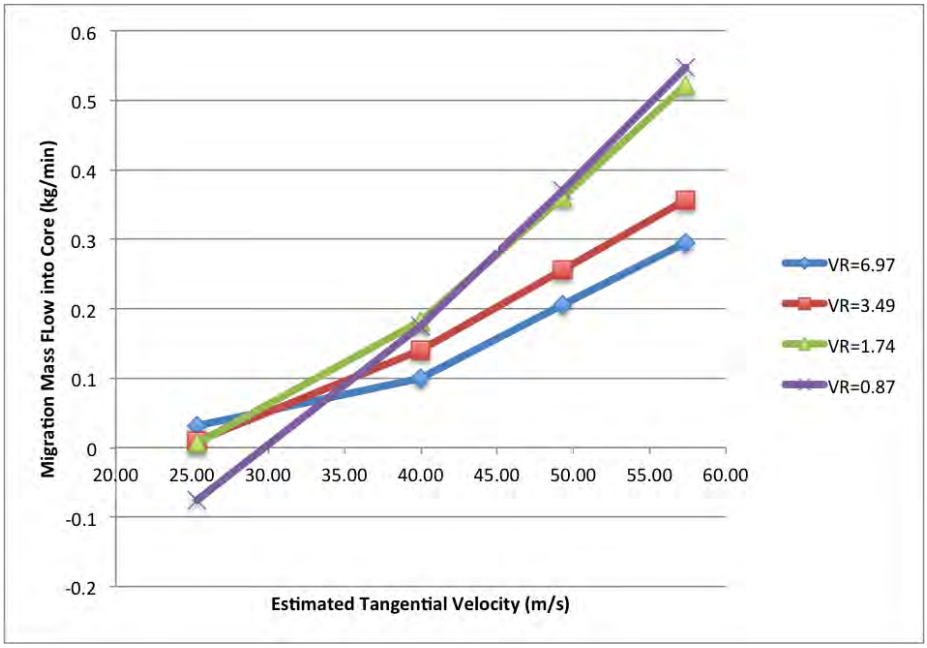

Figure 163. Estimation of migration mass flow(kg/min) from the UCC into the core flow (ϕ) versus estimated tangential velocity (m/s) for $\phi_{UCC} = 2.0$ and VR=0.87-6.97 (MFR=0.025-0.2)

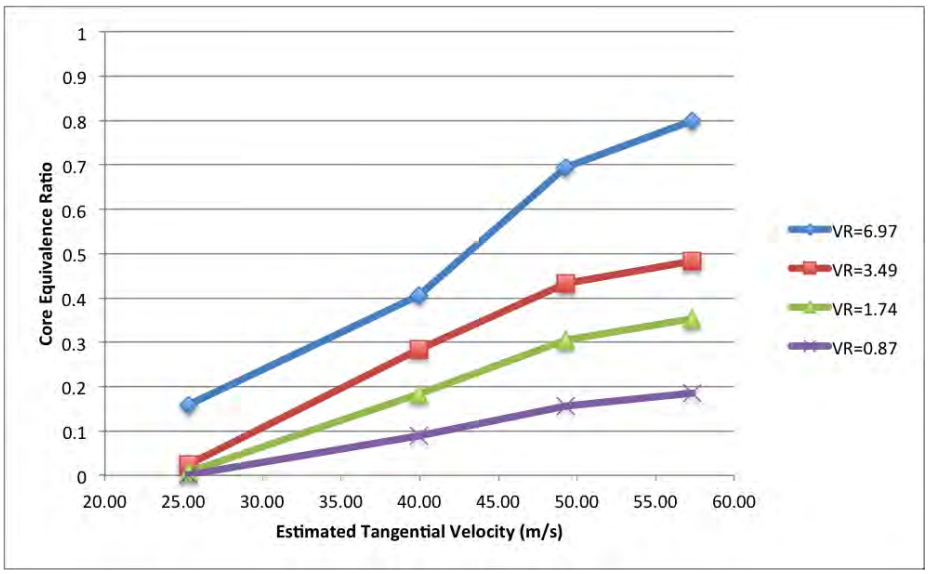

Figure 164. Estimation of the core equivalence ratio (ϕ) versus estimated tangential velocity (m/s) for $\phi_{UCC} = 2.0$ and VR=0.87-6.97 (MFR=0.025-0.2)

This analysis can even be extended another step farther considering that the core flow ϕ corresponds to a temperature based on the fuel-lean temperature vs. ϕ equilibrium data as shown previously in Figure 36. Applying this relation to the data in Figure 164 yields the corresponding core flow temperature values shown in Figure 165. These values can then be compared to the OH PLIF temperature data to determine the accuracy of the predicted temperatures. A comparison of these values to the measured temperatures for both straight and curved sections at the predicted 1000g condition is shown if Figure 166. Comparing the estimated temperature with the straight section first, since the mass flux estimation was derived from data collected on this section, shows reasonable agreement for an experimental correlation with an average 21.7% error with the estimation always over-predicting the measured temperature. However, comparing the estimated temperature with that of the curved section, since the curved section was shown to have higher migration levels, an average error of only 4.1% resulted which was well within the error of the measurement technique of about 7.5%. This demonstrates that the estimation of the migration

quantity produced reasonable results for an experimentally derived correlation.

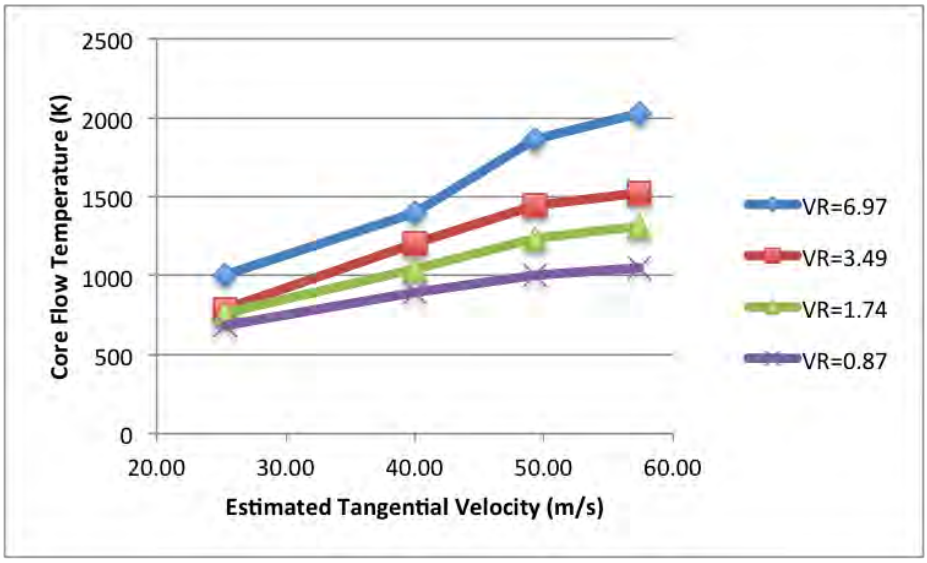

Figure 165. Estimation of the core flow temperature versus estimated tangential velocity (m/s) for $\phi_{UCC} = 2.0$ and VR=0.87-6.97 (MFR=0.025-0.2)

6.2.2.2 Analytical Model Derivation.

A closer examination of Figure 163 shows the trend for all VRs indicated the slope increased with decreasing VR, yet the data followed a similar trend with a common point near the condition of 35 m/s yielding 0.1 kg/min of mass flux into the core flow. Using similar linear curve fits for each line as in Figure 161 these linear equations were recast into the form of Equation 21 where y is the dependent variable, x is the independent variable, m is the slope, and (x_0, y_0) is the common point. This allowed the slope to be written as a simple function of the VR as shown in Equation 22. This allows the relationship between the tangential velocity and the migration mass into the core to also include the dependency on the VR resulting in Equation 23. However, VR is equal to V_{UCC}/V_{core} and when used with Equation 24 results in the recombined Equation 25. Further substituting Equations 7 and 20, result in Equation 26 where the core and UCC $\dot{m}$ values are inputted directly in kg/min with the core

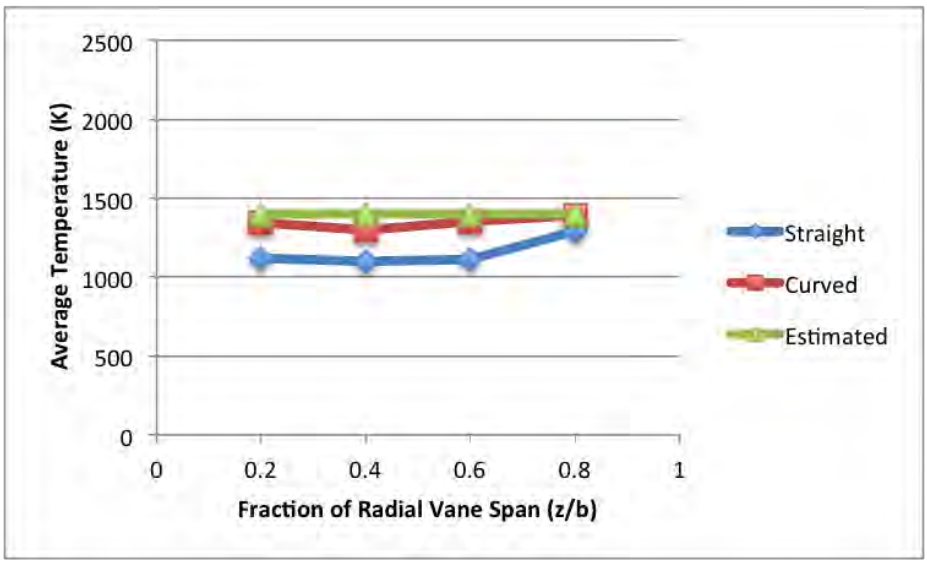

Figure 166. Comparison of the estimated core flow temperature (K), from the mass flux estimation, with the measured temperature (K), using OH PLIF, versus the radial vane span (z/b)

and UCC areas (constant) and measured Temperature/Pressure data in Kelvins and Pascals producing the migration mass into the core in kg/min. Since the vane height investigation concluded that changes in the vane height only produced changes in either the MFR or VR, depending on which parameter is matched, the only other parameter not present in Equations 23, 25 and 26 is the UCC equivalence ratio, ϕ. However, in lieu of repeating the data at different ϕ values, the impact was estimated using the measured changes in density and a ϕ coefficient was computed as shown in Equation 27, where ϕ is the tested value and ϕ_0 is 2.0 which was used for the rest of the data. Using C_ϕ as a multiplier to the slope results in Equation 28 which relates the migration mass into the core based on all of the experimental parameters ($\dot{m_{core}}$, $\dot{m_{UCC}}$, and ϕ). This quantitative relationship can then be used to reasonably predict the temperature rise in the core flow which occurs due to migration from the UCC. A comparison of the model prediction and measured migration mass flow rate with VR = 6.97 is shown in Figure 167. This figure shows that there was significant variation between the prediction and measurement, but the predicted results are

somewhat reasonable. Further, parameter relationships have been defined enabling the UCC design space to be determined to input reasonable flow parameter ranges and yield reasonable turbine inlet conditions. This is effectively an analytical model representing the UCC from a thermodynamic cycle. It is important to note that the migration model derived in this research, while insightful into the combustion physics, may not be representative of the migration values for a different UCC model, but the trends are expected to be the same.

$$y = m(x - x_0) + y_0 \tag{21}$$

$$m = \frac{1.0895 * 10^{-2}}{VR} \tag{22}$$

$$\dot{m}_{migration} = \frac{1.0895 * 10^{-2}}{VR}(V_{tan} - 35) + 0.1 \tag{23}$$

$$V_{tan} = \frac{60AP}{\dot{m}RT} \tag{24}$$

$$\dot{m}_{migration} = (1.0895 * 10^{-2})V_{core}\left[1 - \frac{35}{V_{tan}}\right] + 0.1 \tag{25}$$

$$\dot{m}_{migration} = (1.0895 * 10^{-2})\frac{\dot{m_{core}}R_{core}T_{core}}{60P_{core}A_{core}}\left[1 - 35\frac{60A_{UCC}P_{UCC}}{\dot{m_{UCC}}R_{UCC}T_{UCC}}\right] + 0.1 \tag{26}$$

$$C_\phi = \frac{\phi}{\phi_0} \tag{27}$$

$$\dot{m}_{migration} = (1.0895 * 10^{-2})\frac{\phi}{2}\frac{\dot{m_{core}} R_{core} T_{core}}{60 P_{core} A_{core}} \left[1 - 35\frac{60 A_{UCC} P_{UCC}}{\dot{m_{UCC}} R_{UCC} T_{UCC}}\right] + 0.1 \quad (28)$$

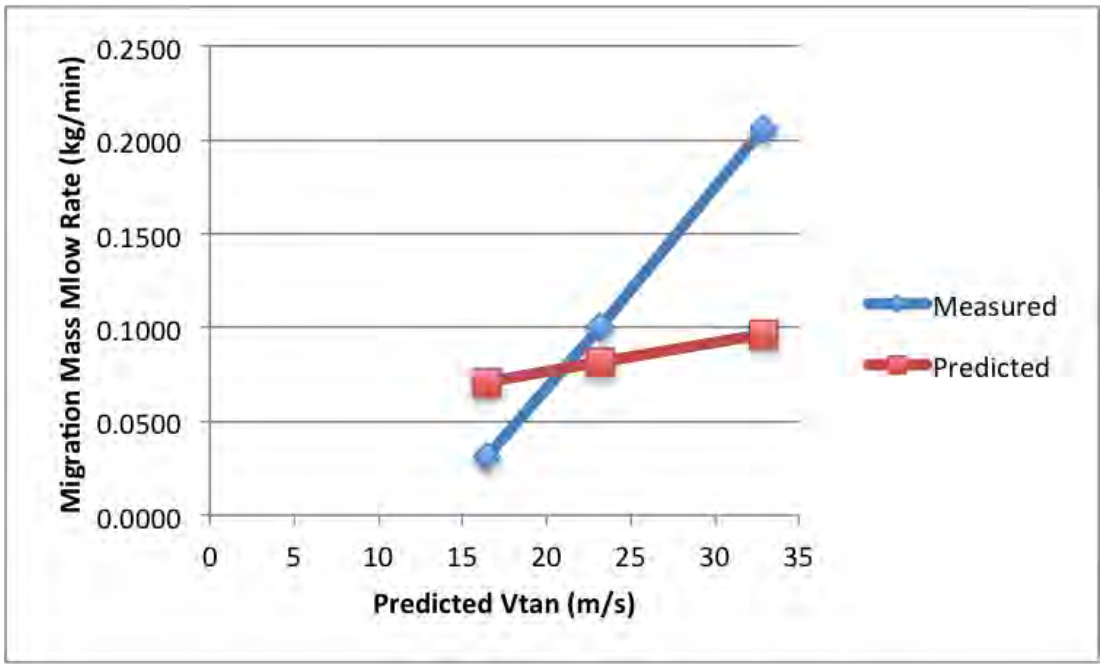

Figure 167. Comparison of the measured and predicted migration mass flow rate (kg/min) vs. the predicted Vtan (m/s)

VII. Conclusions & Recommendations

7.1 Summary

The overarching goal of this research was to yield a quantitative characterization of the centrifugally-loaded flame migration occurring within the UCC. Specifically, this characterization was needed to determine the feasibility and design space for scaling the UCC to a larger diameter. Three objectives were identified and investigations were conducted to address the objectives using PLIF, PIV, HSV, and traditional temperature and pressure measurements. The first objective, the v-shaped flame investigation, was to understand why the ambient UCC exit flame shape with the straight UCC section had a v-shape while the curved section did not as observed by Drenth [9]. The second objective, the vane height investigation, was to understand the effect of scaling the radial vane to a larger height consistent with a larger diameter UCC. The third objective, the g-load investigation, was to understand the implications resultant from adding the g-load to the flame and its effect on the migration into the core flow.

7.1.1 V-Flame Investigation.

Previous research by Drenth documented the elimination of the v-shape flame at the ambient UCC exit with the curved UCC section, but noted discrepancies in the exit area compared to the straight section [9]. The flame shape was investigated extensively using OH-PLIF and for select cases with visual flame images. A variety of flow conditions were tested which corresponded to g-loads from 39 g's (Drenth's condition) up to 1000 g's with the curved section and MFRs from 0.1 to infinity. Once the ambient exit area of the curved UCC section closely matched that of the straight UCC section, a nearly identical v-shape was measured at the ambient exit of

each UCC section with the curved being inclined to the outward radial direction due to the presence of centrifugal loading within that UCC section only. The phenomena observed by Drenth was not the elimination of the v-shape by the g-load, but by the change in the ambient UCC exit area between the straight and curved UCC sections. In Drenth's study, the curved UCC did not exhibit a v-shape due to the funneling of the flame through the constricted exit area.

With the g-load eliminated as a cause of the v-shape, the effect of the core flow on the v-shape was investigated. While the v-shape was present over a range of core flow velocities, the v-shape was eliminated only when the core flow velocity was set to zero, which corresponds to an MFR of infinity. Elimination of the v-shape with an infinite MFR confirmed that the v-shape was a result of the shear layer at the interface of the UCC and core flows. The contribution of each UCC injector on the flame shape was further investigated by isolating each fuel injector individually. This showed that the flame produced by each injector independently filled the windward side of the UCC. However, considering the combined shape showed that injector 1 must fill the windward side due to being injected first and resultantly forcing injector 2 to fill the leeward side which creates the v-shape.

Since the v-shape, or bimodal, flame was a dominant feature, the implications of this feature are important to address as this feature is likely to exist for the annular UCC model. This bimodal distribution in the flame shape likely carries an equally bimodal thermal distribution. A bimodal thermal distribution would likely have lower peaks, depending on the ϕ in the UCC, than a single mode because more of the UCC channel would be filled and peak temperatures must decrease as the heat release is distributed over both modes, which would be beneficial and could potentially yield significantly lower temperatures for both the flow and wall surface with the heat release occurring over a larger volume within the UCC. This would be a significant

benefit to future UCC designs but further investigation is necessary to determine if these effects are significant as this investigation looked only at the flame shape and the measurements were not taken inside the UCC.

While the v-shape was dominant for this UCC geometry, changes in the geometry might be able to counteract the feature. Specifically, angling the fuel and/or air inlets towards the windward and/or leeward side might eliminate the v-shape if directed counter to the preferred side. However, this requires a priori determination of which fuel injector produces a flame to which side and if determined incorrectly would likely increase the bimodal nature of the distribution. Also, like the curved interface of the seeder box with the curved UCC section, the addition of small opposing curvature cavities or possibly simple flame-holding protrusions might be a better alternative to angling the fuel and air inlets as these would likely be unaffected by the preference of a specific injector to a specific side of the UCC. Further, aside from angling the fuel inlet holes, the holes themselves could be moved to either the windward or leeward side, but this would likely increase the bimodal nature of the flame shape as well. Also, the channel width of the UCC could be reduced significantly and would force the physical location of the two modes to move closer until coalescence into a single mode. This investigation determined that changes in the flowfield parameters, both g-load and MFR or VR, did not significantly affect the presence of the v-shape, but further investigation is required to determine the implications of physical geometry changes.

7.1.2 Vane Height Investigation.

This objective was focused on characterizing the effect of increasing radial vane height on the migration of turbulent g-loaded flames within a sectional model of the UCC. The test rig was constructed to represent a section of the full UCC rig

currently used by AFRL/RZTC and to allow optical access for using non-intrusive laser diagnostics. The investigation was centered around using 14, 28, and 56 mm radial vanes in the core flow section while maintaining identical flow conditions for UCC to core air flow ratios, MFR=0.1, 0.2, 0.3. By varying the UCC mass flows the g-load was investigated at 500, 1000, and 2000 g's for the 28mm vane and 1000 g's for the 14 and 56 mm vanes. Propane (C_3H_8) was used with a constant equivalence ratio, $\phi = 2.0$ in the UCC, and two-line OH Planar Laser-Induced Fluorescence (PLIF) thermometry was used along side of High-Speed Video (HSV) to investigate the flame migration from the UCC into the core flow above the radial vanes.

This investigation has shown the insight gained from qualitative and quantitative 2-line OH-PLIF thermometry interrogation at the combustor-turbine interface. For the first time, stream-wise, pitch-wise, and inferred span-wise temperature distributions were analyzed at this interface. The feasibility of flame migration over significantly taller radial vanes was established. It was shown that the higher g-load cases (13,14,26) exhibited higher flamelet distributions and resultantly higher time-averaged temperatures. The optimal MFR for each vane was 0.2 which was consistent with the resultant increased VR as the MFR was held constant over increased vane height. The increased VR likewise increased the flame injection angle which allowed for the flame migration to spread across the larger span. Thus, for a given radial vane height an appropriate injection angle should be chosen to yield the desired exit temperature profile and the core flow velocity adjusted accordingly. However, this may not always be an available option and appropriate design tradeoffs will be necessary. The flame injection angle from the UCC into the core flow was determined to be dependent on the core flow velocity almost exclusively, even independent of g-load range tested which did increase the mass flux quantity from the UCC into the core flow. The g-load did not have a noticeable effect on the flame injection angle, however, it

did impact the quantity of flame migration that exited the UCC and subsequently filled the vane passage.

7.1.3 G-Load Investigation.

The goal of this investigation was to understand the effects of the presence and variation of the g-load on the radial migration of the hot gases exiting the UCC flow path and entering the core flow path. While the main parameter of interest for this study was obviously the g-load, its coupling with the UCC/core air MFR, and resultant VR, was also of interest. Initial results were obtained concurrently on Test Cases 13-15 and 26 with the vane height investigation using PLIF and HSV which indicated increased migration into the core flow with increased g-load. In order to isolate the g-load contribution, Cases 1-3, 13, 14, and 26 were investigated using PLIF, PIV, and HSV for a comparison of the test conditions with and without the g-load. Then, the tangential velocity was measured for several g-load conditions in order to accurately determine the actual g-load relative to the predicted values.

A detailed comparison of the three g-load conditions was conducted for both the straight and curved sections to isolate the effect of the g-load specifically. The straight section visibly had lower flame migration levels in the HSV data which was reinforced by lower temperatures reported by the PLIF data versus the same conditions with the curved UCC section. Exit velocity profiles for both the straight and curved UCC sections were compared with the curved section yielding larger velocity increases over the straight section. The increase in velocity was due to the increased flame migration from the UCC into the core flow. The velocity profile data supported the HSV and PLIF data that higher levels of flame migration occurred in the core flow with the curved UCC section over the straight section. Supporting the vane height investigation trend that the flame angle was dependent on the UCC/core velocity

ratio alone, both the straight and curved UCC sections had nearly identical injection angles for each section across the g-load range. Using both PIV and HSV analysis, the curved section was shown to have higher levels of unsteadiness which could be detrimental to the turbine rotor.

For the first time measurements of the actual tangential velocity were taken for computing the g-load. Higher than predicted values were measured using both PIV and pressure/temperature data. The pressure and temperature data collected in the seeder box were used to estimate the density of the UCC flow and used to compute the tangential velocity, using the classical mass flow rate relation. The PIV measurements collected at the ambient UCC exit were used with a constant density assumption and symmetrical tangential velocity distribution to estimate the exiting mass flow rate. A control volume within the UCC section was established such that the decrease in the mass flow rate from the inlets of the UCC section to the ambient UCC exit must represent the mass flow rate into the core flow. Inline with observed trends, this estimation of the mass flow rate into the core scaled linearly with the UCC input mass flow rates, as expected. Thus, the relationship between the tangential velocity and mass flow rate into the core was demonstrated and a correlation was derived for the specific VR of 6.97.

Not only was the tangential velocity measured for the first time, but also quantifiable estimates for the mass flux into the core flow, which was of greater significance. Additional cases were tested to study the entire VR range of 0.87-6.97 which showed similar nearly linear relationships differing only in slope with an approximate common point for all the lines. These lines showed an increasing mass flux into the core with decreasing VR, but the core ϕ decreased due to the increased core flow air mass. Additionally, using the estimated ϕ to estimate the core flow temperature resulted in reasonable temperature estimates for the straight section, around 22% error, and very

good estimates for the curved section, around 4% error, which was demonstrated to have higher migration levels than the straight section. This confirms the estimation of the migration quantity produced reasonable results. Using the common point, the relationship between the tangential velocity and the core mass flux was recast using the slope as a function of the VR and a relatively simple relation was produced between the VR and the tangential velocity to the core mass flux. Using two additional cases to estimate the relationship with changes in ϕ, a correction coefficient was postulated and an overarching relation between all of the experimental parameters with the core mass flux was derived. While this relation was derived from data taken with the straight section, previous data indicated higher migration levels with the curved section, and the trends are expected to be the same with higher migration values. It is important to note that the migration model derived in this research, while insightful into the combustion physics, may not be representative of the migration values for a different UCC model, but the trends are expected to be the same.

7.2 Conclusions

The overarching goal of this research was to characterize the migration of centrifugally loaded flames in the Ultra Compact Combustor. The v-shaped flame at the ambient UCC exit of the straight UCC section observed by Drenth [9] was determined to be unaffected by the addition of or variations of the centrifugal loading. Drenth's observed change in flame shape was the result of a two-fold difference in the ambient UCC exit area that changed the flow dynamics and resultantly the flame shape. However, the presence of centrifugal loading did change the orientation of the v-shape adding an inclination to the outward radial direction. This only happens at the ambient exit due to the free expansion which is not present in an annular UCC and as such would not likely see the same effect. The ambient UCC exit flame

shape was affected by the UCC/core velocity ratio with the flame distribution being weighted more to the leeward leg at higher ratios due to increased migration into the core which pulled from the windward leg first. When scaling the UCC to a larger radius, it was determined that matching the same UCC/core velocity ratio produced the same flame injection angle into the core flow. This fact can then be used to predict the penetration depth of the flame based on geometry. It was also determined that while the velocity ratio determined the flame injection angle, the g-load affects the quantity of migrating mass from the UCC into the core with higher g-loads yielding higher migration by as much as a factor of three. The velocity ratio was also shown to affect the migration mass with lower ratios yielding higher mass flux quantity but producing lower core flow equivalence ratios due to sufficiently higher core air mass. Higher migration mass at the same velocity ratio directly led to higher core flow temperatures. Straight and curved UCC sections were compared to show that adding a centrifugal load increased the flame migration into the core flow producing higher average core temperatures and more uniform temperature distributions. The first time-resolved PIV and HSV data were collected and analyzed to show increased unsteadiness levels under the presence of a centrifugal load that was dominated by a 130 Hz phenomena. This dominant frequency was manifested as pulsations in the flame migration where significant migration occurred for particular time periods while minimal migration occurred for other time periods. It was also demonstrated that the migrating mass into the core can be estimated using pressure and temperature measurements upstream and PIV measurements downstream of the core flow interface with constant density and tangential velocity profile assumptions. The migrating mass quantity can be used to estimate the core ϕ using the UCC/core mass flow ratio, and subsequently the core flow temperature. The estimated core flow temperatures were in good agreement with the measured values using OH PLIF. The migrating

mass was estimated to scale linearly with tangential velocity, which corresponds to the g-load value, while testing at various UCC/core velocity ratios resulted in similar linear relationships of different slopes. The slope was determined to be a function of the velocity ratio resulting in a simple relation showing the dependence of the mass flux on the tangential velocity and the velocity ratio. Estimates were made to account for changes in the UCC equivalence ratio on the migrating mass resulting in a single, relatively simple, relation showing the dependence of the migrating mass on all of the parameters investigated in this study (tangential velocity, velocity ratio, and UCC ϕ). Using the migrating mass estimations and the UCC/core mass flow ratio, the core flow equivalence ratio can be estimated along with the average combustor exit temperature, which will be similar to the turbine inlet temperature. The quantitative relationships determined in this research provided a detailed description of the migration of centrifugally loaded flames in the Ultra Compact Combustor.

7.3 Recommendations

Throughout the extensive nature of this research, some aspect of almost every part was changed from previous research. However, numerous other recommendations are still left for implementation that likewise cover almost every aspect. These recommendations range from simple to complex and from inexpensive to costly but represent a large list of goals for the immediate, short-term, and long-term.

7.3.1 UCC Design.

While the limitations of sectional models has been discussed both in general and specifically, there are several improvements that can be made. The majority of the data indicated that the migrating flame moved away from the radial vane and towards the upper core flow section wall, in the pitch-wise or y direction, which can be thought

of as the pressure side of the adjacent radial vane. However, due to the created pressure gradient of the vane the suction side is preferred implying the orientation of the radial vane should be reversed, placing the suction side on the upper wall instead. This should significantly improve the effectiveness of the radial vane cavity of this sectional model even though both sides of the vane are not present. This leads to the larger issue that a larger sectional model should be built.

A larger sectional UCC model was originally proposed by Drenth but the proposed concept of essentially doubling the existing model is not feasible. Instead, a new model should be constructed in light of the discussion about the limitations of sectional models. Additional buildup in the UCC section prior to the core flow interface is desired to produce more representative conditions at the interface. Also, after the core flow interface a "build-down" length should be added to remove any potential issues resulting from having the ambient UCC exit near the core flow interface. Additional optical access is desired in the UCC section to allow reasonable measurement of the flow within the channel rather than at the ambient exit, although this will remain a useful measurement location. Additional pressure and temperature measurement locations should be added throughout to provide density computations for tangential velocity estimation and general flow field characterization. Construction of a new model also allows for a more representative radius to be mimicked as the intention is to scale the UCC to a larger class of engines. In addition to increasing the UCC section size, the core flow sections should also be increased to encompass at least one full vane, both sides together, and should have representative surfaces on each wall in the circumferential direction. An illustration of what this model might look like is shown in Figure 168 from Wilson [19]. From this conceptual drawing work has already begun using cold flow tests on a plastic mock-up of the design shown in Figure 169 from Benhassen [20] and in construction of this design out of suitable

materials for combustion experiments by Wilson [19].

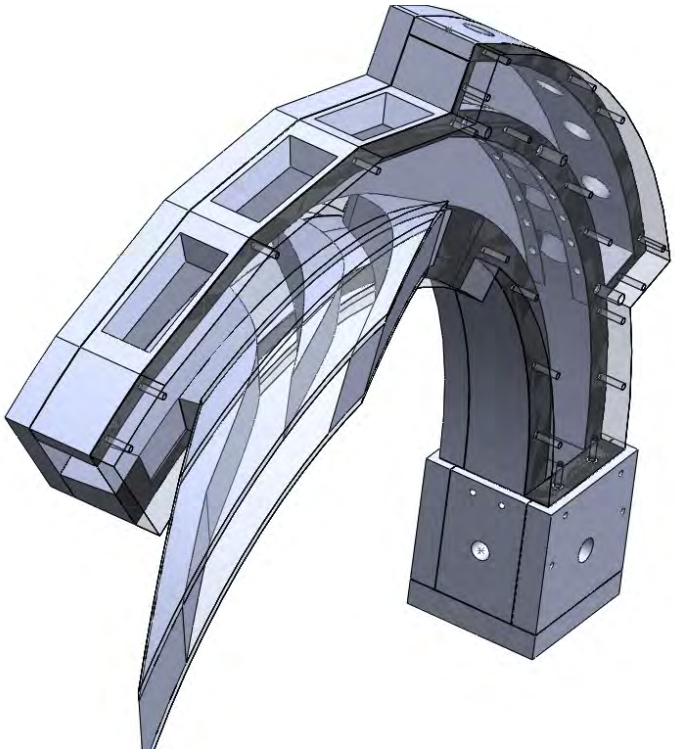

Figure 168. Solidworks model of a fighter-sized UCC sectional model from Wilson [19]

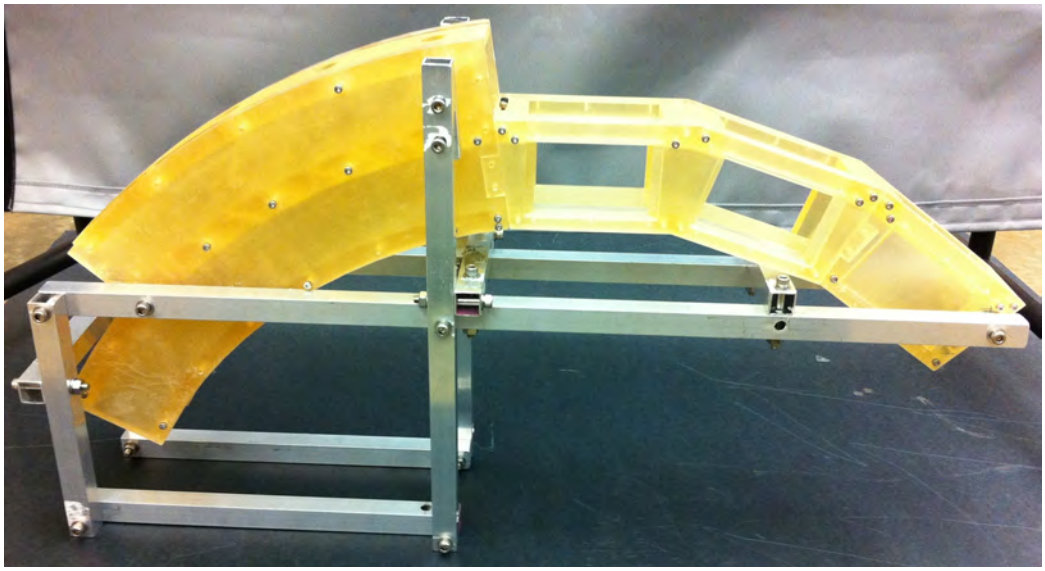

Figure 169. Plastic cold flow model of a future UCC sectional model from Benhassen [20]

7.3.2 PLIF System.

Several improvements could be made to the PLIF system to improve the accuracy and capability of the system. Simultaneous pulse energy measurement during data collection would improve the usability of the system and increase the accuracy by having better pulse energy normalization values. While significant laser power spatial distributions were not visually observed, using suitable dye cells to measure and correct for laser power spatial variations would also improve the measurement accuracy, but would also increase the complexity. Drenth observed laser scatter issues believed to be related to concurrent PIV testing [9], but sufficient care was taken to avoid that with this research yet laser scatter issues persisted. The laser scatter remained an issue, which was corrected for via background subtraction, but would be improved with better camera filters. Instead of the long-pass WG-295 a high transmissivity bandpass filter covering the 300-320 nm range is believed to improve the laser scatter issues. Finally, better ICCD cameras have been on the market for years that provide up to 30 Hz imaging at the camera's full 1024x1024 pixel resolution. This will improve the spatial resolution of the PLIF imaging which was forced down to 512x256 pixels in order to reach 10 Hz. All of these recommendations combined could potentially yield a significant increase in the spatial accuracy of the system and result in the added capability of single-shot temperature measurements.

7.3.3 PIV System.

Several improvements could be made to the PIV system to improve the system. From an overall operation standpoint, the release of the Dantec Dynamic Studio v3.2 software finally added the capability for operation of the system within the software. The release of v3.2 did not occur until after the data was collected for this research and the added capability was not tested. However, the capability exists to save sev-

eral steps in the PIV data collection and processing procedures. Also, upgrades to the software could be purchased to improve the data processing timeline as well. The distributed analysis package would allow all of the COAL Lab computers to collectively process the PIV data, instead of just the single computer which took roughly 7 days to process the entire PIV data collection. Further, additional upgrades are available that would provide insightful analysis into the time domain of the data. While code for similar analysis can be written in MATLAB, the upgrades would provide much simpler means with much easier to interpret data. The upgraded analysis modules are the Proper Orthogonal Decomposition module and the Dynamic Mode Decomposition module. Further, more simple spectral analysis methods may also be used to investigate the transient flow field behavior.

In addition to software upgrades, there are a few hardware upgrades that could be made to the PIV system. First, due to the use of a continuous-wave laser, there were low signal-to-noise ratios for the data. Using a higher power c-w laser would help improve that issue. There are also higher sensitivity cameras that would also help improve the issue. Large out of plane velocity components (span-wise) were indicated but shifting the data collection plane required unfeasible camera geometry due to flame trajectories. However, using a second camera for stereo PIV would allow capture of the third velocity component while imaging from the same direction and may be the only reasonable solution to reaching sensible time-resolved data of the UCC to core flow migration. Finally, the addition of specialized lenses used for complex imaging geometries, or possibly just deflecting the ambient UCC flame away from the camera, may allow for data collection parallel to the radial vane which could be more insightful than the perpendicular planes that were used for this research.

7.3.4 High-Speed Video.

The HSV data proved to be invaluable with regard to the interpretation of planar data, characterizing the flame geometry, and gaining insight into the temporal variability. There is an immense amount of data remaining to be analyzed within the HSV movies. This is both a blessing and a curse because realistic analysis of that quantity of data becomes the issue. However, similar mathematical techniques may be used to analyze time-resolved PIV data such as Proper Orthogonal Decomposition, Dynamic Mode Decomposition, or spectral analysis. Also, the monochrome camera may be used unfiltered for higher acquisition frequencies or using filters to isolate the direct emission from a particular flame species. Color cameras naturally apply bandpass filters, by definition, which isolate emission from specific flame species that could be used as for pyrometric temperature determination. This pyrometry technique could also be paired with the PIV like technique of Particle Streak Velocimetry where rather than the correlation of particle movements between images the particle is illuminated over a longer exposure time creating a streak line of its trajectory which can be converted into velocity. The combination of these two techniques could produce temperature and velocity data from a single image allowing correlation of the instantaneous fields rather than being relegated to a time-averaged comparison.

Appendix A. Laser Diagnostics Not Used in This Research

While PLIF and PIV were used extensively in this research, the AFIT COAL lab has an expansive list of available laser diagnostic techniques. The details of the PLIF and PIV systems are covered in Chapter 3, but background literature on the remaining major techniques are covered in this appendix. This material is included in an appendix for reference as the entire COAL lab suite was considered in the selection of techniques to used for this research. These additional diagnostic techniques are Tunable Diode Laser Absorption Spectroscopy (TDLAS), Laser-Induced Incandescence (LII), Rayleigh scattering, and CARS. According to Serianne, the TDLAS technique is used to measure 1D species concentration, pressure, velocity, and temperature [48]. LII is a technique for imaging the planar soot particle distribution, according to Eckbreth [15]. The Rayleigh scattering technique can be used to measure 2D pressure, temperature, velocity, and species concentration, according to Muraoka and Maeda [49]. CARS is used to measure point-wise pressure, temperature, and species concentration to very high accuracy, according to Eckbreth [15]. This suite of diagnostics form a composite picture designed to be the most effective in combustion diagnostics making the COAL lab the ideal location to conduct research in optimizing the UCC design with each diagnostic having it's own unique advantages and disadvantages.

The advantages and disadvantages of each diagnostic technique were considered in the selection of the diagnostic techniques used in this research. Understanding the spatial variation was important based on the research objectives necessitating planar or 2D measurements which eliminated TDLAS and CARS from further consideration. Temperature was a key parameter of interest, but only PLIF and Rayleigh scattering provided planar measurements. PLIF was selected over Rayleigh scattering due lacking a suitable laser for measuring Rayleigh scattering in a combustion environment. PLIF was also well documented by previous AFIT researchers investigating the UCC,

specifically Koether, Hankins, Lakusta, and Drenth [41; 3; 42; 9]. Velocity was also a key parameter of interest, but only PIV and Rayleigh scattering provided planar velocity data. PIV was selected over Rayleigh scattering for velocity measurement for the same reason that PLIF was selected over Rayleigh scattering, a suitable laser for measuring Rayleigh scattering in a combustion environment was not available. LII was not chosen for this research due to soot not being thought to be a significant issue in the UCC due to the high mixing levels. However, all of the considered laser diagnostic techniques are discussed here for brevity.

A.1 Tunable Diode Laser Absorption Spectroscopy

According to Serianne, TDLAS is a line-averaged laser diagnostic technique using a diode laser with the frequency continuously swept over a specific band [48]. This specific band is targeted to a particular molecular species such that the particular species will absorb photons from the laser at specific wavelengths, according to Serianne [48]. These specific wavelengths are characteristic of the specific species and form that species absorption spectrum, which will be manifested as wavelengths where there is a reduced intensity, according to Serianne [48]. Serianne stated that in actuality, the spectrum is not of discrete lines, but rather a normalized distribution around that particular wavelength [48]. This normalized distribution that results (see Figure A-1) is related to temperature from the FWHM value, as demonstrated by Serianne [48]. Since this absorption curve is generated at the full 20 kHz operation of the diode laser, this can yield time-resolved temperature measurements within the flame at a maximum of around 10kHz due to the Nyquist sampling criterion. While TDLAS has great time-resolution and future applicability to planar measurements, AFIT's current system only provides a line-averaged measurement and not planar data which is of particular interest for this research.

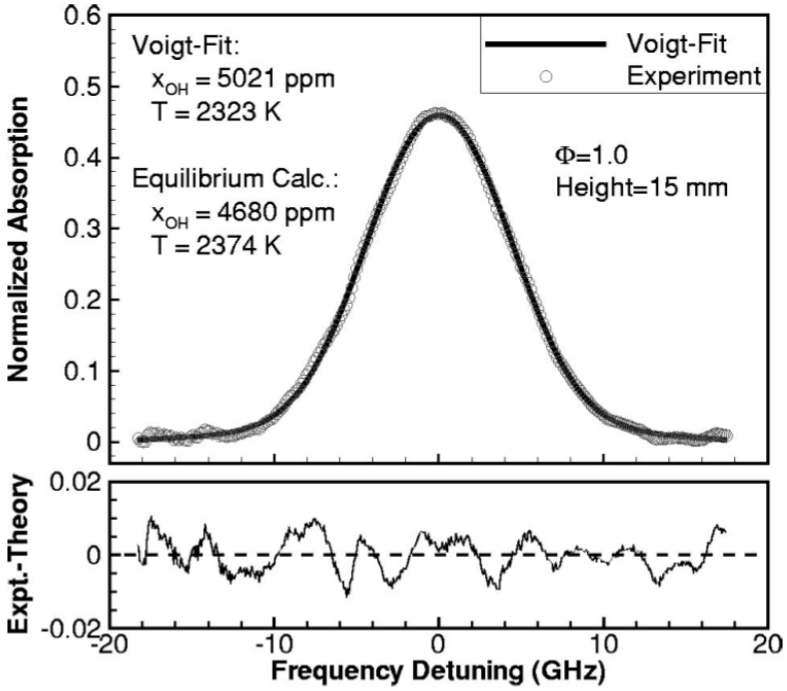

Figure A-1. Single-sweep OH absorption spectrum at 20kHz in a $C_2H_4 - air$ flame from Anderson [21]

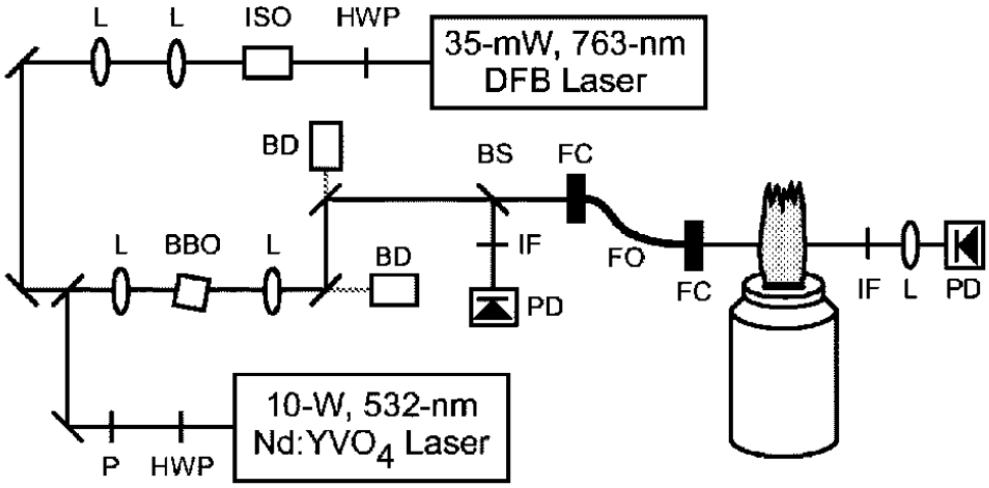

Figure A-2. Example of a TDLAS setup from Anderson [21]

A.2 Laser-Induced Incandescence

According to Eckbreth, LII is a laser-based visulization technique that is used to measure the planar soot particle distributions [15]. In the COAL lab LII setup (see Figure A-3), 532 nm wavelength from the Spectra-Physics PIV400 10 Hz Nd:YAG laser is focused into a sheet and directed into the flame and imaged with an ICCD camera with a 610-650 nm bandpass filter, as documented by Drenth [9]. In order for LII signal to be present two conditions must be met. First, there must be significant soot in the flame which for the test data on the Hencken burner, see Figure A-4, was collected for a $\phi < 2.5$. Second, significant laser energy must be present, above 200 mJ/cm^2 according to Schultz et al., to vaporize the soot particles [63]. As shown in Figure A-4, this technique can be used to show locations with high soot production resultant from localized combustion inefficiency. However, soot production is not believed to be significant in the UCC due to the high mixing levels and this technique was not used.

A.3 Rayleigh Scattering

In contrast to the previously mentioned spectroscopy techniques (PLIF, TDLAS, LII), Rayleigh Scattering uses the given species of interest in the mode to function as a lens, deflecting or scattering the incident laser light from its original path, according to Muraoka & Maeda [49]. According to McCartney, this is the same principle responsible for the blue color of the sky as postulated by Lord Rayleigh, whom the technique is named [64]. Since the incident light is merely deflected it will be on the same order as the incident light, shifted by a value related to the particle velocity as well as temperature and density, according to Muraoka and Maeda [49]. In particular, Rayleigh Scattering uses incident light with a wavelength sufficiently large compared to the interested species' particle size and is an elastic scattering by

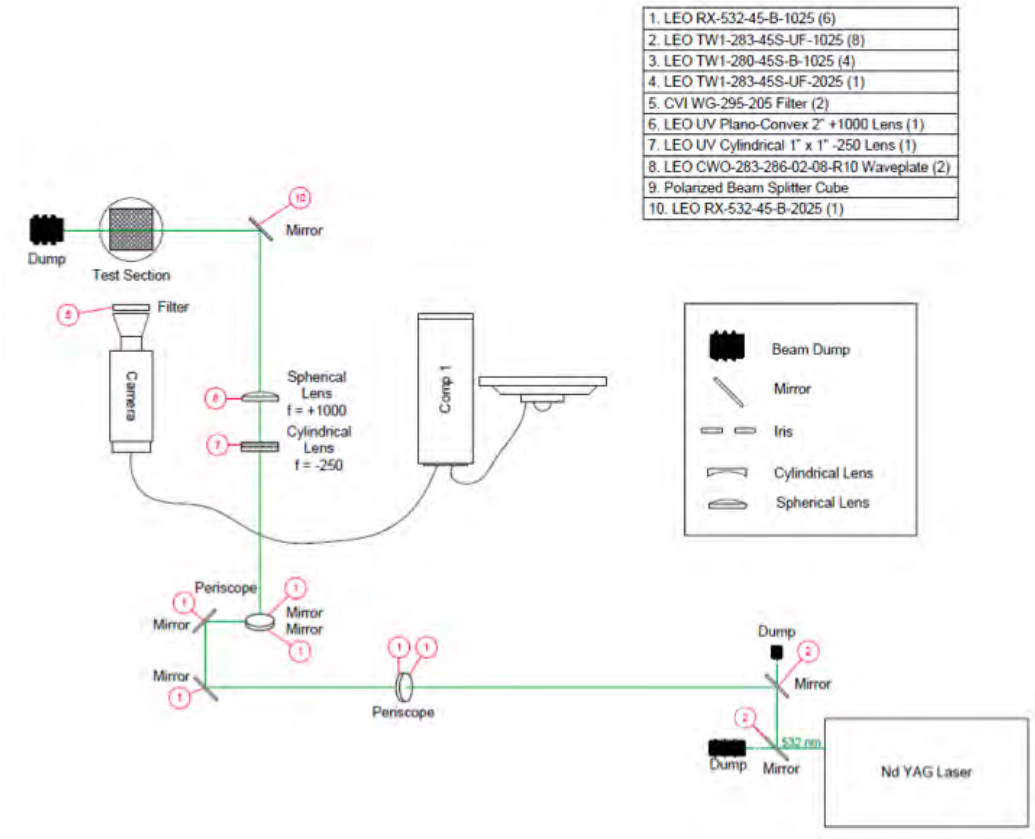

Figure A-3. Schematic of the COAL lab's Laser-Induced Incandescence (LII) setup from Drenth [9]

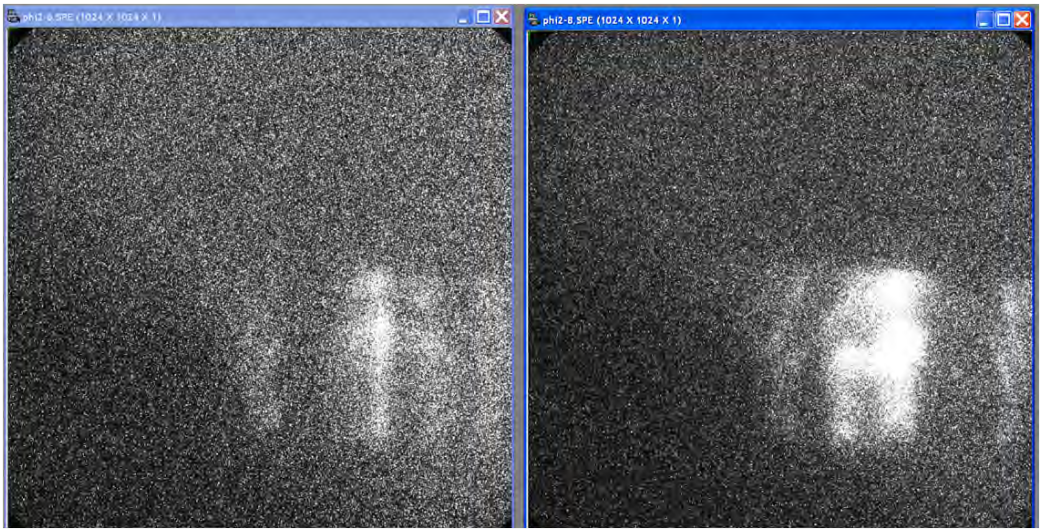

Figure A-4. Example of LII data in the Hencken burner for $\phi > 2.5$

an induced electric dipole from the incident light. The strength of the signal is affected by the molecular cross-section and the gas density. According to Eckbreth, the main drawback to this technique is that it requires very clean flow situations for obtaining accurate measurements [15]. One other drawback is the coupling with Mie Scattering, and prompts the use of molecular filters for decoupling, leading to today's commonplace Filtered Rayleigh Scattering (FRS). In addition to decoupling the Mie and Rayleigh signals, molecular filters also enable application of the technique to less than ideal flows. An FRS setup for studying a buoyant jet is shown in Figure A-5 and an illustration of the FRS process is shown in Figure A-6.

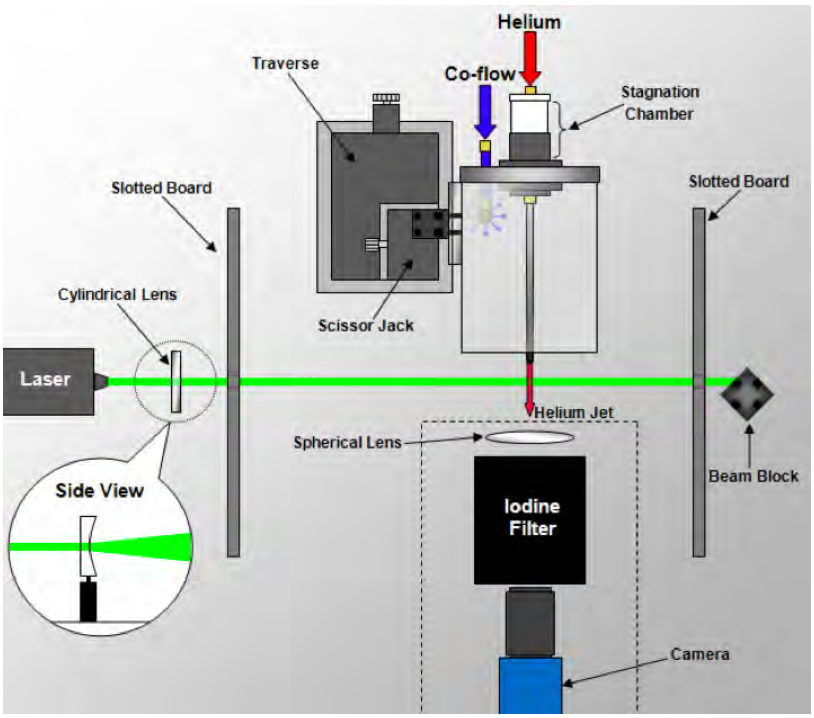

Figure A-5. Example of a Filtered Rayleigh Scattering (FRS) setup from Meents [22]

While a time-resolved FRS system would be immensely useful in the study of turbulent combusting flow, AFIT's current FRS capable lasers are within the visible spectrum which competes with the natural flame chemiluminescence spectrum and was thus not a feasible diagnostic for combustion experiments. However, cold-flow

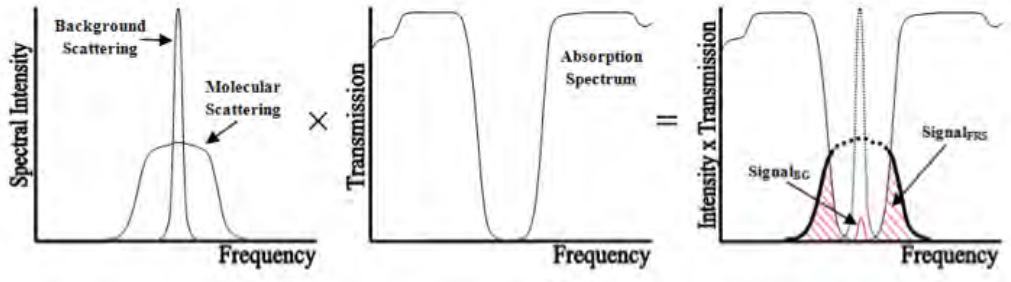

Figure A-6. FRS concept: background/particle & Rayleigh scattering signal (left), molecular filter absorption spectrum (center), and summation of scattering & filtered signal to detector (right) from Boguszko [23]

experiments have already been completed at AFIT by Reeder et al. which investigate the fundamental effects of buoyancy, which is a key phenomenon in the UCC [65]. Also, implementation of a UV based Rayleigh scattering system could feasibly provide a useful diagnostic tool.

A.4 Coherent Anti-Stokes Raman Spectroscopy

CARS is a non-linear technique based on Raman Scattering. According to Muraoka and Maeda, Raman Scattering, like Rayleigh Scattering, uses the interested species particles as a lens to scatter the incident light from it's original path [49]. However, unlike Rayleigh Scattering, in Raman Scattering the wavelength of the scattered light is not on the same order of the incident light as stated by Muraoka and Maeda [49]. This wavelength shift, called the Stokes shift, is randomly both additive, yielding the Stokes frequency, and subtractive, yielding the anti-Stokes frequency, as defined by Muraoka and Maeda [49]. As the name suggests, CARS is only interested in the anti-Stokes frequency, but uses two colors of incident light with a difference equating to the Stokes shift for the interested species, according to Eckbreth [15]. Thus, according to Muraoka and Maeda, this activates the rotation/vibrational modes responsible for Raman Scattering [49]. These two incident colors are sent in as two beams of the first color (ω_1) and one beam of the second color (ω_w), producing

an output from the interested species of a third color (ω_3) such that $\omega_3 = 2\omega_2 - \omega_2$ [8]. The non-linearity of this technique arrises from its susceptibility to polarization from incident light and is dependent on temperature and pressure. While CARS has tremendous diagnostic power, the main intent of this research is to understand larger spatial distributions which become very tedious to investigate with a point technique. The COAL lab currently has a CARS system that is being used to study phenomena of more simple geometry.

Appendix B. Additional V-Flame Results

This appendix contains additional results and conclusions about the v-flame that were not presented in Chapter 4.

B.1 Results

To further investigate the differences between the straight and curved UCC sections, two configurations were identified for each section. The first configuration, which was previously shown, was without combustion in the seeder box. The second configuration being with combustion in the seeder box. As shown previously in Figure 28, a seeder box was added to the inlet of each UCC section for future airflow seeding of micron sized particles for PIV measurements. This was added so that PIV measurements could be taken at similar locations to this study in order to measure the the actual g-load produced for a given test condition for comparison to the predicted g-load. In addition to this function, a third fuel injector was added to the box which nearly doubled the total flame residence length within the UCC section. This should more readily replicate the full annulus condition with the sectional UCC model having a longer residence length even though the full annular build-up is not possible. However, determination of this additional fuel injector's implications to the flame shape must be evaluated to determine if significant changes resulted from the addition since the seeder box did not exist for Drenth's study. Also, due to preserving the span-wise viewpoint over the radial vane it was not possible for the curved section seeder box to have the same interface geometry as the straight section seeder box. This forced the flame from the curved section seeder box to transition through a curved interface into the UCC because the "straight-in" geometry was not feasible as illustrated in Figure 142.

The images in Figure B-1 compare the flame shape at Plane 2 of the straight

section baseline case, V1, to that with the seeder box, V2, showing minimal effect on the shape with the added fuel injector, although a noticeable change in the intensity and weighting of the distribution occurs due to the increased residence length and change in the fuel distribution. However, Figure B-2 shows the same cases, also at Plane 2, with the curved section indicating a noticeable effect such that the v-shape vanishes at this plane. A closer look back at Figure 28 shows the incongruence between the straight and curved section seeder boxes. Examining both straight and curved sections with the seeder box fuel only, Figure B-3 shows case V7 with both sections illustrating the flame shape change with the seeder box addition was isolated to the flame emanating from the seeder box alone, since similarity between the sections without the seeder box fuel has already been established. This confirmed the flame shape change was resultant only from the intentionally, although undesirably, different seeder box geometries. Due to the differences in the geometry of the interface with the seeder box for the curved section, the flame from the curved section seeder box was forced to spread as it encountered the curved interface producing a more uniform shape, as shown in Figure B-3. Since in Case V2 the seeder box has 2/3 of the fuel, the added curvature of the curved section interface will obviously have a dominant influence on the total flame shape. As shown previously in Figure 142, the straight section interface (left) had a "straight-in" geometry that preserved the fuel jet in cross-flow situation present with the other fuel injectors. However, the curved section interface (right) created a situation where the fuel jet impacted the interface wall and caused a diffuse flame shape to result.

Examining the effect of core flow velocity on the flame shape with the curved section (Cases V3, V2, V4), Figure B-4 shows the recovery of the v-shape with the seeder box at higher core flow velocity while decreased core flow velocity eliminates the v-shape at Plane 2. This confirmed the v-shape was caused by the interaction

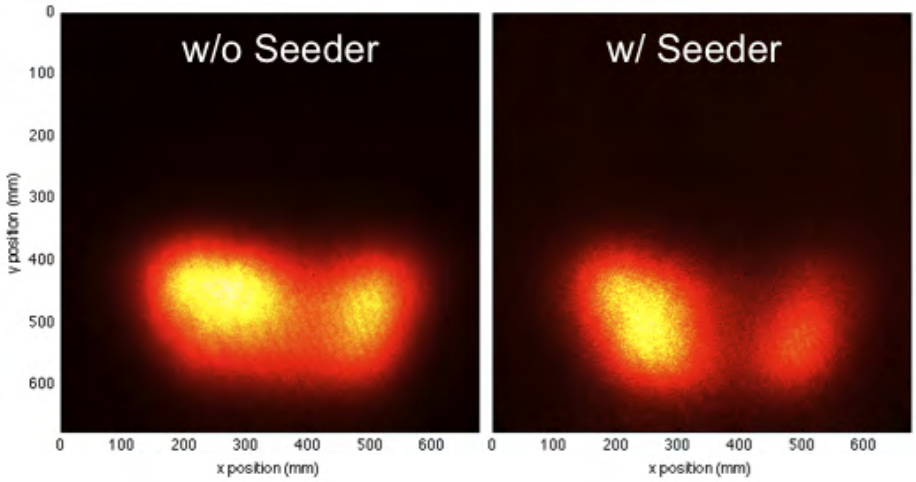

Figure B-1. Flame location data with the straight UCC section at Plane 2 without, Case V1, (left) and with, Case V2, (right) the PIV seeder box

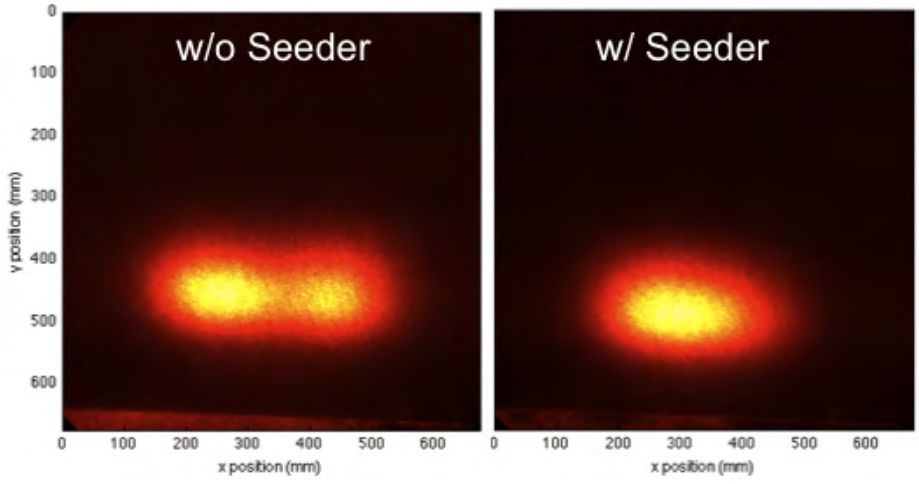

Figure B-2. Flame location data with the curved UCC section at Plane 2 without, Case V1, (left) and with, Case V2, (right) the PIV seeder box

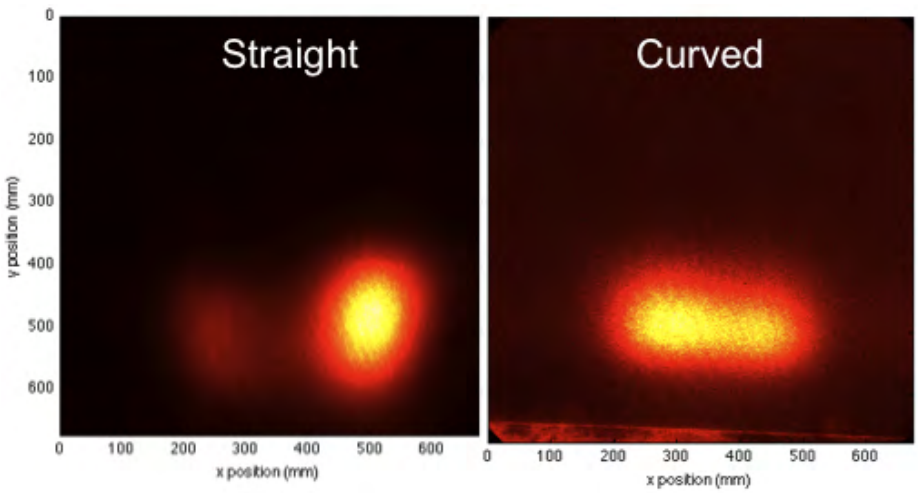

Figure B-3. Flame location data for Case V7, seeder box fuel only, with the straight (left) and curved (right) UCC sections at Plane 2

of the UCC flow with the core flow. It is important to note that this applies to the curved section with the seeder box due to the geometry of the interface for the curved section. It was previously demonstrated that the straight UCC section exhibited the bimodal distribution independent of velocity ratio changes with and without the seeder box, even though the weighting of the distribution changed. However, the distribution change confirms that the presence of the v-shape was the result of shear stress in the core flow direction acting on the flame within the UCC. At lower MFR, and UCC/core velocity ratio near unity, a single-mode flame distribution resulted at Plane 2 with the seeder box. However, as the core flow velocity was increased, and the VR decreased, a higher pressure gradient was created promoting higher mass flux into the core. Since the seeder box fuel occupies innermost radial location, this flow migrates first leaving the flow from injectors 1 & 2 to dominate the flame structure and yield the v-shape. The same radial distribution and migration order existed with the straight UCC section, but the seeder box interface with the straight section was not curved which preserved the jet in cross-flow situation and spreading of the seeder box flame did not occur.

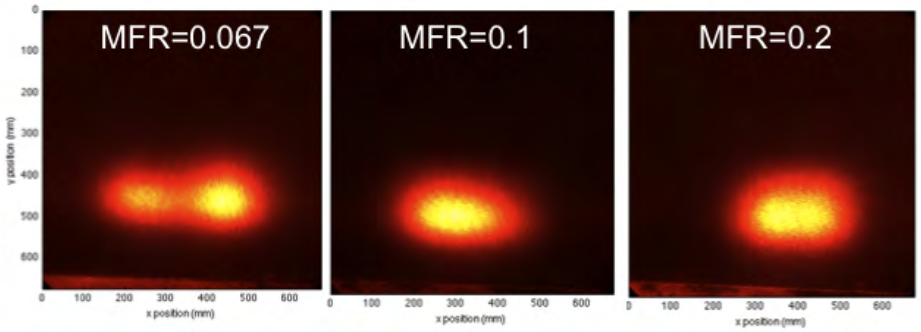

Figure B-4. Flame location data with the curved UCC section at Plane 2 for MFR=0.067 (left), 0.1 (middle), and 0.2 (right) (Cases V3, V2, V4)

Combining this with a closer examination of Case V3 with the curved section at all three planes, as shown in Figure B-5, further illustrates the spatial variability of the v-shape and provided insight into the the actual composition and cause of the v-shape.

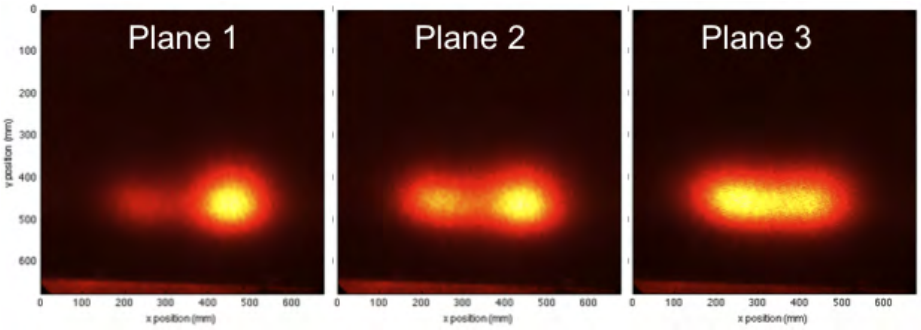

Figure B-5. Flame location data for Case V3, increased core flow, with the curved UCC section at Plane 1 (left), 2 (middle), and 3 (right)

In addition to variations of Drenth's conditions, at nominally 100 g's, (Table 3), Cases 13-15 from the global test matrix (Table 1) were studied to examine the relationship with increasing g-load. Cases 13 & 14 were investigated at all three planes as shown in Figures B-6 & B-7. These figures shows that the presence of the v-shape was present as the g-load was increased from 500 to 1000 g's. Also, the flame shape increased in width due to the increased fuel flow at the higher g-load. Further, increased definition of the v-shape occurred at higher g-load due to increased migration into the core flow bleeding off more of the flame from the seeder

box. Further, as more flame from the seeder box migrated, the flame from the injectors moved toward the inner radial wall which increased the shearing on those flows due to the decreased distance from the interface with the core flow. These cases also had a more uniform distribution shape at Plane 1 due to the higher flow rates in the seeder box over the V Cases. In order to examine changes in core flow velocity, Case 15 was examined as shown in Figure B-8. This figure indicates the reduction of flame on the windward side due to increased migration into the core flow.

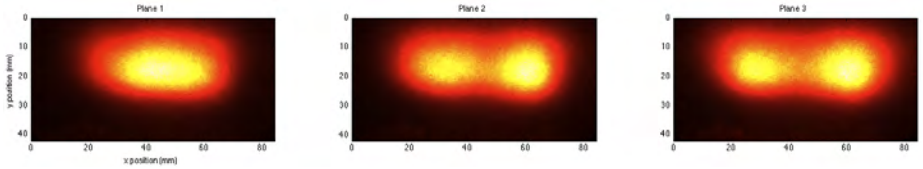

Figure B-6. Flame location data for Case 13 (500g, MFR=0.2, $\phi = 2.0$) with the curved UCC section at Plane 1 (left), 2 (middle), and 3 (right)

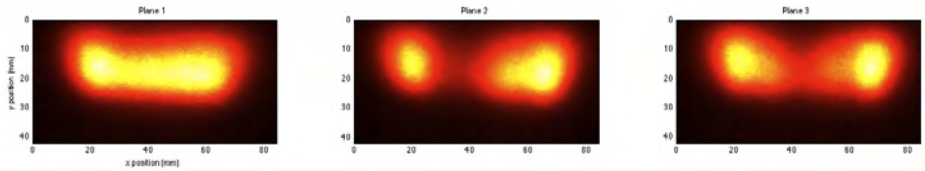

Figure B-7. Flame location data for Case 14 (1000g, MFR=0.2, $\phi = 2.0$) with the curved UCC section at Plane 1 (left), 2 (middle), and 3 (right)

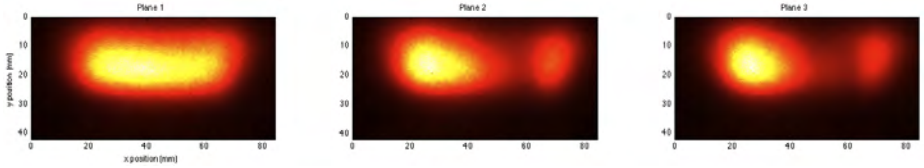

Figure B-8. Flame location data for Case 15 (1000g, MFR=0.1, $\phi = 2.0$) with the curved UCC section at Plane 1 (left), 2 (middle), and 3 (right)

B.2 Conclusion

The addition of the seeder box produced a smearing in the ambient exit flame shape from the curved UCC section on the inner radius due to the curvature of the

seeder box interface with the UCC. The intentional, albeit undesirable, differences in the geometry of each seeder box was a necessity of the seeder box design for the curved section was driven by the need to maintain optical viewing of the core flow section. This change with the seeder box addition was isolated to the flame emanating from the seeder box alone which created a spreading of the seeder box flow due to the necessary transition from the box into the preexisting part of the curved UCC section. While the "straight-in" geometry with the straight section seeder box is more representative of the annular UCC configuration, the curved interface of the curved section seeder box is the only option due to the geometry and minimum size required for functionality with the necessity of maintaining span-wise optical access over the radial vane.

However, the dissolution of the v-shape at Plane 2 was only with the curved section seeder box at lower core flow velocities due to the curvature of the interface between the seeder box and the curved UCC section. As the MFR and VR were decreased, the increased migration resulted in more bleed off of the seeder box flame and the v-shape was recovered at that plane. Otherwise, the v-shape structure was dominant only changing in the weighting of the distribution between the windward and leeward legs as the migration into the core was increased or decreased.

Higher g-load cases were tested indicating no dependence with g-load on the presence of the v-shape and further confirming the causality of the shear layer. Investigating a higher g-load case with higher core flow velocity (and lower velocity ratio) indicated the same trend of decreasing intensity of the windward leg of the v-shape as the core flow velocity increases. This was not surprising due to the increased core flow velocity creating an increased pressure gradient which lead to increased flame migration from the UCC into the core flow. Due to the injection order, the flow migrating from the UCC must follow the injection order of the seeder box, then injector

1, and then injector 2. With seeder box flame migrating first and leaving injector 1 to fill the windward leg of the v-shape, increased migration must come from this leg first due to closer proximity to the core flow interface. Investigating higher g-loads and lower velocity ratios further enhanced the understanding of the formation of the v-shape which existed for a wide range of g-loads and MFRs/VRs.

Appendix C. Laboratory Procedures

The laboratory procedures manual created from this research begins on the next page. These lab procedures were documented by Eric Fuerst.

Combustion Optimization and Analysis Laser (COAL) Laboratory

Procedures for Small Scale UCC Start – Up, Operation, Shut – Down, PLIF Measurement, PIV Measurement, and HSV Measurement

I. Introduction:

In order to conduct a combustion experiment in the COAL Lab, be it with or without the operation of the UCC, it is necessary to understand the operation of several key lab systems. These essential systems include: Labview data acquisition software, mass flow controllers, fuel systems (propane in this case), imaging systems, and laser diagnostic systems such as, Particle Image Velocimetry (PIV) and Planar Laser Induced Fluorescence (PLIF). While the aforementioned processes are, by no means, a definitive list of the capabilities of the COAL Lab, they are fundamental to the conduction of many combustion experiments.

Note: Several of the following steps require up to an hour to complete; so, it is important, that if you need to test by a certain time, to start early.

Combustion experiments may create noise in high decibel ranges; be sure to wear ear protection when necessary.

Before conducting any Laser experiment, make certain to wear proper eye protection and to turn on laser warning light!

Final Shutdown procedures for the Lab are at the end of the document, XIV. Final Shut – Down

To follow is an outline of the various procedures mentioned above:

II. Preliminary Procedures – UCC

Prior to running experiments, a few steps must be completed.

a. Flip the "Equip" switch at the lab control station to the "On" position.

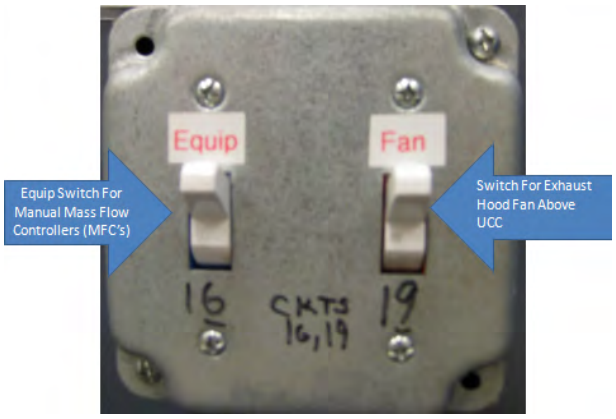

Figure 1: These switches are located at the Lab control station. The "Equip" switch for the Lab control station and the main UCC hood ventilation fan switch are currently shown in the "On" position

b. Turn on the Mass Flow Controllers (MFC's) (only main power switch on both units, not each individual channel)

i. After completing steps **a.** and **b.** approximately **one hour** must elapse prior to sending any mass flow through any line that is controlled by the MKS MFC's

Figure 2: MKS Manual Mass Flow Controllers (MFC's) shown in their "On" configuration. Switches 1-4 on the top MFC are controlled through Labview; while channels 5-8 can only be read in Labview and must be controlled manually.

c. *If conducting PIV experiments, complete the steps for* **start – up** *outlined on* **page 6** *in* **V. Particle Image Velocimetry (PIV)** *directly after* **a.** *and* **b.** *in* **II. Preliminary Procedures.**

d. *If conducting PLIF experiments, complete the steps outlined on* **page 9** *in* **VI. Planar Laser Induced Fluorescence (PLIF)**

e. **f. and g.** can be done together

f. Follow steps for propane start - up in **VII. Fuel Procedures (C_3H_8 – Propane) (page 13)**

g. Follow steps for **Ethylene and Air** start – up, if needed, in **VIII. Other Tank Farm Procedures (page 16)**

h. *If conducting PIV,* Complete steps **1 and 2** in **V. Particle Image Velocimetry (PIV), c. Seeding, i. Seeder Start – Up and Operation. (page 8)**

i. After h. is done, proceed to III. UCC Operation

III. UCC Operation

a. Open Labview file, *Combustion Lab with Flow Control – LeBay* (on desktop)

Figure 3: **"**Combustion Lab with Flow Control – LeBay" labview file shown running.

b. Open the both the manual valves on the Primary and Secondary air lines slowly.
  i. If airflow sounds persistent, check set points in Labview.

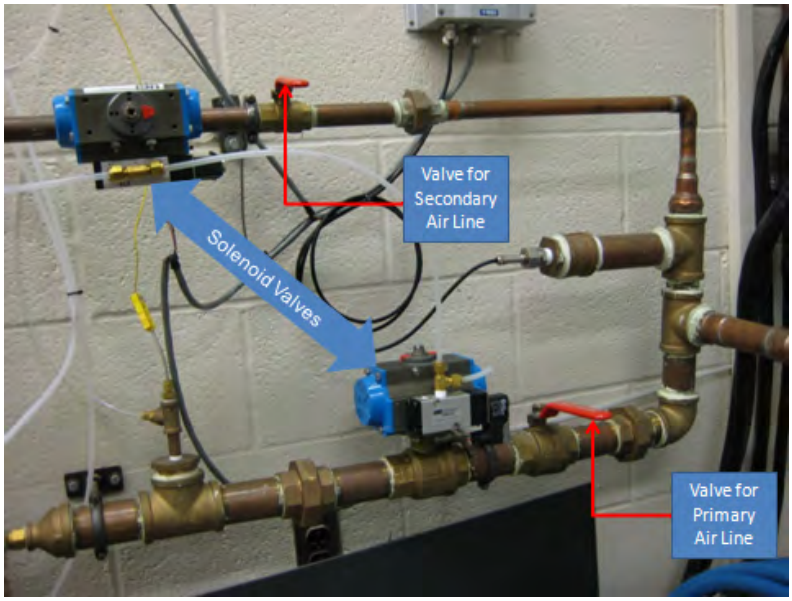

Figure 4: Main and Secondary shop air lines. Both manual valves and solenoid (controlled through Labview) valves are in place to direct flow.

c. Turn the switch for the HVOF to the "off" position and turn the switch for the UCC to the "on" position.

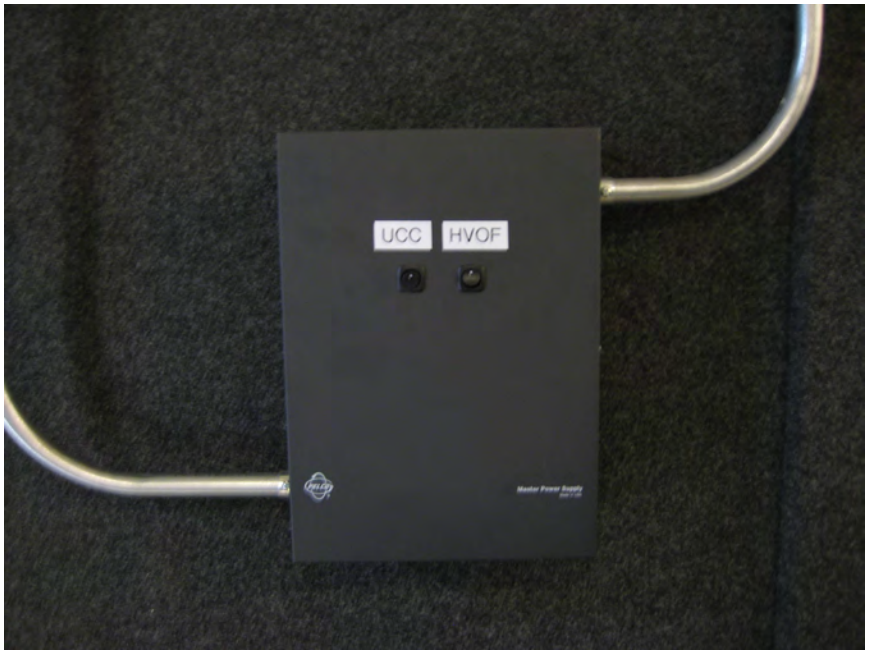

Figure 5: Power supply for Secondary Ventilation System. Pictured, is the UCC switch in the "off" position, while the HVOF switch is in the "on" position.

d. Flip both hood fan switches into the "On" position.
  i. On page 2, Figure 1for "Equip" switch has the switch for Fan 1 on it. Below is the switch for Fan 2, located on the side of the "Hush Room".

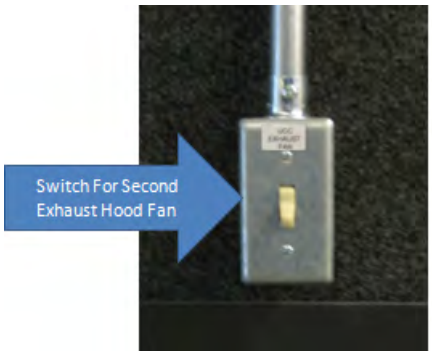

Figure 6: Switch for UCC Secondary ventilation fan, located on the side of the "Hush Room", shown in the "off" position.

e. Press the "run" button (an arrow) in the top left corner of the Labview window following one hour MFC warm up (see Figure 3, page 3).
f. Error message will pop up. Click "Continue"
g. **In Labview (Starting UCC) (Test Flame):**
  i. Set air flow rates
    1. Main (Core Flow)
    2. Secondary (UCC Flow)
    3. Check air set points vs. air readings
  ii. Set fuel flow rates
    1. For channel 7 and channel 8
  iii. Open Solenoids from left to right (Nitrogen is not necessary for basic procedure)
    1. Air
    2. Ethylene
    3. Fuel
  iv. Turn on air and ethylene. (MFC's #5,6)
    1. Setpoint Air: 14 lpm
    2. Setpoint Ethylene: 3 lpm
  v. Set igniter to "On" position
  vi. Turn on UCC Fuel. (MFC #8)
    1. MFC #8 is UCC seeder box fuel
  vii. Set igniter to "Off" position
  viii. Turn on injector fuel. (MFC #7)
  ix. Turn off ethylene and air MFC's
  x. Close ethylene and air Solenoids
h. Proceed to **IV. UCC Shut – Down (page 6)**
i. *If conducting PIV experiments, complete the steps for* **Operation** *in* **V. Particle Image Velocimetry (PIV) (page 7)**

j. *If conducting PLIF experiments, complete the steps for* **Operation** *in* **VI. Planar Laser Induced Fluorescence (PLIF) (page 12)**

IV. UCC Shut – Down

a. It is important to shut the flame down between trials or every ten minutes to allow for cooling.

b. In Labview

i. Turn off Fuel (MFC's #7,8)

ii. Turn off Fuel Solenoid

iii. Keep Main and Secondary Air flow rates at around .5 kg/min between tests in order to cool the UCC metal relatively quickly.

iv. Go back to **III. UCC Operation, h. (page 5)**

c. See **XIV. Final Shut – Down** for procedures to shut the lab down after testing is complete.

V. Particle Image Velocimetry (PIV)

a. Start - Up

i. Turn on the cooling unit for the Verdi V12 Laser (switch is located on right side)

1. Set point should be 18.0 degrees Celsius

Figure 7: Cooling Unit for the Verdi V12 Laser, shown in the "On" configuration.

ii. Turn on Verdi V12 power supply (switch is located on back left side, just above power cord)

Figure 8: Verdi V12 Laser Power Supply, on but in "Standby"

iii. Will boot in “Current Control” (needs to be set to “Light Control”)
iv. Push “menu select” button
v. “Menu” down 15 times to “Light/Current” control
vi. “Menu select” twice
    1. Should read, “In Light Control Mode”
vii. Menu exit twice
viii. After completing steps **i.** through **vii.** approximately **30-45 minutes** must elapse prior to using the laser.
ix. Plug power in for the Phantom-Monochrome (4 pin B/C cord must be plugged into the back of Phantom-Monochrome)
    1. The camera takes about an **hour** to warm up.
x. After the **30-45 min** the laser needs to warm up, insert and turn the key on Verdi V12 Power Supply and turn from standby to laser enable and leave the key inserted. (key on top of power supply)
xi. Return to **page 3, II. Preliminary Procedures—UCC, step e.**

b. Operation

i. Commands

1. s=0: closes shutter
2. s=1: opens shutter
3. p=(enter number): sets the power level of the laser
4. ?p: displays current power level
5. Note: Do not “backspace” in command prompt. If you do, hit enter and retype the command.

ii. Remote desktop to “diodesystem” using computer terminal to left of rig if facing rig

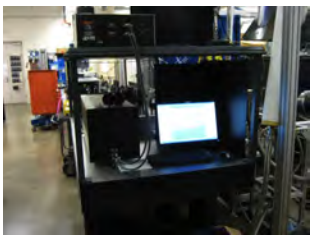

Figure 9: Computer terminal to the left of the rig. Useful for control.

1. Open TightVNC Viewer, type IP Address 100.100.100.4 to open “diodesystem” (**page 18, XI. Remote Desktop)**

iii. Open Verdi V12 Terminal program (command window will appear)

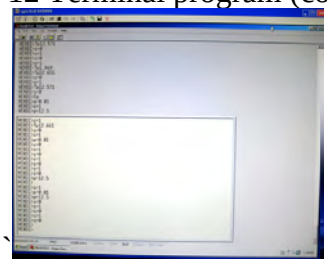

Figure 10: Above, is the command window for the Verdi V12 Laser.

i. Open the shutter ("s=1") (shutter can also be controlled from the Verdi V12 power supply)
    1. Shutter should be closed at all times when not taking data
ii. Set the power level of the laser to 12.5 ("p=12.5")
iii. Open N_2 solenoid (if it isn't already)
iv. Turn on Manual MFC channels 2 and/or 3 at control station (depends on which airflow is needed for seeding)

c. Proceed to **XII. Imaging: Phantom Monochrome and Color**

d. **Seeding**

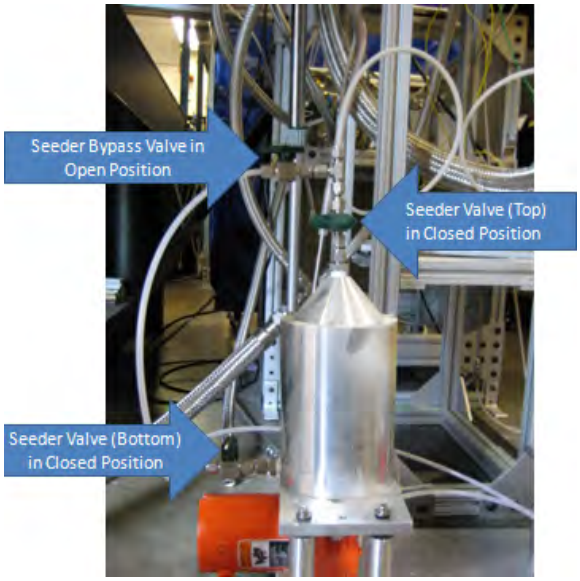

Figure 11: One of two seeders imperative for the use of PIV Laser Flow Diagnostics in the UCC.

i. **Seeder Start – Up and Operation**
    1. Unscrew the tops from each of the seed containers to either make certain that seed is in the apparatus or to clean and insert more seed (if necessary)
        a. If **1.** must be completed, be sure to close shutter on laser (s=0).
        b. In order to clean seeder, see **IX. Seeder Cleaning/Maintenance**
    2. Re-attach the tops of the seed containers.
    3. Open the Seeder Top Valve
    4. Open the Seeder Bottom Valve
    5. Close the Bypass Valve
    6. Adjust vibration motor to achieve desired seeding. (About 50% power is usually sufficient)
        a. 20-60% power is acceptable for continuous running
        b. Any other power setting is subject to 50/50 duty load
    7. When seeding is sufficient, proceed to **page 18, XII. Imaging, a. Phantom Monochrome and Color, iii.**

8. Follow procedures for **Seeder Shut – Down** after each trial to conserve seed.

Figure 12: Control knob for one of the two vibrating motors attached to the seeders shown in the "off" position.

ii. Seeder Shut – Down

1. Open Bypass
2. Close Seeder Bottom Valve
3. Close Seeder Top Valve
4. Turn off vibration motors

e. Imaging (Phantom – Monochrome)

1. Refer to **page 18, XII. Imaging, a. Phantom Monochrome and Color, iii..**

f. Shut – Down

i. Set power level of laser to zero ("p=0")
ii. Close the shutter ("s=0")
iii. Turn key on Verdi V12 Power Supply to "Standby"
1. Return key to the top of the power supply
iv. Turn off Verdi V12 Power Supply
v. Unplug the power for the camera
vi. Turn off cooling unit for Verdi V12

VI. Planar Laser Induced Fluorescence (PLIF)

a. Flushing and Refilling the Dye Laser

i. If need be, follow steps outlinedon **page 19** in **XIII. Flushing and Refilling the Dye Laser.**
ii. If the dye is still satisfactory or after flushing and refilling is complete, start – up of the dye laser may commence.

b. Start – Up

i. Flip switch to the "on" position Spectra Physics YAG Laser Power Supply

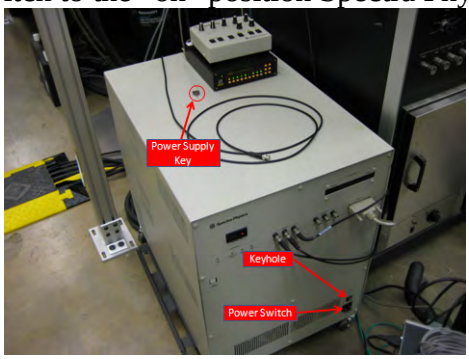

Figure 13: YAG Laser Power Supply with Quanta-Ray timing box on top.

ii. Insert the key into the YAG Laser Power Supply and turn it to the "on" position. (See Figure 12 above)
iii. Flip switch on the timing box, which is located on top of the power supply, to "enable".

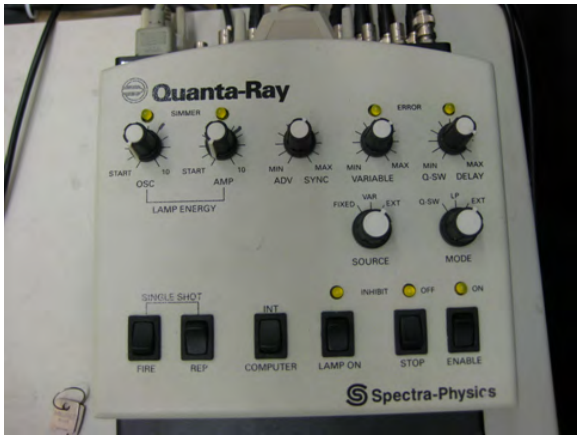

Figure 14: Quanta Ray Timing box for the YAG Laser.

iv. Turn Lamp Energy on the timing box for "Osc" and "Amp" to 10.
    1. 30 minutes must elapse for the lasers to warm up
v. Turn on both Princeton Instruments Camera Power Supplies
    1. About an hour warm up time

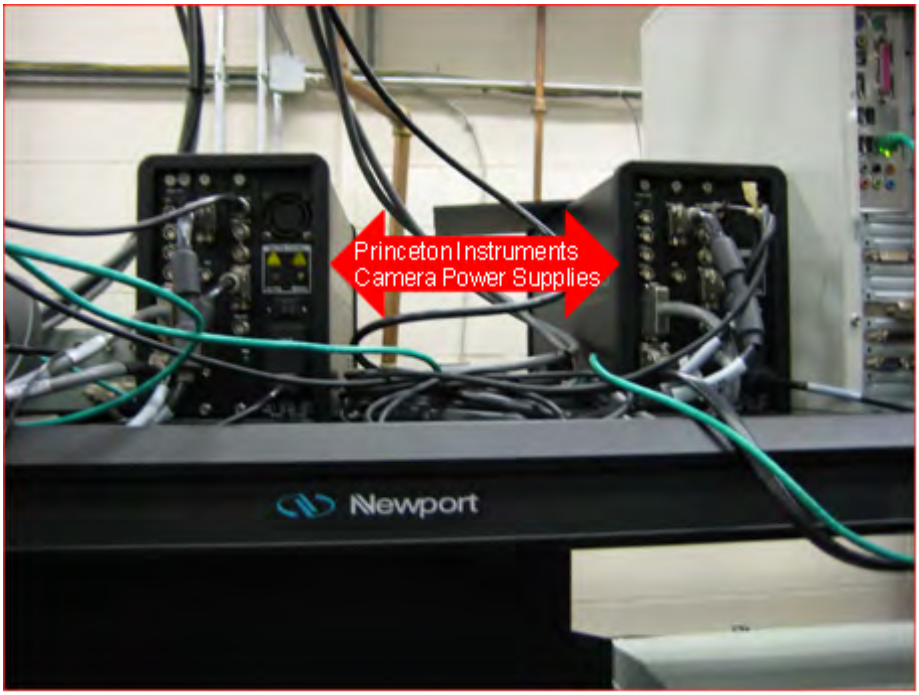

Figure 15: Princeton Instruments Camera Power Supplies, located behind the Test Stand

vi. Follow steps outlined **VII.** and **VIII.** for Propane and Zero Air Start – Up

vii. Open PLIF 1 and PLIF 2 Computers, via Remote Desktop (See **XI. Remote Desktop**)

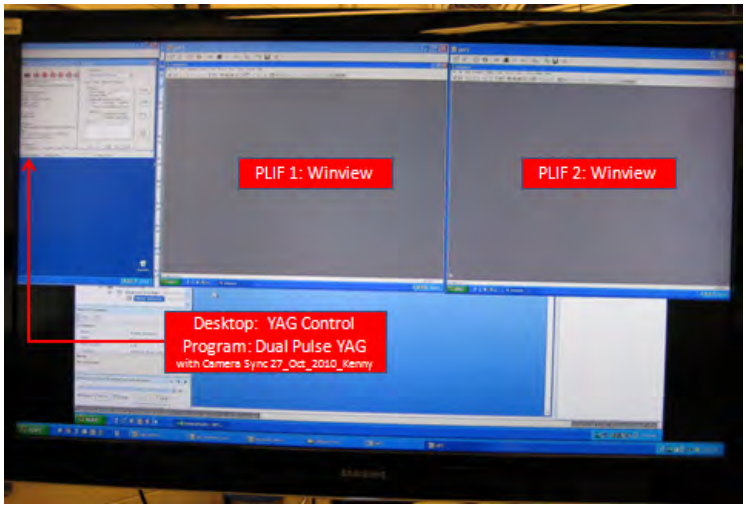

Figure 16: Big screen monitor exhibiting the utility of Remote Desktop. Currently displayed are computers, PLIF 1, PLIF 2, and YAG Control.

1. On PLIF 1 and PLIF 2, open "Winview"
2. Window will pop up
   a. Click on the option, "Restore last settings".
   b. Click "Ok"

viii. Turn on the Dye Laser Pumps (switch located on the back, on the right side of the power cable plug in

ix. Slide shutters to closed position

x. Open the lid of each Dye Laser and remove the beam block. (move it out of the way of any part of the beam) (see Figure 16)

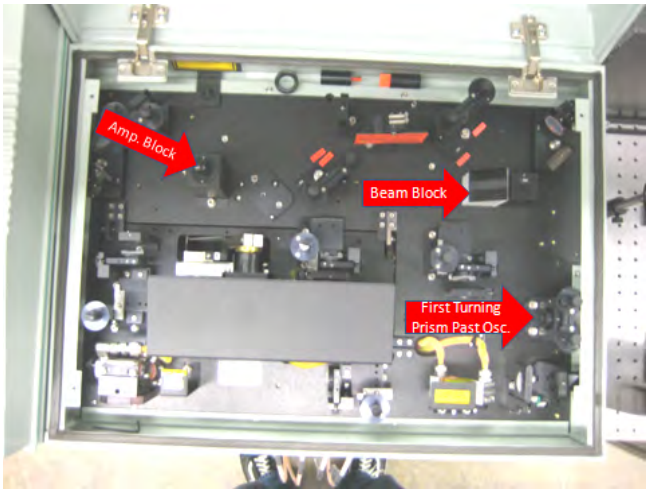

Figure 17: Components inside one of the two Dye Lasers. Highlighted for start – up are the Amp. and Beam blocks.

- **xi.** Lift Amp block (See Figure16)
- **xii.** Open shutters when ready to start experiment.

c. Operation

- **i.** Remote Desktop: YAG Control
- **ii.** Open "Trigger" program
  1. Open file, "Dual Pulse YAG with Camera Sync 27_Oct_2010_Kenny"
  2. Click on "Program"
     - **a.** Click on "Program all channels"
- **iii.** Open Channel F (Camera 2)
  1. Make sure that F is disabled
- **iv.** Get on condition. (start experiment so that the conditions in need of recording are attained)
- **v. The following steps are to be completed in both Winview programs on both computers, PLIF 1 and PLIF 2.**
- **vi.** Click on the "Acquisition" tab
  1. Then click on "Experiment Setup"
     - **a.** Make certain to verify settings:
       - **i.** number of images
       - **ii.** region of int.
       - **iii.** intensifier gain
       - **iv.** Click "Ok"
- **vii.** Click on the "Setup" tab
  1. Then click on "Pulsers"
  2. Click on "Setup Pulsers"
  3. Click on "Gating" tab
  4. Click on "Setup"
     - **a.** Verify settings
       - **i.** Gate width
       - **ii.** Delay
       - **iii.** On – CCD Accumulation
     - **b.** Click "Ok" three times
- **viii.** Measure Dye Laser power before every trial; the power will vary.
  1. Use laser power meter
  2. Make certain that "Time Average" is off
- **ix. Acquisition**
  1. Click "Acquisition" tab
     - **a.** Then click on "Acquire"
  2. Instead of the above – mentioned technique, there is an acquire button, labeled, "Acq"
  3. "Enable" Channel F
  4. After images acquired, "Disable" Channel F
  5. Click on the "File" tab and save images.
  6. Repeat steps **viii.** and **ix.** as needed.

d. Shut – Down

i. Close Winview on both PLIF 1 and 2
ii. Turn lamp energy down on both “Amp” and “Osc”
iii. Stop the timing box
iv. Turn and remove key from power supply
v. Flip the power supply switch to the “Off” position
vi. Turn off Dye Laser Pumps
vii. Return Beam Block
viii. Shut Amp Block
ix. Close shutters
x. Refer to section **VII.** and **VIII.** for Propane and Bottled Gas shut – down
xi. Turn off both of the Princeton Instruments Camera Power Supplies

VII. Fuel Procedures (C_3H_8 – Propane)

a. Propane: Start - Up

i. Get keys for the Tank Farm from the Lab Control station and unlock the Tank Farm.

Figure 18: Lab Control Station showing location of the MKS MFC’s, Key to Tank Farm, Labview Terminal, and Equip switch.

1. **The Tank Farm is to be <u>locked at all times</u>, unless you are in it!**

Figure 19: Pictorial representation of the incorrect and correct states that the tank farm can be left in.

ii. Flip the Vaporizer switch to the "on" position (See Figure 17 on page 14).

Figure 20: Showing location of the power switch for the Vaporizer inside the Tank Farm.

iii. Completely open the valves on top of each of the three large propane tanks.
iv. Open the valves on the hoses from each propane tank.
v. Wait **15-30 minutes** (depending on outside air temperature) for the vaporizer to warm up before proceeding to the next step
vi. Open designated two valves by the vaporizer. (yellow first, then red)

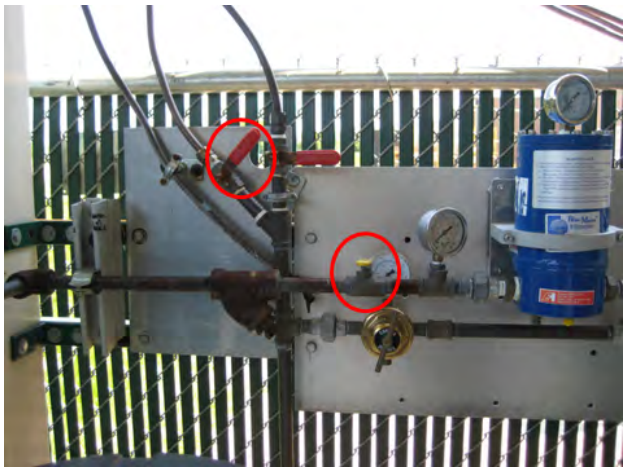

Figure 21: Input (yellow) and Output (red) valves for the Propane Vaporizer, both in the "off" position.

vii. Open Propane valve in lab. (See Photo)

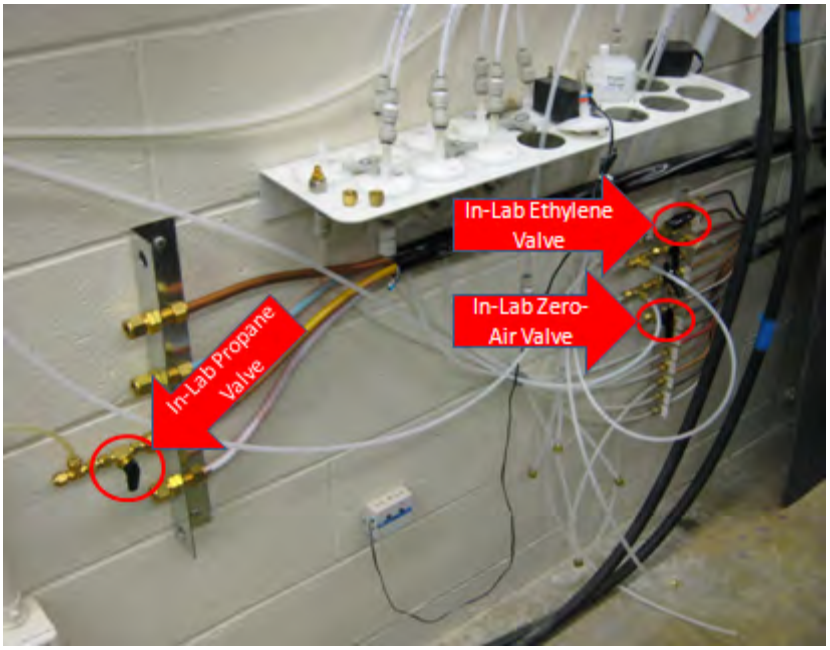

Figure 22: In – Lab Valves for bottled gases and Propane.

b. Propane: Shut – Down and Bleed

- **i. Steps ii. – v. are performed in the Tank Farm**
- **ii.** Close designated two valves by the vaporizer (red first, then yellow).
- **iii.** Close valves on hoses from each Propane tank. (3)
- **iv.** Close completely the valves on top of each of the three large propane tanks. (3)
- **v.** Flip the Vaporizer switch to the "off" position
- **vi.** Open Fuel Solenoid

vii. Steps **1-4** below are performed within to Bleed the Propane Lines
   1. Make certain that the ventilation fans are on.
   2. Set air flow rates for Main and Secondary lines to about .5-1 kg/min
   3. Turn on Fuel (MFC's #7,8)
   4. After Mass Flow for 7 and 8 reads approximately 0, complete the following steps
   5. Turn off Fuel (MFC's #7,8)
   6. Close Fuel Solenoid

viii. Close Propane in-lab valve.

VIII. Other Tank Farm Procedures

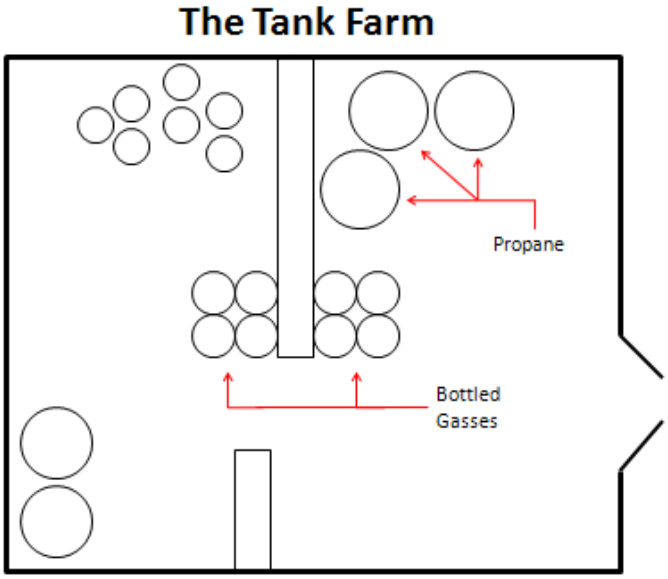

Figure 23: Schematic of Tank Farm, showing location of the entrance, as well as, the three large Propane Tanks and different bottled gases.

a. **Bottled Gases in the Tank Farm, used by the COAL Lab**
   i. Zero Air
   ii. Ethylene
   iii. Hydrogen
   iv. Nitrogen
b. **Bottled Gases: Start – Up**
   i. Open valve directly on top of tank completely. (No need to change the current setting of the regulator)
   ii. Open designated in lab valve. (See Figure 21 on page 16)
c. **Bottled Gases: Shut – Down**
   i. Close valve completely.
   ii. Close designated in lab valve.

IX. Seeder Cleaning/Maintenance

a. Remove Seeder Containers from stand
b. Remove the tops of each of the seeder containers
c. Clean out any excess seed with a paper towel
d. Remove the bottoms of each of the seeder containers
e. Clean out each of the filters
    i. May be necessary to shake or strike against inside of trash can
f. Replace filters if necessary
g. Check condition of each seeder containers o-rings
h. Replace o-rings if necessary
i. Put the seeder containers back together and reattach them to the stand

X. Translation Stage

a. Turn on Power for the Translation Stage Controller
b. Open ESP control utility

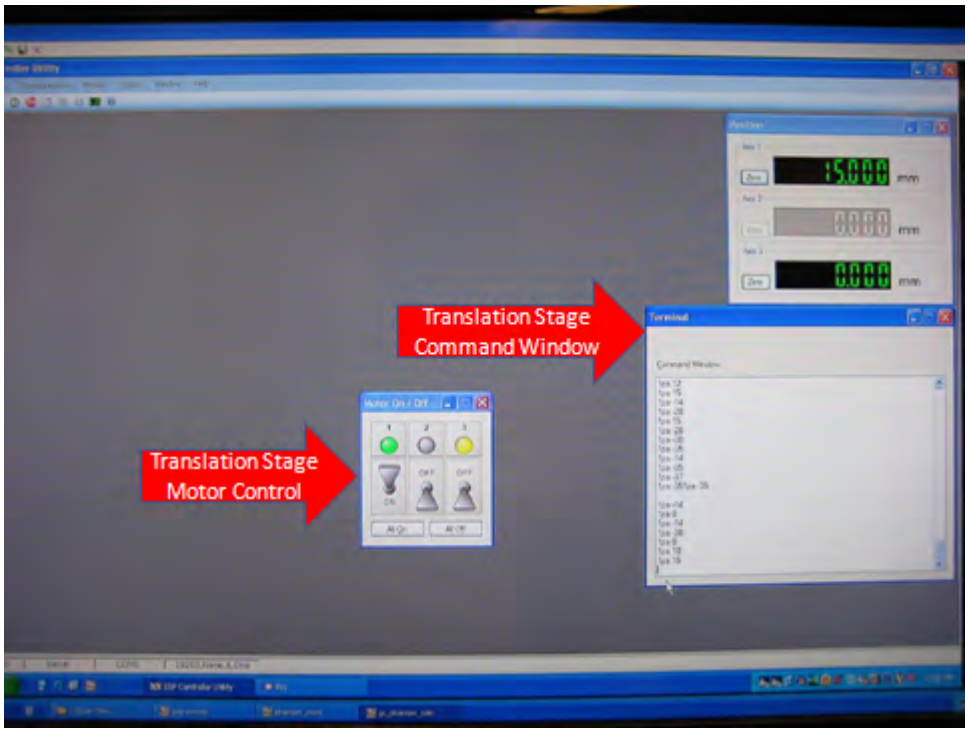

Figure 24: Control windows for the UCC rig Translation Stage. Motor power is currently set to the "on" position.

c. Turn Motor 1 on
d. Type "1pa x"
    i. 1: axis
    ii. p: positive
    iii. a: absolute
e. Note: If you turn Power for the Translation Stage Controller off, the position that it is in at the time of program termination becomes the new zero point.
    i. Return the stage to "0" before turning it off.

ii. "0" is the interface between the core flow wall and the circumferential wall, negative values move into the core flow, away from the UCC

XI. Remote Desktop

a. Can access from any COAL Lab Network Computer
b. Open the TightVNC Viewer (In quick launch by the "Start" button
c. Type in IP Address for particular machine
    i. List of IP Addresses located at Lab Control Terminal
d. Password for Remote Desktop is, "password".

XII. Imaging

a. **Phantom Monochrome (#9575) and Color(#8531)** (Procedure is the same, just change the camera)
    i. Plug the power cable in for the camera.
    ii. Allow an **hour** to warm up
    iii. Open PCC 1.3 on computer next to test rig (in quick launch, next to "Start" button)**.**
    iv. Click on "Live" tab
    v. Choose camera from "Camera" pull down.
        1. Phantom – Monochrome is 9575
    vi. Set amount of images to be taken
    vii. Perform Current Session Reference(CSR)
        1. Ensure lens cap is on Phantom
        2. Click CSR button
        3. Click "OK" on CSR popup
        4. Following CSR completion, remove lens cap
    viii. Click "Capture"
    ix. Click "OK"
    x. **Camera is Ready to image when desired flame and seed conditions have been met.**
        1. **Return to page 5, III. Operation, f. in order to turn flame on**
        2. **Return to page 7, V. Particle Image Velocimetry (PIV), d. Seeding, i. Seeder Start – Up and Operation, 3. to seed flow.**
    xi. Click "Trigger" to record
        1. Image, "0" is when "Trigger" was clicked
    xii. Click on "Play" tab
    xiii. Click "Save Cine" to save
        1. Give the Cine an appropriate file name and location
        2. Set the range of frames to be saved
        3. Click "Save"
        4. Allow the save bar to finish saving before continuing

XIII. Flushing and Refilling the Dye Laser

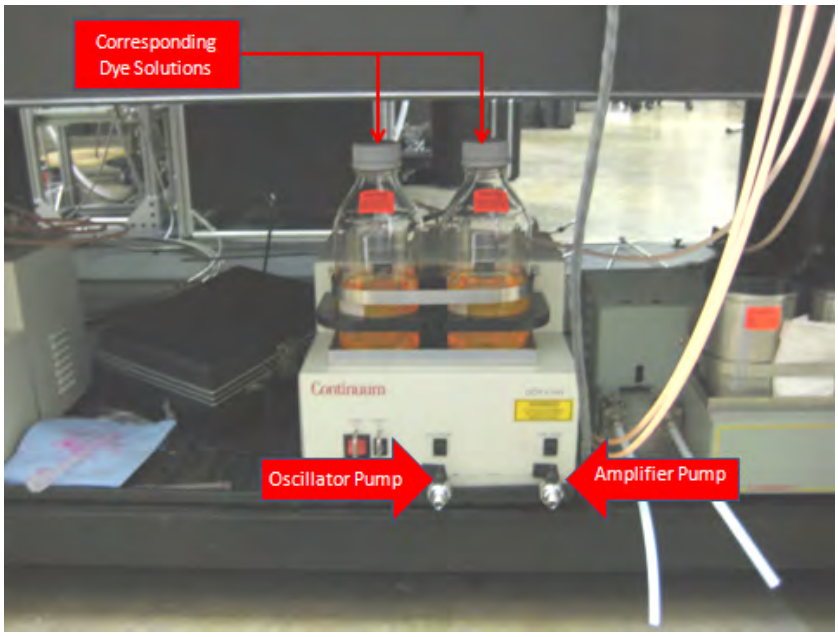

Figure 25: Dye solution Oscillator and Amplifier reservoirs and pumps, below the Dye Lasers.

a. Flushing

- **i.** Drain existing dye out of the pumps using 1000 mL beaker
- **ii.** Tilt the pump, as practical, to aid in drainage
- **iii.** Empty beaker with old dye into waste container using funnel
- **iv.** Drain until leftover dye is gone
- **v.** Attain Methanol from the Flame Locker in the COAL Lab
- **vi.** Pour Methanol (roughly a few 100 mL's)
- **vii.** Open valve for the drain of the pump until clean Methanol can be seen exiting
- **viii.** Close valves immediately so as to minimize methanol loss
- **ix.** Use "Prime" switch for each pump independently to pump Methanol through the entire system
- **x.** Repeat 4-8 until sufficiently diluted

b. Refilling

- **i.** Put 500 mL Methanol into each pump container (oscillator and amplifier pumps)
- **ii.** Drain until you see clean Methanol
- **iii.** Close valves immediately when clean Methanol is observed
- **iv.** Turn pumps on
- **v.** Attain dye concentrate from the Flame locker in the COAL Lab
- **vi.** **Mixing in the Dye**
  1. The dye is from a company called, *Exciton*
  2. They Recommend:

a. For oscillator: 120 mg/L (mg Dye Powder/Liter Methanol)
b. For amplifier: 50 mg/L

3. **We use 500 mL for our dye laser so an adjustment is required:**
   a. For oscillator: Start with 30 mL of concentrate
   b. For amplifier: Start with 6 mL of concentrate
      i. Add more dye carefully to both the oscillator and amplifier based on desired power output

vii. Place a white business card in front of the first turning prism coming out of the oscillator in order to monitor the color change of the laser beam (starts as green from the YAG, but as dye is added, becomes yellowish-green).

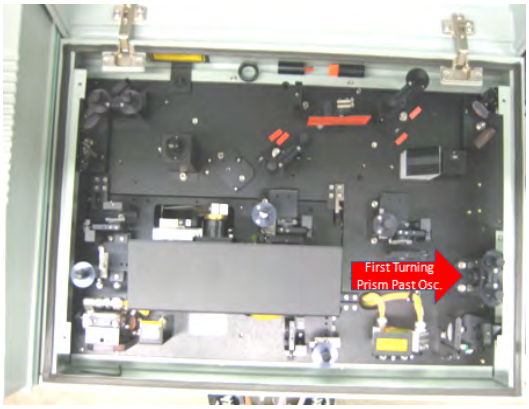

Figure 26: Components inside one of the two Dye Lasers. Highlighted is the First Turning Prism Past the Oscillator.

viii. Remove card from in front of the first turning prism coming out of the oscillator and use it to view the beam at the exit of the laser.

ix. Adjust the doubling crystal alignment wheel in order to better align the doubling crystal and create a more focused beam
   1. Focus the blue beam (UV)

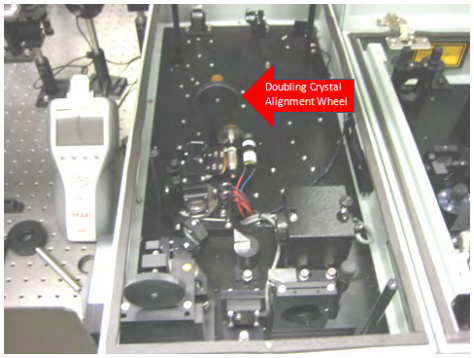

Figure 27: Components inside of one of the two Dye Lasers, located in a separate cavity than that of Figures 16 and 25. Highlighted here is the Doubling Crystal Alignment Wheel, used to focus the UV beam that exits the Dye Laser.

x. Laser is ready for use

XIV. Final Shut – Down

- **a.** Follow steps in either **page 9, V.** or **page 13, VI.** for the appropriate Laser **Shut – Down** procedure.
- **b. The parts that require being in the Tank Farm, can be done at the same time for c. and d.**
- **c.** Follow steps on **page 15, VII. Fuel Procedures (C_3H_8 – Propane), b. Propane Shut – Down**
- **d.** Follow steps on **page 16, VIII. Other Tank Farm Procedures, c. Bottled Gasses: Shut – Down**
- **e. In Labview**
    - **i.** Make sure three square solenoids are closed
        1. Leave the Nitrogen solenoid on
    - **ii.** Make sure air flow rates are set to zero
    - **iii.** Ensure MFC's are off.
    - **iv.** Leave Main and Secondary Air solenoids **Open**
- **f.** Shut off ventilation fans
- **g.** Stop current Labview program.
- **h.** Close Manual Valves on Primary and Secondary Air Lines.
- **i.** Shut off Manual MFC's
- **j.** Shut off "Equip" switch at Lab Control Station

Flushing and Refilling Dye Laser

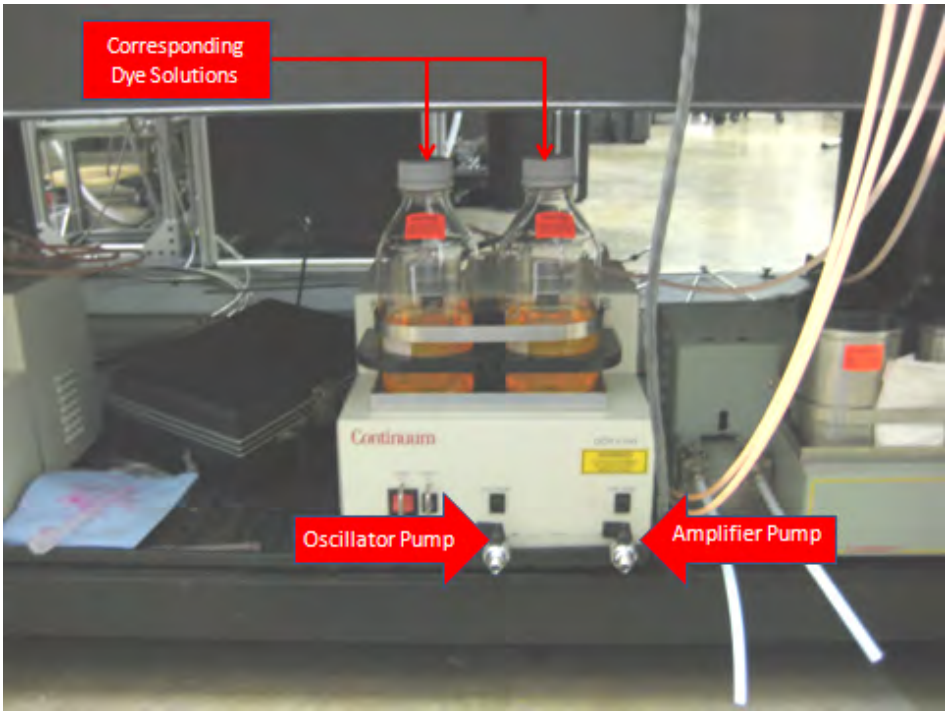

Flushing:

1) Drain existing dye out of the pumps using 1000 mL beaker.
2) Tilt the pump as practical to aid in drainage
3) Empty beaker with old dye into waste container using a funnel.
4) Drain until leftover dye is gone
5) Attain Methanol from the Flame locker in the COAL Lab
6) Pour methanol (roughly a few 100 mL's)
7) Open valve for the drain of the pump until clean methanol can be seen exiting.
8) Close valves immediately so as to minimize methanol loss
9) Use "Prime" switch for each pump independently to pump methanol through the entire system.
10) Repeat 4-8 until sufficiently diluted

Refilling:

1) Put 500 ml methanol into each pump container (oscillator and amplifier pumps)
2) Drain until you see clean methanol
3) Close valves immediately when clean methanol is observed
4) Turn pumps on
5) Attain dye concentrate from the Flame locker in the COAL Lab
6) **Mixing in the Dye**
-The dye is from a company called, *Exciton.*
-They recommend:
-For oscillator: 120 mg/L (mg Dye Powder/Liter Methanol)

-For amplifier: 50 mg/L

-**We use 500 mL for our dye laser so an adjustment is required**:

-For oscillator: start with, 30 mL of concentrate

-For amplifier: start with, 6 mL of concentrate

-Add more dye carefully based on desired power output.

7) Place a white business card in front of the first turning prism coming out of the oscillator in order to monitor the color change of the laser beam (starts as green, but as dye is added, becomes yellowish-green)

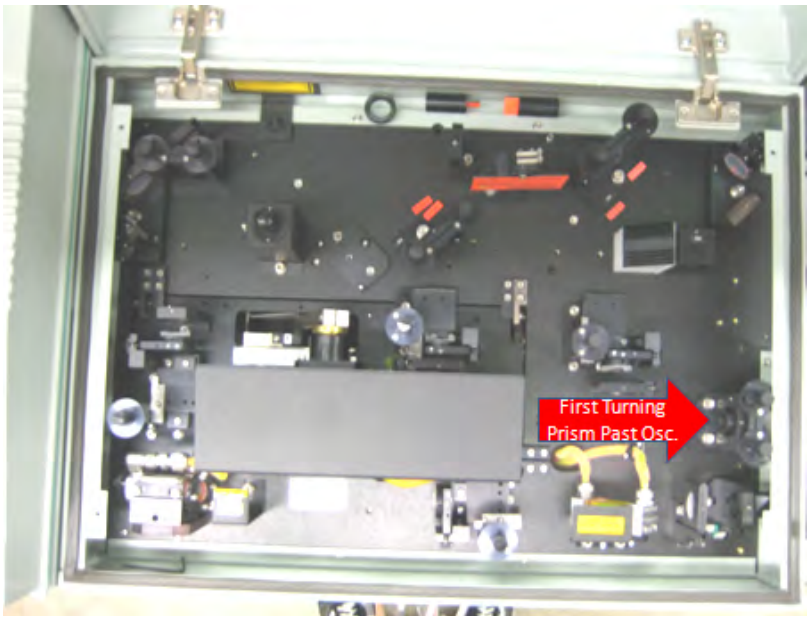

8) Remove card from in front of the first turning prism coming out of the oscillator and use it to view the beam at the exit of the laser.

9) Adjust the doubling crystal alignment wheel in order to better align the doubling crystal and create a more focused beam.

-focus the blue beam (UV)

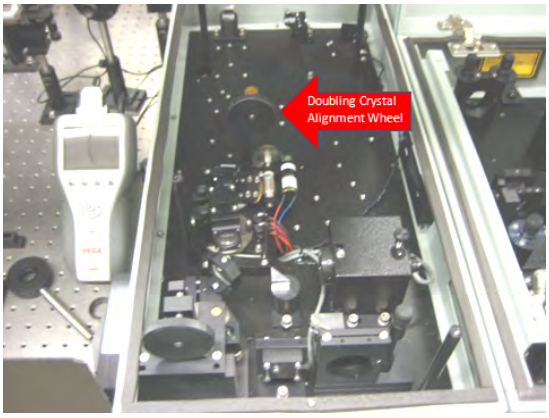

10) Laser is ready to use

Bibliography

[1] Mattingly, J., *Elements of Gas Turbine Propulsion*, McGraw Hill, Inc., New York, NY, 1996.

[2] Zelina, J., Sturgess, G. J., Mansour, A., and Hancock, R. D., "Fuel Injection Design Optimization for an Ultra-Compact Combustor," *2003 International Symposium on Air Breathing Engines*, ISABE. 2003-1089, 2003.

[3] Hankins, T. B., *Laser Diagnostic System Validation and Ultra-Compact Combustor Characterization*, Master's thesis, AFIT/GAE/ENY/08-M14. Graduate School of Engineering and Management, Air Force Institute of Technology (AU), Wright-Patterson AFB, OH, March 2008.

[4] Greenwood, R. T., *Numerical Analysis and Optimization of the Ultra-Compact Combustor*, Master's thesis, AFIT/GAE/ENY/05-M10. Graduate School of Engineering and Management, Air Force Institute of Technology (AU), Wright-Patterson AFB, OH, March 2005.

[5] Sirignano, W. A. and Liu, F., "Performance Increases for Gas-Turbine Engines Through Combustion Inside the Turbine," *Journal of Propulsion and Power*, Vol. 15, No. 1, 1999.

[6] Roquemore, W. M., Shouse, D., Burrus, D., Johnson, A., Cooper, C., and Duncan, B., "Trapped vortex combustor concept for gas turbine engines," *39th Aerospace Sciences Meeting & Exhibit*, AIAA-2001-0483, 2001.

[7] Zelina, J., Sturgess, G. J., and Shouse, D. T., "The Behavior of an Ultra-Compact Combustor (UCC) Based on Centrifugally Enhanced Turbulent Burning Rates," *40th AIAA/ASME/SAE/ASEE Joint Propulsion Conference*, AIAA 2004-3541, 2004.

[8] Anderson, W. S., *Design, Construction, and Validation of the AFIT Small Scale Combustion Facility and Sectional Model of the Ultra-compact Combustor*, Master's thesis, AFIT/GAE/ENY/07-M01. Graduate School of Engineering and Management, Air Force Institute of Technology (AU), Wright-Patterson AFB, OH, March 2007.

[9] Drenth, A. C., *Laser-Induced Fluorescence and Synthetic Jet Fuel Analysis in the Ultra Compact Combustor*, Master's thesis, AFIT/GAE/ENY/09-D03. Graduate School of Engineering and Management, Air Force Institute of Technology (AU), Wright-Patterson AFB, OH, December 2009.

[10] Zelina, J., Ehret, R. D., Hancock, D. T., Shouse, D. T., Roquemore, W. M., and Sturgess, G. J., "Ultra-Compact Combustion Technology Using High Swirl for Enhanced Burning Rate," *38th AIAA/ASME/SAE/ASEE Joint Propulsion Conference*, AIAA 2002-3725, 2004.

[11] Bohan, B. T., *Analysis of Flow Migration in an Ultra-Compact Combustor*, Master's thesis, AFIT/GAE/ENY/11-M02. Graduate School of Engineering and Management, Air Force Institute of Technology (AU), Wright-Patterson AFB, OH, March 2011.

[12] Law, C. K., *Combustion Physics*, Cambridge University Press, 2006.

[13] Lewis, G. D., "Swirling flow combustion – fundamentals and application," *9th AIAA/SAE Joint Propulsion Conference*, AIAA 73-1250, 1973.

[14] Lapsa, A. P. and Dahm, W. J., "Hyperacceleration effects on turbulent combustion in premixed step-stabilized flames," *Proceedings of the 32nd Combustion Institute*, 2009.

[15] Eckbreth, A. C., *Laser Diagnostics for Combustion Temperature and Species*, CRC Press, 1988.

[16] Kostka, S., Roy, S., Lakusta, P., Meyer, T. R., Renfro, M. W., Gord, J. R., and Branam, R. D., "Comparison of line-peak and line-scanning excitation in two-color laser-induced fluorescence thermometry of OH," *Applied Optics*, Vol. 38, No. 32, 2009.

[17] Dantec Dynamics, *2D PIV Reference Manual (2nd edition)*, DK-2740 Skuvlunde, Denmark, 2006.

[18] Cross, C., Lubarsky, E., Shcherbik, D., Bonner, K., Klusmeyer, A., Zinn, B. T., and Lovett, J. A., "Determination of Equivalence Ratio and Oscillatory Heat Release Distributions in Non-Premixed Bluff Body-Stabilized Flames Using Chemiluminescence Imaging," *ASME Turbo Expo 2011*, GT1011-45579, 2011.

[19] Wilson, J., Bohan, B., LeBay, K., and Polanka, M., "Design of a Fighter Sized UCC Section," *AIAA DCASS 2011*, 1 March 2011.

[20] Benhassen, F., *Time Resolved Filtered Rayleigh Scattering Measurement of a Centrifugally Loaded Buoyant Jet*, Master's thesis, AFIT/GAE/ENY/11-M01. Graduate School of Engineering and Management, Air Force Institute of Technology (AU), Wright-Patterson AFB, OH, March 20011.

[21] Anderson, T. N., Lucht, R. P., Meyer, T. R., Roy, S., and Gord, J. R., "Diode-laser-based ultraviolet-absorption sensor for high-speed detection of the hydroxyl radical," *Optics Letters*, Vol. 30, No. 11, 2005.

[22] Meents, S. M., *Filtered Rayleigh Scattering Measurements in a Buoyant Flow Field*, Master's thesis, AFIT/GAE/ENY/08-M22. Graduate School of Engineering and Management, Air Force Institute of Technology (AU), Wright-Patterson AFB, OH, March 2009.

[23] Boguszko, M. and Elliot, G. S., "Property measurement utilizing atomic/molecular filter-based diagnostics," *Progress in Aerospace Sciences*, Vol. 41, 2005.

[24] Egolfopoulos, F. N., "Principles of Combustion Course Lecture," Spring Semester 2007.

[25] Karbuz, S., "US Military energy consumption - facts and figures," *Energy Bulletin*, 2007.

[26] AIAA Position Paper, "Versatile Affordable Advanced Turbine Engines (VAATE) Initiative," *Air Breathing Propulsion Technical Committee*, AIAA, 2006.

[27] Yonezawa, Y., Toh, H., Goto, S., and Obata, M., "Development of the jet-swirl high loading combustor," *26th AIAA/SAE/ASME/ASEE Joint Propulsion Conference*, AIAA-90-2451, 1990.

[28] Quaale, R. J., Anthenian, R. A., Zelina, J., and Ehret, J., "Flow Measurements Within a High Swirl Ultra Compact Combustor for Gas Turbine Engines," *2003 International Symposium on Air Breathing Engines*, ISABE 2003-1141, 2003.

[29] Thomas, L. M., *Flow Measurements Using Particle Image Velocimetry in the Ultra Compact Combustor*, Master's thesis, AFIT/GAE/ENY/09-D04. Graduate School of Engineering and Management, Air Force Institute of Technology (AU), Wright-Patterson AFB, OH, December 2009.

[30] Vogeler, K., "The Potential of Sequential Combustion for High Bypass jet Engines," *ASME Turbo Expo 1998*, ASME 98-GT-311, 2-5 June 1998.

[31] Lukachko, S. P., Kirk, D. R., and Waitz, I. A., "Turbine Durability Impacts of High Fuel-Air Ratio Combustors, Part 1: Potential For Intra-Turbine Oxidation of Partially-Reacted Fuel," *ASME Turbo Expo 2002*, GT-2002-30077, 2002.

[32] Kirk, D. R., Guenette, G. R., Lukachko, S. P., and Waitz, I. A., "Gas Turbine Engine Durability Impacts of High Fuel-Air Ratio Combustors Part 2: Near Wall Reaction Effects on Film-Cooled Heat Transfer," *ASME Turbo Expo 2002*, GT-2002-30182, 2002.

[33] Sekar, B., Thornburg, H. J., Briones, A. M., and Zelina, J., "Effect of Trapped Vortex Combustion with Radial Vane Cavity Arrangements on Predicted Inter-Turbine Burning Performance," *7th International Energy Conversion Engineering Conference*, AIAA-2009-4603, 2009.

[34] Briones, A., Sekar, B., Thornburg, H., and Zelina, J., "Effect of Vane Notch and Ramp Design on the Performance of a Rectangular Inter-Turbine Burner," *48th Aerospace Sciences Meeting*, AIAA-2010-0581, 2010.

[35] Hiddeman, M. and Marx, P., "Operating Experience with the Latest Upgrade of Alstom's Sequential Combustion GT26 Gas Turbine," *ASME Turbo Expo 2010*, GT2010-23571, 2010.

[36] Zelina, J., Greenwood, R. T., and Shouse, D. T., "Operability and Efficiency Performance of Ultra-Compact, High Gravity (g) Combustor Concepts," *ASME Turbo Expo 2006*, GT-2006-90119, 2006.

[37] Zelina, J., Shouse, D. T., and Hancock, R. D., "Ultra-Compact Combustors for Advanced Gas Turbine Engines," *ASME Turbo Expo 2004*, GT-2004-53155, 2004.

[38] Radtke, J. T., *Efficiency and Pressure Loss Chracteristics of an Ultra-Compact Combustor with Bulk Swirl*, Master's thesis, AFIT/GAE/ENY/07-J18. Graduate School of Engineering and Management, Air Force Institute of Technology (AU), Wright-Patterson AFB, OH, June 2007.

[39] Anisko, J., *Numerical Investigation of Cavity-Vane Interactions Within the Ultra-Compact Combustor*, Master's thesis, AFIT/GAE/ENY/06-M01. Graduate School of Engineering and Management, Air Force Institute of Technology (AU), Wright-Patterson AFB, OH, March 2006.

[40] Moenter, D. S., *Design and Numerical Simulation of Two Dimensional Ultra-compact Combustor Model Sections for Experimental Observation of Cavity-Vane Flow Interactions*, Master's thesis, AFIT/GAE/ENY/06-S07. Graduate School of Engineering and Management, Air Force Institute of Technology (AU), Wright-Patterson AFB, OH, September 2006.

[41] Koether, S. J., *Validation of the AFIT Small Scale Combustion Facility and OH Laser-Induced Fluorescence of an Atmospheric Laminar Premixed Flame*, Master's thesis, AFIT/GAE/ENY/07-S03. Graduate School of Engineering and Management, Air Force Institute of Technology (AU), Wright-Patterson AFB, OH, September 2007.

[42] Lakusta, P. J., "Laser-Induced Fluorescence and Performance Analysis of the Ultra-Compact Combustor," June 2008.

[43] Turns, S. R., *An Introduction to Combustion (2nd Ed.)*, Cambridge University Press, Cambridge, UK, 1996.

[44] Heffernen, J. J., *Characterization of Horizontally-Issuing Reacting Buoyant Jets*, Master's thesis, AFIT/GAE/ENY/11-M12. Graduate School of Engineering and Management, Air Force Institute of Technology (AU), Wright-Patterson AFB, OH, March 2011.

[45] Kolhe, P. S. and Agrawal, A. K., "Role of Buoyancy on Instabilities and Structure of Gas Jet Diffusion Flames," *Flow, Turbulence and Combustion*, Vol. 89, 2007.

[46] Subbarao, E., "The Effects of Reynolds Number and Richardson Number on the Structure of a Vertical Co-flowing Buoyant Jet," *20th Fluid Dynamics, Plasma Dynamics and Lasers Conference*, AIAA 89-1800, 1989.

[47] Sherif, S. A. and Pletcher, R. H., "Jet Wake Thermal Characteristics of Heated Turbulent Jet in Cross Flow," *1st National Fluid Dynamics Conference*, AIAA/ASME/SIAM/APS A88-48776, 2009.

[48] Serianne, C. R., *Tunable Diode Laser Absorption Spectroscopy Verification Analysis for Use in the Combustion Optimization and Analysis Laser Laboratory*, Master's thesis, AFIT/GAE/ENY/09-M17. Graduate School of Engineering and Management, Air Force Institute of Technology (AU), Wright-Patterson AFB, OH, March 2009.

[49] Muraoka, K. and Maeda, M., *Laser-aided diagnostics of plasmas and gases*, Institute of Physics, 2001.

[50] Seitzman, J. M., Hanson, R. K., DeBarber, P. A., and Hess, C. F., "Application of quantitative two-line OH planar laser induced fluorescence for temporally resolved planar thermometry in reacting flow," *Applied Optics*, Vol. 33, No. 18, 20 June 1994.

[51] Cattolica, R. J., "OH rotational temperature from two-line laser excited fluorescence," *Applied Optics*, Vol. 20, 1981.

[52] Lucht, R. P., Laurendeau, N. M., and Sweeney, D. W., "Temperature measurement by two-line laser-saturated OH fluorescence in flames," *Applied Optics*, Vol. 21, No. 20, 15 October 1981.

[53] Meier, U. E., Wolff-Gabmann, D., and Stricker, W., "LIF imaging and 2D temperature mapping in a model combustor at elevated pressure," *Aerospace Science and Technology*, Vol. 4, 28 March 2000.

[54] Giezendanner-Thoben, R., Meier, U., Meier, W., Heinze, J., and Aigner, M., "Phase-locked two-line OH planar laser-induced fluorescence thermometry in a pulsating gas turbine model combustor at atmospheric pressure," *Applied Optics*, Vol. 44, No. 31, 01 November 2005.

[55] Welle, E. J., Roberts, W. L., Carter, C. D., and Donbar, J. M., "The response of a propane-air counter-flow diffusion flame subjected to a transient flow field," *Combustion and Flame*, Vol. 135, 20 June 2003.

[56] Hancock, R. D., Bertagnolli, K. E., and Lucht, R. P., "Nitrogen and Hydrogen CARS Temperature Measurements in a Hydrogen-Air Flame Using a Near-Adiabatic Flat-Flame Burner," *Combustion and Flame*, Vol. 109, 1997.

[57] Chan, V. S., Delaure, Y. M., Murray, D. B., and Fitzpatrick, J. A., "Optical considerations for time-resolved digital PIV measurement in a single bubble flow against heated boundaries," *Measurement Science and Technology*, Vol. 15, 2004.

[58] Murphy, M. J. and Adrian, R. J., "PIV space-time resolution of flow behind blast waves," *Experiments in Fluids*, Vol. 49, 2010.

[59] Schmidt, J., Kostka, S., Lynch, A., and Ganguly, B., "Simultaneous particle image velocimetry and chemiluminescence visualization of millisecond-pulsed current–voltage-induced perturbations of a premixed propane/air flame," *Experiments in Fluids*, Vol. 51, 2011.

[60] Melling, A., "Tracer particles and seeding for particle image velocimetry," *Measurement Science and Technology*, Vol. 8, 1997.

[61] Sincock, A. L., *Design of a Film Cooling Experiment for Rocket Engines*, Master's thesis, AFIT/GAE/ENY/10-M23. Graduate School of Engineering and Management, Air Force Institute of Technology (AU), Wright-Patterson AFB, OH, March 2010.

[62] Mathieu, J. and Scott, J., *An Introduction to Turbulent Flow*, McGraw-Hill, Inc., New York, NY, 2000.

[63] Schultz, C., Kock, B. F., Hofmann, M., Michelsen, H., Will, S., Bougie, B., Suntz, R., and Smallwood, G., "Laser-induced incandescence: recent trends and current questions," *Applied Physics B - Lasers and Optics*, Vol. 83, No. 1, 2006.

[64] McCartney, E. J., *Optics of the Atmosphere: Scattering by Molecules and Particles*, John Wiley and Sons, 1976.

[65] Reeder, M. F., Huffman, R. E., Branam, R. D., LeBay, K. D., and Meents, S. M., "Near-field development of gas-phase horizontal laminar jets with positive and negative buoyancy measured with filtered Rayleigh scattering," *Experiments in Fluids*, Vol. 50, 2010.

REPORT DOCUMENTATION PAGE

Form Approved
OMB No. 0704–0188

1. REPORT DATE (DD–MM–YYYY)	2. REPORT TYPE	3. DATES COVERED *(From — To)*
10-28-2011	Doctoral Dissertation	Aug 2008 – Oct 2011

4. TITLE AND SUBTITLE

Characterization of Centrifugally-Loaded Flame Migration for Ultra-Compact Combustors

5a. CONTRACT NUMBER

5b. GRANT NUMBER

5c. PROGRAM ELEMENT NUMBER

6. AUTHOR(S)

Kenneth D. LeBay, Capt., USAF

5d. PROJECT NUMBER

5e. TASK NUMBER

5f. WORK UNIT NUMBER

7. PERFORMING ORGANIZATION NAME(S) AND ADDRESS(ES)
Air Force Institute of Technology
Graduate School of Engineering and Management (AFIT/ENY)
2950 Hobson Way
WPAFB OH 45433-7765

8. PERFORMING ORGANIZATION REPORT NUMBER

AFIT/DS/ENY/11-22

9. SPONSORING / MONITORING AGENCY NAME(S) AND ADDRESS(ES)
Air Force Research Laboratory
Combustion Branch, Turbine Engine Division (AFRL/RZTC)
1950 5th St Bldg 490, Rm 114
WPAFB, OH 45433
PH: 937-255-7487 Email: Joseph.Zelina@WPAFB.AF.MIL

10. SPONSOR/MONITOR'S ACRONYM(S)
AFRL/RZTC

11. SPONSOR/MONITOR'S REPORT NUMBER(S)

12. DISTRIBUTION / AVAILABILITY STATEMENT
APPROVED FOR PUBLIC RELEASE; DISTRIBUTION UNLIMITED

13. SUPPLEMENTARY NOTES
This material is declared a work of the U.S. Government and is not subject to copyright protection in the United States.

14. ABSTRACT

The Air Force Research Laboratory (AFRL) has designed an Ultra Compact Combustor (UCC) showing viable merit for significantly reducing gas turbine combustor length making it a viable candidate for implementation as an inter-turbine burner and realization of efficiency benefits from the resulting near constant temperature cycle. This concept uses an off-axis combustor cavity and projects approximately 66% length reduction over a conventional combustor. The annular nature of the cavity creates high angular acceleration levels, on the order of 500-3500 g's, resulting in strong centrifugal and buoyant forces. This unique combination works to significantly reduce the required burn time and subsequently required combustor size. However, currently tested experimental models are in the 10-20 cm diameter range while application to larger-scale commercial and military engines would require a UCC in the 50-60 cm diameter range. The Air Force Institute of Technology's Combustion Optimization and Analysis Laser (COAL) laboratory was specifically designed to study the underlying UCC dynamics and investigate the feasibility of scaling the UCC to the significantly larger diameter range. Using a sectional model of AFRL's annular UCC allows customization of the UCC model to investigate varying several parameters of interest associated with the UCC scaling. Several diagnostic methods were used such as Particle Image Velocimetry (PIV) for fowfield measurements, two-line Planar Laser-Induced Fluorescence (PLIF) of the hydroxyl (OH) radical for 2-D temperature profiles, single-line PLIF for qualitative flame location, and high-speed video to investigate flame migration trajectory.

The overarching goal of this research was to characterize the migration of centrifugally loaded flames in the Ultra Compact Combustor. The v-shaped flame at the ambient UCC exit of the straight UCC section observed by Drenth was determined to be unaffected by the addition of or variations of the centrifugal loading. Drenth's observed change in flame shape was the result of an two-fold difference in the ambient UCC exit area that changed the flow dynamics and resultantly the flame shape. However, the presence of centrifugal loading did change the orientation of the v-shape adding an inclination to the outward radial direction. The ambient UCC exit flame shape was affected by the UCC/core velocity ratio with the flame distribution being weighted more to the leeward leg at higher ratios due to increased migration into the core which pulled from the windward leg first. When scaling the UCC to a larger radius, it was determined that matching the same UCC/core velocity ratio produced the same flame injection angle into the core flow which can then be used to predict the penetration depth of the flame based on geometry. It was also determined that while the velocity ratio determines the injection angle, the g-load affects the quantity of mass flux from the UCC into the core with higher g-loads yielding higher mass flux. The velocity ratio was also shown to affect the mass flux with lower ratios yielding higher mass flux quantity but producing lower core flow equivalence ratios due to sufficiently higher core air mass. Higher mass flux at the same velocity ratio directly leads to higher core flow temperatures and higher planer vorticity. It was also demonstrated that the mass flux into the core can be estimated using pressure & temperature measurements upstream and PIV measurements downstream of the core flow interface with constant density and tangential velocity profile assumptions. The mass flux quantity can be used to estimate the core Á using the UCC/core mass flow ratio, and subsequently the core flow temperature. The estimated core flow temperatures were in good agreement with the measured values using OH PLIF. The mass flux was estimated to scale linearly with tangential velocity, which corresponds to the g-load value, while testing at various UCC/core velocity ratios resulted in similar linear relationships of different slopes. The slope was determined to be a function of the velocity ratio resulting in a simple relation showing the dependence of the mass flux on the tangential velocity and the velocity ratio. Estimates were made to account for changes in the UCC equivalence ratio on the mass flux resulting in a single, relatively simple, relation showing the dependence of the mass flux on all of the parameters investigated in this study (tangential velocity, velocity ratio, & UCC equivalence ratio). Using the mass flux estimations and the UCC/core mass flow ratio, the core flow equivalence ratio can be estimated along with the average combustor exit temperature, which will be similar to the turbine inlet temperature. The quantitative relationships determined in this research provided a detailed description of the migration of centrifugally loaded flames in the Ultra Compact Combustor.

15. SUBJECT TERMS
Combustion, centrifugal load, ultra compact combustors, flame migration

16. SECURITY CLASSIFICATION OF:			17. LIMITATION OF ABSTRACT	18. NUMBER OF PAGES	19a. NAME OF RESPONSIBLE PERSON
a. REPORT	b. ABSTRACT	c. THIS PAGE	UU	316	Dr. Marc D. Polanka (ENY)
U	U	U			19b. TELEPHONE NUMBER (Include Area Code) (937)255-3636, ext 4714 Marc.Polanka@afit.edu